INFORMATION TO USERS

This manuscript has been reproduced from the microfilm master. UMI films the text directly from the original or copy submitted. Thus, some thesis and dissertation copies are in typewriter face, while others may be from any type of computer printer.

The quality of this reproduction is dependent upon the quality of the copy submitted. Broken or indistinct print, colored or poor quality illustrations and photographs, print bleedthrough, substandard margins, and improper alignment can adversely affect reproduction.

In the unlikely event that the author did not send UMI a complete manuscript and there are missing pages, these will be noted. Also, if unauthorized copyright material had to be removed, a note will indicate the deletion.

Oversize materials (e.g., maps, drawings, charts) are reproduced by sectioning the original, beginning at the upper left-hand corner and continuing from left to right in equal sections with small overlaps.

UMI®

.

University of Alberta

Surface Effects of Microchannel Wall on Microfluidics

By

Jun Yang ©

A thesis submitted to the Faculty of Graduate Studies and Research in partial fufillment of the requirements for the degree of **Doctor of Philosophy**

Department of Mechanical Engineering

Edmonton, Alberta, Canada

Spring 2004

Canada

Abstract

Microfluidics is widely used in MEMS (microelectromechanical system) devices. Because of the large ratio of surface area to liquid volume of microfluidics, surface effects significantly influence the fluid behavior. In this thesis, two surface effects: electrical double layer (EDL) and hydrophobicity are studied. We have performed fundamental modelling of time-dependent electrokinetic flow in rectangular, circular and parallel-plate microchannels. A new model, combining electrokinetic phenomena with slippage of microfluidics, is created and the corresponding analytical solutions of time-dependent electrokinetic slip flow in rectangular, circular and parallel-plate microchannels are obtained. According to our study, electrokinetic phenomena and hydrophobicity should be considered simultaneously. Electroosmotic flow with a moving front is a typical case governed by EDL phenomena and surface hydrophobicity. In this thesis, we first propose an analytical model to describe this phenomena. Based on these models, we further study the microfluidic flow in a heterogeneous microchannel with nonuniform surface potential and hydrophobicity. We also investigate the effects of different EDL models on microchannel flow. Comparison of these models suggests that the Possion-Boltzmann equation is still a valid model to describe the charge distribution in EDL of microfluidics.

According to the above theoretical study, potential applications of microfluidics are proposed. A new method to determine zeta potential (or surface potential) and slip length is proposed, which overcomes the defect of the current zeta potential measurement method on hydrophobic surfaces. We also extend our research to membrane science, where a method is proposed to determine unknown parameters and structure of multilayer membranes by means of a high frequency alternating electric field. By means of streaming current or streaming potential, we designed two novel electrokinetic batteries, allowing us to light up two LEDs. We also found that slip coating

can improve efficiency of microfluidic MEMS devices. A promising slip coating for MEMS devices, Self-Assembled Monolayers (SAMs), is proposed. In experiments, we observed slippage of flow on $Au/S(CH_2)_{17}CH_3$ Self-Assembled Monolayers (SAMs). The slip lengths of SAMs were experimentally determined.

Acknowledgements

I highly appreciate all those who provided support and encouragement during my PhD program.

I would like to acknowledge my adviser, Professor Daniel Y. Kwok, for his patient guidance, continual support and helpful suggestions in my research. With his introduction, I began to know that surface/interface science was so important and is promising research field. I am fully grateful for what he has done for me in these years.

I sincerely thank my co-adviser, Professor Jacob H. Masliyah, for his advice, guidance, patience and encouragement. Professor Jacob H. Masliyah guided me into another big area, electrokinetic phenomena.

I also sincerely thank my initial adviser, Professor Abhijit Bhattacharyya, for his initial recruitment into the booming area, microfluidics.

I would also like to express my greatest thanks to the Chair of our department, Professor Larry W. Kostiuk, for his suggestion and equipment support.

I would like to express my gratitude to a supervisory committee member, Professor Chongqing Ru.

Also, I thank the founder of the modified Poisson-Boltzmann equation, Professor Christopher W. Outhwaite, from Sheffield University, for his help and discussion.

At last, I highly acknowledge financial support from the Alberta Ingenuity Scholarship.

Table of Contents

List of Tables

List of Figures

Chapter 1

Introduction

1.1 Microfluidic MEMS devices

During the past two decades, microfabrication technology has a significant impact on biology, medicine, chemistry, aerospace, mechanical and electrical engineering. Requirement of transportation of fluids in or between MEMS (microelectromechanical system) devices causes a fast development of microfluidic MEMS devices, which realizes transport processes in microscale through microchannel flows. In recent report of System Planning Corporation [1], the MEMS device market is predicted to be tripled up to 11.5 billion by the year 2003. The estimated microfluidic market is on the order of 3 to 4.5 billions with an annual growth rate of 25% to 35% [2].

Typical microfluidic devices include microvalves, flow transducers, micropumps and heat exchangers. Microvalves are used for flow control and can be classified into two categories: active (with an actuator) and passive microvalves (without an actuator) [3, 4]. Micro flow transducers are classified into micro flow sensors and micro flow actuators. Micro flow sensors have been used to measure flow velocity [5], pressure [6, 7], temperature [6] and shear stress [8]. Microflow actuators normally provide force or displacement under electrostatic or electromagnetic field. Micropumps can be divided into two categories: mechanical and non-mechanical pumps. The former usually utilizes moving parts to deliver a constant fluid volume in each pump cycle [9]; The latter adds momentum to fluids for pumping by converting other form of energy

1

into the kinetic energy. Mechanical pumps are mostly used in macroscale pumps with relatively large size and large flow rate [2]. When smaller size is required, moving parts of mechanical pumps become the shortcoming. Non-mechanical pumps without moving parts can overcome this deficiency. Readily-made nonmechanical pumps are electrodynamic pumps [10], electrokinetic pumps [11] and electrowetting pumps [12, 13], whose sizes can be the order of microns. Furthermore, implantable micropump and drug delivery systems [14, 15] are also a promising idea in medicine. Patients who need periodic injection, can be liberated from seeing a doctor frequently. Heat exchangers are the most important parts of a cooling system. Its ability to efficiently transfer heat between fluids is important in various applications such as automobile radiators, air conditioning, electrical cooling and aerospace applications. As energy density in microchip becomes higher, industry begins to look for heat exchangers working by liquids with high efficiency. By constraining the flow to narrow channels, the efficiency of heat transfer can be significantly enhanced as the surface area to volume ratio increases, causing the convective resistance at the solid/fluid interface to be reduced [16, 17].

1.2 Lab-on-a-chip technology

In the market report [1], microfluidic devices for DNA detection, protein analysis, medicine testing and drug delivery are emphasized. Because of its less time, cost and sample/reagent consumption, portability and simpleness to control, Lab-on-a-chip becomes the most promising microfluidic technology to substitute for traditional methods in chemistry and biology. Harrison [18] first proposed the idea of Lab-on-a-chip by means of electroosmosis. An electric field was used to drive liquid sample from one reservoir to another through a microchannel. Harrison's group developed this chemical detection technology in a microchannel network, so that more complex chemical experiments can be fulfilled on a glass or silicon chip [19, 20, 21].

2

The entire Lab-on-a-chip experimental process includes filtration, transport/pumping, mixing, separation and reaction. Electroosmosis is often used to drive testing liquid into detection zone. Electrophoresis is often used to separate cells or proteins from reagent. Pressure-driven flow is also a useful pumping method on a microchip [22]. In this case, gas pressure, micro-peristaltic and positive displacement are common choices.

There are many functional technologies to manufacture biochip/microarray-chip [23, 24]. Here, we only emphasize two of the most popular techniques: traditional lithographic technique and the soft lithography technique. Traditional lithographic technique uses an electromagnetic radiation, typically ultraviolet (UV) light to "print" a designed pattern onto a surface, e.g. silicon, covered with photoresist. Recently developed soft lithography technique fills a heat or UV-curable polymer in a template, made by traditional lithographic techniques, to cast numerous replicas of the desired devices [25, 26]. Based on soft lithography techniques, glass and silicon are not the only choice for the substrates of microfluidic systems. Polymer plays a more important role in the substrates of microchips [27].

1.3 Surface effects on microfluidics

Microfluidics is a multi-disciplinary research. Many physical and chemical phenomena, which can normally be neglected in traditional fluid mechanics, are involved. The most noticeable feature of microfluidics is that chemical and physical properties of surfaces are no longer negligible. Because of the relatively large surface-to-volume and surface-force-to-body-force ratios in micron-scale configurations, surface effects dominate most of the transport phenomena in microchannels [28], which cause apparent differences between microfluidics and macrofluidics. Since the traditional hydrodynamic theory cannot predict microfluidic behavior, fundamental understanding including interactions between liquid and solid wall becomes an essential issue. In

3

Israelachvili's book [29], several kinds of surface forces are introduced. In general, van der Waals, electrostatic and hydrate forces should be considered. In this thesis, we consider electrostatic force induced by electrical double layer; the van der Waals force and hydrate force reflected by surface tension (or hydrophobicity).

1.3.1 Electrical double layer and electrokinetic phenomena

In 1808, Reuss discovered electroosmotic effects [30]. In 1859, Quinke [31] discovered the streaming potential phenomenon. Electrokinetic phenomena are essential issues in colloid and interface/surface science. Electrokinetic theory is widely applied for many fields: chemistry, chemical engineering, aerospace science, biology, medicine, environment, civil and mechanical engineering. Electrokinetic phenomena have already played very important roles in industry: mining, ceramics, paints, pharmaceutics, paper making, waste water treatment and petroleum.
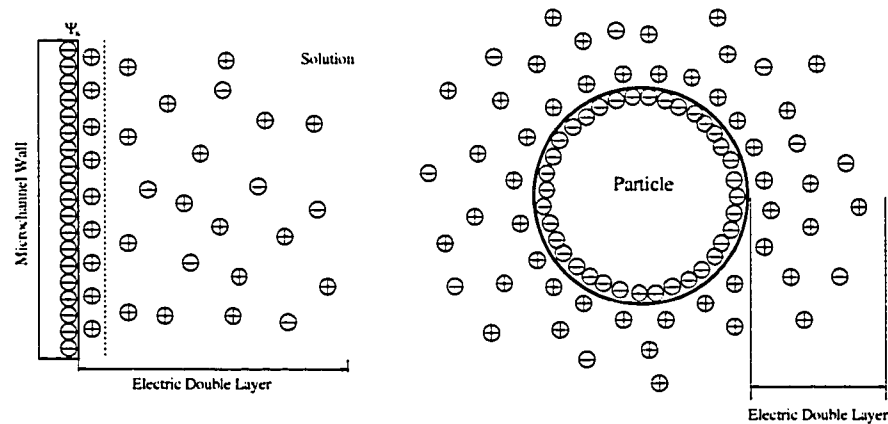
Figure 1.1: Schematic of an electrical double layer near a plate wall and surround a particle.

Electrical double layer

In general, electrically neutral liquids have a distribution of electrical charges near a surface because of a charged solid surface [32, 33, 34]. This region is known as

4

electrical double layer (EDL), which induces electrokinetic phenomena. In Figure 1.1, we show two schematic diagrams for electrical double layer near a plate surface or a charged particle. The density of counter-ions (opposite in sign to the charge of solid surface) is larger than that of the co-ions (the same in sign as the charges of solid surface) in most place of EDL [32, 33]. EDL is normally accounted from the solid surface to where the net charge decreases to zero (neutral) [32, 33].
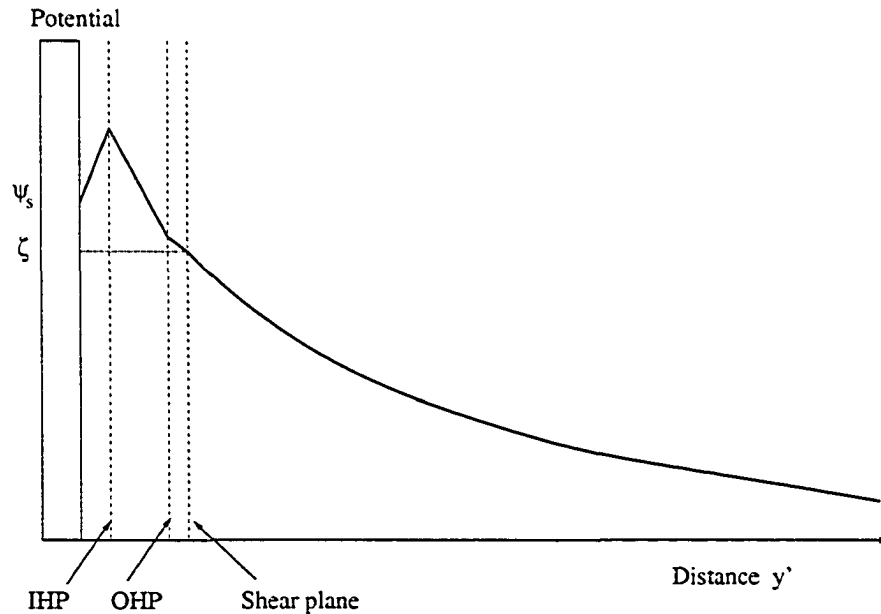
Figure 1.2: Schematic of potential distribution in an electrical double layer.

The concept of electrical double layer was proposed by Helmholtz [35] over a century ago. Gouy [36] and Chapman [37] independently introduced the theory of diffusion layer. In general, the electrical double layer is divided into two layers: an inner/compact layer of immobile counter-ions and a diffusion layer formed by a cloud of hydrated ions that transitions from the extreme excess of counter-ions at the boundary of inner layer to a balance of counter-ions and co-ions in the neutral bulk solution [32, 33]. To describe the ionic and potential distribution in the electrical double layer, many artificial models have been created. At present, the most widely

5

accepted and detailed model is shown in Figure 1.2. In Figure 1.2, the inner layer is further divided by inner Helmholtz plane (IHP), outer Helmholtz plane (OHP) and shear plane. The potential at shear plane is normally called the zeta potential. Outside the shear plane along the y' direction, the diffusion layer begins [32, 33].

The origins of interfacial charges come from the following various mechanism [32, 33, 38]:

1. Ionization of surface group,

2. Differential dissolution of ions from surfaces of sparingly soluble crystals,

3. Isomorphic substitution,

4. Charged crystal surface,

5. Specific ion adsorption.

The first mechanism is the most common mechanism for EDL formation.

On the mathematical side, the most popular model to describe the ionic and potential distribution in EDL is Poisson-Boltzmann equation, which is based on the following premises [33, 32]:

1. Ions are point charge.

2. The ionic adsorption energy is purely electrostatic.

3. The average electric potential (as occurring in Poisson's law) is identified with the potential of mean force (in Boltzmann equation).

4. The solvent is primitive.

Firstly, the Poisson equation is

$$\nabla^2 \psi = -\frac{\rho}{\epsilon} , \qquad (1.3.1)$$

6

where ψ is the potential due to the double layer at an equilibrium state (i.e., no liquid motion with no applied external field), ρ is the free charge density and ϵ is the permittivity of the medium. Using Boltzmann equation, for a symmetrical $z_0 : z_0$ valent electrolyte, we can express the Poisson-Boltzmann equation as

$$\nabla^2 \psi(x, y, z) = \frac{2n_\infty z_0 e}{\epsilon} \sinh[\frac{z_0 e \psi(x, y, z)}{kT}] . \tag{1.3.2}$$

where z_0 is the valence of the symmetrical electrolyte, e is the elementary charge, n_∞ is the ionic concentration in an equilibrium electrochemical solution at the neutral state with $\psi = 0$, k is the Boltzmann constant and T is the absolute temperature. Invoking the Debye-Hückel approximation for low surface potentials ($z_0 e \psi / kT \ll 1$), we have $\sinh(z_0 e \psi / kT) \approx z_0 e \psi / kT$ and the total charge density becomes

$$\rho = \frac{-2n_\infty e^2 z_0^2}{kT} \psi . \tag{1.3.3}$$

Finally, the definition of the reciprocal of the double layer thickness for a ($z_0 : z_0$) electrolyte is given as

$$\kappa = \sqrt{\frac{2n_\infty e^2 z_0^2}{\epsilon kT}} . \tag{1.3.4}$$

Combining Eq.(1.3.4) with the Debye-Hückel approximation, Eq.(1.3.2) results in the linearized Poisson-Boltzmann equation:

$$\nabla^2 \psi(x, y, z) = \kappa^2 \psi(x, y, z) . \tag{1.3.5}$$

In fact, Debye-Hückel approximation gives a good agreement with experiments when zeta potential is up to 100 mV [33].

Even though Poisson-Boltzmann equation has been successfully applied for many problems, it still has some defects as outlined below [32]

1. The finite sizes of the ions are neglected.

2. Non-Coulombic interaction between counter- and co-ions and surface is disregarded.

7

3. Incomplete dissociation of the electrolyte is ignored.

4. The solvent is considered to be primitive.

5. The surface charge is assumed to be homogeneous and smeared-out.

6. Image forces between ions and the surface are neglected.

Ion size is an obvious feature, which should be considered, especially for a very narrow microchannel. When the surface potential is higher than 100 mV, Poisson-Boltzmann equation predicts local concentrations to exceed the amount that is physically available in space [32]. Ion-ion correlations are still very important and should appear in Poisson-Boltzmann equation. If the surface charge is not homogeneous, image force in the solid also plays an important role.

To overcome Poisson-Boltzmann equation's shortcomings, many improvements have been done [39, 40, 41, 42, 43, 44, 45]. However, more molecular parameters are involved and computation becomes more expensive. Basically, all new models come from the statistical mechanics. A review about electrical double layer from the statistical mechanics point of view has been published [46]. Two contributions should be mentioned here: Cassou's hypernetted chain-mean spherical (HNC/MS) integral equation [40, 41, 42] and Outhwaite's modified Poisson-Boltzmann equation [44, 45]. The former considers the ionic size, ionic concentration and ionic interaction effect. Other than the above effects, the latter model additionally includes the image force of solid surface.

Electrokinetic phenomena

Actually, electrokinetics is the general term associated with the bulk relative motion between two charged phases. The electrokinetic phenomena arise when attempts are made to shear off the mobile part of the electrical double layer from a charged surface [38, 47]. If an external electric field is applied to the electrical double layer, the two

8
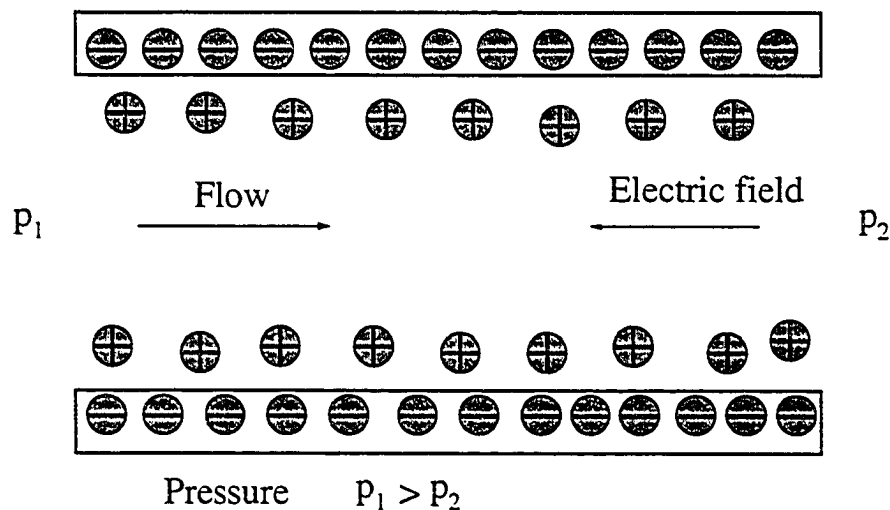
Figure 1.3: Schematic of streaming potential.

charged phases with counter charges intend to move along counter direction. As a result, solvent will be carried with the motion of the two phases. In this case, the solvent appears to be moved by a body force. On the other hand, if solvent moves under an external force, moveable ions in electric double layer will redistribute and form an electric field [32, 33, 38].

The four principal electrokinetic phenomena are streaming potential, electroosmosis, electrophoresis and sedimentation. For pressure driven flow, the effect of EDL during an externally applied pressure gradient is to retard liquid flow, at equilibrium, resulting in a streaming potential (Figure 1.3). For electric field driven flow without an external pressure gradient, EDL induces fluid flow under an external electric field (electroosmotic pumping, Figure 1.4). Motion of charged particles in a stationary electrolyte under an applied external electric field is called electrophoresis (Figure 1.5). A sedimentation potential is created, when charged particles are moved under gravitational or centrifugal fields (Figure 1.6) [38]. Streaming potential, electroosmosis and electrophoresis are commonly used experimental methods to determine zeta potential. These processes are summarized in Table 1.1.

9
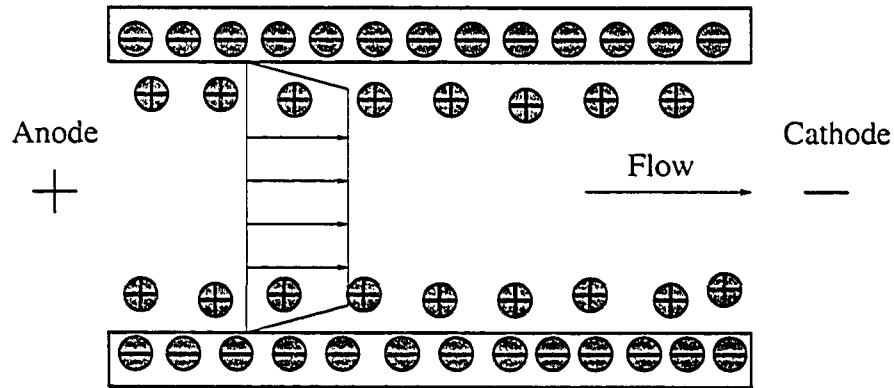
Figure 1.4: Schematic of electroosmosis.

Table 1.1: A summary of electrokinetic phenomena

Phenomena	Moving phase	Driving force	what is caused
Streaming potential	liquid	pressure gradient	potential
Electroosmosis	liquid	external electric field	liquid movement
Electrophoresis	particles	external electric field	particle movement
Sedimentation	particles	gravitational or centrifugal fields	potential

1.3.2 Literature review of electrokinetic flow in microchannel

Applications of electrokinetics in cooling of microelectronics [16, 48, 49], lab-on-a-chip diagnostic devices [18] and *in vivo* drug delivery systems [14, 15] are possible, by relying the flow to be time-dependent (e.g. oscillatory). Therefore, it is desirable to carry out time-dependent studies of the flow hydrodynamics in microchannels inclusive of EDL effects. A review of the open literature shows that modelling on the flow hydrodynamics with EDL effects has been confined primarily to steady state response. Von Smoluchowski [50, 51] studied electroosmotic flow in case of a very thin EDL thickness and formulated the basic electrokinetic relationships. Debye and Hückel [52] determined the ionic distribution by means of linearized Poisson-Boltzmann equation. One of the earliest systematic studies was by Rice and Whitehead [53] who studied steady-state liquid flow induced by a pressure gradient or an electric field

10
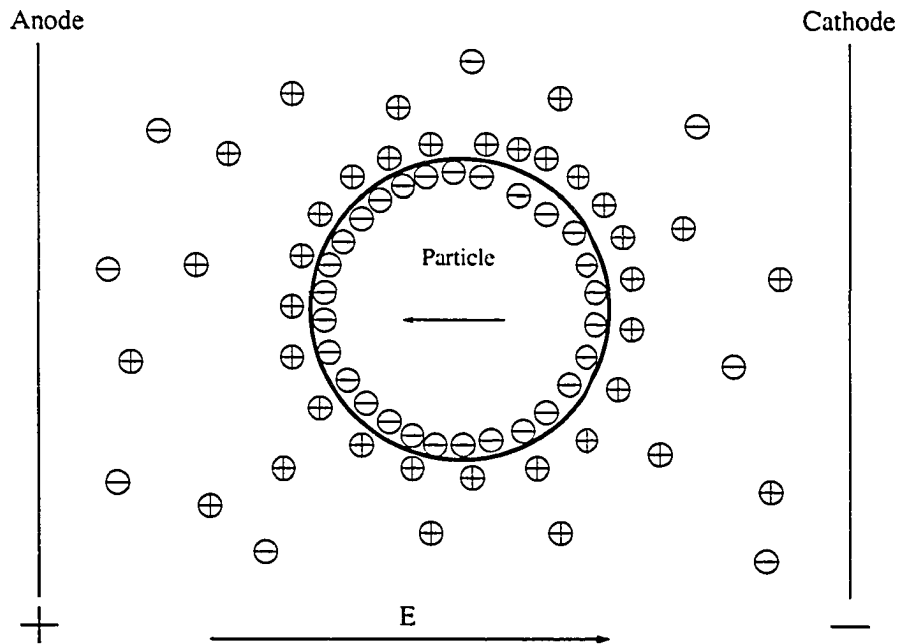
Figure 1.5: Schematic of electrophoresis.

in thin circular capillaries. Levine *et al.* [54] studied the electrokinetic steady flow in a narrow parallel-plate microchannel. Burgreen and Nakache [55] provided the complete analytical solutions of electrokinetic flow in parallel-plate slit. Levine *et al.* [56] carried out a semi-analytical extension of Rice and Whitehead's work for high surface potential. Recently, studies in electrokinetic flow in microchannels have been a hot topic. On the theoretical side, Yang *et al.* [57] studied the steady state flow in rectangular microchannels; Mala *et al.* [58] studied flow behavior in parallel-plate microchannels; Bowen and Jenner [59] studied electroviscous effects in charged capillaries and provided a numerical method to solve Poisson-Boltzmann equation; Cassou [40] analytically solved electrokinetic flow in a parallel-plate slit by his three-point-extension hypernetted-chain-mean-spherical (TPE HNC/MS) theory. On the numerical side, Hu *et al.* [60] studied the intersecting rectangular microchannels; Liu and Masliyah [61] numerically addressed the problem of microchannels in varying

11
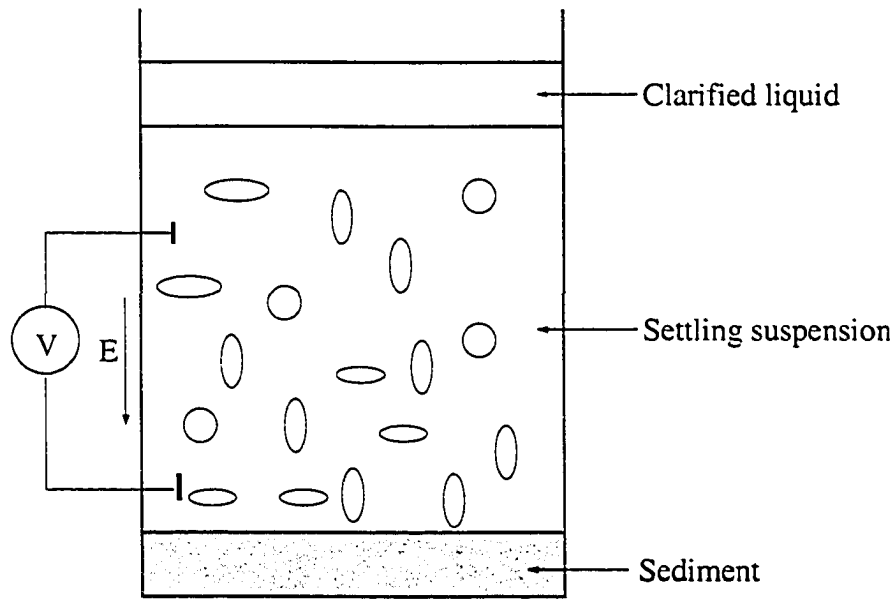
Figure 1.6: Schematic of sedimentation potential.

cross-sections; Ren and Li [62] numerically simulated electroosmotic dispensing processes for lab-on-a-chip; Bianchi *et al.* [63] developed a finite element formulation for electroosmotic flow in T-junction microchannel networks. On the experimental side, Rahman and Gui [64] measured water flow in silicon wafer microchannels. Their results showed that the friction coefficients was slightly higher than those predicted by traditional theory. Sinton *et al.* [65] visualized microfluidic on-chip injection processes through fluorescent dye; Ren and Li [66] studied electroviscous effects for different liquid flows in microchannels; Reppert *et al.* [67] measured frequency-dependent streaming potential in pores diameter from 1 mm to 34 μm.

The above studies have a common theme in which the interactions between solid miccrochannel wall and microfluidics were studied under steady-state conditions, so that the time-dependent response of the electric and flow fields has not been studied. The issue of time-dependent flow with electrokinetic effects has been addressed in the context of electroosmosis by Söderman and Jönsson [68], Santiago [69], Keh and Tseng

12

[70] and Yang [71] for circular, parallel plate and rectangular microchannels. However, their solutions focus on transient problems and are only valid for the special case of a constant, externally applied electric field. We have not been able to locate any work in the open literature that presents a unified treatment of streaming potential and electroosmosis for arbitrary time-dependent pressure gradients and externally applied electric fields. There are also quite a few contributions on time-dependent studies of liquid flow in macrochannels (without accounting for EDL effects); more detail can be found from the theory of time-dependent laminar flows by Rott [72]. Two specific examples are the pulsating laminar flow in a circular pipe (Uchida [73]). For rectangular channel, for example, the work of Drake [74], O'Brien [75], Fan and Chao [76]. However, there are some limitations in their solution. Drake's [74] solution is restricted only to the condition, $w/h > 1$ (where $2w$ and $2h$ are the width and height of the channel), and such a solution does not remain unchanged (and hence, violates symmetry) if w is interchanged with h, and x is interchanged with y (where x and y are two coordinates in a cartesian orthonormal coordinate system). O'Brien's [75] solution is free of the aforesaid limitations but cannot satisfy the no-slip boundary condition at the four corners of the rectangular channel. Fan and Chao's solutions cannot analytically reduce to solutions of parallel-plate, when $w \to \infty$.

All listed papers above focus on an uniform microchannel. In real life, microchannels with heterogeneous surfaces are more common than idealized microchannels with homogeneous surfaces. Fabrication defect, material impurity and chemical adsorption of solution can cause nonuniform surface potentials in a microchannel. Recent interest in electroosmotic flow over heterogeneous surfaces came from the study of Norde *et al.* [77], who studied the relationship between protein adsorption with streaming potential. Ajdari [78, 79] presented a theoretical solution for electroosmosis flow on inhomogeneous and charged surfaces. Stroock *et al.* [80] studied electroosmosis flow on a surface with patterned charges. Their results agree well with theory [78, 79].

13

Ren and Li [81] numerically studied electroosmotic flow in heterogeneous circular microchannel with axially varying surface potential. Anderson and Idol [82] studied electroosmosis through pores with nonuniformly charged walls. They showed that the mean electroosmotic velocity within the capillary was given by the classical Helmholtz equation with the local surface potential replaced by the average surface potential. Keely *et al.* [83] theoretically provided the flow profile inside a capillary with nonuniform surface potentials. Herr *et al.* [84] theoretically and experimentally investigated electroosmotic flow in cylindrical capillaries with nonuniform wall surface charge distribution. They used a nonintrusive caged-fluorescence imaging technique to image the electroosmotic flow. They observed parabolic velocity profile induced by pressure gradient due to heterogeneity of capillary surface. However, most of the above studies [81, 82, 83, 84] assumed uniform electric fields. Mathematically, the assumption of uniform electric field in a non-uniform microchannel satisfies the requirement of flow rate continuity, but does not automatically guarantee that current continuity is maintained. In fact, current and flow rate continuity cannot be automatically satisfied if a uniform electric field is assumed in nonuniformed microchannels. In this thesis, we will indeed show a slight variation of electric field distribution in a nonuniform microchannel for electroosmotic flow.

On the other hand, according to the open literature, pressure driven flow (streaming potential) through a heterogeneous microchannel has not been reported. Because streaming potential is the most common method to measure zeta potential, studying pressure driven flow in a heterogeneous microchannel is helpful to design zeta potential measurement experiments. In this case, we should also consider a nonuniform electric field and pressure distribution in the heterogeneous microchannel. Hence, a net zero current can be satisfied everywhere in the nonuniform microchannels.

14

Hydrophilic surface   Hydrophobic surface
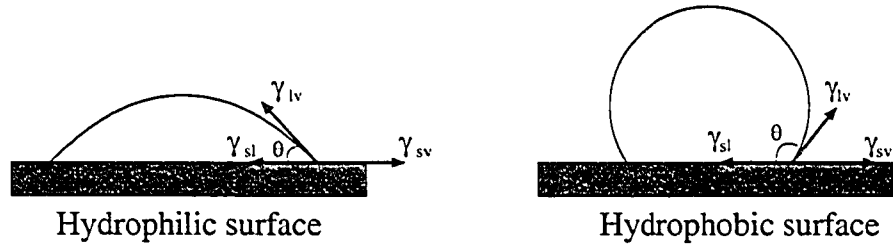
Figure 1.7: Schematics of contact angle phenomena

1.3.3 Interpretation of liquid slippage by wettability

Wetting and non-wetting phenomena, the advancing or receding of a liquid at liquid-solid-vapor three phase interface, are very common in many natural and industrial processes, such as coatings, paintings, condensation of stream, cleaning by using detergent and leaving or penetrating of raindrops on clothes. The most direct observation of wettability is to measure contact angles at liquid-solid-vapor interfaces (Figure 1.7). At thermodynamic equilibrium state, the relation of the solid-vapor interfacial tension γ_{sv}, the solid-liquid interfacial tension γ_{sl}, the liquid-vapor interfacial tension γ_{lv} and contact angle θ is given by the well-known Young's equation:

$$\gamma_{lv} cos(\theta) = \gamma_{sv} - \gamma_{sl} ,$$
(1.3.6)

Thermodynamically, for per unit area, the free energy of cohesion of solid W_{ss}, the free energy of cohesion of liquid W_{ll} and free energy of adhesion of a solid-liquid pair W_{sl} can be related to the three interfacial tensions γ_{sv}, γ_{sl} and γ_{lv} by the following equations [85]:

$$W_{ll} = 2\gamma_{lv} ,$$

$$W_{ss} = 2\gamma_{sv} ,$$

$$W_{sl} = \gamma_{lv} + \gamma_{sv} - \gamma_{sl} ,$$
(1.3.7)

Eqs. 1.3.7 imply liquid behavior on a solid surface can reflect the strength of solid-liquid interaction. For a hydrophobic surface, water does not wet the surface and has

15

a large contact angle (Even though hydrophobicity is a relative concept, we usually define a hydrophobic surface with a contact angle $\theta > 90°$ [86].).

These wetting and non-wetting phenomena are easy to be observed at liquid-solid-vapor interfaces. We can have direct feeling of solid-liquid interactions through contact angle measurements. If there are only two phases, liquid and solid (for example, liquid flowing through a channel), questions arise: what roles do solid-liquid interactions play? What is the difference of flows in a hydrophobic channel from those in a hydrophilic channel? Does the traditional no slip boundary condition of flows still hold in a hydrophobic microchannel?

1.3.4 Literature review of slippage of flow

For hundreds of years, traditional no slip boundary condition at the solid channel wall has been successfully used to model many macroscopic fluid mechanical problems. However, the no slip boundary condition cannot provide a universal description of tangential momentum transport at solid-liquid interfaces. In fact, liquid molecules do not have to have the same tangential velocity as that of solid wall. Slippage may happen at liquid/solid interfaces. Navier [87] proposed a Navier slip boundary condition several hundred years ago. The slip boundary condition relates the velocity at solid surface to be proportional to shear stress [88], which can be expressed as

$$\vec{v} \mid_{wall} = \beta \frac{\partial \vec{v}}{\partial \vec{n}} \mid_{wall} , \qquad (1.3.8)$$

where $\vec{v}$ is the velocity vector, β is the slip coefficient and $\vec{n}$ is the unit vector normal to the interfaces. We also call $-\beta$ as slip length, which was firstly defined by Brochard and de Gennes [89].

Slippage of gas flow has been easily observed in experiments [90, 91]. The first order model and the second order model can provide good slip boundary conditions for gas flow [92]. Slippage of polymer has also been found by de Gennes [89, 93]. However, slippage of simple liquid seems hard to be detected. The reason to cause this

16

difficulty is that an ideal surface is difficult to make and keep unchanged. Pit *et al.* [94] observed slippage at a microscopic scale and pointed out that "the corresponding slip length remained however poorly determined, due to the difficulty of controlling the surface quality (roughness) and hydrophobic treatments". Blake [95] also pointed out that the surface roughness might weaken, even delete the effect of slippage. Both surface roughness and the strength of the solid-liquid interactions can act on slippage, in antagonist ways. Helmoholtz and Von Piotrowski [96] are often credited with finding some evidence of slippage (friction) between the boundary of a solid and a liquid flowing over it [86]. In 1956, Schnell [97] was probably the first scientist to detect reliable slippage of water in a glass capillary pretreated with dimethyldichlorosilane [86]. Relying on better experimental conditions, recently, numerous experiments have directly or indirectly shown that slippage can happen near a hydrophobic microchannel wall even for very low Reynolds numbers. In the case of moderate Reynolds numbers, Watanabe *et al.* [98] observed tap water slippage in a 16 mm diameter acrylic-resin-coated pipe and obtained a 14% drag reduction for Reynolds numbers between 10^2 to 10^3. For Reynolds number $\ll 1$, Tretheway and Meinhart measured the velocity profile of water flowing through a $30 \times 300 \ \mu m^2$ octadecyltrichlorosilane (OTS) coated rectangular microchannel and observed a 1 μm slip length [99]. Zhu and Granick [100] measured the hydrodynamic force of water against a methyl-terminated self-assembled monolayer (SAM) on mica and found that when the flow rate exceeds a critical level, partial slip occurs. It was demonstrated that the classical no-slip boundary condition of fluid flow failed for several systems with hydrophobic surfaces even when the flow velocity is as small as nm/s. It was concluded that "the onset of slip varied systematically with contact angle", which depends on the solid surface energy for a given liquid. Churaev *et al.* [101] observed liquid slippage in hydrophobized quartz capillaries with radius ranging from 0.88 μm to 5.8 μm. The average velocity was found to be several μm per second and the Reynolds number is of

17

the order of 10^{-6}. Cheng and Giordano [102] observed several ten nanometer slippage on photoresist coatings in nanometer-scale channels. Cottin-Bizonne *et al.* [103] used a Dynamic Surface Force Apparatus (DSFA) to measure hydrodynamic force of thin liquid films. Flows of two polar liquids, water and glycerol, on a hydrophilic Pyrex surface and a hydrophobic octadecyltrichlorosilane (OTS) SAM on Pyrex surface were investigated. No slip boundary conditions were found for both fluids on hydrophilic surfaces. More than one hundred nanometer slip lengths were found on hydrophobic surfaces. Meanwhile, slippage is also found in many molecular dynamic simulations. Thompson and Troian [104] employed molecular dynamics simulations to probe the fluid behavior at the solid-liquid interface and found that surface properties can lead to large fluctuations in the apparent no-slip/slip boundary condition. Molecular dynamic simulations by Barrat and Bocquet [105, 106] of Lennard-Jones liquids have shown that the no slip boundary condition holds on hydrophilic surface. On the contrary, even for a partial wetting surface, slip effects occur [103]. Recent popular simulation method, Lattice Boltzmann method, shows the apparent liquid slip can also result from nanoscale chemical heterogeneity [107]. Thus, liquid slip is evidenced even for very low Reynolds numbers in microchannels, especially for microchannels with hydrophobic surface.

However, none of these studies have considered the effects of surface potentials on fluid flow. Clearly, they all suggested that liquid slip occurs for water flow over hydrophobic surfaces at small scale. At a micron scale, we have already discussed that the electrokinetic phenomena are important to microfluidics. For a better description of microfluidics, we believe that one should combine these two phenomena, electrokinetic and slippage of liquids, because they have counter-effect on liquid for pressure driven flow in microchannels: the former retards fluid movement and the latter increases fluid velocity. If one considers only electrokinetic effect and ignores slip condition, the EDL effect would be underestimated. Similarly, if slip condition is

18

considered without accounting for electrokinetic effect, the slip coefficient would also be underestimated. Therefore, it is important to address and combine both electrokinetic effects and slip condition in the description of fluid flow in microchannels.

1.4 Scope and objectives of thesis

According to current research of microfluidics, electrokinetic transport phenomena are one of the most important parts in this area. At least, two fundamental problems have not been fully solved. One is time-dependent electrokinetic flows, which are real in most of microfluidic MEMS devices; the other is effects of wettability of solid surface on electrokinetic microflows. These fundamental understandings are helpful to precisely control microflows and design or optimize microfluidic MEMS devices. The main objectives of this thesis are: to consider surface effects of microchannels based on present theory and models, and to obtain analytical solutions of microflows in circular, parallel-plate and rectangular microchannels; in addition, based on our theoretical study, some potential applications of microfluidics will be proposed; finally, we will experimentally investigate microfluidics in microchannels and realize some of applications.

In Chapter 2, using the Debye-Hückel approximation of Poisson-Boltzmann equation of EDL, we obtain analytical solutions velocity, flow rate and current of time-dependent electrokinetic flows in rectangular, circular and parallel-plate microchannels. Oscillating electroviscous effects and arbitrary time dependent flow in parallel-plate microchannel are studied.

In Chapter 3, using Navier slip boundary condition to describe flow behavior on hydrophobic solid surface, and combining with electrokinetic phenomena, we obtain analytical solutions of time-dependent electrokinetic slip flows in rectangular, circular and parallel-plate microchannels with hydrophobic surfaces. Considering effects of slippage, a new method is proposed to simultaneously determine zeta potential and

19

slip length of an hydrophobic surface. We also find the efficiency can be greatly improved by slippage for pressure or electric field driven flow.

In Chapter 4, considering heterogeneity of surface potential and hydrophobicity of microchannels, we give out general solutions of microflows in a nonuniform microchannel consisting of n different sections. Pressure and electric field distributions are obtained. This topic is also extended to study flows through multilayer membranes. A nondestructive method is proposed to image the micro-structures of multilayer membranes by high frequency electric fields.

In Chapter 5, electroosmosis flow with moving front is first studied by us. In this case, the external electric field provides the main driving force. Slippage and capillary force dependent on surface wettability are considered simultaneously. An equation to describe time-dependent electroosmosis flows with moving front is obtained.

In Chapter 6, effects of modified Poisson-Boltzmann model (MPB), modified Gouy-Chapman theory (MGC), Poisson-Boltzmann equation (PB) and linearized Poisson-Boltzmann equation (LPB) on ionic distribution in EDL and electrokinetic flows are studied. For microfluidics, Poisson-Boltzmann equation is fairly good, but not for nanofluidics. This research is a good starting point for nanofluidics.

In Chapter 7, Electrokinetic batteries consisting of a microchannel array, by means of streaming current and streaming potential, are proposed respectively [108]. Preliminary experiments prove the feasibility of electrokinetic batteries.

In Chapter 8, we propose a promising slip coating, Self-Assembled Monolayers (SAMs), which are transparent and of nanoscale thickness. To deeply understand wettability of SAMs surface, effects of nano-crystalline on hydrophobicity of SAMs [109] are studied. A microfluidic experimental system is built. Slip lengths of SAMs are experimentally determined.

In Chapter 9, we conclude the study of this thesis, summarize some theoretical and experimental results and emphasize potential applications. We also point out

20

several directions, that our research will go in the future.

.

Chapter 2

Time-dependent Electrokinetic Flows in Microchannels

2.1 Introduction

From the earliest systematic studies of electrokinetic flows in circular capillary by Rice and Whitehead [53] and in parallel-plate slit by Burgreen and Nakache [55] to recent studies of the electrokinetic flow in rectangular microchannels by Yang *et al.* [57], most of these studies focused on steady state. A few studies of electroosmotic flow by Söderman and Jönsson [68], Santiago [69], Keh and Tseng [70] and Yang [71] for circular, parallel plate and rectangular microchannels only limited to transient problems and were only valid for the special case of a constant, externally applied electric field. However, in most of microfluidic MEMS devices, electrokinetic flows including pressure driven flows and electric field driven flows are time-dependent. Periodic problems are so common in nature or industry. For example, alternating electric field with wide-range varying frequencies are often directly used as energy sources or driving forces. Especially, some patients require implantable micropumps to provide medicine periodically. So, understanding oscillating electrokinetic flows becomes indispensable. Furthermore, oscillating solutions can be used to study more general time-dependent problems through superposition of time-harmonic solutions weighted by appropriate Fourier coefficients [110, 111]. Understanding the behavior

22

of time-dependent electrokinetic flows provides us a guidance to design and control microfluidic devices.

In this chapter, we give the solution of oscillatory flow in microchannels with rectangular, circular and parallel-plate cross-sections, where a sinusoidal pressure gradient and a sinusoidal electric field are both applied along the axis of the microchannels. We invoke the Debye-Hückel approximation for a low surface potential; this allows us to obtain analytical solutions for the distribution of electric charges (Poisson's equation) and the velocity field (Navier Stokes' equation). The resulting solutions of rectangular microchannels are demonstrated not only to be symmetric with respect to x and y, but also satisfy the no-slip boundary condition at all locations on the channel wall and are also analytically reducible to the parallel plate solution. This somewhat compensates some limitations of previous studies [74, 75, 76] of channel flow without EDL effects. The resulting solutions are then used to carry out parametric studies of EDL effects at various frequencies and microchannel dimensions.

2.2 Electrokinetic flow in rectangular microchannel

In this section, we introduce the boundary value problem for oscillating liquid flow in an infinitely extended microchannel with rectangular cross-section; see Figure 2.1. A cartesian orthonormal coordinate system, (x, y, z), is used where the z-axis is taken to coincide with the microchannel central axis. All field quantities, except for pressure, are taken to be dependent on x, y, t and independent of z. Here t denotes time.

23
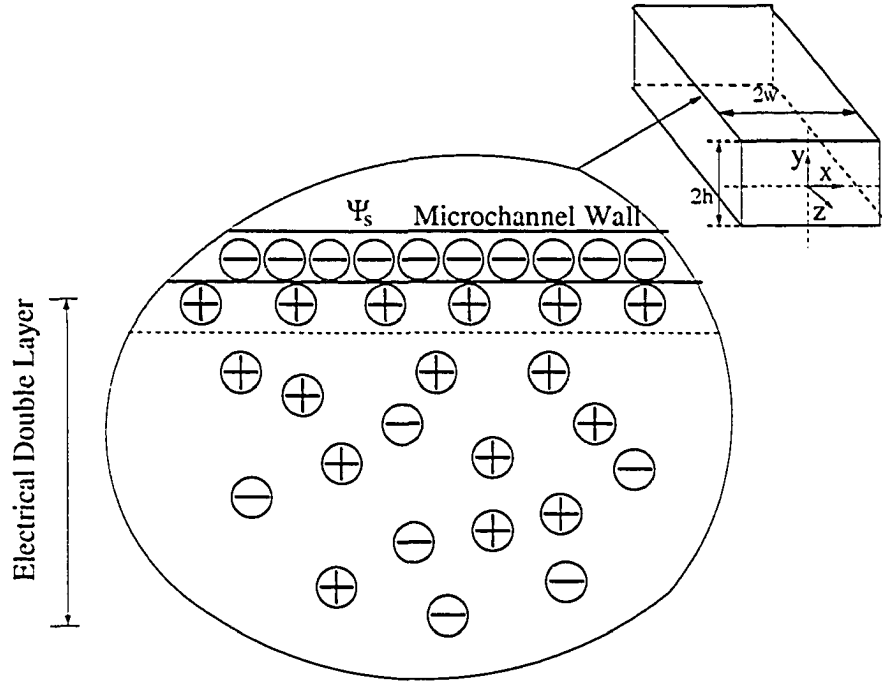
Figure 2.1: Schematic of the coordinate system in the rectangular microchannel.

2.2.1 Controlling equations and boundary conditions

Electrical field

The total electric potential, u, at a location, (x, y, z), at a given time, t, is taken to be

$$u(x, y, z, t) = \psi(x, y) + [u_0 - zE'_z(t)] , \qquad (2.2.1)$$

where $\psi(x, y)$ is the potential due to the double layer at the equilibrium state (i.e. no fluid motion and no applied external field), u_0 is the potential at $z = 0$ (i.e. $u_0 \equiv u(x, y, 0, t)$) and $E'_z(t)$ is the spatially uniform, time-dependent electric field strength. The time-dependent flow to be studied here is assumed to be sufficiently slow such that the charge distribution along x and y is relaxed at its steady state (as is true for most MEMS) [110, 111]. Further, it is assumed that any induced magnetic fields are small enough to be negligible such that the electric field may still be defined

24

as $-\vec{\nabla}u$ [112]; this definition may then be used to obtain the Poisson's equation

$$\nabla^2 u = -\frac{\rho}{\epsilon} \, , \qquad\qquad (2.2.2)$$

where ρ is the net charge density and ϵ is the permittivity of the medium. With Eq.2.2.1, Eq.2.2.2 reduces to

$$\frac{\partial^2 \psi}{\partial x^2} + \frac{\partial^2 \psi}{\partial y^2} = -\frac{\rho}{\epsilon} \, . \qquad\qquad (2.2.3)$$

The conditions imposed on $\psi(x,y)$ are

$$\psi(\pm w, y) = \psi_1 \quad , \quad \psi(x, \pm h) = \psi_2 \quad , \quad \frac{\partial \psi}{\partial x}(0, y) = 0 \quad , \quad \frac{\partial \psi}{\partial y}(x, 0) = 0 \, , \quad (2.2.4)$$

where w and h are half of the width and height of the rectangular channel, and ψ_1 and ψ_2 are the surface potentials on the vertical and horizontal walls, respectively. We shall now determine the double layer potential due to a symmetric electrolyte. The cations and anions will be identified as species 1 and 2, respectively. Based on the assumption of thermodynamic equilibrium, the Boltzmann equation provides the local charge density, ρ_i, of the ith species. Thus

$$\rho_i = z_i e n_{i\infty} exp\left[-\frac{z_i e \psi}{kT} \right] \, , \qquad (i = 1, 2) \, , \qquad (2.2.5)$$

where z_i is the valence of the ith species, e is the elementary charge, $n_{i\infty}$ is the ionic concentration of the ith species in equilibrium electrochemical solution at the neutral state where $\psi = 0$, k is the Boltzmann constant and T is the absolute temperature [110, 111]. Invoking the Debye-Hückel approximation for low surface potential, $z_i e \psi / kT << 1$, we have $\sinh(z_0 e \psi / kT) \approx z_0 e \psi / kT$, and the total charge density follows from Eqs.2.2.3 and 2.2.5 as

$$\rho = \sum_{i=1}^{2} \rho_i = \frac{-2n_{\infty}e^2 z_0^2}{kT} \psi \, , \qquad\qquad (2.2.6)$$

where we have used $z_1 = -z_2 = z_0$ and n_∞ is the ionic concentration in equilibrium electrochemical solution at the neutral state. Finally, the definition of the reciprocal

25

of the double layer thickness for a $(z_0 : z_0)$ electrolyte is given as

$$\kappa = \sqrt{\frac{2n_\infty e^2 z_0^2}{\epsilon kT}} \ , \tag{2.2.7}$$

and the insertion of Eq.2.2.6 in Eq.2.2.3 results in

$$\frac{\partial^2 \psi(x,y)}{\partial x^2} + \frac{\partial^2 \psi(x,y)}{\partial y^2} = \kappa^2 \psi(x,y) \ . \tag{2.2.8}$$

Hydrodynamic field

Inclusion of the body force due to the electric potential in the Navier-Stokes equation leads to

$$-\frac{1}{\mu}\frac{\partial p}{\partial z} + \left(\frac{\partial^2 v}{\partial x^2} + \frac{\partial^2 v}{\partial y^2}\right) + \frac{1}{\mu}\rho E_z' = \frac{1}{\nu}\frac{\partial v}{\partial t} \ , \tag{2.2.9}$$

where we take the pressure gradient, $\frac{\partial p}{\partial z} \equiv \frac{\partial p}{\partial z}(t)$, to be position-independent, μ is the viscosity and ν is the kinematic viscosity of the liquid [110, 111]. The initial condition and boundary conditions for the velocity field are

$$v(x,y,0) = 0 \ ,$$

$$v(\pm w, y, t) = 0 \quad , \quad v(x, \pm h, t) = 0 \ ,$$

$$\frac{\partial v(0,y,t)}{\partial x} = 0 \quad , \quad \frac{\partial v(x,0,t)}{\partial y} = 0 \ , \tag{2.2.10}$$

The electric current is determined by integrating the electric current density over the microchannel cross-section

$$i(t) = \int_{-h}^{h}\int_{-w}^{w} \rho v \ dxdy + \frac{z_0 eD}{kT}\int_{-h}^{h}\int_{-w}^{w}(\rho_1 - \rho_2)E_z' \ dxdy \ , \tag{2.2.11}$$

where D is the ions' diffusion coefficient. The first term on the right side of Eq.2.2.11 is due to bulk convection and the second term is due to charge migration [38]. Due to the assumption of an infinitely extended microchannel, the contribution to Eq.2.2.11 due to concentration gradients vanishes [110, 111]. Using Eq.2.2.5 for a $(z_0 : z_0)$ electrolyte, we have $\rho_1 - \rho_2 = 2z_0 en_\infty cosh(z_0 e\psi/kT)$. The Debye-Hückel approximation

26

implies that $cosh(z_0e\psi/kT) \approx 1$ and $\rho_1 - \rho_2 = 2z_0en_\infty$. With this simplification, Eq.2.2.11 becomes

$$i = \int_{-h}^{h} \int_{-w}^{w} \rho v \, dx dy + \frac{2z_0^2e^2n_\infty D}{kT}(4wh)E_z' \ . \tag{2.2.12}$$

The normalized equations

In this section, we give the normalized governing equations and boundary and initial conditions. Using a yet unknown characteristic velocity, $\langle v \rangle$, the following normalized quantities are defined as

$$V = \frac{1}{\langle v \rangle}v \quad , \quad X = \frac{x}{h} \quad , \quad Y = \frac{y}{h} \quad ,$$

$$W = \frac{w}{h} \quad , \quad \Psi = \frac{z_0e}{kT}\psi \quad , \quad E_z = \frac{z_0eh}{kT}E_z' \ . \tag{2.2.13}$$

where V, X, Y, W, Ψ and E_z are the normalized velocity, x coordinate, y coordinate, width of the channel, surface potential and strength of electric field, respectively. The normalized counterparts of Eqs.2.2.8 and 2.2.4 become, respectively

$$\frac{\partial^2\Psi(X,Y)}{\partial X^2} + \frac{\partial^2\Psi(X,Y)}{\partial Y^2} = K^2\Psi \ ,$$

$$\Psi(\pm W, Y) = \Psi_1 \ , \ \Psi(X, \pm 1) = \Psi_2 \ , \ \frac{\partial \Psi}{\partial X}(0,Y) = 0 \ , \ \frac{\partial \Psi}{\partial Y}(X,0) = 0 \ , \tag{2.2.14}$$

whereas Eqs.2.2.9, 2.2.10 and 2.2.12 become, respectively

$$-\frac{\partial P}{\partial Z} + \frac{\partial^2 V}{\partial X^2} + \frac{\partial^2 V}{\partial Y^2} - K^2\Psi E_z = \frac{\partial V}{\partial \tau} \ ,$$

$$V(X,Y,0) = 0 \ ,$$

$$V(\pm W, Y, \tau) = 0 \quad , \quad V(X, \pm 1, \tau) = 0 \ ,$$

$$\frac{\partial V(0,Y,\tau)}{\partial X} = 0 \quad , \quad \frac{\partial V(X,0,\tau)}{\partial Y} = 0 \ , \tag{2.2.15}$$

$$I = \int_{-1}^{1} \int_{-W}^{W} -K^2\Psi V \, dX dY + \frac{2h^2 z_0^4 e^4 \mu D n_\infty}{\epsilon^2 k^3 T^3} 4W E_z$$

$$= \int_{-1}^{1} \int_{-W}^{W} -K^2\Psi V \, dX dY + 4W\Sigma K^2 E_z \ , \tag{2.2.16}$$

$$Q = \int_{-1}^{1} \int_{-W}^{W} V \, dX dY \tag{2.2.17}$$

27

where P, I and Q are the normalized pressure, current and flow rate, respectively. In deriving Eqs.(2.2.14)–(2.2.17), the following normalized quantities have been identified

$$\bar{\rho} = \frac{h^2 e z_0}{\epsilon k T}\rho \quad , \quad K = \kappa h \quad , \quad P = \frac{h}{\mu\langle v\rangle}p \quad ,$$

$$\tau = \frac{\nu}{h^2}t \quad , \quad I = \frac{e z_0}{\epsilon k T\langle v\rangle}i \quad , \quad \Sigma = \frac{z_0^2 e^2 \mu D}{\epsilon k^2 T^2} \quad , \qquad (2.2.18)$$

where $\bar{\rho}$, K, τ and Σ are the normalized charge density, reciprocal of the double layer thickness, time and conductivity, respectively. Further, the expression for the characteristic velocity is identified as

$$\langle v\rangle = \frac{\epsilon k^2 T^2}{\mu h e^2 z_0^2} \cdot \qquad (2.2.19)$$

We wish to point out that our normalizing schemes in Eqs.(2.2.18) and (2.2.19) are different from those of other authors [58, 60, 113], as we do not employ the ionic concentration at equilibrium n_∞ to normalize the charge density ρ. The choice of this selection is important as we intend to study the effects of electrolyte concentration indirectly through K on flow properties; otherwise, the results would have been misleading since it makes no sense to study a quantity that has already been used for normalization. Finally, the following four normalized quantities are also given here as

$$\Omega = \frac{h^2}{\nu}\omega \quad , \quad \bar{\Omega} = \Omega\frac{\mu}{\bar{\mu}} \quad , \quad \bar{\tau} = \frac{\bar{\nu}}{h^2}t \quad , \quad Q = \frac{q}{\langle v\rangle h^2} \quad , \qquad (2.2.20)$$

where the parameters ω is the frequency of the external oscillating field, $\bar{\mu}$, $\bar{\nu}$ and q are the apparent viscosity, apparent kinematic viscosity and volumetric flow rate respectively; these parameters will be discussed in detail in the next section.

2.2.2 Analytical solutions

We shall use a complex variable approach to obtain an analytical solution for a sinusoidal periodicity in the electrohydrodynamic field [110, 111]. Thus, a general field

28

quantity, A, may be defined as the real part of the complex number, $A^*e^{j\Omega\tau}$, where A^* is complex, $j = \sqrt{-1}$, Ω is the normalized frequency of oscillation (defined in Eq.2.2.20), and τ is normalized time (defined in Eq.2.2.18). It is written as

$$A = Re[A^*e^{j\Omega\tau}] \ . \tag{2.2.21}$$

The phase angle, ϕ, is defined as

$$\phi = \tan^{-1}\frac{Im(A^*)}{Re(A^*)} \ , \tag{2.2.22}$$

where $Im(A^*)$ and $Re(A^*)$ are the imaginary and real part of A^*, respectively. An alternate representation of Eq.2.2.21 is

$$A = Re[|A^*|e^{j(\Omega\tau+\phi)}] \text{ where } |A| = |A^*| \text{ and } |A^*| = \sqrt{Im^2(A^*) + Re^2(A^*)} \ . \tag{2.2.23}$$

With the notation of Eq.2.2.21, we shall seek the solution of the boundary value problem for the following specific dependencies

$$-\frac{\partial P}{\partial Z} = Re[P^*e^{j\Omega\tau}] \quad , \quad E_z = Re[E_z^*e^{j\Omega\tau}] \ . \tag{2.2.24}$$

We consider the class of solutions where the amplitudes of the pressure gradient and the electric field are frequency-dependent, i.e. $P^* \equiv P^*(\Omega)$ and $E_z^* \equiv E_z^*(\Omega)$. The solution for Ψ will then follow from Eqs.2.2.14 and V from the first two of Eqs.2.2.17. Thus $V = Re[V^*e^{j\Omega\tau}]$, where

$$V^* \equiv V^*(X,Y,\Omega) = V_P^*(X,Y,\Omega)P^*(\Omega) + V_E^*(X,Y,\Omega)E_z^*(\Omega) \ ; \tag{2.2.25}$$

The expressions for $V_P^*(X,Y,\Omega)$ and $V_E^*(X,Y,\Omega)$ are given at the end of this section. The normalized electric current will follow from Eq.2.2.17 and is written as

$$I = Re[I^*e^{j\Omega\tau}] \quad \text{where} \quad I^* \equiv I^*(\Omega) = I_P^*(\Omega)P^*(\Omega) + I_E^*(\Omega)E_z^*(\Omega) \ . \tag{2.2.26}$$

The volumetric flow rate, q, is defined as

$$q = \int_{-h}^{h}\int_{-w}^{w} v \, dxdy \ . \tag{2.2.27}$$

29

Using the definition in Eq.2.2.20 as well as using Eqs.2.2.24 and 2.2.25, the normalized flow rate, Q, becomes

$$Q = Re[Q^*e^{j\Omega\tau}] \quad \text{where} \quad Q^* \equiv Q^*(\Omega) = Q_P^*(\Omega)P^*(\Omega) + Q_E^*(\Omega)E_z^*(\Omega) , \quad (2.2.28)$$

where the expressions for $Q_P^*(\Omega)$ and $Q_E^*(\Omega)$ are given at the end of this section. During pressure driven flow, the amplitude of the electric field strength induced by the streaming potential, $E_z^*(\Omega)$, is found by setting $I^* = 0$ in Eq.2.2.26. Thus

$$E_z^*(\Omega) = -\frac{I_P^*(\Omega)}{I_E^*(\Omega)}P^*(\Omega) \quad \text{for} \quad I^* = 0 . \quad (2.2.29)$$

During pressure driven flow, Eq.2.2.29 may be substituted in Eqs.2.2.25 and 2.2.28 to determine the normalized liquid velocity and the volumetric flow rate, respectively. Alternatively, the velocity, current and flow rate during electroosmosis follow from Eqs.2.2.25, 2.2.26 and 2.2.28 by setting $P^*(\Omega) = 0$ in those equations.

The presence of the streaming potential translates to an increased "drag" on the flow, resulting in an apparent viscosity which is higher than the true liquid viscosity. This is referred to as the electroviscous effect [53], and is characterized by defining an apparent viscosity, $\bar{\mu}$. For the steady state problem in channels with circular cross-section, Rice and Whitehead [53] defined $\bar{\mu}$ by proposing that the flow rate (inclusive of EDL effects and computed with the true liquid viscosity) be set equal to the flow rate without EDL effects and with μ being replaced by $\bar{\mu}$ [110, 111]. Adopting the same approach here, the dimensional flow rate follows from Eqs.2.2.19 - 2.2.20 and 2.2.28 - 2.2.29 as

$$q = \frac{\epsilon k^2 T^2 h}{e^2 z_0^2} \, Re \left[\frac{1}{\mu} \left(Q_P^*(\Omega) - Q_E^*(\Omega)\frac{I_P^*(\Omega)}{I_E^*(\Omega)} \right) P^*(\Omega)e^{j\Omega\tau} \right] . \quad (2.2.30)$$

The expression for the flow rate without EDL effects follows by first setting $E_z^*(\Omega) = 0$ in Eq.2.2.28, and then using Eqs.2.2.19 and 2.2.20. In the resulting expression for flow rate (denoted as $q_{apparent}$), μ is replaced by $\bar{\mu}$. We obtain

$$q_{apparent} = \frac{\epsilon k^2 T^2 h}{e^2 z_0^2} \, Re \left[\frac{1}{\bar{\mu}}Q_P^*(\bar{\Omega})P^*(\bar{\Omega})e^{j\bar{\Omega}\tau} \right] , \quad (2.2.31)$$

30

where $\bar{\Omega}$ is the normalized apparent frequency and $\bar{\tau}$ is the normalized time calculated using the apparent kinematic viscosity, $\bar{\nu}$ (where $\bar{\nu} = \bar{\mu}/\rho_d$, ρ_d is the mass density of the liquid). The normalized quantities, $\bar{\Omega}$ and $\bar{\tau}$, have both been defined in Eq.2.2.20. We now set $q = q_{apparent}$, and using Eqs.2.2.30 and 2.2.31, we obtain

$$Re\left[\frac{1}{\mu}\left(Q_P^*(\Omega) - Q_E^*(\Omega)\frac{I_P^*(\Omega)}{I_E^*(\Omega)}\right)P^*(\Omega)e^{j\Omega\tau}\right] = Re\left[\frac{1}{\bar{\mu}}Q_P^*(\bar{\Omega})P^*(\bar{\Omega})e^{j\bar{\Omega}\bar{\tau}}\right] \quad (2.2.32)$$

Note that $\bar{\Omega}\bar{\tau} = \Omega\tau$. Further, assuming that the amplitude of the imposed pressure gradient is a constant quantity, P_0, we have $P^*(\Omega) = P^*(\bar{\Omega}) = P_0$. For arbitrary $P_0 e^{j\Omega\tau}$, Eq.2.2.32 reduces to

$$\frac{\bar{\mu}}{\mu} = \frac{Q_P^*(\bar{\Omega})}{Q_P^*(\Omega) - Q_E^*(\Omega)\frac{I_P^*(\Omega)}{I_E^*(\Omega)}} \quad (2.2.33)$$

The resulting apparent viscosity, $\bar{\mu}$, is a complex quantity. At steady state (which is recovered by setting $\Omega, \bar{\Omega} = 0$ in Eq.2.2.33), we have checked that the imaginary component of $\bar{\mu}/\mu$ vanishes. A similar exercise was carried out by Bhattacharyya *et al.* [110, 111] for microchannels with a circular cross-section. Eq.2.2.33 is an implicit equation in $\bar{\mu}$, and hence, the ratio, $\bar{\mu}/\mu$, has to be determined numerically.

The analytical solution is now given. Prior work on flow in rectangular microchannels (without EDL effects; see Drake [74], O'Brien [75], Fan and Chao [76]) do not satisfy the conditions of the boundary value problem completely. Our analytical solution is free of these drawbacks. We solve Eq.2.2.14 by recognizing that it is the superposition of Eqs.2.2.34 and 2.2.35.

$$\frac{\partial^2 \Psi_A(X,Y)}{\partial X^2} + \frac{\partial^2 \Psi_A(X,Y)}{\partial Y^2} = K^2\left(\Psi_A + \frac{1}{2}\Psi_1\right) ,$$

$$\Psi_A(\pm W, Y) = 0 , \quad \frac{\partial \Psi_A}{\partial X}(0, Y) = 0 , \quad \Psi_A(X, \pm 1) = \frac{1}{2}(\Psi_2 - \Psi_1) , \quad \frac{\partial \Psi_A}{\partial Y}(X, 0) = 0 ,$$

$$(2.2.34)$$

$$\frac{\partial^2 \Psi_B(X,Y)}{\partial X^2} + \frac{\partial^2 \Psi_B(X,Y)}{\partial Y^2} = K^2\left(\Psi_B + \frac{1}{2}\Psi_2\right) ,$$

$$\Psi_B(\pm W, Y) = -\frac{1}{2}(\Psi_2 - \Psi_1) , \quad \frac{\partial \Psi_B}{\partial X}(0, Y) = 0 , \quad \Psi_B(X, \pm 1) = 0 , \quad \frac{\partial \Psi_B}{\partial Y}(X, 0) = 0 .$$

$$(2.2.35)$$

31

Once Eqs.2.2.34 and 2.2.35 are solved for $\Psi_A(X,Y)$ and $\Psi_B(X,Y)$, respectively, the required potential follows from the expression,

$$\Psi(X,Y) = \Psi_A(X,Y) + \Psi_B(X,Y) + \frac{1}{2}(\Psi_1 + \Psi_2) .$$

It is given by

$$\Psi = \sum_{n=1}^{\infty}\left\{\left[\frac{2(\Psi_2 - \Psi_1)(-1)^{n+1}}{(2n-1)\pi} + \frac{2K^2\Psi_1(-1)^{n+1}}{(2n-1)\pi\left[K^2 + \frac{(2n-1)^2\pi^2}{4W^2}\right]}\right]\right.$$
$$\times\frac{\cosh\sqrt{K^2 + \frac{(2n-1)^2\pi^2}{4W^2}}Y}{\cosh\sqrt{K^2 + \frac{(2n-1)^2\pi^2}{4W^2}}} - \left.\frac{2K^2\Psi_1(-1)^{n+1}}{(2n-1)\pi\left[K^2 + \frac{(2n-1)^2\pi^2}{4W^2}\right]}\right\}\cos\frac{(2n-1)\pi}{2W}X$$

$$+ \sum_{m=1}^{\infty}\left\{\left[\frac{2(\Psi_1 - \Psi_2)(-1)^{m+1}}{(2m-1)\pi} + \frac{2K^2\Psi_2(-1)^{m+1}}{(2m-1)\pi\left[K^2 + \frac{(2m-1)^2\pi^2}{4}\right]}\right]\right.$$
$$\times\frac{\cosh\sqrt{K^2 + \frac{(2m-1)^2\pi^2}{4}}X}{\cosh\sqrt{K^2 + \frac{(2m-1)^2\pi^2}{4}}W} - \left.\frac{2K^2\Psi_2(-1)^{m+1}}{(2m-1)\pi\left[K^2 + \frac{(2m-1)^2\pi^2}{4}\right]}\right\}\cos\frac{(2m-1)\pi}{2}Y$$

$$+\frac{1}{2}\Psi_1 + \frac{1}{2}\Psi_2 . \tag{2.2.36}$$

The symmetry expected in the expression for Ψ is obvious by interchanging Ψ_1 with Ψ_2 and X/W with Y. Using Green's functions, the solution of Eqs.2.2.15 can be written as

$$V = \int_{\tau'=0}^{\tau}\int_{Y'=0}^{1}\int_{X'=0}^{W} G(X,Y,\tau|X',Y',\tau') \times [P^* - K^2\Psi E_z^*]e^{j\Omega\tau'}dX'dY'd\tau' \tag{2.2.37}$$

where $G(X,Y,\tau|X',Y',\tau')$ is the Green's function , which may be found by using the separation of variable method. The Green's function has this expression [114]

$$G(X,Y,\tau|X',Y',\tau') = \frac{4}{W}\sum_{m=1}^{\infty}\sum_{n=1}^{\infty}e^{\lambda_1(\tau-\tau')}\cos\left[\frac{(2m-1)\pi}{2W}X\right]\cos\left[\frac{(2m-1)\pi}{2W}X'\right]$$
$$\times\cos\left[\frac{(2m-1)\pi}{2}Y\right]\cos\left[\frac{(2m-1)\pi}{2}Y'\right] , \tag{2.2.38}$$

where

$$\lambda_1 = -\left(\frac{(2m-1)\pi}{2W}\right)^2 - \left(\frac{(2n-1)\pi}{2}\right)^2 . \tag{2.2.39}$$

32

All oscillations ($0 \leq \Omega \leq \infty$)

The Eq.2.2.36 may be used in Eq.2.2.38 to obtain the solution for the velocity field. The normalized current will follow from Eq.2.2.17, and the normalized volumetric flow rate will follow from Eqs.2.2.20 and 2.2.27. For the periodic problem, the determined quantities may be cast in the form of Eqs.2.2.25 - 2.2.28. The expressions are given below.

$$
V_P^*(X,Y,\Omega) = \frac{16}{\pi^2} \sum_{m=1}^{\infty} \sum_{n=1}^{\infty} \frac{1}{j\Omega - \lambda_1} \frac{(-1)^{m+n}}{(2m-1)(2n-1)}
$$
$$
\times \cos\left[\frac{(2m-1)\pi}{2W}X\right] \cos\left[\frac{(2n-1)\pi}{2}Y\right] ,
$$

$$
V_E^*(X,Y,\Omega) = \frac{-4K^2}{W} \sum_{m=1}^{\infty} \sum_{n=1}^{\infty} \frac{\lambda}{j\Omega - \lambda_1} \cos\left[\frac{(2m-1)\pi}{2W}X\right] \cos\left[\frac{(2n-1)\pi}{2}Y\right] ,
$$

$$
I_P^*(\Omega) = \frac{-64K^2}{\pi^2} \sum_{m=1}^{\infty} \sum_{n=1}^{\infty} \frac{\lambda}{(j\Omega - \lambda_1)} \frac{(-1)^{m+n}}{(2m-1)(2n-1)} ,
$$

$$
I_E^*(\Omega) = \frac{16K^4}{W} \sum_{m=1}^{\infty} \sum_{n=1}^{\infty} \frac{1}{(j\Omega - \lambda_1)}\lambda^2 + 4W\Sigma K^2 ,
$$

$$
Q_P^*(\Omega) = \frac{256}{\pi^4} \sum_{m=1}^{\infty} \sum_{n=1}^{\infty} \frac{1}{j\Omega - \lambda_1} \frac{W}{(2m-1)^2(2n-1)^2} ,
$$

$$
Q_E^*(\Omega) = I_P^*(\Omega) . \tag{2.2.40}
$$

where

$$
\lambda = \left[\frac{(\Psi_2 - \Psi_1)(-1)^{m+n}}{(2m-1)} + \frac{\Psi_1 K^2(-1)^{m+n}}{(2m-1)\left[K^2 + \frac{(2m-1)^2\pi^2}{4W^2}\right]}\right] \frac{W}{2} \frac{2n-1}{K^2 - \lambda_1}
$$
$$
+ \left[\frac{(\Psi_1 - \Psi_2)(-1)^{m+n}}{(2n-1)} + \frac{\Psi_2 K^2(-1)^{m+n}}{(2n-1)\left[K^2 + \frac{(2n-1)^2\pi^2}{4}\right]}\right] \frac{1}{2W} \frac{2m-1}{K^2 - \lambda_1}
$$
$$
- \frac{2\Psi_1 K^2 W(-1)^{m+n}}{(2m-1)(2n-1)\pi^2\left[K^2 + \frac{(2m-1)^2\pi^2}{4W^2}\right]} - \frac{2\Psi_2 K^2 W(-1)^{m+n}}{(2m-1)(2n-1)\pi^2\left[K^2 + \frac{(2n-1)^2\pi^2}{4}\right]}
$$
$$
+ \frac{2W(\Psi_1 + \Psi_2)(-1)^{m+n}}{(2m-1)(2n-1)\pi^2} . \tag{2.2.41}
$$

33

Note that the theory without EDL effects follows from Eqs.2.2.40 by setting $\Psi_1 = \Psi_2 = 0$. Finally, note that V_P^* and V_E^* are symmetric. We have also checked that the velocity satisfies the no-slip boundary condition at the channel wall completely, even at its four corners. Finally, when $W \to \infty$, we have checked that Eqs.2.2.36 and 2.2.40 reduced to expressions for parallel plates; see the section 2.4 for parallel-plate microchannels.

Steady state ($\Omega = 0$)

The steady state response follows from Eqs.2.2.40 by setting $\Omega = 0$.

$$V_P^*(X, Y, 0) = \frac{16}{\pi^2} \sum_{m=1}^{\infty} \sum_{n=1}^{\infty} \frac{1}{-\lambda_1} \frac{(-1)^{m+n}}{(2m-1)(2n-1)}$$
$$\times \cos\left[\frac{(2m-1)\pi}{2W}X\right] \cos\left[\frac{(2n-1)\pi}{2}Y\right] ,$$

$$V_E^*(X, Y, 0) = \frac{-4K^2}{W} \sum_{m=1}^{\infty} \sum_{n=1}^{\infty} \frac{\lambda}{-\lambda_1} \cos\left[\frac{(2m-1)\pi}{2W}X\right] \cos\left[\frac{(2n-1)\pi}{2}Y\right] \lambda ,$$

$$I_P^*(0) = \frac{-64K^2}{\pi^2} \sum_{m=1}^{\infty} \sum_{n=1}^{\infty} \frac{1}{(-\lambda_1)} \frac{(-1)^{m+n}}{(2m-1)(2n-1)} \lambda ,$$

$$I_E^*(0) = \frac{16K^4}{W} \sum_{m=1}^{\infty} \sum_{n=1}^{\infty} \frac{1}{(-\lambda_1)} \lambda^2 + 4W\Sigma K^2 ,$$

$$Q_P^*(0) = \frac{256}{\pi^4} \sum_{m=1}^{\infty} \sum_{n=1}^{\infty} \frac{1}{-\lambda_1} \frac{W}{(2m-1)^2(2n-1)^2} ,$$

$$Q_E^*(0) = I_P^*(0) . \tag{2.2.42}$$

Before closing this section, we note that the streaming potential and electroosmosis are dual effects of the same phenomenon. Mazur and Overbeek [115] used the principles of non-equilibrium theromodynamics and the Onsager reciprocal relations to demonstrate this duality by proving the existence of a general identity involving streaming potential and electroosmosis [110, 111]. Their Eq.1 is reproduced below (all quantities are dimensional)

$$\frac{q}{i}\bigg|_{\partial p/\partial z = 0} = \frac{E'_z}{\partial p/\partial z}\bigg|_{i=0} , \tag{2.2.43}$$

34

where the left hand side of Eq.2.2.43 is the ratio, q/i, determined for electroosmosis $(\partial p/\partial z = 0)$ whereas the right hand side, $E'_z/[\partial p/\partial z]$, is the ratio determined for streaming potential $(i = 0)$. Rice and Whitehead [53] proved Eq.2.2.43 with respect to their steady state solution for microchannels with circular cross-section. The key issue behind Eq.2.2.43 is that the electrokinetic effects are linearly dependent on the pressure gradient and electric field (see the end of the first paragraph of section 3 in Mazur and Overbeek [115]), summarized in the linear phenomenological relations of their Eq.36. For the oscillating flow problem addressed in this thesis, it is the complex counterpart of "q" ($q^* e^{j\omega t}$ or, in normalized form, $Q^* e^{j\Omega \tau}$) that is linearly dependent on the pressure gradient and electric field [110, 111]. Therefore, we write Eq.2.2.43 in a normalized form and replace all the real quantities by their complex counterparts leading to

$$\frac{Q^*}{I^*}\bigg|_{P^*=0} = -\frac{E_z^*}{P^*}\bigg|_{I^*=0} . \tag{2.2.44}$$

Using Eqs.2.2.26 to 2.2.29, Eq.2.2.44 reduces to

$$Q_E^*(\Omega) = I_P^*(\Omega) . \tag{2.2.45}$$

Note that Eq.2.2.45 is an outcome of the analytical solution; see the last of Eq.2.2.40. An identical relation was obtained by Bhattacharyya et $al.$ [110] for oscillating flow in microchannels with circular cross-section.

2.2.3 Parametric studies and discussion

In this section, we use Eq.2.2.40 for parametric studies on streaming potential and electroosmosis. In particular, the effect of the normalized reciprocal thickness, K, of the EDL, the normalized frequency, Ω, and the normalized half width, W, are studied for the following fixed values of the normalized surface potential, $\Psi_s = 1.95$, normalized conductivity, $\Sigma = 3.85$, amplitude of the normalized pressure gradient, $P^*(\Omega) = 200$, amplitude of the electric field, $E_z^*(\Omega) = 39$. From a practical point of

35

Pressure driven flow
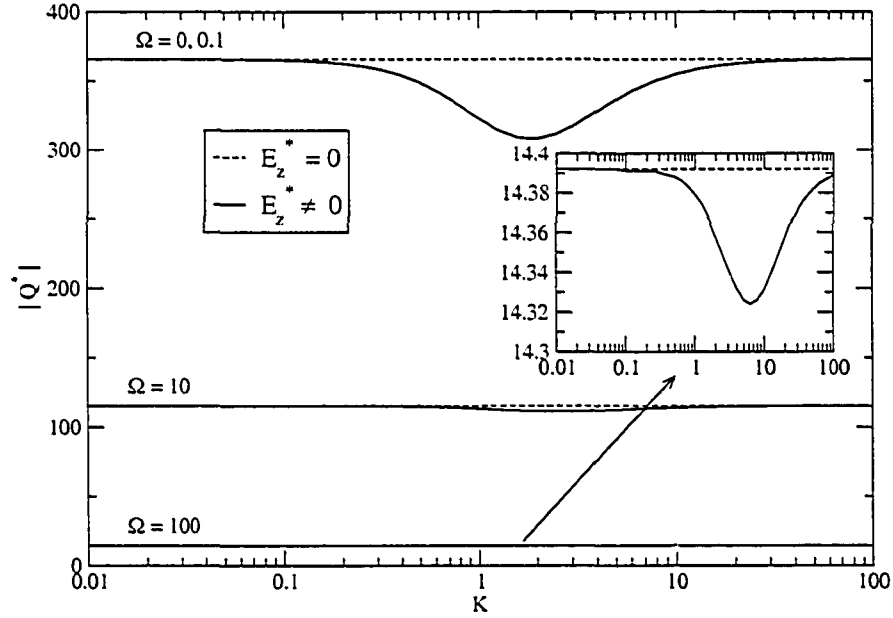
Figure 2.2: Dependence of the amplitude, $|Q^*|$, of the normalized flow rate, on K, for different normalized frequency, Ω.

view, these four parameters can represent a dimensional surface potential of 50 mV (the Debye-Hückel approximation can give a good prediction even when the surface potential is up to 100 mV [19]), a diffusion coefficient, D, of 2 $(10^{-9}m^2/s)$ pressure gradient at the order of 10^6 Pa/m and electric field at the order of 10^5 V/m. Finally, we note that the time dependence of a quantity, A, is completely determined if its amplitude, $|A|$ or $|A^*|$, and phase angle, ϕ, are both known (see Eq.2.2.23). Therefore, in the sequel, for a particular time-dependent quantity, e.g. the streaming potential, we shall focus solely on the study of its amplitude and phase angle. In all case, we will use $\Psi_1 = \Psi_2 = \Psi_s$ [111].

Pressure driven flow

The amplitude of the streaming potential follows from Eq.2.2.29 and consequently, the amplitude of the volumetric flow rate is provided by Eq.2.2.28. Figure 2.2 shows

36

Pressure driven flow
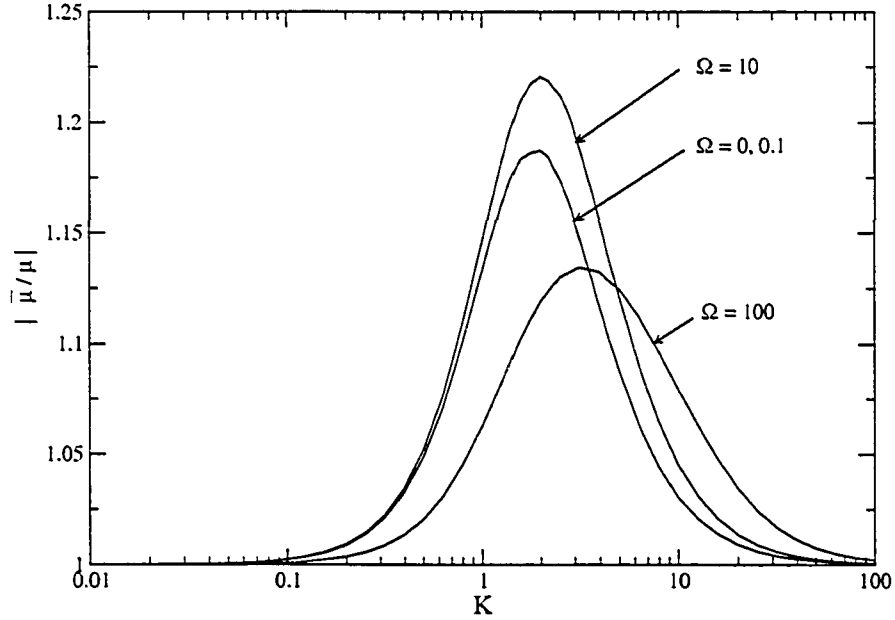
Figure 2.3: Dependence of the amplitude, $|\bar{\mu}/\mu|$, of the normalized apparent viscosity, on K, for different normalized frequency, Ω.

the amplitude of the normalized flow rate, $|Q^*|$, with respect to the normalized reciprocal thickness, K, of the EDL on a log-scale for four normalized frequencies, $\Omega = 0, 0.1, 10, 100$ (all at $W = 2$). Dashed curves correspond to the analysis without EDL effects (this follows by setting $E_z^*(\Omega) = 0$ in Eq.2.2.28) whereas the solid curves correspond to analysis with EDL effects. It is observed that as Ω increases, there is a significant decrease in the amplitude of the flow rate. Because the liquid molecules cannot response the change of pressure gradient at the same step, the flow cannot reach the highest velocity of steady state. This is the same reason that the amplitude difference of flow rate between the result with EDL effect and without EDL effect become smaller as the frequency rises. While the dashed curves are expectedly not a function of K, the solid curves demonstrate that for a fixed Ω, there is a non-monotonic dependence of $|Q^*|$ on K; this is especially prominent at low values of Ω

37

(e.g. $\Omega = 0.1$). The curves for $\Omega = 100$ may convey the impression that the effects of the EDL are not as important at that frequency. In reality, the flow rate at such a high frequency is already quite low, even when neglecting EDL effects. Inclusion of EDL effects does significantly reduce the flow rate even further; this is illustrated in the inset that has been included. The effects of the EDL at the frequencies studied are more apparent in Figure 2.3, which follows next [111].

Pressure driven flow
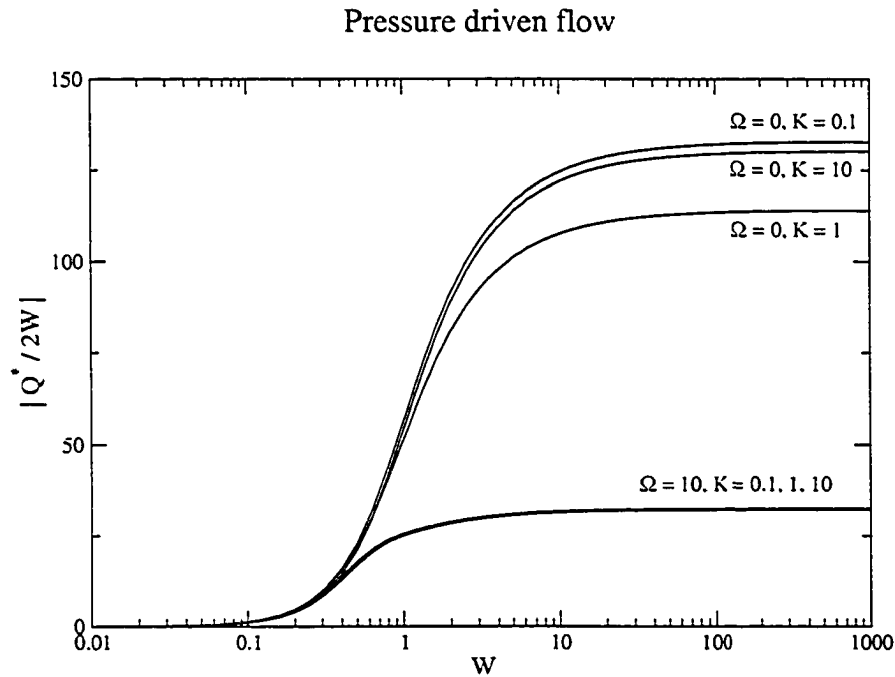
Figure 2.4: Dependence of the amplitude, $|Q^*/2W|$, of the normalized flow rate per unit width of microchannel, on W, for K and Ω values.

The reduced flow rate due to the streaming potential results in an apparent liquid viscosity, $\bar{\mu}$, which is higher than the true liquid viscosity, μ. This phenomenon is referred to as the electroviscous effect, and its strength may be quantified by calculating the ratio, $\bar{\mu}/\mu$. Rice and Whitehead [53] demonstrated (in their Fig.8) that their steady state solution for circular microchannels predicted a maximum in the electroviscous effect (i.e. $\bar{\mu}/\mu$) with respect to the channel radius, a (or equivalently, the normalized reciprocal EDL thickness, K). Burgreen and Nakache [55] provided

38

an experimental confirmation of such a maximum for flow in capillary slits. The ratio, $\bar{\mu}/\mu$, has been derived and given in Eq.2.2.33, and is shown in Figure 2.3 (at $W = 2$) with respect to K. It is observed that the maximum value of $|\bar{\mu}/\mu|$ at a given Ω occurs at precisely the same value of K, at which the amplitude of the flow rate, $|Q^*|$ is a minimum; see Figure 2.2. Since $|\bar{\mu}/\mu|$ is independent of the pressure gradient, the value of K at which the minimum $|Q^*|$ occurs will always remain the same, irrespective of the value of $P^*(\Omega)$. An explanation of the non-monotonic dependence of $|\bar{\mu}/\mu|$ on K is now given. Using Eqs.2.2.28, 2.2.29 and 2.2.45, we have

$$Q^* = \left[Q_P^*(\Omega) - \frac{I_P^*(\Omega)^2}{I_E^*(\Omega)} \right] P^*(\Omega) . \tag{2.2.46}$$

Note that $Q_P^*(\Omega)$ is independent of K, whereas $I_P^*(\Omega)$ and $I_E^*(\Omega)$ are dependent on K (see Eq.2.2.40). The following observations are valid for all Ω. We have checked that as $K \to 0$, $I_P^*(\Omega) \to \text{o}(K^2) = 0$ whereas $I_E^*(\Omega) \to \text{o}(K^2) = 0$, implying that $I_P^{*2}(\Omega)/I_E^*(\Omega) \to 0$ and $Q^* \to Q_P^*(\Omega)P^*(\Omega)$ (theory without EDL effects). On the other hand, as $K \to \infty$, $I_P^*(\Omega) \to \text{constant}$ and $I_E^*(\Omega) \to \infty$. Thus, as $K \to \infty$, the expression, $I_P^{*2}(\Omega)/I_E^*(\Omega) \to \text{o}(1/K^2) \to 0$ and $Q^* \to Q_P^*(\Omega)P^*(\Omega)$ (theory without EDL effects). The limiting values of $K \to 0$ corresponds to an infinitely dilute electrolyte (or with an infinitely thick EDL) whereas $K \to \infty$ corresponds to an infinitely thin EDL. The former case implies a uniform potential while the latter case implies a zero potential along the microchannel width and height (see Eq.2.2.14), leading to the disappearance of the effects of the EDL on the volumetric flow rate [111].

Here, we summarize these quantities' limitation in table 2.1

We have studied the dependence of the normalized flow rate per unit width of the microchannel, $|Q^*/2W|$, on the normalized width, W, of the rectangular microchannel; see Figure 2.4. For given electrolyte and surface potential, the parameter, $|Q^*/2W|$, increases with an increase in W. Beyond $W = 100$, $|Q^*/2W|$ approaches an asymptotic value corresponding to that for $W \to \infty$ (flow rate between parallel

39

Table 2.1: Some limitations of quantities for $K \to 0$ and $K \to \infty$

	I_P^*	I_E^*	$E_z^* = -P^* I_P^*/I_E^*$	Q_E^*	$Q_E^* E_z^*$
$K \to 0$	$o(K^2) = 0$	$o(K^2) = 0$	constant	$o(K^2) = 0$	0
$K \to \infty$	constant	$o(K^2) = \infty$	$o(1/K^2) = 0$	constant	0

plates). The flow rate is particularly sensitive to the EDL effects for non-oscillatory flows, where $\Omega = 0$. Comparing the top three curves for $K = 0.1, 1, 10$ and $\Omega = 0$ with the bottom three curves where $K = 0.1, 1, 10$ and $\Omega = 10$, this sensitivity disappears at $\Omega = 10$, since all three curves virtually coincide with each other.

Pressure driven flow
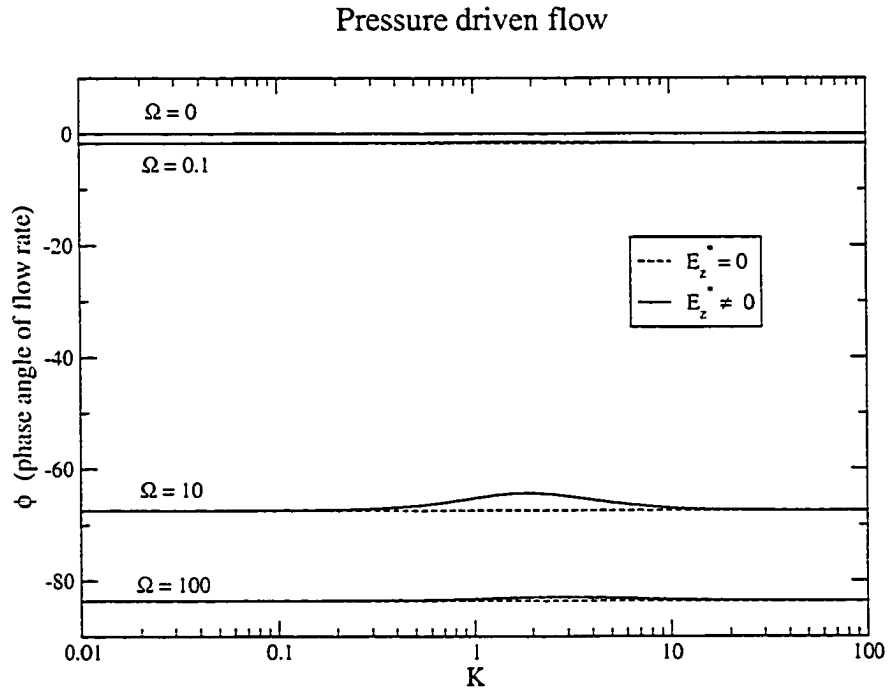
Figure 2.5: Dependence of the phase angle, ϕ, of the normalized flow rate on K, for different normalized frequency, Ω.

In Figure 2.5, the phase angle of the volumetric flow rate, defined in Eq.2.2.22, is plotted. Within the range, $0 \le \Omega \le 100$, the phase angle is negative; this indicates that the flow rate always lags behind the pressure gradient except at the steady state

40

($\Omega = 0$) when they are in phase, $\phi = 0$. At a given Ω, the ϕ vs. K dependence is non-monotonic, accompanied by a sharp reduction in the magnitude of ϕ (as evidenced by the peaks). The dashed curves are expectedly insensitive to K as those pertain to the theory without EDL effects. And the difference of phase angle between the flow rate with EDL effect and that without EDL effect, become more obvious as the frequency goes up. As Ω increases, ϕ becomes more negative. This implies that the flow rate lags behind the pressure gradient and the phase lag increases with increasing Ω. The effect of the EDL is to slightly reduce this phase lag. It is mostly apparent at $\Omega = 10$. Figure 2.6 shows the sensitivity of the normalized apparent viscosity, $|\bar{\mu}/\mu|$, on W.

Pressure driven flow
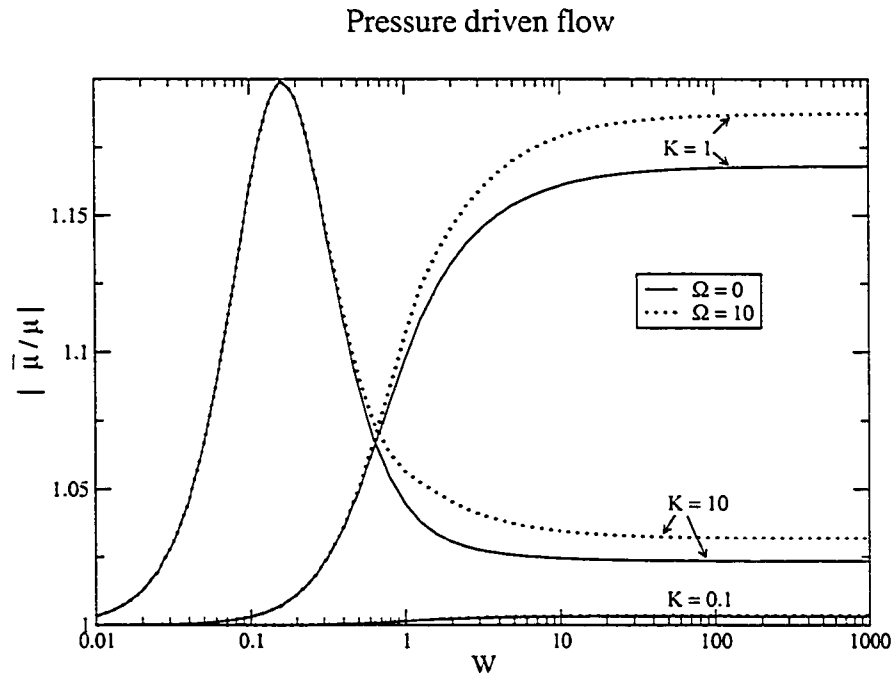
Figure 2.6: Dependence of the amplitude, $|\bar{\mu}/\mu|$, of the normalized apparent viscosity on W, for different K and Ω values.

Note that for $K = 10$, there is a maximum electroviscous effect around $W \approx 0.1$. In general, with an increase in frequency from $\Omega = 0$ to 10, $|\bar{\mu}/\mu|$ increases; this is true for $K = 0.1, 1, 10$. Figure 2.6 provides information to optimize geometries of rectangular microchannels.

41

Electric field driven flow
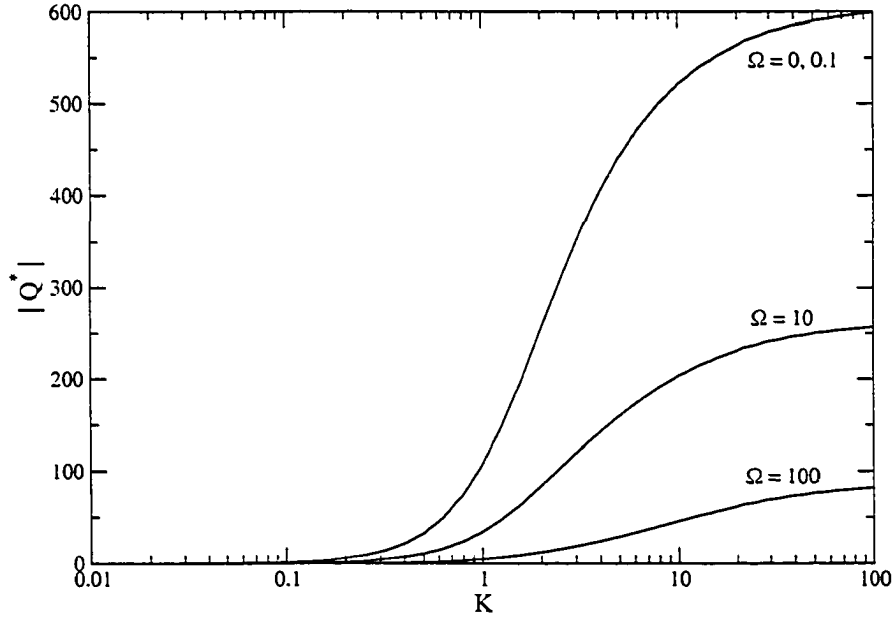
Figure 2.7: Dependence of the amplitude of the normalized electroosmotic flow rate, $|Q^*|$, on K, for different normalized frequency, Ω.

Electric field driven flow

After setting $P^*(\Omega) = 0$, the amplitude of the normalized volumetric flow rate and current during electroosmosis follow from Eqs.2.2.28 and 2.2.26, respectively. Figure 2.7 gives the amplitude of the flow rate, $|Q^*|$ vs. K for four different values of $\Omega = 0, 0.1, 10, 100$. It is seen that at a given Ω, $|Q^*|$ approaches a finite asymptotic value as K increases whereas $|Q^*| \rightarrow 0$ as K decreases. Note, from Eq.2.2.25, that during electroosmosis (i.e. $P^*(\Omega) = 0$), we have

$$Q^*(\Omega) = Q_E^*(\Omega) E_z^*(\Omega) .$$ (2.2.47)

As $K \rightarrow 0$, $Q_E^*(\Omega) \rightarrow 0$; whereas as $K \rightarrow \infty$, $Q_E^*(\Omega) \rightarrow$ constant due to a uniform velocity profile. Our numerical results show that $Q^*(\Omega)$ remians constant for K from 10^3 up to 10^6.

The phase angle, ϕ, of the flow rate is given in Figure 2.8. The positive values of ϕ

42

Electric field driven flow
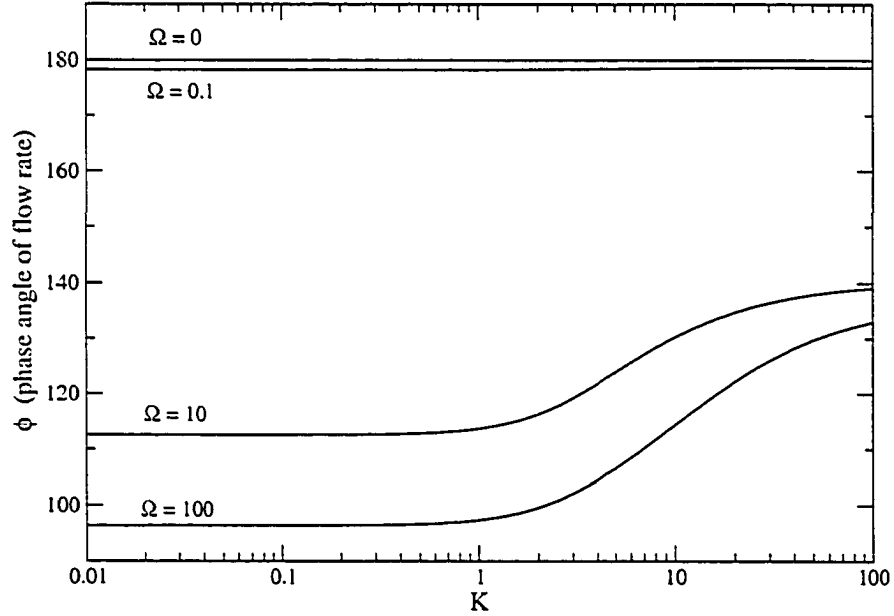
Figure 2.8: Dependence of the phase angle, ϕ, of the normalized flow rate on K, for different normalized frequency, Ω.

imply that the flow rate leads the external electric field, and the effect of an increasing Ω is to reduce the phase angle, and bring the flow rate more in phase with the electric field. The variation of $|Q^*/2W|$ with W is shown in Figure 2.9 at $K = 0.1, 1, 10$ for non-oscillatory flows having $\Omega = 0$ and for oscillatory flows with $\Omega = 10$. While the effect of a higher Ω is to reduce the flow rate, the effect of an increasing W is to enhance the flow rate until it reaches the asymptotic value for $W \rightarrow \infty$, the case of parallel plates [111].

In Figure 2.10 we plot the dependence of the amplitude, $|I^*|$, of the normalized electroosmotic current, on the normalized reciprocal EDL thickness, K, for different normalized frequencies, Ω. When K increases, the normalized amplitude of current increases, since the corresponding electrolyte concentration increases.

In Figure 2.11, we plot the dependence of the phase angle, ϕ, of the normalized

43

Electric field driven flow
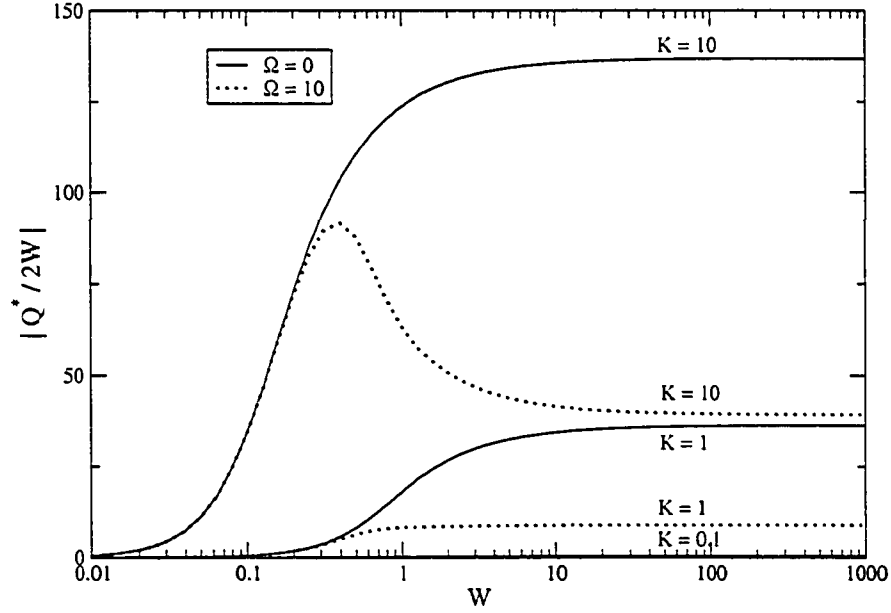
Figure 2.9: Dependence of the amplitude of the normalized electroosmotic flow rate, $|Q^*/2W|$, on W, for different K and Ω values.

electroosmotic current, on the normalized reciprocal EDL thickness, K, for different normalized frequencies, Ω. Because the phase angle of current is very small for different normalized frequencies, the current changes almost at the same step as the external electric field.

2.3 Electrokinetic flow in circular microchannel

In this section, we consider the boundary value problem for oscillating liquid flow in an infinitely extended circular microchannel [110]. A cylindrical coordinate system, (r, θ, z), is used where the z-axis is taken to coincide with the microchannel central axis; in Figure 2.12, all field quantities will be taken to depend on the radial coordinate, r, and time, t.

44

Electric field driven flow
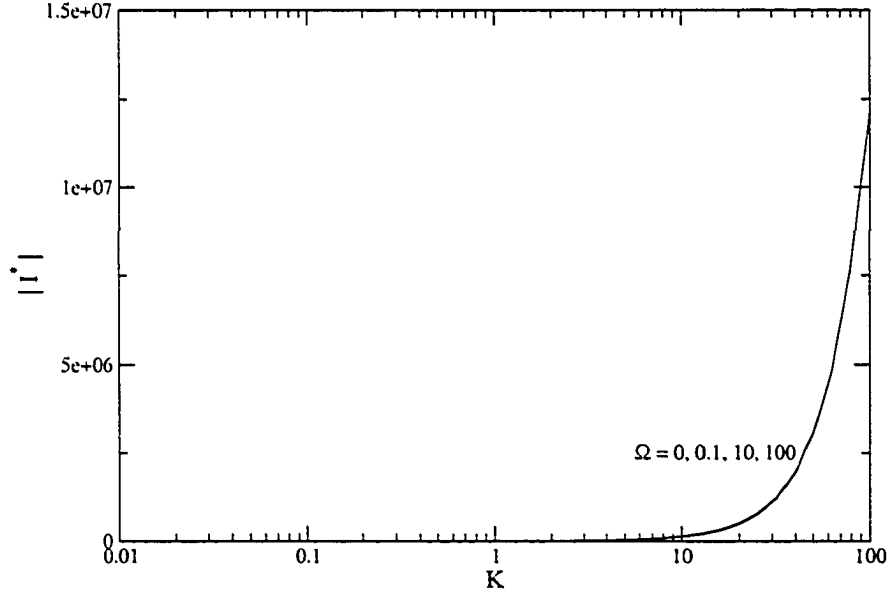
Figure 2.10: Dependence of the amplitude, $|I^*|$, of the normalized electroosmotic current, on the normalized reciprocal EDL thickness, K, for different normalized frequencies, Ω.

The corresponding Poisson-Boltzmann equation and its boundary condition is

$$\frac{1}{r}\frac{d}{dr}\left(r\frac{d\psi(r)}{dr}\right) = \kappa^2\psi .$$

$$\psi(a) = \psi_s \quad \text{and} \quad \psi(0) \text{ is finite} , \tag{2.3.1}$$

where a is the radius of the microchannel and ψ_s is the surface potential. The modified Navier-Stokes equation becomes

$$-\frac{1}{\mu}\frac{\partial p}{\partial z} + \frac{1}{r}\frac{\partial}{\partial r}\left(r\frac{\partial v}{\partial r}\right) + \frac{1}{\mu}\rho E_z' = \frac{1}{\nu}\frac{\partial v}{\partial t} ,$$

$$v(a,t) = 0 \quad , \quad \frac{\partial v(0,t)}{\partial r} = 0 . \tag{2.3.2}$$

The electric current density along the microchannel may be integrated over the channel cross-section to give the electric current

$$i = 2\pi \int_0^a \rho v r dr + \frac{2\pi z_0 e D}{kT}E_z' \int_0^a (\rho_1 - \rho_2)r dr , \tag{2.3.3}$$

45

Electric field driven flow
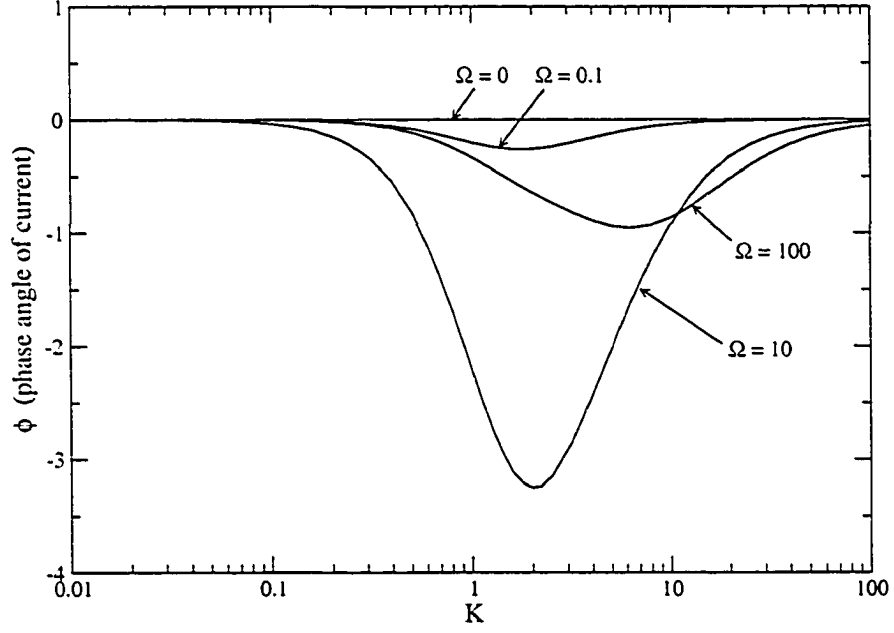
Figure 2.11: Dependence of the phase angle, ϕ, of the normalized electroosmotic current, on the normalized reciprocal EDL thickness, K, for different normalized frequencies, Ω.

and the flow rate can be written as

$$q = 2\pi \int_0^a vr\,dr \ . \tag{2.3.4}$$

We define the following normalized quantities for the cylindrical coordinate system

$$V = \frac{1}{\langle v \rangle}v \ , \quad R = \frac{1}{a}r \ , \quad \Psi = \frac{z_0 e}{kT}\psi \ , \quad E_z = \frac{z_0 ea}{kT}E_z' \ , \quad \bar{\rho} = \frac{a^2 e z_0}{\epsilon kT}\rho \ ,$$

$$K = \kappa a \ , \quad P = \frac{a}{\mu\langle v \rangle}p \ , \quad \tau = \frac{\nu}{a^2}t \ , \quad I = \frac{e z_0}{\epsilon kT\langle v \rangle}i \ , \quad \Sigma = \frac{z_0^2 e^2 \mu D}{\epsilon k^2 T^2} \ ,$$

$$\langle v \rangle = \frac{\epsilon k^2 T^2}{\mu a e^2 z_0^2} \ , \quad \Omega = \frac{a^2}{\nu}\omega \ , \quad Q = \frac{q}{\langle v \rangle a^2} \ , \quad \bar{\Omega} = \Omega\frac{\mu}{\bar{\mu}} \ , \quad \bar{\tau} = \frac{\bar{\nu}}{a^2}t \tag{2.3.5}$$

46
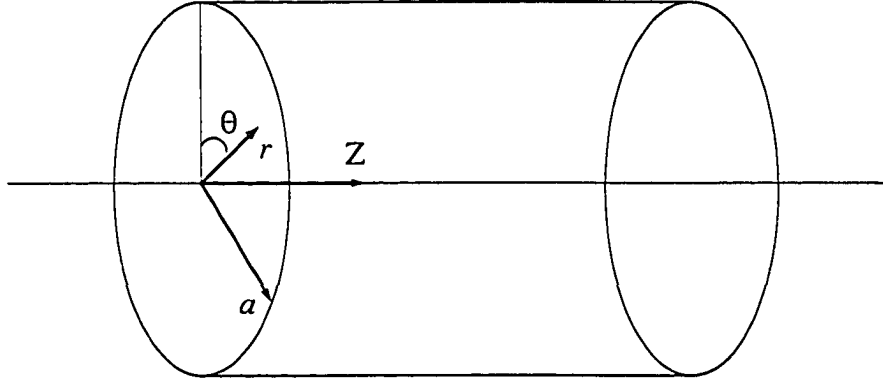
Figure 2.12: A schematic of the circular microchannel, with the associated cylindrical coordinate system.

2.3.1 Analytical solutions

Just following the same procedure of section 2.2, we give out analytical solutions of $V_P^*(\Omega)$, $V_E^*(\Omega)$, $I_P^*(\Omega)$, $I_E^*(\Omega)$, $Q_P^*(\Omega)$ and $Q_E^*(\Omega)$ for circular microchannels:

$$V_P^*(R,\Omega) = \frac{1}{j\Omega}\left[1 - \frac{J_0(R\sqrt{-j\Omega})}{J_0(\sqrt{-j\Omega})}\right] ,$$

$$V_E^*(R,\Omega) = \frac{K^2\Psi_s}{K^2 - j\Omega}\left[\frac{J_0(jKR)}{J_0(jK)} - \frac{J_0(R\sqrt{-j\Omega})}{J_0(\sqrt{-j\Omega})}\right] ,$$

$$I_P^*(\Omega) = 2\pi K^2\Psi_s\left\{\frac{1}{\Omega K}\frac{J_1(jK)}{J_0(jK)} - \frac{1}{\Omega^2 + j\Omega K^2}\left[jK\frac{J_1(jK)}{J_0(jK)}\right.\right.$$
$$\left.\left. - \sqrt{(-j\Omega)}\frac{J_1(\sqrt{-j\Omega})}{J_0(\sqrt{-j\Omega})}\right]\right\} ,$$

$$I_E^*(\Omega) = -\frac{2\pi K^4\Psi_s^2}{K^2 - j\Omega}\left\{\frac{1}{2}\left[1 + \frac{J_1^2(jK)}{J_0^2(jK)}\right] - \frac{1}{j\Omega - K^2}\left[jK\frac{J_1(jK)}{J_0(jK)}\right.\right.$$
$$\left.\left. - \sqrt{-j\Omega}\frac{J_1(\sqrt{-j\Omega})}{J_0(\sqrt{-j\Omega})}\right]\right\} + \pi\Sigma K^2 ,$$

$$Q_P^*(\Omega) = \frac{2\pi}{j\Omega}\left[\frac{1}{2} - \frac{1}{\sqrt{-j\Omega}}\frac{J_1(\sqrt{-j\Omega})}{J_0(\sqrt{-j\Omega})}\right] ,$$

$$Q_E^*(\Omega) = I_P^*(\Omega) . \tag{2.3.6}$$

where J_0 and J_1 are the zeroth- and first-order Bessel functions of the first kind. The Eqs.[2.3.6] may be reduced to the following special cases: steady state ($\Omega = 0$), slow oscillations ($\Omega \ll 1$) and fast oscillations ($\Omega \gg 1$). We point out that the latter

47

two special cases are given with respect to the normalized frequency, Ω, and thus, for example, a "slow" oscillation implies a low normalized frequency and *may not* necessarily imply a low dimensional frequency, $\omega \ll 1$. The special cases are given next.

Steady state ($\Omega = 0$)

The steady state response follows from Eqs.[2.3.6] by setting $\Omega = 0$. The solutions were originally obtained by Rice and Whitehead [53].

$$V_P^*(R,0) = \frac{1}{4}(1 - R^2) ,$$

$$V_E^*(R,0) = -\Psi_s \left[1 - \frac{J_0(jKR)}{J_0(jK)} \right] ,$$

$$I_P^*(0) = -\pi\Psi_s \left[1 - \frac{2}{jK}\frac{J_1(jK)}{J_0(jK)} \right] ,$$

$$I_E^*(0) = -\pi\Psi_s^2 K^2 \left[1 - \frac{2}{jK}\frac{J_1(jK)}{J_0(jK)} + \frac{J_1^2(jK)}{J_0^2(jK)} \right] + \pi\Sigma K^2 ,$$

$$Q_P^*(0) = \frac{\pi}{8} ,$$

$$Q_E^*(0) = I_P^*(0) . \tag{2.3.7}$$

Slow oscillations ($\Omega \ll 1$)

All terms higher than order 3 in the series expansion for the Bessel functions involving the normalized frequency, Ω, in Eqs.[2.3.6] are dropped, and we obtain

$$V_P^*(R,\Omega) = \frac{1 - R^2}{4 + j\Omega} ,$$

$$V_E^*(R,\Omega) = \frac{K^2\Psi_s}{K^2 - j\Omega} \left[\frac{J_0(jKR)}{J_0(jK)} - \frac{4 + j\Omega R^2}{4 - j\Omega} \right] ,$$

$$I_P^*(\Omega) = 2\pi K^2\Psi_s \left\{ \frac{1}{\Omega K}\frac{J_1(jK)}{J_0(jK)} - \frac{1}{\Omega^2 + j\Omega K^2} \left[jK\frac{J_1(jK)}{J_0(jK)} \right. \right.$$
$$\left. \left. + \frac{\Omega^2 - 8j\Omega}{16 + 4j\Omega} \right] \right\} ,$$

$$I_E^*(\Omega) = \frac{-2\pi K^4 \Psi_s^2}{K^2 - j\Omega} \left\{ \frac{1}{2} \left[1 + \frac{J_1^2(jK)}{J_0^2(jK)} \right] - \frac{1}{j\Omega - K^2} \left[jK \frac{J_1(jK)}{J_0(jK)} \right. \right.$$

$$\left. \left. + \frac{\Omega^2 - 8j\Omega}{16 + 4j\Omega} \right] \right\} + \pi \Sigma K^2 ,$$

$$Q_P^*(\Omega) = \frac{2\pi}{j\Omega} \left[\frac{1}{2} - \frac{\Omega + 8}{16 + 4j\Omega} \right] ,$$

$$Q_E^*(\Omega) = I_P^*(\Omega) . \qquad\qquad (2.3.8)$$

Fast oscillations $(\Omega \gg 1)$

The approximation, $J_m(x) = \sqrt{2/\pi x} \cos(x - \pi m/2 - \pi/4)$ for $\mid x \mid \gg 1$ (Abramowitz and Stegun [116])is used to reduce Eqs.[2.3.6] and to obtain

$$V_P^*(R,\Omega) = \frac{1}{jK} \left[1 - \sqrt{\frac{1}{R}} e^{(-1-j)(1-R)\sqrt{\frac{\Omega}{2}}} \right] ,$$

$$V_E^*(R,\Omega) = \frac{K^2 \Psi_s}{K^2 - j\Omega} \left[\frac{J_0(jKR)}{J_0(jK)} - \sqrt{\frac{1}{R}} e^{(-1-j)(1-R)\sqrt{\frac{\Omega}{2}}} \right] ,$$

$$I_P^*(\Omega) = 2\pi K^2 \Psi_s \left\{ \frac{1}{\Omega K} \frac{J_1(jK)}{J_0(jK)} - \frac{1}{\Omega^2 + j\Omega K^2} \left[jK \frac{J_1(jK)}{J_0(jK)} + (1+j)\sqrt{\frac{\Omega}{2}} \right] \right\} ,$$

$$I_E^*(\Omega) = \frac{-2\pi K^4 \Psi_s^2}{K^2 - j\Omega} \left\{ \frac{1}{2} \left[1 + \frac{J_1^2(jK)}{J_0^2(jK)} \right] - \frac{1}{jK - K^2} \left[jK \frac{J_1(jK)}{J_0(jK)} \right. \right.$$

$$\left. \left. + (1+j)\sqrt{\frac{\Omega}{2}} \right] \right\} + \pi \Sigma K^2 ,$$

$$Q_P^*(\Omega) = \frac{2\pi}{j\Omega} \left[\frac{1}{2} + (1+j)\sqrt{\frac{1}{2\Omega}} \right] ,$$

$$Q_E^*(\Omega) = I_P^*(\Omega) . \qquad\qquad (2.3.9)$$

2.3.2 Parametric studies and discussion

The following fixed values of the normalized surface potential, $\Psi_s = 1.95$, normalized conductivity, $\Sigma = 3.85$, amplitude of the normalized pressure gradient, $P^*(\Omega) = 200$, amplitude of the electric field, $E_z^*(\Omega) = 39$ are used in parametric study. We have studied the dependence of $\mid \bar{\mu}/\mu \mid$ on the normalized frequency, Ω, at three different values of K (0.1, 1, 10); see Figure 2.13. It can be observed that the apparent viscosity attains a maximum as a function of Ω at the values of K studied. This points

49

Pressure driven flow
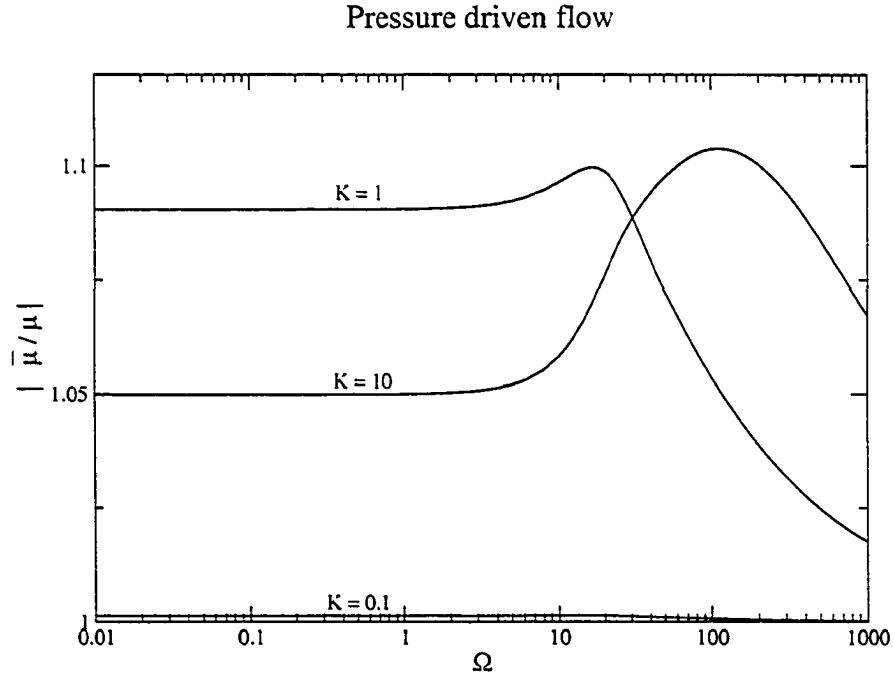
Figure 2.13: Dependence of the amplitude, $|\bar{\mu}/\mu|$, of the normalized apparent viscosity, on the normalized frequency, Ω, for the different K values.

to a conclusion that not only the electroviscous effect is dependent on the normalized reciprocal EDL thickness, but also K is dependent on the normalized frequency. Finally, in Figure 2.14, we compare the normalized apparent viscosity of a circular microchannel (Bhattacharyya et al. [110]) with that of a square microchannel. For the parameters studied, a circular microchannel has a slightly more pronounced electroviscous effects. The results of Figure 2.14 would indicate that a square microchannel can be approximated by a circular one.

To verify our oscillating electrokinetic flow model, we indirectly compare our results with those of other's experiments. Reppert et al. [67] measured frequency-dependent streaming potential in pores diameter from 1 mm to 34 μm. In their paper, they proved that Packard's model [117] (or Helmholtz-Smoluchowski equation) had a good fit to the experimental data. Actually, Packard's model or Helmholtz-Smoluchowski equation is based on the assumption of an infinite thin EDL, or we

50

Pressure driven flow
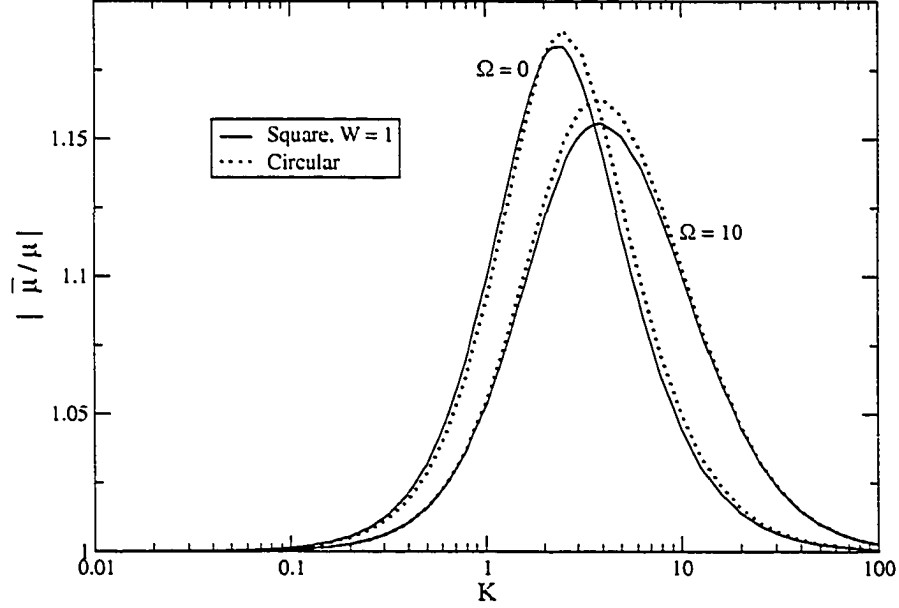
Figure 2.14: Dependence of the amplitude, $|\bar{\mu}/\mu|$, of the normalized apparent viscosity on K for two different microchannel geometries: Square and circular cross-section.

can say Helmholtz-Smoluchowski equation does not consider the structure of EDL. In Figure 5 of their paper [67], they used their equation 16 to generate the normalized coupling coefficient of the real and imaginary parts for three capillaries with different radiuses, 100 μm, 50 μm and 10μm. In our model, just as Eq. 2.2.23,

$$E_z = Re[E_z^* e^{j\Omega\tau}] = Re[E_z^* e^{j\omega t}] = Re[|E_z^*|e^{j(\omega t + \phi)}] . \qquad (2.3.10)$$

The normalized complex component of streaming potential only relates to $e^{j(\omega t + \phi)}$, which corresponds to the coupling coefficient of the real and imaginary components of [67]. For comparing our results to their Figure 5, we use 0.1M KCl as testing example, which has a thin EDL. Some parameters related to 0.1M KCl are: the reciprocal of the double layer thickness $\kappa = 1.03 \times 10^9$ m^{-1} and conductivity $\sigma = 1.28217$ S/m [38]. Using our model, we plot the normalized coupling coefficients of the real and imaginary parts for three capillaries with different radiuses, 100 μm, 50 μm and 10 μm,

51
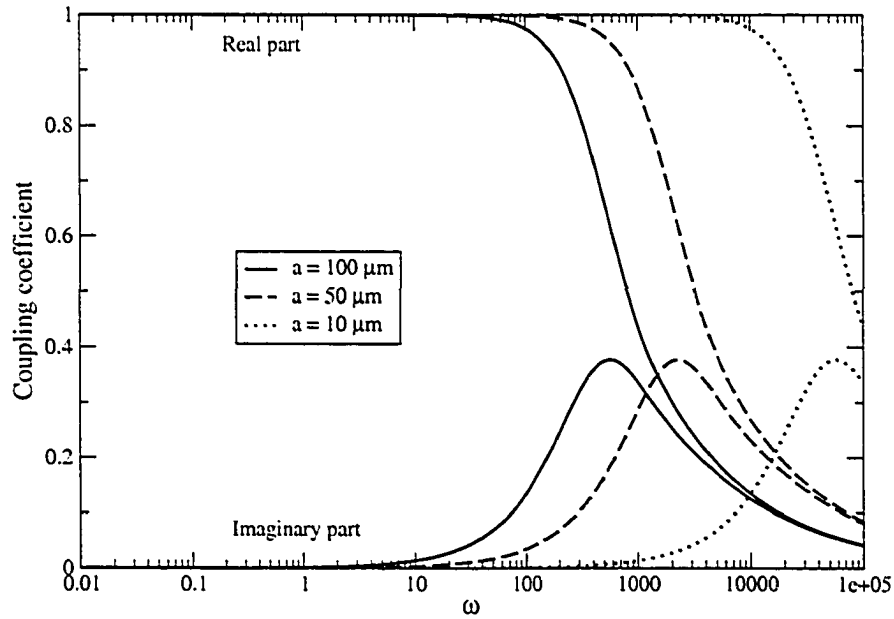
Figure 2.15: Normalized coupling coefficients of the real and imaginary parts for three capillaries with different radiuses.

in Figure 2.15. Our Figure 2.15 is almost the same as their Figure 5. Since they did not provide enough experimental details, such as surface potential, we cannot compare our model with their experimental data directly. However, because their experiments strongly support Packard's model or Helmholtz-Smoluchowski equation, we believe that our model is also correct. Furthermore, our model overcomes two limitations of their model: firstly, we consider convective current caused by electroosmotic flow, which is induced by streaming potential; secondly, our model is not limited to an infinite thin EDL.

2.4 Electrokinetic flow in parallel-plate microchannels

The problem of oscillatory flow in microchannels between two parallel plates is a special case of the rectangular microchannel problem addressed in section 2.2. We

52
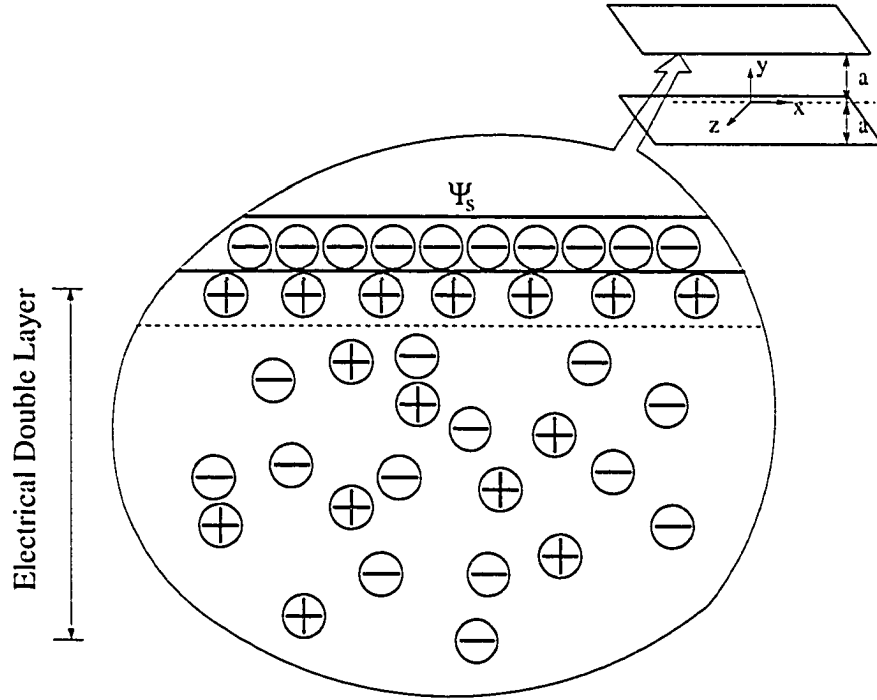
Figure 2.16: Schematic of an electrical double layer at the channel wall.

give the solutions for the parallel plate geometry here (see Figure 2.16), (i) derived from the first principles (*i.e.* starting from the boundary value problem for the parallel plates) and, (ii) derived from Eq.2.2.40 by setting $W \to \infty$.

The boundary value problem for flow between parallel plates is now summarized. Assuming that the y-axis is perpendicular to the parallel plates (refer Figure 2.1 and let $w \to \infty$), Eq. 2.2.8, Eq. 2.2.9 and corresponding boundary conditions become

$$\frac{\partial^2 \psi(y)}{\partial y^2} = \kappa^2 \psi$$

$$\psi(\pm h) = \psi_2 \quad , \quad \frac{\partial \psi}{\partial y}(0) = 0 \; , \tag{2.4.1}$$

$$-\frac{1}{\mu}\frac{\partial p}{\partial z} + \frac{\partial^2 v}{\partial^2 y} + \frac{1}{\mu}\rho E'_z = \frac{1}{\nu}\frac{\partial v}{\partial t} \; ,$$

$$v(\pm h, t) = 0 \quad , \quad \frac{\partial v}{\partial y}(0, t) = 0 \; , \tag{2.4.2}$$

53

The definition of volumetric flow rate, q, per unit width of the parallel plate is

$$q = 2 \int_0^h v \, dy \ , \tag{2.4.3}$$

whereas the electric current is

$$i(t) = 2 \int_0^h \rho v \, dy + \frac{2z_0 e D}{kT} \int_0^h (\rho_1 - \rho_2) E_z' \, dy \ . \tag{2.4.4}$$

Using the relevant normalized quantities (see Eq.2.2.13), Eqs. 2.4.1-2.4.4 become

$$\frac{\partial^2 \Psi}{\partial Y^2} = K^2 \Psi \ ,$$

$$\Psi(\pm 1) = \Psi_2 \quad , \quad \frac{\partial \Psi}{\partial Y}(0) = 0 \ ,$$

$$-\frac{\partial P}{\partial Z} + \frac{\partial^2 V}{\partial Y^2} - K^2 \Psi E_z = \frac{\partial V}{\partial \tau} \ ,$$

$$V(\pm 1, \tau) = 0 \quad , \quad \frac{\partial V(0, \tau)}{\partial Y} = 0 \ ,$$

$$I = -2 \int_0^1 K^2 \Psi V \, dY + 2\frac{2h^2 e^4 z_0^4 \mu D n_\infty}{\epsilon^2 k^3 T^3} E_z = -2 \int_0^1 K^2 \Psi V \, dY + 2\Sigma K^2 E_z \ ,$$

$$Q = 2 \int_0^1 V \, dY \ , \tag{2.4.5}$$

In deriving Eq.2.4.5, we have made use of the normalized quantities in Eq.2.2.18 except I, which is given by $I = \frac{he z_0}{\epsilon kT \langle v \rangle} i$. The expression for $\langle v \rangle$ is given in Eq.2.2.19. In order to obtain the solutions, we also use the first three normalized quantities in Eq.2.2.20 whereas Q is defined for this problem as $Q = \frac{q}{\langle v \rangle h}$. Solving Eqs.2.4.5, the spatially 1-dimensional analog of Eqs.2.2.36 and 2.2.40 is

$$\Psi(Y) \quad = \Psi_2 \frac{\cosh KY}{\cosh K} \ ,$$

$$V_P^*(Y, \Omega) \quad = \frac{1}{j\Omega} \left[1 - \frac{\cosh(Y\sqrt{j\Omega})}{\cosh(\sqrt{j\Omega})} \right] \ ,$$

$$V_E^*(Y, \Omega) \quad = \frac{K^2 \Psi_2}{K^2 - j\Omega} \left[\frac{\cosh(KY)}{\cosh(K)} - \frac{\cosh(Y\sqrt{j\Omega})}{\cosh(\sqrt{j\Omega})} \right] \ ,$$

$$I_P^*(\Omega) \quad = \frac{2K^2 \Psi_2}{j\Omega \cosh(K)} \left[\frac{1}{\cosh(\sqrt{j\Omega})} \left(\frac{\sinh(K + \sqrt{j\Omega})}{2(K + \sqrt{j\Omega})} + \frac{\sinh(K - \sqrt{j\Omega})}{2(K - \sqrt{j\Omega})} \right) \right.$$

$$\left. - \frac{\sinh(K)}{K} \right] \ ,$$

54

$$I_E^*(\Omega) = \frac{-2K^4\Psi_2^2}{(K^2 - j\Omega)\cosh(K)} \left[\frac{1}{\cosh(K)} \left(\frac{1}{2} + \frac{\sinh(K)\cosh(K)}{2K} \right) \right.$$
$$\left. - \frac{1}{\cosh(\sqrt{j\Omega})} \left(\frac{\sinh(K + \sqrt{j\Omega})}{2(K + \sqrt{j\Omega})} + \frac{\sinh(K - \sqrt{j\Omega})}{2(K - \sqrt{j\Omega})} \right) \right] + 2\Sigma K^2 \ ,$$

$$Q_P^*(\Omega) = \frac{2}{j\Omega} \left(1 - \frac{1}{\sqrt{j\Omega}} \frac{\sinh(\sqrt{j\Omega})}{\cosh(\sqrt{j\Omega})} \right) \ ,$$

$$Q_E^*(\Omega) = I_P^*(\Omega) \ . \qquad (2.4.6)$$

We now demonstrate that Eqs.2.4.6 will follow from the rectangular microchannel solution by setting $W \to \infty$; for brevity, we demonstrate the limiting case for the first three of Eqs.2.4.6. When $W \to \infty$, Eq.2.2.36 reduces to

$$\Psi = \frac{\Psi_2}{2} \frac{\cosh KY}{\cosh K} - \sum_{m=1}^{\infty} \frac{K^2}{K^2 + \frac{(2m-1)^2\pi^2}{4}} \frac{2\Psi_2(-1)^{m+1}}{(2m-1)\pi} \cos \frac{(2m-1)\pi}{2} Y + \frac{\Psi_2}{2} \ . (2.4.7)$$

The following Fourier series expansion

$$1 - \frac{\cosh KY}{\cosh K} = \sum_{m=1}^{\infty} \frac{K^2}{K^2 + \frac{(2m-1)^2\pi^2}{4}} \frac{4(-1)^{m+1}}{(2m-1)\pi} \cos \frac{(2m-1)\pi}{2} Y \ , \qquad (2.4.8)$$

is used in Eq.2.4.7 to obtain the first of Eqs.2.4.6. Next, the second and third Eqs.2.4.6 may be re-written as

$$V_P^*(Y,\Omega) = \frac{1}{j\Omega} \left[1 - \frac{\cos(Y\sqrt{-j\Omega})}{\cos(\sqrt{-j\Omega})} \right] \ , \qquad (2.4.9)$$

$$V_E^*(Y,\Omega) = \frac{K^2\Psi_2}{K^2 - j\Omega} \left[\frac{\cos(jKY)}{\cos(jK)} - \frac{\cos(Y\sqrt{-j\Omega})}{\cos(\sqrt{-j\Omega})} \right] \ . \qquad (2.4.10)$$

where we have used $\cos(jz) = \cosh(z)$. When $W \to \infty$, the first and second of Eqs.2.2.40 become

$$V_P^*(X,Y,\Omega) = \frac{4}{\pi} \sum_{n=1}^{\infty} \frac{1}{j\Omega + \left[\frac{(2n-1)\pi}{2}\right]^2} \cos\left[\frac{(2n-1)\pi}{2} Y \right] \ , \qquad (2.4.11)$$

$$V_E^*(X,Y,\Omega) = -K^2\Psi_2\pi \sum_{n=1}^{\infty} \frac{2n-1}{j\Omega + \left[\frac{(2n-1)\pi}{2}\right]^2} \frac{(-1)^{n+1}}{K^2 + \left[\frac{(2n-1)\pi}{2}\right]^2} \cos\left[\frac{(2n-1)\pi}{2} Y \right] \ .$$

$$(2.4.12)$$

Then, when we expand Eq.2.4.9 and Eq.2.4.10 as the orthogonal series of $\cos[(2n - 1)\pi Y/2]$, Eq.2.4.9 and Eq.2.4.10 can reduce to Eq.2.4.11 and Eq.2.4.12, respectively.

55

2.4.1 Arbitrary time-dependent electrokinetic flows

Arbitrary time-dependent pressure or electrical field input for the microchannel system may be expanded as Fourier series of complex form. Here we take into account a time-dependent function $f(\tau)$, which is continuous at the range of $[\tau_0, \tau_0 + \tau_2]$. Thus, $f(\tau)$ can be expanded as

$$f(\tau) = \sum_{n=-\infty}^{n=\infty} C_n e^{\frac{j2n\pi\tau}{\tau_2}} = \sum_{n=-\infty}^{n=\infty} C_n e^{j\Omega_n\tau} , \qquad (2.4.13)$$

where

$$C_n = \frac{1}{\tau_2} \int_{\tau_0}^{\tau_0+\tau_2} f(\tau) e^{\frac{-j2n\pi\tau}{\tau_2}} \, d\tau , \qquad (2.4.14)$$

$j = \sqrt{-1}$ and $\Omega_n = 2n\pi/\tau_2$. Note, C_n is time independent. With the definition of Eq.2.4.13, arbitrary time-dependent input (pressure or electric field) can be considered superposition of many oscillating input with different frequencies, Ω_n. So, we shall seek the solution of the boundary value problem for the following specific dependencies

$$-\frac{\partial P_n}{\partial Z} = P_n^* e^{j\Omega_n\tau} \qquad , \qquad E_{z,n} = E_{z,n}^* e^{j\Omega_n\tau} . \qquad (2.4.15)$$

We consider the class of solutions where the amplitudes of the pressure gradient and the electric field could be frequency-dependent, i.e. $P_n^* \equiv P_n^*(\Omega_n)$ and $E_{z,n}^* \equiv E_{z,n}^*(\Omega_n)$. The solutions for Ψ and V will then follow from the first three equations of Eqs.2.4.6. Thus

$$V = \sum_{n=-\infty}^{n=\infty} V_n^* e^{j\Omega_n\tau} , \text{where}$$

$$V_n^* \equiv V_n^*(Y, \Omega_n) = V_P^*(Y, \Omega_n)P_n^*(\Omega_n) + V_E^*(Y, \Omega_n)E_{z,n}^*(\Omega_n) ; \qquad (2.4.16)$$

The expression for $V_P^*(Y, \Omega_n)$ and $V_E^*(Y, \Omega_n)$ will be given at the end of this section. The normalized electric current will follow from corresponding solutions of Eqs.2.4.6 and may be written as

$$I = \sum_{n=-\infty}^{n=\infty} I_n^* e^{j\Omega_n\tau} \text{ where } I_n^* \equiv I_n^*(\Omega_n) = I_P^*(\Omega_n)P_n^*(\Omega_n) + I_E^*(\Omega_n)E_{z,n}^*(\Omega_n) \quad (2.4.17)$$

56

The volumetric flow rate, q, is defined as $q = 2\int_0^a v\,dy$. Using the definitions in Eq.2.2.20, Eqs.2.4.15 and 2.4.16, the normalized flow rate, Q_n, becomes

$$Q = \sum_{n=-\infty}^{n=\infty} Q_n^* e^{j\Omega_n\tau} \quad \text{where}$$

$$Q_n^* \equiv Q_n^*(\Omega_n) = Q_P^*(\Omega_n)P_n^*(\Omega_n) + Q_E^*(\Omega_n)E_{z,n}^*(\Omega_n)\,. \tag{2.4.18}$$

During pressure driven flow, the amplitude of the nth streaming potential, $E_{z,n}^*(\Omega_n)$, is found by setting $I_n^* = 0$ in Eq.2.4.17. Thus

$$E_{z,n}^*(\Omega_n) = -\frac{I_P^*(\Omega_n)}{I_E^*(\Omega_n)}P_n^*(\Omega) \quad \text{for} \quad I_n^* = 0\,. \tag{2.4.19}$$

During pressure driven flow, Eq.2.4.19 may be substituted in Eqs.2.4.16 and 2.4.18 to determine the normalized liquid velocity and the volumetric flow rate, respectively. Alternatively, the velocity, current and flow rate during electroosmosis follow from Eqs.2.4.16, 2.4.17 and 2.4.18 by setting $P_n^*(\Omega) = 0$ in those equations.

2.4.2 Parametric studies and discussion

In this section, we will mainly focus on time-dependent electrokinetic flows in parallel-plate microchannels. The following fixed values of the normalized surface potential, $\Psi_s = 1.95$, normalized conductivity, $\Sigma = 3.85$, are used.

Microflow under time-dependent pressure gradients

We choose four kinds of pressure input

$$-\frac{\partial P}{\partial Z} = \begin{cases} 2\times 10^2, & (m-1)\times\tau_2 \le \tau < (m-1)\times\tau_2 + \tau_1 \\ 1\times 10^2, & (m-1)\times\tau_2 + \tau_1 \le \tau < m\times\tau_2 \end{cases}$$

1. $\tau_1 = 1,\ \tau_2 = 3$

2. $\tau_1 = 10^6,\ \tau_2 = 3\times 10^6$

$$-\frac{\partial P}{\partial Z} = \begin{cases} 2\times 10^2 \times \frac{\tau}{\tau_1}, & (m-1)\times\tau_2 \le \tau < (m-1)\times\tau_2 + \tau_1 \\ -2\times 10^2 \times \frac{\tau-\tau_2}{\tau_2-\tau_1}, & (m-1)\times\tau_2 + \tau_1 \le \tau < m\times\tau_2 \end{cases}$$

Pressure driven flow
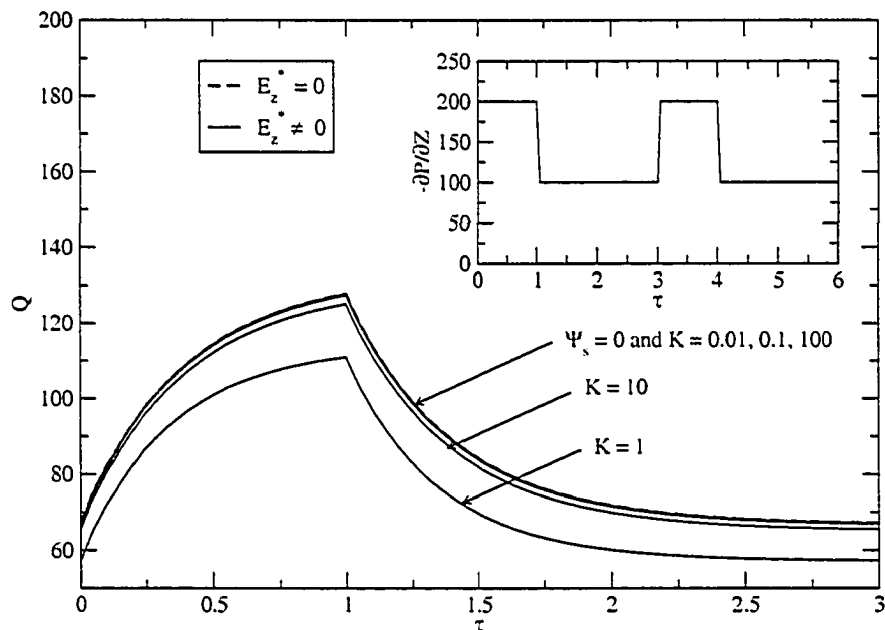
Figure 2.17: The flow rate, Q, as a function of normalized time under a pulsatile pressure gradient with a relatively short period.

3. $\tau_1 = 1$, $\tau_2 = 3$

4. $\tau_1 = 10^6$, $\tau_2 = 3 \times 10^6$

The normalized pressure gradient, $-\partial P/\partial Z = 200$ can correspond to a pressure gradient at the order of 10^6 Pa/m for a 10 μm high channel. If h is the order of 10^{-6} m and ν is the order of 10^{-6} m^{2}s^{-1}, nondimensional time $\tau = 1$ and $\tau = 10^6$ can correspond to the orders of dimensional time μs and s, respectively. We plot the normalized flow rate with respect to the normalized time at different normalized reciprocal thickness of EDL $K = 0.01, 0.1, 1, 10, 100$. The normalized flow rate under a pulsatile pressure gradient with a relatively short period is plotted in Figure 2.17. Because $K = 0.01, 0.1$ and $K = 100$ correspond to very thick and very thin electrical double layers, respectively, EDL effect will disappear under these two conditions. The normalized flow rates at $K = 0.01, 0.1, 100$ are very close to the flow rate without EDL

58

Pressure driven flow
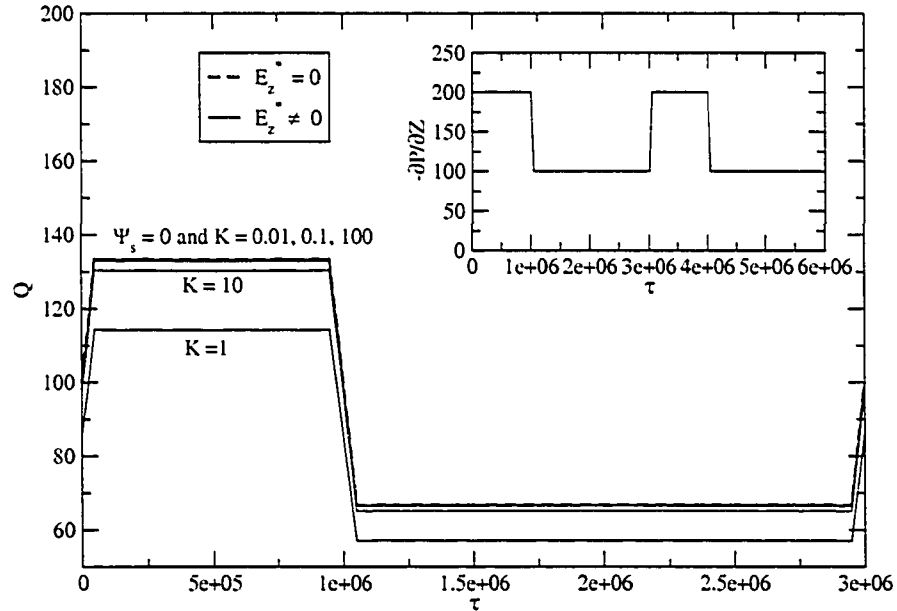
Figure 2.18: The flow rate, Q, as a function of normalized time under a pulsatile pressure gradient with a relatively long period.

effect ($\Psi_s = 0$ or $E_z^* = 0$), which confirms our theoretical derivation (see Table 2.1). The minimum normalized flow rate always happens at $K = 1$, since the electroviscous effect reaches its maximum. Because the period of applied pressure is too short, the flow cannot fully develop during the period. Comparing Figure 2.17 with Figure 2.18, the normalized time τ, to allow flow to fully develop, should be a little larger than 1, since the normalized flow rate of $K = 0.01$ in Figure 2.17 reaches 1.28×10^2 at $\tau = 1$, which is very close to the fully developed flow rate, 1.34×10^2 (see Figure 2.18). Because the period of applied pressure in Figure 2.18 is long enough, the flow can fully develop and keep up with the change of the pressure gradient. In Figure 2.19 and 2.20, we plot the normalized flow rates change with the normalized time under two triangle pressure inputs. In Figure 2.19, the flow cannot fully develop and cannot keep the same step with the change of the pressure gradient. The minimum and maximum of normalized flow rate do not happen at the same time of the minimum

59

Pressure driven flow
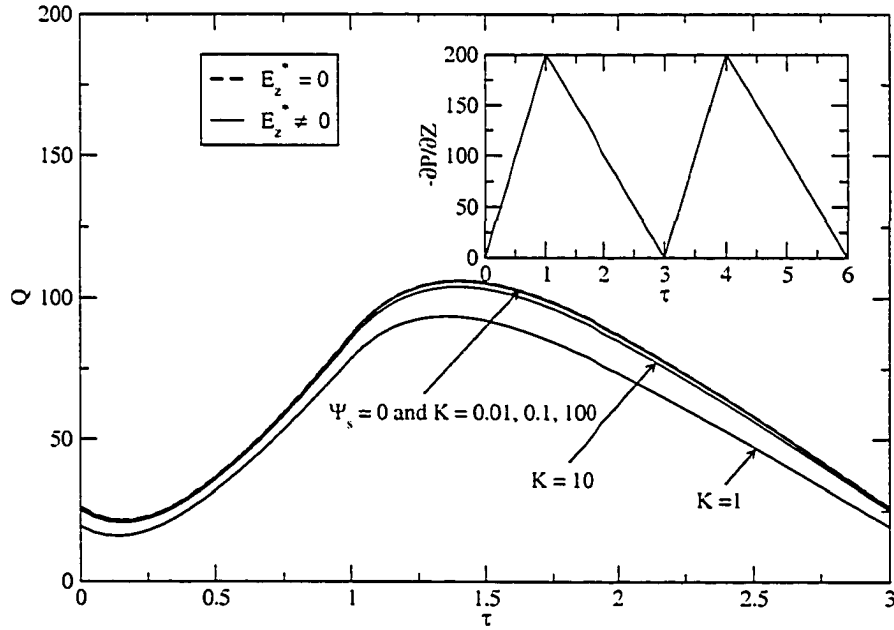
Figure 2.19: The flow rate, Q, as a function of normalized time under a triangle pressure gradient with a relatively long period.

and maximum of normalized pressure gradient. There is a lag between the pressure gradient and the flow rate. In Figure 2.20, since the period of the pressure gradient becomes larger, the profile of the flow rate can keep a triangle.

Microflows under time-dependent electric fields

We choose four kinds of electric field input:

$$E_z = \begin{cases} 78, & (m-1) \times \tau_2 \leq \tau < (m-1) \times \tau_2 + \tau_1 \\ 39, & (m-1) \times \tau_2 + \tau_1 \leq \tau < m \times \tau_2 \end{cases}$$

1. $\tau_1 = 1, \ \tau_2 = 3$

2. $\tau_1 = 10^6, \ \tau_2 = 3 \times 10^6$

$$E_z = \begin{cases} 78\frac{\tau}{\tau_1}, & (m-1) \times \tau_2 \leq \tau < (m-1) \times \tau_2 + \tau_1 \\ -78\frac{\tau-\tau_2}{\tau_2-\tau_1}, & (m-1) \times \tau_2 + \tau_1 \leq \tau < m \times \tau_2 \end{cases}$$

60
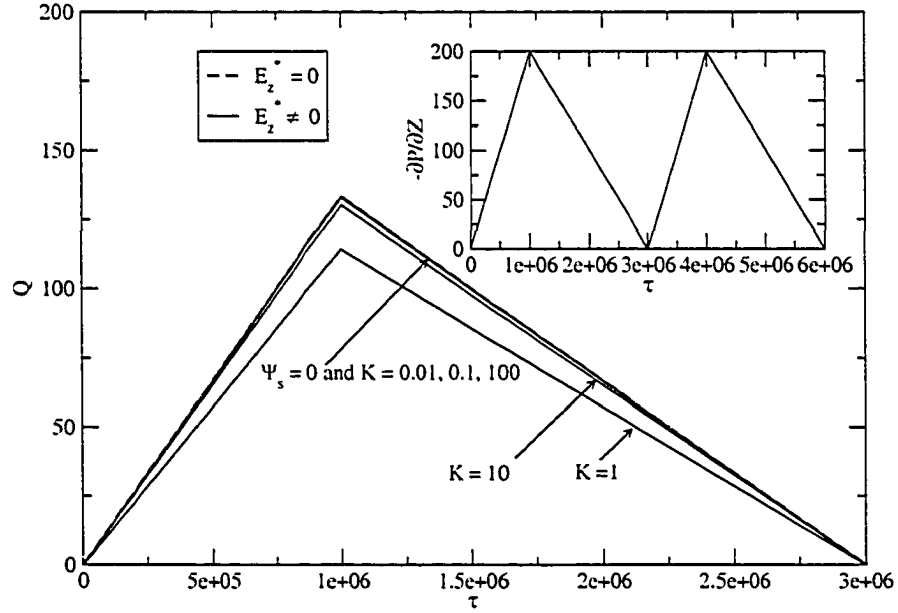
Figure 2.20: The flow rate, Q, as a function of normalized time under a triangle pressure gradient with a relatively long period.

1. $\tau_1 = 1$, $\tau_2 = 3$

2. $\tau_1 = 10^6$, $\tau_2 = 3 \times 10^6$

The normalized strength of electric field, $E_z = 39$ can correspond to an electric field at the order of 10^5 V/m for a 20 μm high channel. We give out the normalized flow rate with respect to the normalized time at different normalized reciprocal thickness of EDL $K = 1, 10, 100$. In Figures 2.21, 2.22, 2.23, 2.24, we plot the normalized flow rates change with the normalized time under pulsatile or triangle electric fields with relatively short or long periods. In all figures, the normalized flow rates increase as K increase, since more concentrated solutions can cause larger electroosmotic flow rates.

61

Electric field driven flow
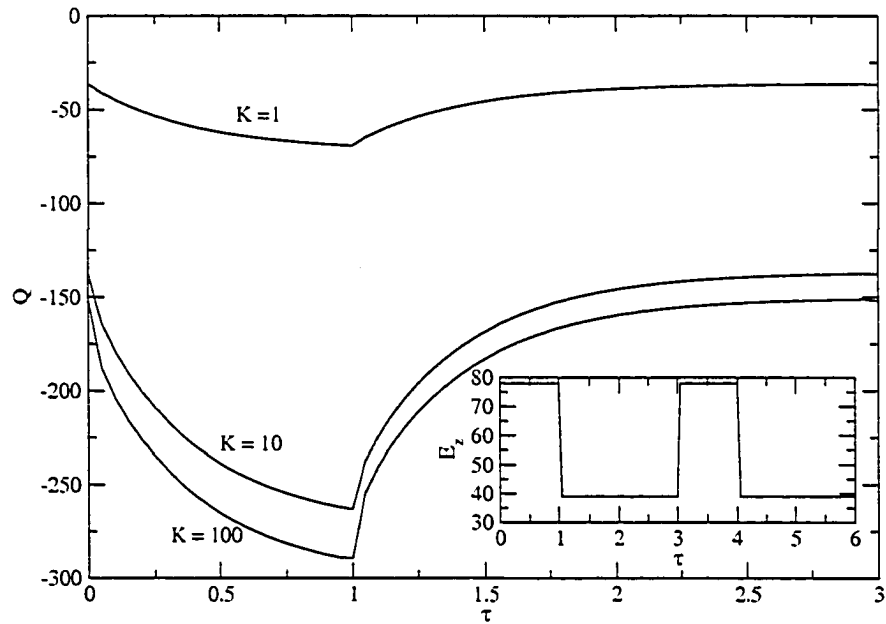
Figure 2.21: The flow rate, Q, as a function of normalized time under a pulsatile electric field with a relatively short period.

2.5 Conclusions

Using Debye-Hückel approximation of Poisson-Boltzmann equation of EDL, we obtain analytical solutions of time-dependent electrokinetic flow in rectangular, circular and parallel-plate microchannels. Oscillating flow rates, currents and electroviscous effects are studied. Experimental results [67] indirectly support our oscillating solutions. Arbitrary time-dependent electrokinetic flows can be obtained through superposition of time-harmonic solutions weighted by appropriate Fourier coefficients.

62

Electric field driven flow
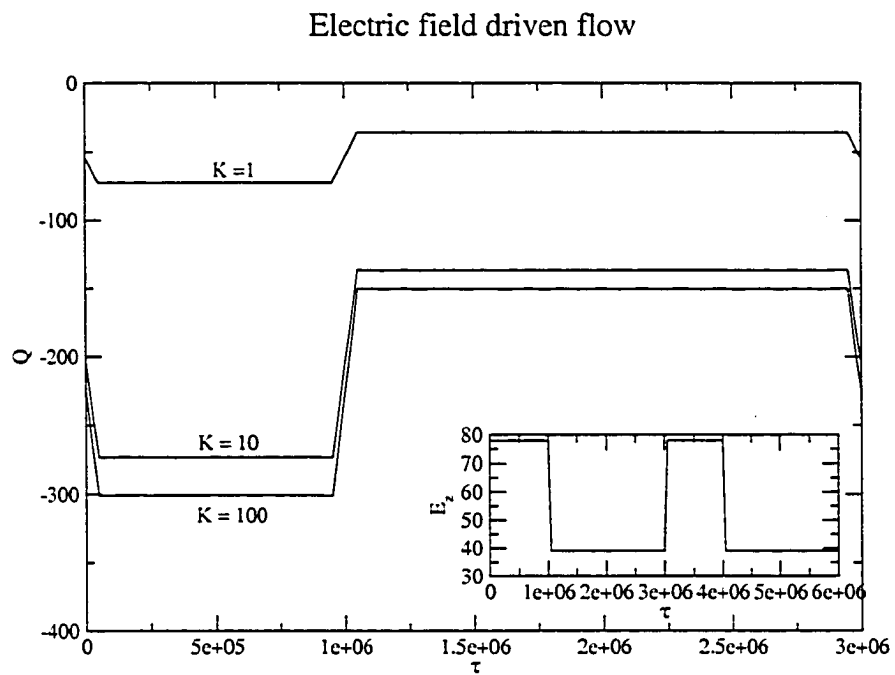
Figure 2.22: The flow rate, Q, as a function of normalized time under a pulsatile electric field with a relatively long period.

63

Electric field driven flow
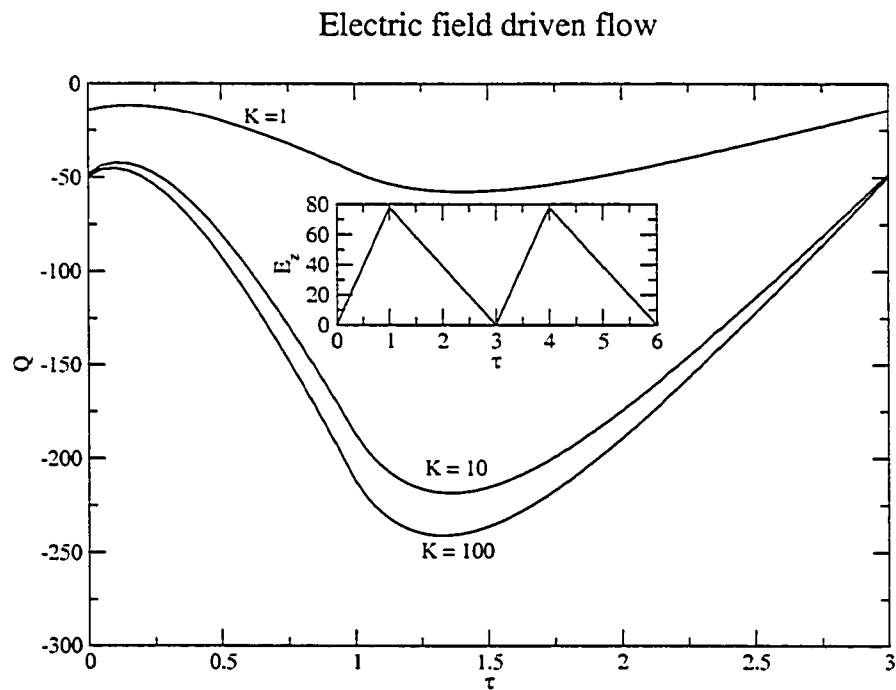
Figure 2.23: The flow rate, Q, as a function of normalized time under a triangle electric field with a relatively short period.

Electric field driven flow
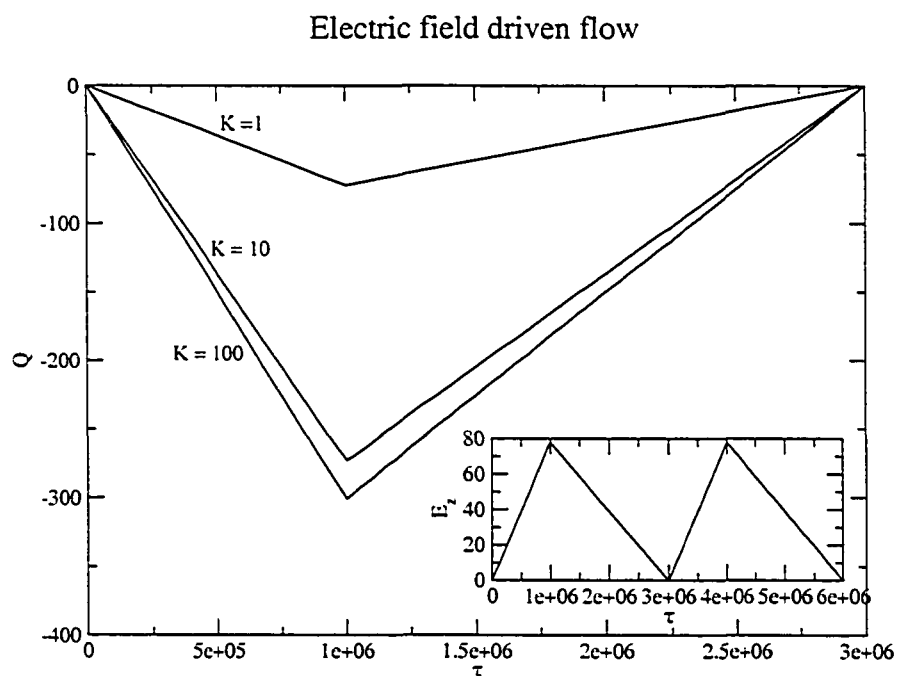
Figure 2.24: The flow rate, Q, as a function of normalized time under a triangle electric field with a relatively long period.

65

Chapter 3

Time-dependent Electrokinetic Slip Flow in Microchannels

3.1 Introduction

Recently, as some indirect or direct experimental results of slippage of liquid on non-wetting surfaces have been found, fluid behavior on lyohpobic surface are of interests to scientists and engineers. Even though a perfect, mathematical expression of slippage has not been found, scientists believe the essential reason of slippage is related to solid-liquid interaction. The widely accepted mathematical description is the simple Navier slip boundary condition

$$\vec{v} = \beta \frac{\partial \vec{v}}{\partial \vec{n}} \, . \tag{3.1.1}$$

Obviously, slippage and EDL do affect fluid behavior simultaneously. To the best of our knowledge, no systematical study combining slippage effects with EDL effects on microfluidics has been done. In this chapter, we investigate flow behavior under these two surface effects.

The whole mathematical procedure is very similar to that of Chapter 2. Here, we mainly present some results.

66

3.2 Electrokinetic slip and time-dependent flow in rectangular microchannels

3.2.1 Analytical solutions

After introducing slip boundary condition, hydrodynamic equations have slight change. Inclusion of the body force due to electric field in the Navier-Stokes equation and its boundary conditions lead to

$$-\frac{1}{\mu}\frac{\partial p}{\partial z} + \left(\frac{\partial^2 v}{\partial x^2} + \frac{\partial^2 v}{\partial y^2}\right) + \frac{1}{\mu}\rho E_z' = \frac{1}{\nu}\frac{\partial v}{\partial t} , \qquad (3.2.1)$$

$$v(x,y,0) = 0 ,$$

$$v(w,y,t) = \beta_1 \frac{\partial v}{\partial x}(w,y,t) \quad , \quad v(x,h,t) = \beta_2 \frac{\partial v}{\partial y}(x,h,t) ,$$

$$\frac{\partial v(0,y,t)}{\partial x} = 0 \quad , \quad \frac{\partial v(x,0,t)}{\partial y} = 0 , \qquad (3.2.2)$$

where μ, ν, β_1 and β_2 are the viscosity, the kinematic viscosity of the liquid, the slip coefficients for the x [width] and y [height] planes, respectively.

The normalized slip coefficients are

$$B_1 = \frac{\beta_1}{h} \quad , \quad B_2 = \frac{\beta_2}{h} . \qquad (3.2.3)$$

All other normalized quantities are the same as corresponding quantities of Chapter 2. Then, the normalized Navier-Stokes equation and its boundary condition are

$$-\frac{\partial P}{\partial Z} + \frac{\partial^2 V}{\partial X^2} + \frac{\partial^2 V}{\partial Y^2} - K^2 \Psi E_z = \frac{\partial V}{\partial \tau} ,$$

$$V(X,Y,0) = 0 ,$$

$$V(W,Y,\tau) = B_1 \frac{\partial V}{\partial X}(W,Y,\tau) \quad , \quad V(X,1,\tau) = B_2 \frac{\partial V}{\partial Y}(X,1,\tau) ,$$

$$\frac{\partial V(0,Y,\tau)}{\partial X} = 0 \quad , \quad \frac{\partial V(X,0,\tau)}{\partial Y} = 0 , \qquad (3.2.4)$$

67

Time-dependent solutions

Using Green's functions, the time-dependent solution of Eqs.(2.2.15) can be written as

$$V = \int_{\tau'=0}^{\tau} \int_{Y'=0}^{1} \int_{X'=0}^{W} G(X,Y,\tau|X',Y',\tau') \times \left[-\frac{\partial P}{\partial Z}(Z') - K^2 \Psi E_z(\tau') \right] dX' dY' d\tau' \ ,$$

$$(3.2.5)$$

where $G(X,Y,\tau|X',Y',\tau')$ is the Green's function [114], which may be obtained by separation of variables:

$$G(X,Y,\tau|X',Y',\tau') = \frac{4}{W} \sum_{m=1}^{\infty} \sum_{n=1}^{\infty} e^{-(\tau-\tau')(\gamma_m^2/W^2+\gamma_n^2)} \frac{\gamma_m^2 B_1^2 + W^2}{\gamma_m^2 B_1^2 + W^2 - WB_1}$$

$$\times \frac{\gamma_n^2 B_2^2 + 1}{\gamma_n^2 B_2^2 + 1 - B_2} \cos(\gamma_n Y) \cos(\gamma_n Y') \cos\left(\gamma_m \frac{X}{W}\right) \cos\left(\gamma_m \frac{X'}{W}\right) \quad (3.2.6)$$

where γ_m and γ_n are determined by $\gamma_m \tan \gamma_m = -\frac{W}{B_1}$ and $\gamma_n \tan \gamma_n = -\frac{1}{B_2}$. When $B_1 = 0, B_2 = 0$, the corresponding Green's function has the following expression [114]

$$G(X,Y,\tau|X',Y',\tau') = \frac{4}{W} \sum_{m=1}^{\infty} \sum_{n=1}^{\infty} e^{\lambda_1(\tau-\tau')} \cos\left[\frac{(2m-1)\pi}{2W}X\right] \cos\left[\frac{(2m-1)\pi}{2W}X'\right]$$

$$\times \cos\left[\frac{(2m-1)\pi}{2}Y\right] \cos\left[\frac{(2m-1)\pi}{2}Y'\right] \ ,$$

$$(3.2.7)$$

where

$$\lambda_1 = -\left(\frac{(2m-1)\pi}{2W}\right)^2 - \left(\frac{(2n-1)\pi}{2}\right)^2 \ . \qquad (3.2.8)$$

Using Eqs.(2.2.16), (2.2.17) and (3.2.5), we can obtain the flow rate and current. During pressure-driven flow, the strength of the electric field induced by the streaming potential E_z is found by setting $I = 0$. During pressure-driven flow, solved streaming potential E_z may be substituted into Eqs.(2.2.17) to determine the normalized volumetric flow rate. Alternatively, the velocity, current and flow rate during electroosmosis follow from Eqs.(3.2.5), (2.2.17) and Eq.(2.2.16) by setting $\left(-\frac{\partial P}{\partial Z}\right) = 0$ in those equations.

68

Oscillatory solution

We also use a complex variable approach to obtain an analytical solution for a sinusoidal periodicity in the electrohydrodynamic field. For oscillating problem, following the definitions of Chapter 2, we have

$$
V_P^* = 4 \sum_{m=1}^{\infty} \sum_{n=1}^{\infty} \xi \frac{\sin \gamma_n \sin \gamma_m}{\gamma_n \gamma_m} \cos(\gamma_n Y) \cos\left(\frac{\gamma_m}{W} X\right) ,
$$

$$
V_E^* = \frac{-4K^2}{W} \sum_{m=1}^{\infty} \sum_{n=1}^{\infty} \xi \Delta(c,d) \cos(\gamma_n Y) \cos\left(\frac{\gamma_m}{W} X\right) ,
$$

$$
I_P^* = -16 K^2 \sum_{m=1}^{\infty} \sum_{n=1}^{\infty} \xi \Delta(r,s) \frac{\sin \gamma_n \sin \gamma_m}{\gamma_n \gamma_m} ,
$$

$$
I_E^* = \frac{16 K^4}{W} \sum_{m=1}^{\infty} \sum_{n=1}^{\infty} \xi \Delta(r,s) \Delta(c,d) + 4W\Sigma K^2 ,
$$

$$
Q_P^* = \frac{16}{W} \sum_{m=1}^{\infty} \sum_{n=1}^{\infty} \xi \frac{W^2}{\gamma_n^2 \gamma_m^2} \sin^2 \gamma_n \sin^2 \gamma_m ,
$$

$$
Q_E^* = I_P^* , \tag{3.2.9}
$$

where we define Δ and ξ as

$$
\Delta(c,d) = \sum_{c=1}^{\infty} \left\{ \frac{\sqrt{K^2 + \frac{(2c-1)^2 \pi^2}{4W^2}} \tanh \sqrt{K^2 + \frac{(2c-1)^2 \pi^2}{4W^2}} \cos \gamma_n + \gamma_n \sin \gamma_n}{K^2 + \frac{(2c-1)^2 \pi^2}{4W^2} + \gamma_n^2} \right.
$$

$$
\times \frac{-4W \cos \gamma_m}{4\gamma_m^2 - (2c-1)^2 \pi^2} \times \left[\Psi_2 - \Psi_1 + \frac{4W^2 K^2 \Psi_1}{4W^2 K^2 + (2c-1)^2 \pi^2} \right]
$$

$$
\left. + \frac{16 W^3 K^2 \Psi_1 \cos \gamma_m \sin \gamma_n}{[4W^2 K^2 + (2c-1)^2 \pi^2][4\gamma_m^2 - (2c-1)^2 \pi^2] \gamma_n} \right\} +
$$

$$
\sum_{d=1}^{\infty} \left\{ \frac{\left[\sqrt{K^2 + \frac{(2d-1)^2 \pi^2}{4}} \tanh(\sqrt{K^2 + \frac{(2d-1)^2 \pi^2}{4}} W) \cos \gamma_m + \frac{\gamma_m}{W} \sin \gamma_m \right] (-4 \cos \gamma_n)}{\left[K^2 + \frac{(2d-1)^2 \pi^2}{4} + \frac{\gamma_m^2}{W^2} \right] [4\gamma_n^2 - (2d-1)^2 \pi^2]} \right.
$$

$$
\times \left[\Psi_1 - \Psi_2 + \frac{4K^2 \Psi_2}{4K^2 + (2d-1)^2 \pi^2} \right] + \left. \frac{16 W K^2 \Psi_2 \cos \gamma_n \sin \gamma_m}{[4K^2 + (2d-1)^2 \pi^2][4\gamma_n^2 - (2d-1)^2 \pi^2] \gamma_m} \right\}
$$

$$
+ \frac{W(\Psi_1 + \Psi_2)}{2\gamma_n \gamma_m} \sin \gamma_n \sin \gamma_m . \tag{3.2.10}
$$

$$
\xi = \frac{W^2}{\gamma_m^2 + W^2 \gamma_n^2 + j\Omega} \frac{\gamma_m^2 B_1^2 + W^2}{\gamma_m^2 B_1^2 + W^2 - W B_1} \frac{\gamma_n^2 B_2^2 + 1}{\gamma_n^2 B_2^2 + 1 - B_2} . \tag{3.2.11}
$$

69

Note that the theory with liquid slip and without EDL effects follows from Eqs.(3.2.9) by setting $\Psi_1 = \Psi_2 = 0$. The steady state response follows from Eqs.(3.2.9) by setting $\Omega = 0$. When $B_1 = 0$ and $B_2 = 0$, we employ Eq.(3.2.7) as the Green's function for the solution with no slip. Eqs. 3.2.9 reduce to Eqs. 2.2.40 in Chapter 2. We note that, for electrokinetic slip flows, Onsager reciprocal relations still holds. This can be proved by $Q_E^*(\Omega) = I_P^*(\Omega)$ in Eqs. 3.2.9.

(a)   (b)

(c)   (d)
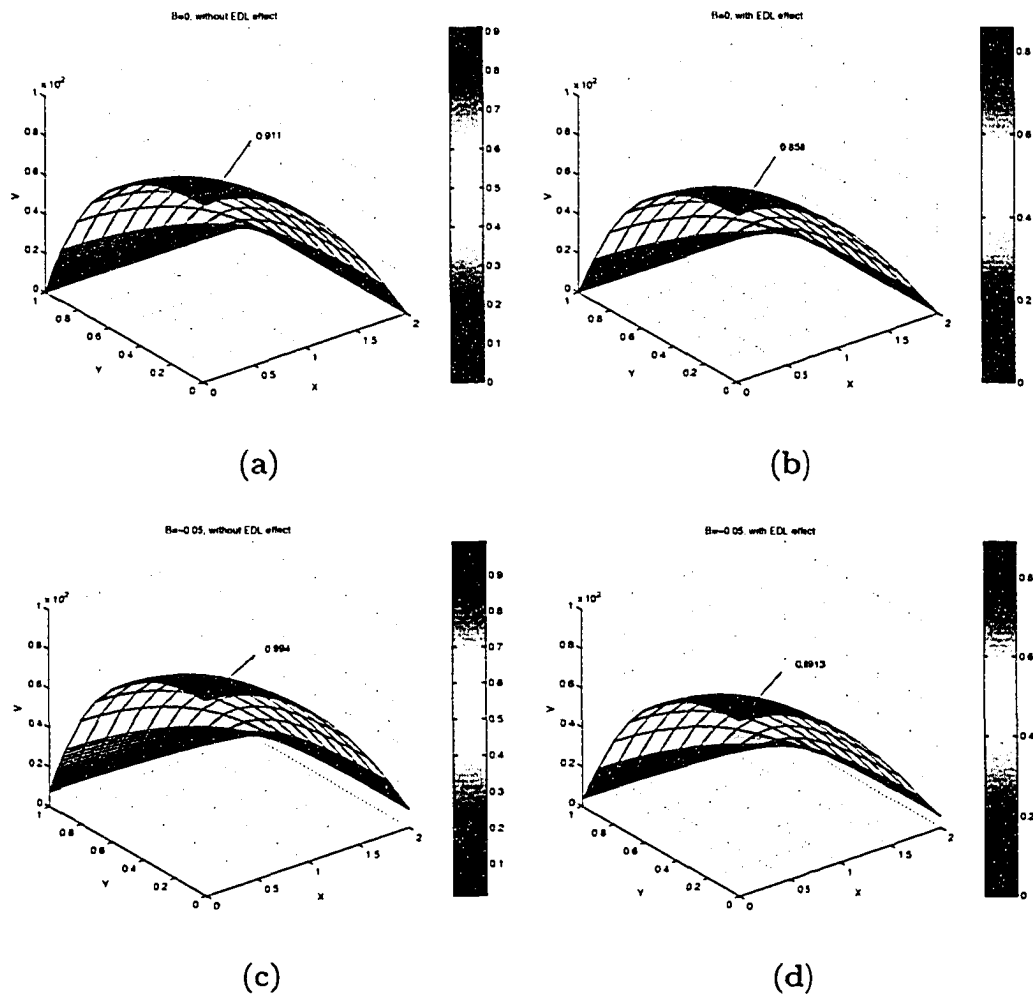
Figure 3.1: profiles of the normalized velocity (a) no slip and without electrokinetic: $B = 0$ and $E_z = 0$ (b) no slip and with electrokinetic: $B = 0$ and $E_z \neq 0$ (c) slip and without electrokinetic: $B = -0.05$ and $E_z = 0$ and (d) slip and with electrokinetic: $B = -0.05$ and $E_z \neq 0$

70

3.2.2 Results and discussion

In Eq.(3.2.9), we see that variations in Ψ_s, B_1, B_2, Ω and K all affect fluid flow in a rectangular cross-section microchannel. For example, the concentration of liquid or channel size can be varied to obtain different K values. B depends on the surface energetics between the solid-liquid interface. The value of Ψ_s can depend on the concentration, solution pH and channel wall material. The larger the Ψ_s value is, the more noticeable the electrokinetic effects become. Thus, one would observe a larger streaming potential and smaller flow rate in a pressure-driven flow, and larger electroosmotic flow and current in an electric-field-driven flow. Intuitively, a larger slip coefficient, of course, would cause a larger flow rate in both pressure and electric-field-driven flow. For pressure-driven flow, since water molecules bring charges to the other end of the channel to induce an electric field (streaming potential), the flow with larger slip coefficient would build up a larger streaming potential to make the total current equal to zero. However, because the increase in $Q_P^* P^*$ induced by liquid slip is larger than the increase in $Q_E^* E_z^*$, the total flow rate still increases due to slip at the channel wall.

Let us examine here the effect of the normalized thickness K^{-1} in the EDL and the normalized slip coefficients B_1 and B_2 on steady state flow for a given set of parameters that represents a typical system. We have selected the following values for our calculations: the amplitude of the normalized pressure gradient, $P^*(\Omega) = 200$ (for pressure-driven flow), the amplitude of the electric field, $E_z^*(\Omega) = 39$ (for electric-field-driven flow), the normalized slip coefficient, the normalized width of rectangular microchannel, $W = 2$ (which means the ratio of the width to the height is 2), $B_1 = B_2 = B = -0.05$, the normalized conductivity, $\Sigma = 3.85$, and the normalized surface potential, $\Psi_1 = \Psi_2 = \Psi_s = -3.9$. These parameters represent, in the dimensional case, a surface potential of -100 mV (Debye-Hückel approximation gives a good agreement with experiments, when zeta potential is up to 100 mV [33]), a diffusion

71

coefficient $D \approx 2 \times 10^{-9}$ m^2/s for an infinitely dilute KCl electrolyte [118], a pressure gradient at the order of 10^6 Pa/m, an electric field at the order of 10^5 V/m and a slip length of 1 μm for a microchannel with a half height of 10 μm.

3.2.3 Pressure-driven flow

Many microfluidic MEMS devices work under a pressure gradient induced by mechanical parts, such as a membrane and a piezoelectric film. When pressure gradient drives a flow, a streaming potential builds up by the accumulated ions between the two ends of the microchannel. Moving ions induced by the streaming potential, which form the conductive current [the second term in Eq.(2.2.12)], will bring water molecules to move opposite to the flow direction because of the interaction between ions and water. This phenomenon is typically described by a larger apparent flow viscosity. However, liquid slippage induced by hydrophobic surfaces can reduce flow resistance and increase velocity for pressure driven flow.

To investigate the effect of liquid slip on flow resistance, we specify $K = 10$ and plot the profiles of the normalized velocity in Figure 3.1 for the following four cases:

(a) no slip and without electrokinetic: $B = 0$ and $E_z = 0$

(b) no slip and with electrokinetic: $B = 0$ and $E_z \neq 0$

(c) slip and without electrokinetic: $B = -0.05$ and $E_z = 0$

(d) slip and with electrokinetic: $B = -0.05$ and $E_z \neq 0$

We find that EDL has a counter effect on flow velocity. In addition to Figure 3.1, we also select the velocity profile along y-axis in Figure 3.2. Liquid slip in electrokinetic flow with a 5% slip coefficient can decrease flow resistance by about 12%. We plot the normalized flow rate with respect to the normalized reciprocal thickness K in Figure 3.3. For the cases of

1. no slip and without electrokinetic: $B = 0$ and $E_z = 0$ (solid line) and

2. no slip and with electrokinetic: $B = 0$ and $E_z \neq 0$ (dotted line)

72

Pressure driven flow

Figure 3.2: Profiles of the normalized velocity along y-axis
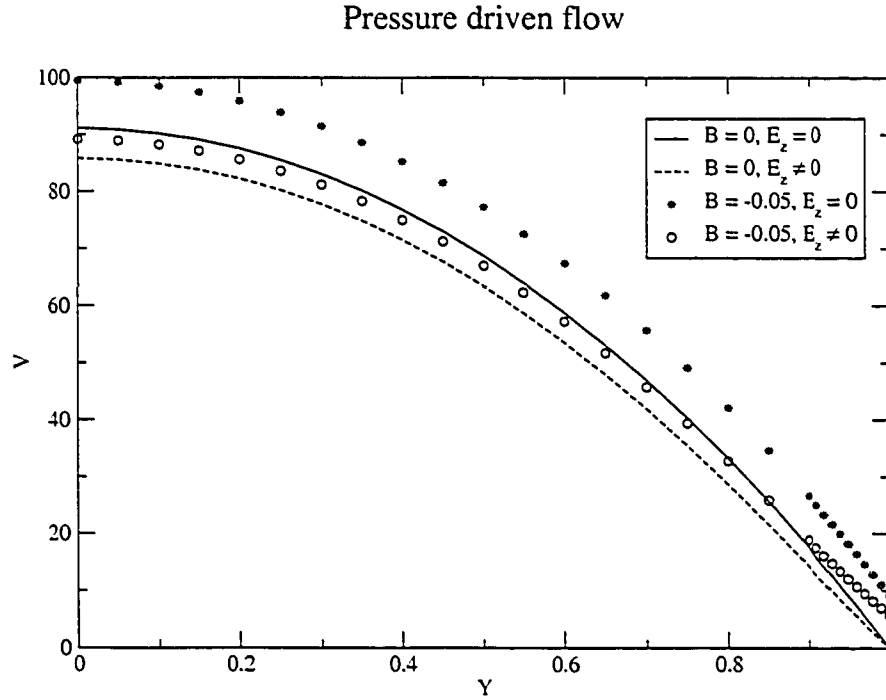
3. slip and without electrokinetic: $B = -0.05$ and $E_z = 0$ (stars) and

4. slip and with electrokinetic: $B = -0.05$ and $E_z \neq 0$ (circles).

case 1 and 2 suggest that EDL affects flow rate over a large range of K. Similar conclusion can be made by comparing case 3 and case 4. In general, EDL causes a large reduction in flow rate; whereas, liquid slip counteracts the effect by EDL and induces a larger flow rate. In Figure 3.3, when $B = 0$, EDL effect disappears as $K \to 0$ or $K \to \infty$, since $K \to 0$ implies a uniform EDL in the microchannel and $K \to \infty$ implies a very thin double layer thickness [110]. When there is liquid slip (circles), electrokinetic phenomenon disappears as $K \to 0$. However, as $K \to \infty$, EDL effect still exists. This result suggests that liquid slip can enhance EDL effect on fluid flow in rectangular microchannels. Since slip induces higher velocity and hence increases the convection current [first term in Eq.(2.2.12)], a larger streaming

73

Pressure driven flow
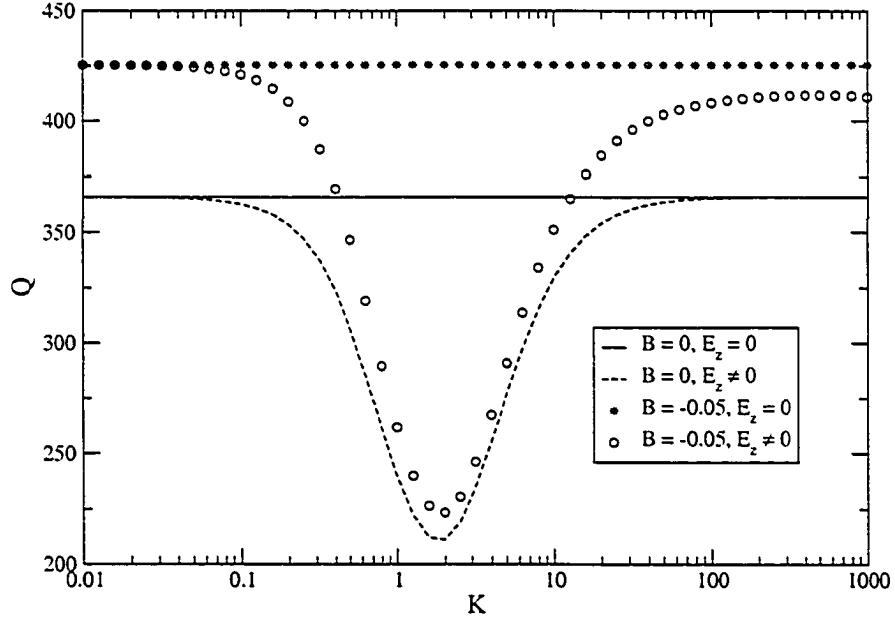
Figure 3.3: Effects of electrokinetic and liquid slip on the normalized flow rate in steady state ($\Omega = 0$).

potential is needed to reach a balance, $I = 0$. This fact is confirmed in Figure 3.4 where we see the streaming potential with slip (circles) is larger than that with no-slip (dotted line).

For pressure-driven flow, it is of interest to examine the pressure gradient with slip and that without slip at a given flow rate. Thus, based on Eq.(3.2.9), we equate the flow rate with slip to that without slip. Thus, setting

$$[Q_P^*(B \neq 0) - Q_E^*(B \neq 0)\frac{I_p^*(B \neq 0)}{I_E^*(B \neq 0)}]P^* = [Q_P^*(B = 0) - Q_E^*(B = 0)\frac{I_p^*(B = 0)}{I_E^*(B = 0)}]\bar{P}^*$$

yields

$$\frac{P^*}{\bar{P}^*} = \frac{Q_P^*(B = 0) - Q_E^*(B = 0)\frac{I_p^*(B=0)}{I_E^*(B=0)}}{Q_P^*(B \neq 0) - Q_E^*(B \neq 0)\frac{I_p^*(B\neq0)}{I_E^*(B\neq0)}} . \tag{3.2.12}$$

The results are plotted in Figure 3.5 as $P^*/\bar{P}^*$ vs. B for different K values. In Figure 3.5, when $K \gg 1$, the ratio $P^*/\bar{P}^*$ approaches 0.83 for a 10% slip. That is, there is

74

Pressure driven flow
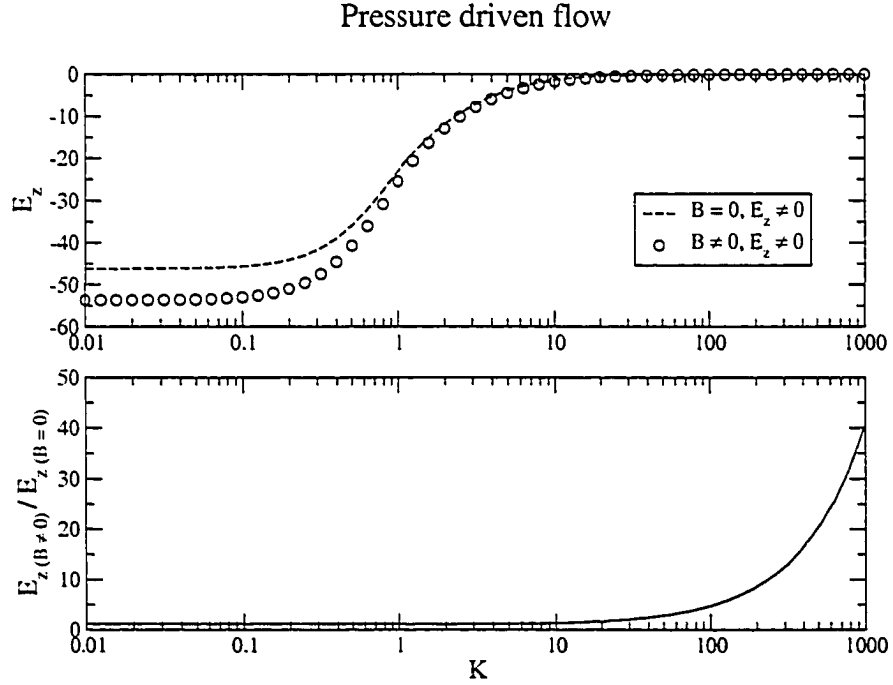
Figure 3.4: Effects of liquid slip on the normalized streaming potential in steady state $(\Omega = 0)$.

a 17% improvement in the pressure gradient with a 10% slip. When $K \ll 1$ for the same slip, the ratio $P^*/\bar{P}^*$ approaches 0.75. This represents a 25% improvement in the pressure gradient when there is a 10% slip. For MEMS devices using pure (deionized) water as the working fluid, K is much less than 1 and hence an improvement of more than 25% can be achieved for only a 10% slip. We wish to point out that inducing a slip length of 10% is not entirely impossible. Several authors have observed directly or indirectly a 14% drag reduction [98] or a 1–2 μm slip length in a microchannel with hydrophobic surfaces [99]; the former implies a 4% slip length ($B = -0.04$) and the latter a 7% slip length ($B = -0.07$).

The time-dependent electrokinetic slip flow response is illustrated by the following applied pressure gradient

$$-\frac{\partial P}{\partial Z} = \begin{cases} 2 \times 10^2, & (m-1) \times \tau_2 \le \tau < (m-1) \times \tau_2 + \tau_1 \\ 0, & (m-1) \times \tau_2 + \tau_1 \le \tau < m \times \tau_2 \end{cases}$$

75

Pressure driven flow
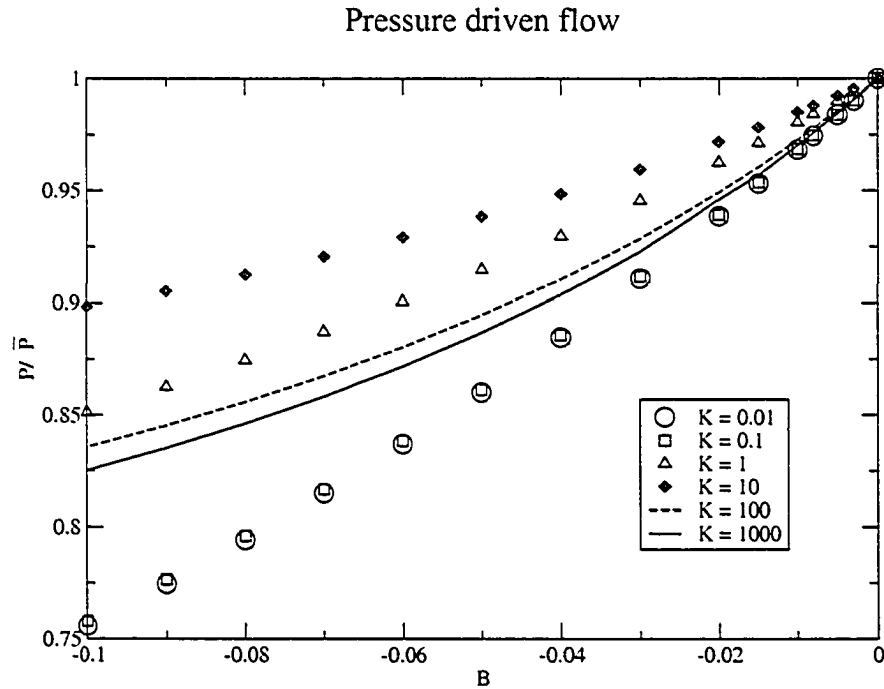
Figure 3.5: The reduction of pressure gradient in pressure-driven flow

where $\tau_1 = 1$, $\tau_2 = 3$ and $m = 1, 2, 3, \cdots$. The results are shown in Figure 3.6, where the above rectangular periodic pressure gradient is applied for $K = 1$ and $K = 10$, respectively, with a slip coefficient of $B = -0.05$. Since the electroviscous effect for $K = 1$ is larger than that of $K = 10$, the flow rate for the former is smaller than that of the latter, in agreement with the result in Figure 3.3. It can be seen in Figure 3.6 that the flow requires some response time to react to the change in the pressure gradient. For $K = 10$, it takes longer time to reach a steady state.

3.2.4 Electroosmotic pumping flow

Other than pressure gradient, electric field can be used to move the ions in the electrical double layer and such ions will carry water molecules because of viscosity, resulting in fluid flow. We normally call such electric-field-driven phenomena as "electroosmotic pump". A plot of the normalized flow rate Q with respect to K is

76

Pressure driven flow
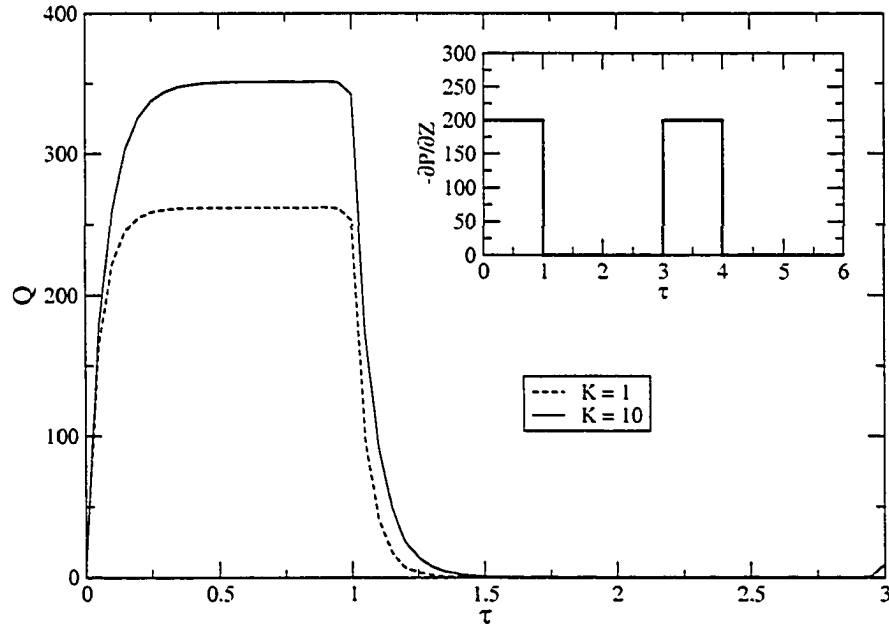
Figure 3.6: The normalized flow rate under a rectangular periodic pressure gradient for $K = 1$ and $K = 10$, respectively, with $B = -0.05$.

given in Figure 3.7. When there is a uniform and thick EDL occupying the whole channel, $K \rightarrow 0$ (for a fixed channel size). As $K \rightarrow 0$, $Q^* \rightarrow 0$. When there is a very thin EDL, $K \rightarrow \infty$. When $K \rightarrow \infty$, $Q^*(B = 0) \rightarrow constant$, since the profile of velocity becomes uniform in microchannel. As K increases, the flow rate with slip quickly increases because the amount of movable ions increases. Since the resistance decreases significantly with liquid slip in the vicinity near the wall, the moving ions carry the solvent molecules easily. Since EDL is in the same region of the boundary layer, liquid slip can magnify electroosmotic flow several times. Results in Figure 3.7 suggest that liquid slip can increase the flow rate (at the same electric field) for electro-osmotic pumping by about 20% as $K \rightarrow 0$ and more than 50 times when K $= 1000$.

We plot in Figure 3.8 the normalized flow rate under a rectangular electric field

77

Electric field driven flow
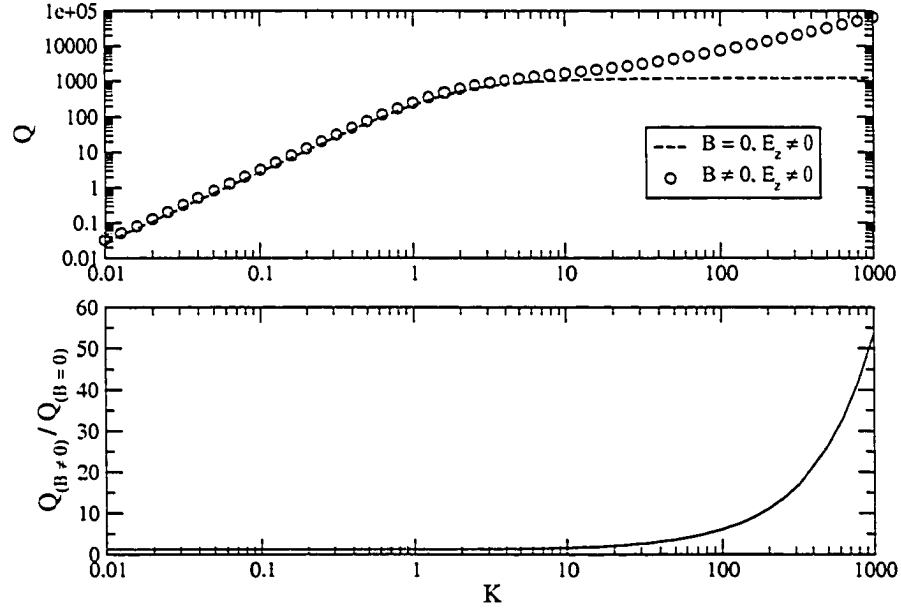
Figure 3.7: Effects of liquid slip and electrokinetic on the normalized flow rate with respect to K in steady state ($\Omega = 0$).

input expressed by

$$E_z = \begin{cases} 39, & 0 \leq \tau < 1.0 \\ 0, & \tau > 1.0 \end{cases}$$

Since the normalized time $\tau = 1.0$ corresponds to a dimensional time of 10^{-4} s for water in a 10 μm channel, the flow is not fully developed. Thus, the electroosmotic flow between $0 \leq \tau \leq 1.0$ is still at the developing process even though a constant electric pulse is applied.

Another time-dependent response is illustrated by the following external electric field

$$E_z = \begin{cases} 39, & (m - 1) \times \tau_2 \leq \tau < (m - 1) \times \tau_2 + \tau_1 \\ 0, & (m - 1) \times \tau_2 + \tau_1 \leq \tau < m \times \tau_2 \end{cases}$$

where $\tau_1 = 1$, $\tau_2 = 3$ and $m = 1, 2, 3 \cdots$. The results are shown in Figure 3.9, where the above time-dependent rectangular periodic electric field is applied for $K = 1$ and $K = 10$, respectively, with a slip coefficient of $B = -0.05$. A larger K value implies a

78

Electric field driven flow
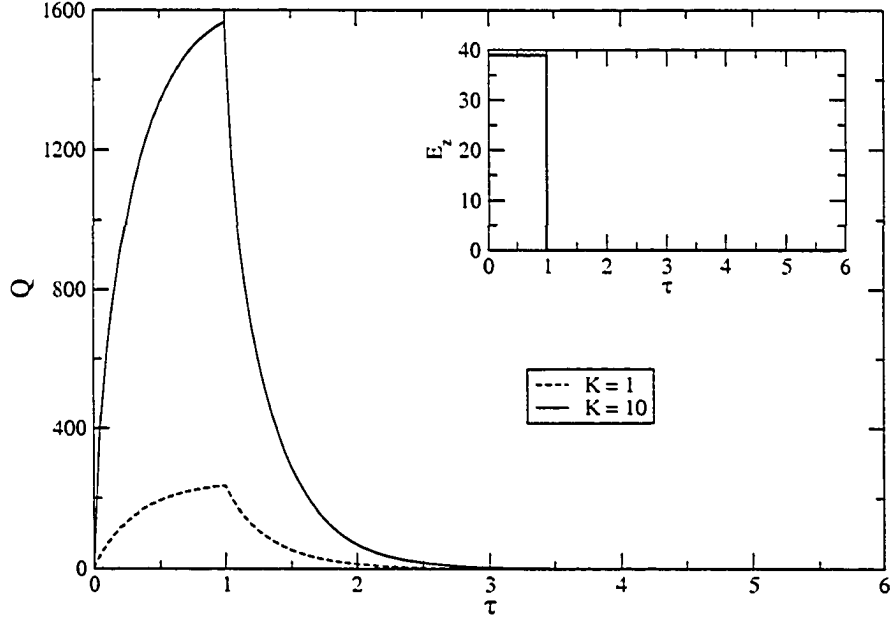
Figure 3.8: The normalized flow rate under a rectangular electric field for $K=1$ and $K=10$

higher solution concentration, causing a larger electroosmotic flow rate [Figure 3.7]. It can be seen in Figure 3.9 that electroosmotic flow also requires some response time to react to the change in the external electric field. For $K = 10$, it also takes longer time to reach steady state since the EDL thickness is thinner.

Here we equate the electro-osmotic flow rate with slip to that without slip. Thus, equating Eqs.(3.2.9) and (2.2.40) and setting $Q_E^*(B \neq 0)E_z^* = Q_E^*(B = 0)\bar{E}_z^*$ yield

$$\frac{E_z^*}{\bar{E}_z^*} = \frac{\frac{-64}{\pi^2}\sum_{m=1}^{\infty}\sum_{n=1}^{\infty}\frac{\lambda}{(j\Omega-\lambda_1)}\frac{(-1)^{m+n}}{(2m-1)(2n-1)}}{-16\sum_{m=1}^{\infty}\sum_{n=1}^{\infty}\xi\Delta(r,s)\frac{\sin\gamma_n\sin\gamma_m}{\gamma_n\gamma_m}} . \tag{3.2.13}$$

We plot these results in Figure 3.10 as $E_z^*/\bar{E}_z^*$ vs. B for different K values. It is apparent that for $K \leq 1$, the electric field decreases by about 30% when there is a 10% slip length. A 10% slip length ($B = -0.1$) represents, for example, a 1 μm slip length in a 20 μm channel ($h = 10$ μm). When $K = 1000$, one could achieve a 90% reduction in electric field when there is only a slip length of 1% ($B = -0.01$) and

79

Electric field driven flow
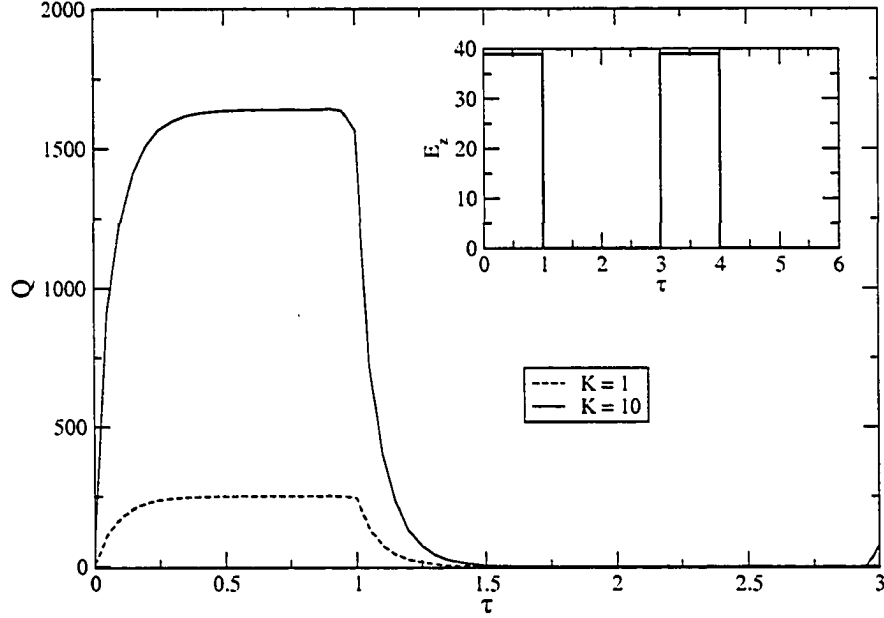
Figure 3.9: The normalized flow rate under a rectangular periodic electric field for $K = 1$ and $K = 10$, respectively, with $B = -0.05$.

a 99% reduction when the slip length is 10% ($B = -0.1$). As pointed out above, inducing a slip length of 10% is not entirely impossible and can be easily achieved by surface modifications. This possibility relies on the capability to control surface charges and surface hydrophobicity independently.

3.3 Electrokinetic slip flow in circular microchannels

3.3.1 Analytical solutions

For circular microchannels, considering slip boundary condition, Navier-Stokes equation and its boundary condition are

$$-\frac{1}{\mu}\frac{\partial p}{\partial z} + \frac{1}{r}\frac{\partial}{\partial r}\left(r\frac{\partial v}{\partial r}\right) + \frac{1}{\mu}\rho E'_z = \frac{1}{\nu}\frac{\partial v}{\partial t} \,,$$

$$v(a,t) = \beta\frac{\partial v}{\partial r} \quad \text{and} \quad \frac{\partial v(0,t)}{\partial r} = 0 \,, \tag{3.3.1}$$

80

Electric field driven flow
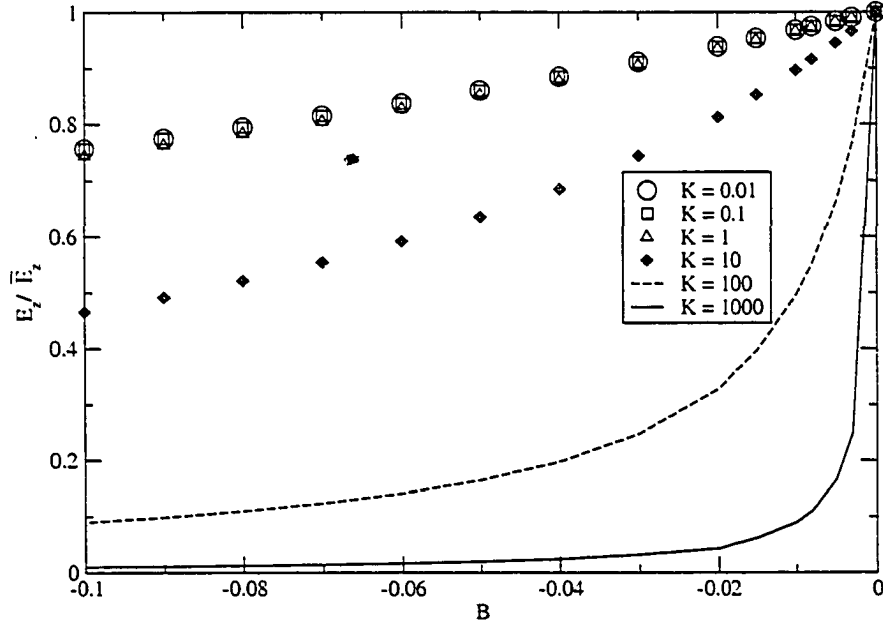
Figure 3.10: The reduction of external electric field in electroosmotic pump

where β is the slip coefficient and $-\beta$ is the slip length. Defining the normalized slip coefficient $B = \beta/a$, the normalized Navier-Stokes equation and its boundary condition become

$$-\frac{\partial P}{\partial Z} + \frac{1}{R}\frac{\partial}{\partial R}\left(R\frac{\partial V}{\partial R}\right) - K^2\Psi E_z = \frac{\partial V}{\partial \tau} , \qquad (3.3.2)$$

$$V(1,\tau) = B\frac{\partial V}{\partial R} , \qquad \frac{\partial V(0,\tau)}{\partial R} = 0 , \qquad (3.3.3)$$

Analytical solutions are sought here for a sinusoidal periodicity in the electrohydrodynamic fields and this is best addressed by using complex variables.

$$V_P^*(R,\Omega) = \frac{1}{j\Omega}\left[1 - \frac{J_0(R\sqrt{-j\Omega})}{J_0(\sqrt{-j\Omega}) + B\sqrt{-j\Omega}J_1(\sqrt{-j\Omega})}\right]$$

$$V_E^*(R,\Omega) = \frac{K^2\Psi_s}{K^2 - j\Omega}\left\{\frac{J_0(jKR)}{J_0(jK)} - \left[1 + jBK\frac{J_1(jK)}{J_0(jK)}\right]\right.$$
$$\left.\times \frac{J_0(R\sqrt{-j\Omega})}{J_0(\sqrt{-j\Omega}) + B\sqrt{-j\Omega}J_1(\sqrt{-j\Omega})}\right\}$$

81

$$I_P^*(\Omega) = 2\pi K^2 \Psi_s \left\{ \frac{1}{\Omega K} \frac{J_1(jK)}{J_0(jK)} + \frac{1}{j\Omega J_0(jK)} \times \frac{1}{J_0(\sqrt{-j\Omega}) + B\sqrt{-j\Omega}J_1(\sqrt{-j\Omega})} \right.$$

$$\left. \times \frac{jKJ_1(jK)J_0(\sqrt{-j\Omega}) - \sqrt{-j\Omega}J_0(jK)J_1(\sqrt{-j\Omega})}{j\Omega - K^2} \right\}$$

$$I_E^*(\Omega) = -\frac{2\pi K^4 \Psi_s^2}{K^2 - j\Omega} \left\{ \frac{1}{2}\left[1 + \frac{J_1^2(jK)}{J_0^2(jK)} \right] - \frac{1}{J_0(\sqrt{-j\Omega}) + B\sqrt{-j\Omega}J_1(\sqrt{-j\Omega})} \right.$$

$$\left. \times \frac{1}{J_0(jK)} \left[1 + jBK\frac{J_1(jK)}{J_0(jK)} \right] \frac{jKJ_1(jK)J_0(\sqrt{-j\Omega}) - \sqrt{-j\Omega}J_0(jK)J_1(\sqrt{-j\Omega})}{j\Omega - K^2} \right\}$$

$$+\pi\Sigma K^2$$

$$Q_P^*(\Omega) = \frac{2\pi}{j\Omega} \left\{ \frac{1}{2} - \frac{1}{\sqrt{-j\Omega}} \frac{J_1(\sqrt{-j\Omega})}{J_0(\sqrt{-j\Omega}) + B\sqrt{-j\Omega}J_1(\sqrt{-j\Omega})} \right\}$$

$$Q_E^*(\Omega) = \frac{2\pi K^2 \Psi_s}{K^2 - j\Omega} \left\{ \frac{1}{jK}\frac{J_1(jK)}{J_0(jK)} - \left[1 + jBK\frac{J_1(jK)}{J_0(jK)} \right] \right.$$

$$\left. \times \frac{J_1(\sqrt{-j\Omega})}{\sqrt{-j\Omega}} \frac{1}{J_0(\sqrt{-j\Omega}) + B\sqrt{-j\Omega}J_1(\sqrt{-j\Omega})} \right\} \tag{3.3.4}$$

where J_0 and J_1 are the zeroth- and first-order Bessel functions of the first kind.

When $\Omega \to 0$, Eq.(3.3.4) reduces to those of steady state.

$$V_P^*(R,0) = \frac{1}{4}(1 - R^2) - \frac{B}{2}$$

$$V_E^*(R,0) = -\Psi_s \left[1 - \frac{J_0(jKR)}{J_0(jK)} + jBK\frac{J_1(jK)}{J_0(jK)} \right]$$

$$I_P^*(0) = -\pi\Psi_s \left[1 - \frac{2}{jK}\frac{J_1(jK)}{J_0(jK)} + jBK\frac{J_1(jK)}{J_0(jK)} \right]$$

$$I_E^*(0) = -\pi\Psi_s^2 K^2 \left\{ 1 - \frac{2}{jK}\frac{J_1(jK)}{J_0(jK)}\left[1 + jBK\frac{J_1(jK)}{J_0(jK)} \right] \right.$$

$$\left. + \frac{J_1^2(jK)}{J_0^2(jK)} \right\} + \pi\Sigma K^2$$

$$Q_P^*(0) = \frac{\pi}{8} - \frac{\pi}{2}B$$

$$Q_E^*(0) = -\pi\Psi_s \left[1 + jBK\frac{J_1(jK)}{J_0(jK)} - \frac{2}{jK}\frac{J_1(jK)}{J_0(jK)} \right] \tag{3.3.5}$$

If the slip coefficient $B = 0$, all quantities reduce to those of the electrokinetic flow with no slip condition. If $\Psi_s = 0$ and $B = 0$, all quantities reduce to those of macroflow with no EDL effect and no slip condition.

82

3.3.2 Results and discussion

Here, let us examine the effect of the normalized thickness K^{-1} in the EDL, and the normalized slip coefficient B on flow velocity. We have selected the following values for our calculations: the amplitude of normalized pressure gradient, $P^*(\Omega) = 200$, the amplitude of electric field, $E_z^*(\Omega) = 39$, the normalized slip coefficient, $B = -0.05$, the normalized conductivity, $\Sigma = 3.85$, and the normalized surface potential, $\Psi_s = 3.9$.
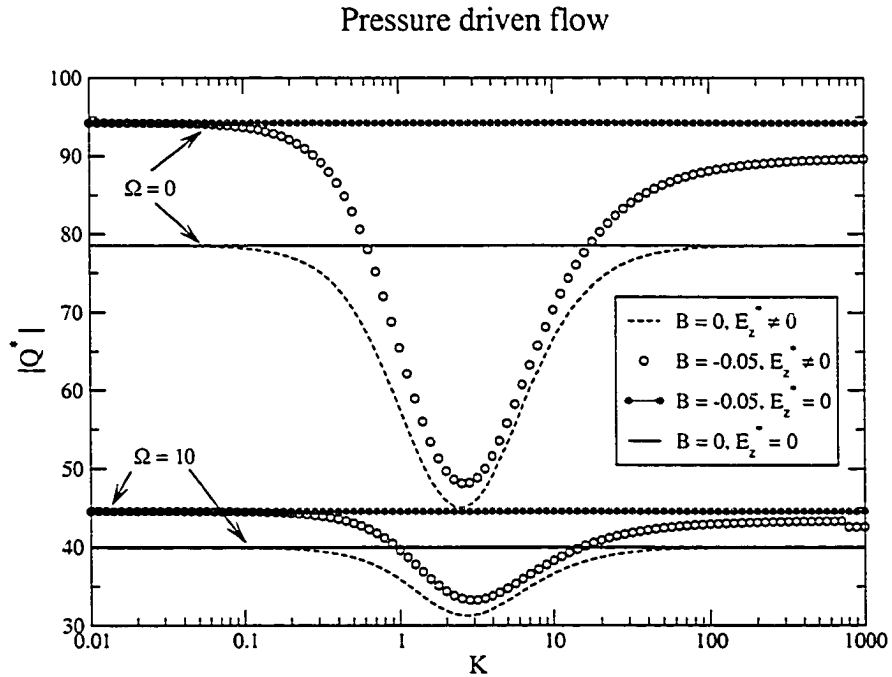
Figure 3.11: Effects of liquid slip with electrokinetics on the amplitude of the normalized flow rate with respect to K for pressure-driven flow.

Pressure driven flow

When pressure gradient drives a flow, electroviscous effect due to presence of an electrical double layer reduces flow rate. On the other hand, slippage of flow due to surface hydrophobicity has a counter effect. We plot the amplitude of the normalized velocity with respect to the normalized reciprocal of the double layer thickness in Figure 3.11 for $\Omega = 0$ and $\Omega = 10$ for the following four cases.

1. no slip and without electrokinetic: $B = 0$ and $E_z^* = 0$ (solid line) and

2. no slip and with electrokinetic: $B = 0$ and $E_z^* = 39$ (dashed line)

3. slip and without electrokinetic: $B = -0.05$ and $E_z^* = 0$ (stars) and

4. slip and with electrokinetic: $B = -0.05$ and $E_z^* = 39$ (circles).

Cases 1 and 2 suggest that EDL affects flow rate over a large range of K. Similar conclusion can be made by comparing cases 3 and 4. In general, EDL causes a large reduction in flow rate; whereas, liquid slip counteracts the effect by EDL and induces a larger flow rate. In Figure 3.11, when $B = 0$, EDL effect disappears as $K \rightarrow 0$ or $K \rightarrow \infty$, since $K \rightarrow 0$ implies a uniform EDL in the microchannel and $K \rightarrow \infty$ implies a very thin double layer thickness [119]. When there is liquid slip (circles), electrokinetic phenomenon disappears as $K \rightarrow 0$. However, as $K \rightarrow \infty$, EDL effect still exists. This result suggests that liquid slip can enhance EDL effect on fluid flow in circular microchannels. When the normalized frequency Ω increases to 10, the corresponding flow rates for the four cases decrease since the flow lags behind the changing pressure gradient.

We wish to emphasize that the presence of EDL retards flow rate, while slip condition induces higher flow velocity. Both phenomena cause the observed flow rate to be different from the traditional one (without EDL effect and slip condition), and can result in an apparent viscosity $\bar{\mu}$. The ratio of the apparent viscosity to liquid viscosity $|\bar{\mu}/\mu|$ with respect to K is shown in Figure 3.12. In this figure, if we consider only the slip condition and no electrokinetic effect ($B \neq 0$ and $E_z^* = 0$, stars), the viscosity ratio $|\bar{\mu}/\mu|$ would be smaller than 1, suggesting that the observed apparent viscosity would be smaller than the true liquid viscosity when slip condition is considered. Thus, slip condition enhances fluid movement. With the presence of electrokinetic, the effect of slip condition on viscosity can be obtained by comparing the the following two cases:

84

1. slip and with electrokinetic: $B \neq 0$ and $E_z^* \neq 0$ (circles) and

2. no slip and with electrokinetic: $B = 0$ and $E_z^* \neq 0$ (dotted line),

That is, a higher apparent viscosity would be predicted if slip condition is neglected.

Pressure driven flow
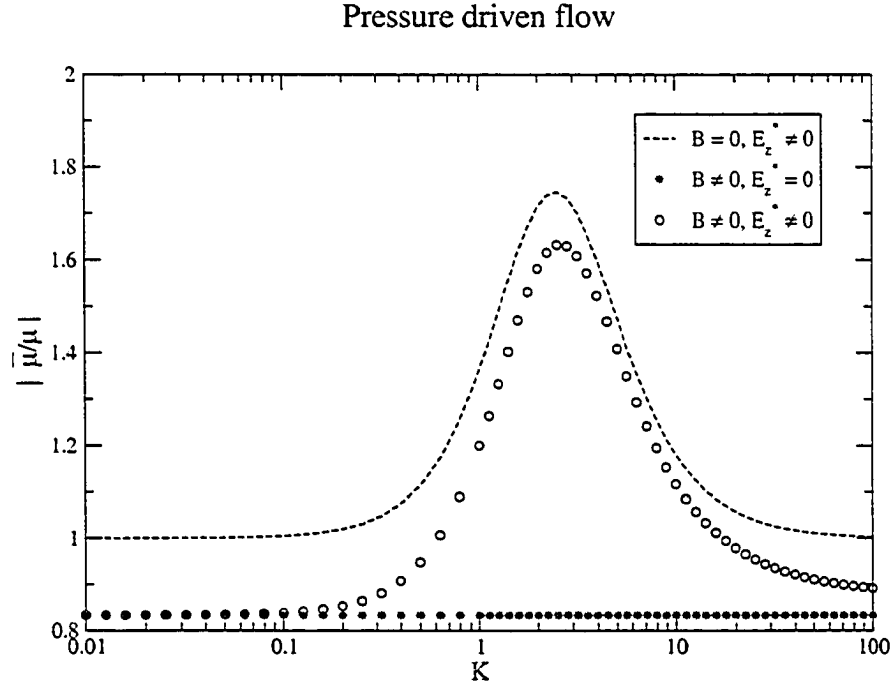
Figure 3.12: Effect of slip condition and electrokinetic on the ratio of the apparent viscosity to true liquid viscosity $|\bar{\mu}/\mu|$ with respect to K in steady state ($\Omega = 0$).

Electric field driven flow

A plot of the normalized flow rates with respect to K at different frequencies are given in Figure 3.13. As expected, the flow rate decreases as the oscillation frequency is reduced. When there is a uniform and thick EDL occupying the whole channel, $K \rightarrow 0$ (for a fixed channel size). As $K \rightarrow 0$, $Q^* \rightarrow 0$. When there is a very thin EDL, $K \rightarrow \infty$. When $K \rightarrow \infty$, $Q^*(B = 0) \rightarrow constant$, since the profile of velocity becomes uniform in the microchannel. When K increases, the flow rate with slip quickly increases because the amount of movable ions increases. The resistance is

85

expected to decrease when there is liquid slip, since the moving ions in the interfacial region near the wall easily carry the molecules. As EDL is in the same boundary layer region, liquid slip would magnify the electroosmotic flow up to several times. In the lower part of Figure 3.13, we also compare the non-dimensional flow rates with and without slip at different frequencies. It is apparent that for $K < 1$, the flow rate with slip is nearly 1.2 times larger than that without slip. As $K \geqslant 1$, this ratio increases monotonically to 50 at $K = 1000$. For a typical electrolyte solution, EDL is small and K is usually larger than 1000. Phenomenologically, the presence of a slip layer will have a relatively more important role on flow velocity if the EDL is smaller. Thus, introduction of slip at the solid-liquid interface by the channel materials would enhance fluid flow rate and reduce the flow resistance by at least 50 times, in this specific example.

We also plot the normalized current with respect to K in Figure 3.14. We see that the normalized current decreases as K decreases from 0.1 to 0.01 and that the currents appear to be identical for the cases of slip and non-slip. In the lower part of Figure 3.14, we show that there is indeed a small difference between the two currents. The normalized current ratio increases from 1 to 1.4 as K varies from 2 to 1000. It is apparent that fluid slip has a much smaller effect on the current because the conduction current is much larger than the convection one.

From the results presented here, we have shown that both EDL effect and slip condition cannot be ignored. In some experiments [98], attempts have been make to measure slip length from the velocity profile or flow rate without consideration of EDL effect. Thus, a smaller slip length would have obtained. On the other hand, in EDL experiments, slip condition should also be considered, especially for hydrophobic solid surfaces.
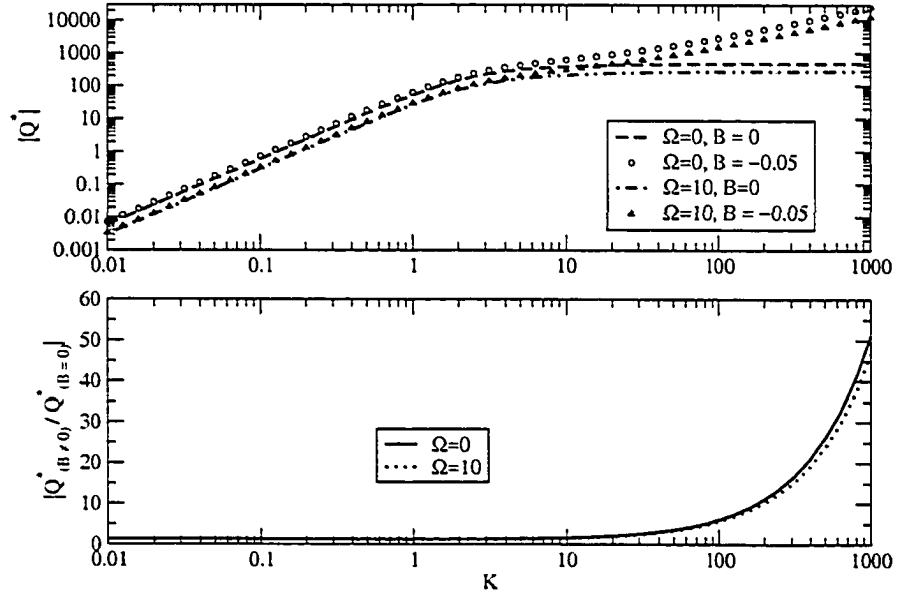
Figure 3.13: Effects of slip condition with electrokinetic on the amplitude of the normalized flow rate with respect to K for electric field driven flow.

3.4 Electrokinetic slip flow in parallel-plate microchannels

If $W \to \infty$, the rectangular microchannel can be considered a parallel-plate microchannel. When $W \to \infty$, the normalized velocity, current and flow rate of Eqs.3.2.9 reduce to the normalized velocity, current and flow rate of a parallel-plate microchannel:

$$V_P^*(Y, \Omega) = \frac{1}{j\Omega}\left[1 - \frac{\cosh(Y\sqrt{j\Omega})}{\cosh(\sqrt{j\Omega}) - B\sqrt{j\Omega}\sinh(\sqrt{j\Omega})}\right],$$

$$V_E^*(Y, \Omega) = \frac{\Psi_s K^2}{K^2 - j\Omega}\left[\left(BK\frac{\sinh(K)}{\cosh(K)} - 1\right)\frac{\cosh(Y\sqrt{j\Omega})}{\cosh(\sqrt{j\Omega}) - B\sqrt{j\Omega}\sinh(\sqrt{j\Omega})} + \frac{\cosh(KY)}{\cosh(K)}\right],$$
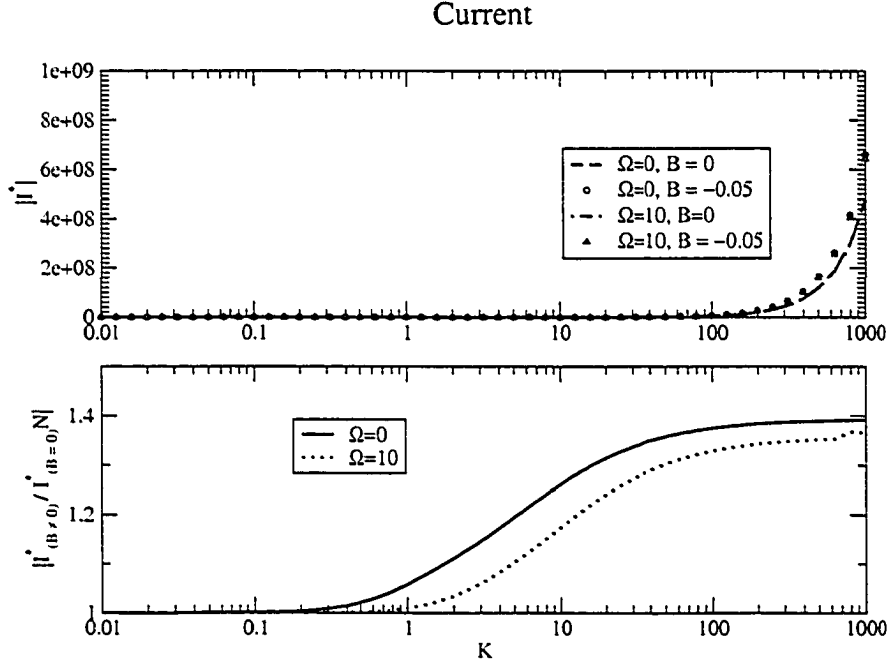
Current

Figure 3.14: Effects of liquid slip with electrokinetics on the amplitude of the normalized current with respect to K.

$$I_P^*(\Omega) = \frac{-2\Psi_s K^2}{j\Omega \cosh(K)} \left\{ \frac{\sinh(K)}{K} - \frac{1}{\cosh(\sqrt{j\Omega}) - B\sqrt{j\Omega}\sinh(\sqrt{j\Omega})} \right.$$

$$\left. \times \left[\frac{\sinh(K + \sqrt{j\Omega})}{2\left(K + \sqrt{j\Omega}\right)} + \frac{\sinh(K - \sqrt{j\Omega})}{2\left(K - \sqrt{j\Omega}\right)} \right] \right\}$$

$$I_E^*(\Omega) = \frac{-2\Psi_s^2 K^4}{(K^2 - j\Omega)\cosh(K)} \left\{ \frac{1}{\cosh(K)} \left(\frac{1}{2} + \frac{\sinh(K)\cosh(K)}{2K} \right) \right.$$

$$+ \frac{1}{\cosh(\sqrt{j\Omega}) - B\sqrt{j\Omega}\sinh(\sqrt{j\Omega})} \left[\frac{\sinh(K + \sqrt{j\Omega})}{2\left(K + \sqrt{j\Omega}\right)} + \frac{\sinh(K - \sqrt{j\Omega})}{2\left(K - \sqrt{j\Omega}\right)} \right]$$

$$\left. \times \left(BK\frac{\sinh(K)}{\cosh(K)} - 1 \right) \right\} + 2\Sigma K^2 ,$$

$$Q_P^*(\Omega) = \frac{2}{j\Omega} \left(1 - \frac{1}{\sqrt{j\Omega}} \frac{\sinh(\sqrt{j\Omega})}{\cosh(\sqrt{j\Omega}) - B\sqrt{j\Omega}\sinh(\sqrt{j\Omega})} \right) ,$$

$$Q_E^*(\Omega) = \frac{2\Psi_s K^2}{K^2 - j\Omega} \left\{ \frac{\sinh(K)}{K\cosh(K)} \right.$$

$$+ \left. \left(BK\frac{\sinh(K)}{\cosh(K)} - 1 \right) \frac{1}{\sqrt{j\Omega}} \frac{\sinh(\sqrt{j\Omega})}{\cosh(\sqrt{j\Omega}) - B\sqrt{j\Omega}\sinh(\sqrt{j\Omega})} \right\} \quad (3.4.1)$$

88

When $\Omega \to 0$, Eq.(3.4.1) reduces to those of steady state.

$$V_P^*(Y,0) = \frac{1 - Y^2 - 2B}{2},$$

$$V_E^*(Y,0) = \Psi_s \left[\frac{\cosh(KY)}{\cosh(K)} - 1 + BK\frac{\sinh(K)}{\cosh(K)} \right],$$

$$I_P^*(0) = -2\Psi_s \left[1 - \frac{\sinh(K)}{K\cosh(K)} - BK\frac{\sinh(K)}{\cosh(K)} \right],$$

$$I_E^*(0) = \frac{-2\Psi_s^2 K^2}{\cosh(K)} \left\{ \frac{1}{\cosh(K)} \left(\frac{1}{2} + \frac{\sinh(K)\cosh(K)}{2K} \right) \right.$$

$$\left. - \frac{\sinh(K)}{K} + B\frac{\sinh^2(K)}{\cosh(K)} \right\} + 2\Sigma K^2,$$

$$Q_P^*(0) = \frac{2}{3} - 2B,$$

$$Q_E^*(0) = 2\Psi_s \left[\frac{\sinh(K)}{K\cosh(K)} - 1 + BK\frac{\sinh(K)}{\cosh(K)} \right]. \tag{3.4.2}$$

If the slip coefficient $B = 0$, all quantities become those of the electrokinetic flow with no slip condition. If $\Psi_s = 0$ and $B = 0$, all quantities become those of macroflow with no EDL effect and no slip.

3.5 A new method to determine zeta potential and slip length

For simplicity, we use solutions of a parallel-plate microchannel to show the effects of slippage on the zeta potential measurement. Here, we also propose a new method to determine Zeta potential and slip coefficient simultaneously [120].

The traditional zeta potential measurement method resorts to streaming potential phenomena by using the following equation

$$E_z^*(0) = -\frac{I_P^*(0)}{I_E^*(0)} P^*(0) \quad \text{for} \quad I^* = 0. \tag{3.5.1}$$

In experiments, for certain input P^*, we use measured E_z^* to calculate the zeta potential/ surface potential (here, we ignore the difference between zeta potential and

89

surface potential) Ψ_s. For hydrophobic surface, if we don't take slippage into account, we will use the following equation

$$E_z^*(\bar{\Psi}_s, B = 0) = -\frac{I_P^*(\bar{\Psi}_s, B = 0)}{I_E^*(\bar{\Psi}_s, B = 0)}P^* , \qquad (3.5.2)$$

where $\bar{\Psi}_s$ is called apparent zeta potential without considering slippage. However, the true zeta potential Ψ_s should come from

$$E_z^*(\Psi_s, B \neq 0) = -\frac{I_P^*(\Psi_s, B \neq 0)}{I_E^*(\Psi_s, B \neq 0)}P^* , \qquad (3.5.3)$$

Equating Eq.3.5.2 to Eq.3.5.3, we can study the effect of slip coefficient B on calculated zeta potential by

$$\frac{I_P^*(\Psi_s, B \neq 0)}{I_E^*(\Psi_s, B \neq 0)} = \frac{I_P^*(\bar{\Psi}_s, B = 0)}{I_E^*(\bar{\Psi}_s, B = 0)} , \qquad (3.5.4)$$

Assuming $\Sigma = 3.85$ and $\Psi_s = -1.95$, we plot apparent zeta potential $\bar{\Psi}_s$ with respect to B for different K in Figure 3.15. We find traditional zeta potential measurement method could cause some deviation from the true zeta potential of hydrophobic surface. More hydrophobic, more error might be caused. Eqs. 3.4.2 indicate that we can determine the true zeta potential and slip coefficient simultaneously, only if we measure enough experimental quantities other than streaming potential and pressure drop, such as flow rate or current.

3.6 Conclusions

After introducing Navier slip boundary condition to describe flow behavior on hydrophobic solid surface, and combining with electrokinetic phenomena, we obtain analytical solutions of time-dependent electrokinetic slip flows in rectangular, circular and parallel-plate microchannels with hydrophobic surfaces. From the results presented above, we have shown that both EDL effect and slip condition cannot be ignored. In some experiments, attempts have been made to measure slip length from the velocity profile or flow rate without consideration of EDL effect. Thus, a smaller

90

Apparent zeta potential
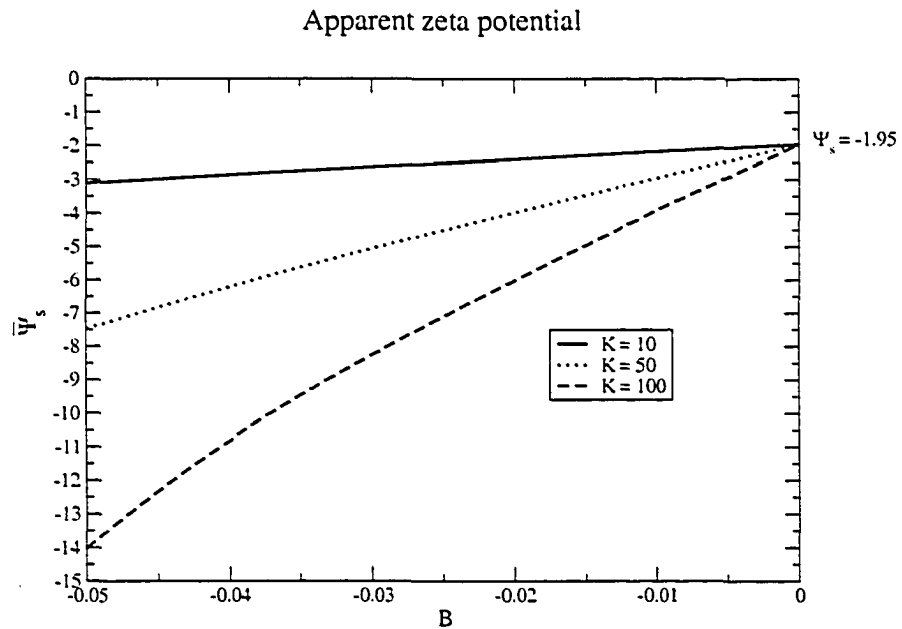
Figure 3.15: Comparison of the apparent zeta potential $\bar{\Psi}_s$ with the true zeta potential Ψ_s using Eq.3.5.4

slip length would have obtained. On the other hand, in EDL experiments, slip condition should also be considered, especially for hydrophobic solid surfaces. Otherwise, a smaller surface potential will be predicted. Considering effect of slippage, a new method to simultaneously determine zeta potential and slip length of an hydrophobic surface is proposed. We are also aware of efficiency of pressure/electric field driven flow improved by slippage.

Chapter 4

Electrokinetic Slip Flow in Microchannels with Non-uniform Surface Potential and Hydrophobicity

4.1 Introduction

The presence of an electrical double layer at the solid-liquid interface and its electrokinetic phenomena have been used to develop various chemical and biological instruments [18, 14, 15]. A common assumption is the uniformity of surface properties during electrokinetic fluid transport in microchannels [32, 53, 54, 110, 119, 121]. Nevertheless, surface heterogeneity can easily arise from fabrication defects or chemical adsorption onto microchannels. For example, Norde et al. [77] studied the relationship between protein adsorption with streaming potential. Ajdari [78, 79] presented a theoretical solution for electroosmosis flow on inhomogeneous charged surface. Stroock et al. [80] studied electroosmosis flow on a surface with patterned charge. Their results agree well with theory [78, 79]. Ren and Li [81] numerically studied electroosmotic flow in a heterogeneous circular microchannel with axially various surface potential. Anderson and Idol [82] studied electroosmosis through pores with nonuniformly charged walls. They showed that the mean electroosmosis velocity within the capillary was given by the classical Helmholtz equation with the local

92

surface potential replaced by the average surface potential. Keely *et al.* [83] theoretically gave out a flow profile inside a capillary with nonuniform surface potential. Herr *et al.* [84] theoretically and experimentally investigated electroosmosis flow in cylindrical capillaries with nonuniform wall surface charge distribution. They used a nonintrusive caged-fluorescence imaging technique to image the electroosmosis flow. They observed parabolic velocity profile induced by pressure gradient due to heterogeneity of capillary surface. However, most of the above studies [81, 82, 83, 84] assumed uniform electric fields. Mathematically, the assumption of uniform electric field in a non-uniform microchannel satisfies the requirement of flow rate continuity, but does not automatically guarantee that current continuity is maintained. Indeed, current and flow rate continuity cannot be automatically satisfied if a uniform electric field is assumed in non-uniformed microchannels. In our following study, we indeed show a slightly various electric field distribution in a nonuniform microchannel for electroosmosis flow.

Uniformity of electric field distribution in non-uniform microchannels results from the limitation of the Poisson-Boltzmann model which assumes that the permittivity of the medium is constant everywhere [32]. Thus, the permittivity in the electrical double layer (EDL) is assumed to be the same as that of the bulk solution, implying that the two regions should have a uniform electric field. In fact, the charge distribution in EDL is different from that in the bulk solution and hence the two permittivities should be different. Since EDL and bulk solution with different surface potentials have its own permittivity, a heterogeneous microchannel with non-uniform surface potential should have a non-uniform electric field distribution. A comprehensive model of heterogeneous non-uniform microchannels should also include the different permittivities, conductivities and electric fields in various places. The difference in the permittivities can be considered to be small; and, for simplicity, we consider in this paper the difference of electric field in non-uniform microchannels. Further, to

93

the best of our knowledge, pressure-drive flow (streaming potential) through heteroge-neous microchannels has not been reported. It is well known that streaming potential is one of the most common methods to measure zeta potential. Studying pressure-driven flow in heterogeneous microchannels is helpful to the design of zeta potential measurements. Thus, we also consider a non-uniform electric field distribution in heterogeneous microchannels where a zero net current is satisfied everywhere.

Furthermore, a surface with non-uniform hydrophobicity is also quite common. For example, the hydrophobicity of surface is easy to be changed by chemical deposi-tion or adsorption. According to our previous study, slippage of microfluidics due to hydrophobicity of surface should be influenced by heterogeneity of surface hydropho-bicity. Basically, conservation conditions should be satisfied in such problem. Even though this is a popular problem, no published literature addressed this.

In this chapter, we creat a theoretical model, a microchannel with different surface potentials and hydrophobicities in every section. Based on this model, we study effects of different surface potentials and hydrophobicities on oscillating electrokinetic slip flow. Understanding of this problem is helpful to guide us design or pattern microchannels.
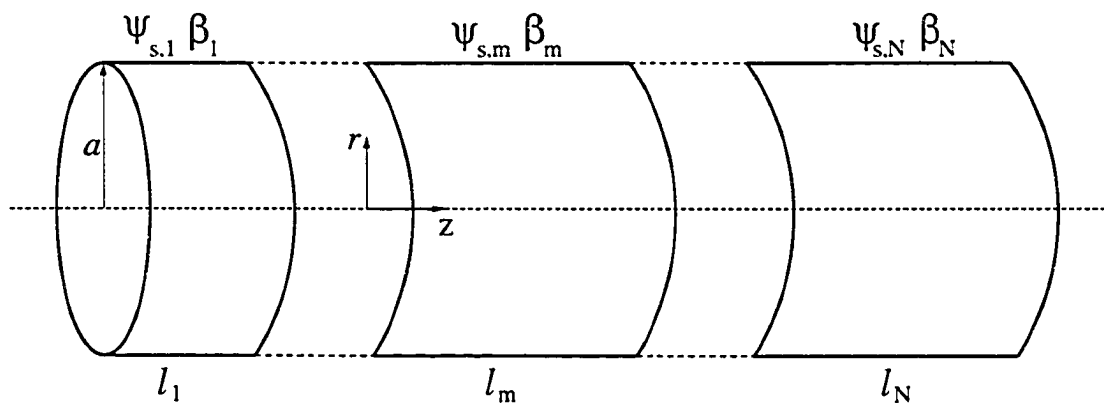
Figure 4.1: The schematic of nonuniform microchannel

94

4.2 Assumptions and theory

We consider a non-uniform microchannel with N sections shown in Figure 4.1, where l is the length of each section and subscript m implies quantities relating to the mth section. We assume each section to be long enough for a fully developed flow and neglect the disturbance across regions between two sections. In the mth section, we consider a boundary value problem for oscillating electrolyte flow driven by an oscillating pressure gradient and electric field; A local cylindrical coordinate system (r, θ, z) is used for every section where the z-axis is taken to coincide with the microchannel central axis. Origins of local cylindrical coordinate systems are at the beginning of each section. All field quantities are taken to depend on the radial coordinate r and time t. The boundary value problem with the relevant field equations and boundary conditions are given below. In parametric study, we mainly study electrokinetic slip flow in a nonuniform circular microchannel. But, the following derivation about current (or charge flux) and flow rate (or mass flux) continuities is general and suitable for microchannels with different geometries.

4.2.1 Nonuniform electrical field assumption

Because each section has its own physical or chemical properties, electrical double layer in each layer has its own surface potential and ion distribution. So that we should consider different medium in every section. Even though permittivities of solution in electrical double layer of each section are different, which causes different electric fields, for simplicity, we only consider the deviations of electric field strengths among each section. The potential of mth section, u_m, at location (x, y, z) at a given time t is taken to be

$$u_m \equiv u_m(x, y, z, t) = \psi_m(x, y, z) + \left[u_{0,m} - zE'_{z,m}(t)\right] , \qquad (4.2.1)$$

95

where $\psi_m(x, y, z)$ is the potential of mth section due to the double layer at equilibrium state (i.e., no liquid motion with no applied external field); $u_{0,m}$ is the potential at beginning of mth section $z = 0$ (i.e., $u_{0,m} \equiv u_m(0,0,0,t)$); and $E'_{z,m}(t)$ is the spatially uniform in mth layer and time-dependent electric field strength. The potential u_m in Eq.(4.2.1) is axisymmetric and, when $E'_{z,m}(t)$ is time-independent, Eq.(4.2.1) is similar to Eq.(6.1) of Masliyah [38]. With assumption of Eq. 4.2.1, the potential related to cross section can be uncoupled from the axial electric field, so that we don't need solve three-dimensional Nernst-Planck equation. Here, we also define the normalized potential $U_m = \frac{z_0 e}{kT} u_m$.

Flow rate and current continuity

Each section has its own normalized parameters: pressure gradient, P_m^*, strength of electric field, $E_{z,m}^*$, surface potential, $\Psi_{s,m}$, slip coefficient, B_m, and the length, L_m, where $L_m = l_m/a$ for a circular microchannel or $L_m = l_m/h$ for a rectangular or parallel-plate microchannel. $V_{P,m}^*$, $V_{E,m}^*$, $Q_{P,m}^*$, $Q_{E,m}^*$, $I_{P,m}^*$, $I_{E,m}^*$ for rectangular, circular, parallel-plate microchannels can be found in Chapter 3.

For each section, $E_{z,m}^*$ and P_m^* are field quantities and uniform. For the whole microchannel, the total current, I_{total} and flow rate, Q_{total} are the same for any section due to continuity of current and flow rate. The total pressure drop and potential drop of the microchannel are the summation of those of each section. So, we have the following relationship.

$$Q_{total} = Re[Q_{total}^* e^{j\Omega\tau}] = Re[(Q_{P,m}^*(\Omega)P_m^*(\Omega) + Q_{E,m}^*(\Omega)E_{z,m}^*(\Omega))e^{j\Omega\tau}] \quad (4.2.2)$$

$$I_{total} = Re[I_{total}^* e^{j\Omega\tau}] = Re[(I_{P,m}^*(\Omega)P_m^*(\Omega) + I_{E,m}^*(\Omega)E_{z,m}^*(\Omega))e^{j\Omega\tau}], \quad (4.2.3)$$

$$\Delta P = Re[P^* L e^{j\Omega\tau}] = Re[\sum_{m=1}^{N} P_m^* L_m e^{j\Omega\tau}], \quad (4.2.4)$$

$$\Delta U = Re[E_z^* L e^{j\omega t}] = Re[\sum_{m=1}^{N} E_{z,m}^* L_m e^{j\Omega\tau}], \quad (4.2.5)$$

96

where $L = \sum_{m=1}^{N} L_m$, is the total normalized length and U is normalized total potential. Based on those Eqs. 4.2.2 - 4.2.5, we can determine the relationship of pressure gradient and strength of electric field between all sections. We will express all quantities as functions of the corresponding quantities of the first section.

Pressure driven flow

In this case, the known input is total normalized pressure gradient P^*. At equilibrium, for mth section, the strength of streaming potential is

$$E_{z,m}^* = -\frac{I_{P,m}^*}{I_{E,m}^*} P_m^* \quad (m = 1......N) . \tag{4.2.6}$$

Continuity of current is satisfied automatically. From Eq.4.2.2, we have

$$Q_{P,m}^*(\Omega)P_m^*(\Omega) + Q_{E,m}^* E_{z,m}^* = Q_{P,1}^*(\Omega)P_1^*(\Omega) + Q_{E,1}^* E_{z,1}^* . \tag{4.2.7}$$

Substituting Eq. 4.2.6 in Eq. 4.2.7, we can find relationship between the pressure gradient in the mth section and that of the first section,

$$P_m^* = \frac{Q_{P,1}^* - \frac{(I_{P,1}^*)^2}{I_{E,1}^*}}{Q_{P,m}^* - \frac{(I_{P,m}^*)^2}{I_{E,m}^*}} P_1^* \tag{4.2.8}$$

From Eq. 4.2.4, we have

$$P^*L = P_1^* \sum_{m=1}^{N} L_m \frac{Q_{P,1}^* - \frac{(I_{P,1})^2}{I_{E,1}}}{Q_{P,m}^* - \frac{(I_{P,m})^2}{I_{E,m}}} \tag{4.2.9}$$

According to the known pressure gradient, we can solve the pressure gradient of every section. The total streaming potential (potential drop) should be the summation of potential drop in each section,

$$E_z^* = P^* \sum_{m=1}^{N} \left[-L_m \frac{I_{P,m}^*}{I_{E,m}^*} \frac{Q_{P,1}^* - \frac{(I_{P,1})^2}{I_{E,1}}}{Q_{P,m}^* - \frac{(I_{P,m})^2}{I_{E,m}}} \frac{1}{\sum_{m=1}^{N} L_m \frac{Q_{P,1}^* - \frac{(I_{P,1})^2}{I_{E,1}}}{Q_{P,m}^* - \frac{(I_{P,m})^2}{I_{E,m}}}} \right] . \tag{4.2.10}$$

97

Electroosmosis flow or electric field driven flow

In this case, the known inputs are normalized total strength of electric field, E_z^* and the normalized pressure gradient, P^* (Normally, we open the both sides of electroosmotic system in atmosphere to eliminate effect of hydrostatic so that $P^* = 0$). Continuities of current and flow rate can be expressed as

$$Q_{P,m}^*(\Omega)P_m^*(\Omega) + Q_{E,m}^*E_{z,m}^* = Q_{P,1}^*(\Omega)P_1^*(\Omega) + Q_{E,1}^*E_{z,1}^* , \qquad (4.2.11)$$

$$I_{P,m}^*(\Omega)P_m^*(\Omega) + I_{E,m}^*E_{z,m}^* = I_{P,1}^*(\Omega)P_1^*(\Omega) + I_{E,1}^*E_{z,1}^* . \qquad (4.2.12)$$

Note that $Q_{E,m}^* = I_{P,m}$. P_m^* and E_m^* can be solved from Eqs. 4.2.11 and 4.2.12

$$P_m^* = \frac{I_{P,m}^*I_{P,1}^* - I_{E,m}^*Q_{P,1}^*}{(I_{P,m}^*)^2 - I_{E,m}^*Q_{P,m}^*}P_1^* + \frac{I_{P,m}^*I_{E,1}^* - I_{E,m}^*I_{P,1}^*}{(I_{P,m}^*)^2 - I_{E,m}^*Q_{P,m}^*}E_{z,1}^* , \qquad (4.2.13)$$

$$E_{z,m}^* = \frac{I_{P,m}^*Q_{P,1}^* - Q_{P,m}^*I_{P,1}^*}{(I_{P,m}^*)^2 - I_{E,m}^*Q_{P,m}^*}P_1^* + \frac{I_{P,m}^*I_{P,1}^* - Q_{P,m}^*I_{E,1}^*}{(I_{P,m}^*)^2 - I_{E,m}^*Q_{P,m}^*}E_{z,1}^* , \qquad (4.2.14)$$

Following Eqs. 4.2.4 and 4.2.5, we can obtain a set of equations

$$P^*L = P_1^* \sum_{m=1}^{N} L_m \frac{I_{P,m}^*I_{P,1}^* - I_{E,m}^*Q_{P,1}^*}{(I_{P,m}^*)^2 - I_{E,m}^*Q_{P,m}^*} + E_{z,1}^* \sum_{m=1}^{N} L_m \frac{I_{P,m}^*I_{E,1}^* - I_{E,m}^*I_{P,1}^*}{(I_{P,m}^*)^2 - I_{E,m}^*Q_{P,m}^*} , \qquad (4.2.15)$$

$$E_z^*L = P_1^* \sum_{m=1}^{N} L_m \frac{I_{P,m}^*Q_{P,1}^* - Q_{P,m}^*I_{P,1}^*}{(I_{P,m}^*)^2 - I_{E,m}^*Q_{P,m}^*} + E_{z,1}^* \sum_{m=1}^{N} L_m \frac{I_{P,m}^*I_{P,1}^* - Q_{P,m}^*I_{E,1}^*}{(I_{P,m}^*)^2 - I_{E,m}^*Q_{P,m}^*} . \qquad (4.2.16)$$

For brevity, let's write Eqs. 4.2.15 and 4.2.16 as

$$P^*L = A_{11}P_1^* + A_{12}E_{z,1}^* , \qquad (4.2.17)$$

$$E_z^*L = A_{21}P_1^* + A_{22}E_{z,1}^* , \qquad (4.2.18)$$

where

$$A_{11} = \sum_{m=1}^{N} L_m \frac{I_{P,m}^*I_{P,1}^* - I_{E,m}^*Q_{P,1}^*}{(I_{P,m}^*)^2 - I_{E,m}^*Q_{P,m}^*} ,$$

$$A_{12} = \sum_{m=1}^{N} L_m \frac{I_{P,m}^*I_{E,1}^* - I_{E,m}^*I_{P,1}^*}{(I_{P,m}^*)^2 - I_{E,m}^*Q_{P,m}^*} ,$$

$$A_{21} = \sum_{m=1}^{N} L_m \frac{I_{P,m}^*Q_{P,1}^* - Q_{P,m}^*I_{P,1}^*}{(I_{P,m}^*)^2 - I_{E,m}^*Q_{P,m}^*} ,$$

$$A_{22} = \sum_{m=1}^{N} L_m \frac{I_{P,m}^*I_{P,1}^* - Q_{P,m}^*I_{E,1}^*}{(I_{P,m}^*)^2 - I_{E,m}^*Q_{P,m}^*} . \qquad (4.2.19)$$

Solving the above two equations, we can obtain

$$P_1^* = \frac{A_{22}L}{A_{11}A_{22} - A_{21}A_{12}}P^* - \frac{A_{12}L}{A_{11}A_{22} - A_{21}A_{12}}E_z^* , \qquad (4.2.20)$$

$$E_{z,1}^* = -\frac{A_{21}L}{A_{11}A_{22} - A_{21}A_{12}}P^* + \frac{A_{11}L}{A_{11}A_{22} - A_{21}A_{12}}E_z^* , \qquad (4.2.21)$$

Then, $E_{z,m}^*$ and P_m^* could be

$$P_m^* = \frac{I_{P,m}^* I_{P,1}^* - I_{E,m}^* Q_{P,1}^*}{(I_{P,m}^*)^2 - I_{E,m}^* Q_{P,m}^*}\left(\frac{A_{22}L}{A_{11}A_{22} - A_{21}A_{12}}P^* - \frac{A_{12}L}{A_{11}A_{22} - A_{21}A_{12}}E_z^*\right)$$
$$+\frac{I_{P,m}^* I_{E,1}^* - I_{E,m}^* I_{P,1}^*}{(I_{P,m}^*)^2 - I_{E,m}^* Q_{P,m}^*}\left(-\frac{A_{21}L}{A_{11}A_{22} - A_{21}A_{12}}P^* + \frac{A_{11}L}{A_{11}A_{22} - A_{21}A_{12}}E_z^*\right) , \quad (4.2.22)$$

$$E_{z,m}^* = \frac{I_{P,m}^* Q_{P,1}^* - Q_{P,m}^* I_{P,1}^*}{(I_{P,m}^*)^2 - I_{E,m}^* Q_{P,m}^*}\left(\frac{A_{22}L}{A_{11}A_{22} - A_{21}A_{12}}P^* - \frac{A_{12}L}{A_{11}A_{22} - A_{21}A_{12}}E_z^*\right)$$
$$+\frac{I_{P,m}^* I_{P,1}^* - Q_{P,m}^* I_{E,1}^*}{(I_{P,m}^*)^2 - I_{E,m}^* Q_{P,m}^*}\left(-\frac{A_{21}L}{A_{11}A_{22} - A_{21}A_{12}}P^* + \frac{A_{11}L}{A_{11}A_{22} - A_{21}A_{12}}E_z^*\right) , \quad (4.2.23)$$

If both sides of electroosmotic system open to atmosphere, which imply $P^* = 0$, we can know from Eq. 4.2.22 that $P_m^* \neq 0$. Because of the heterogeneity of the microchannel, pressure gradients are induced to make the continuities of current and flow rate. We also can derive expressions of total current I_{total} and total flow rate Q_{total}, which are measurable by experiments.

$$I_{total}^* = I_{P,m}^* P_m^* + I_{E,m}^* E_{z,m}^* , \qquad (4.2.24)$$

$$Q_{total}^* = Q_{P,m}^* P_m^* + I_{P,m}^* E_{z,m}^* . \qquad (4.2.25)$$

Let's focus on a common electroosmosis experimental system with $P^* = 0$.

$$I_{total}^* = \frac{(A_{11}I_{E,1}^* - A_{12}I_{P,1}^*)L}{A_{11}A_{22} - A_{21}A_{12}}E_z^* , \qquad (4.2.26)$$

$$Q_{total}^* = \frac{(A_{11}I_{P,1}^* - A_{12}Q_{P,1}^*)L}{A_{11}A_{22} - A_{21}A_{12}}E_z^* , \qquad (4.2.27)$$

$$\frac{Q_{total}^*}{I_{total}^*} = \frac{A_{11}I_{P,1}^* - A_{12}Q_{P,1}^*}{A_{11}I_{E,1}^* - A_{12}I_{P,1}^*} . \qquad (4.2.28)$$

Eq. 4.2.28 is a function of frequency Ω, surface potential $\Psi_{s,m}$, which includes information of surface potential, slip coefficient and length of each section.

99

4.3 Parametric study and discussion

4.3.1 Electrokinetic flow in a microchannel with nonuniform surface potential

Since slip boundary condition is independent of frequency, for clearance, we firstly only relate frequency or time-dependent problem to electrokinetic flow. We study here the effect of the normalized thickness K^{-1} in the EDL, and the normalized frequency Ω on velocity profile, pressure distribution and electric field distribution. We have selected the following values for our calculations: the amplitude of normalized total pressure gradient, $P^*(\Omega) = 2 \times 10^2$, the amplitude of the strength of total electric field, $E_z^*(\Omega) = 0$ or 10, the normalized frequency, $\Omega = 10$, the normalized conductivity, $\Sigma = 3.85$, which implies a diffusion coefficient $D \approx 2 \times 10^{-9}$ m^2/s for an KCl electrolyte [118]. A nonuniform microchannel consists of 8 sections with the same normalized length $L_m = 50$. Along the flow direction, normalized surface potentials $\Psi_{s,m}$ are respectively: -0.96, -1.37, -1.76, -2.15, -2.54, -2.93, -3.32, -3.71. They correspond to the dimensional surface potentials of -25mV, -35mV, -45mV, -55mV, -65mV, -75mV, -85mV and -95mV, respectively (Debye-Hückel approximation gives a good agreement with experiments, when zeta potential is up to 100mV [33]).

Table 4.1: Pressure gradient $-\frac{\partial P_m}{\partial Z}$, electric field strength $E_{z,m}$, magnitude of the flow rate $|Q^*|$ and the strength of total streaming potential E_z^* in a non-uniform circular microchannel for $K = 10$ with $\Omega = 0$ and 10, for pressure-driven flow.

	section 1	section 2	section 3	section 4	section 5
$\Omega = 0$	$-\frac{\partial P_1}{\partial Z} = 187.82$	$-\frac{\partial P_2}{\partial Z} = 190.06$	$-\frac{\partial P_3}{\partial Z} = 192.98$	$-\frac{\partial P_4}{\partial Z} = 196.55$	$-\frac{\partial P_5}{\partial Z} = 200.7$
	$E_{z,1} = -0.376$	$E_{z,2} = -0.522$	$E_{z,3} = -0.664$	$E_{z,4} = -0.8$	$E_{z,5} = -0.93$
	section 6	section 7	section 8	$|Q^*|$	$|E_z|$
	$-\frac{\partial P_6}{\partial Z} = 205.37$	$-\frac{\partial P_7}{\partial Z} = 210.5$	$-\frac{\partial P_8}{\partial Z} = 216.02$	72.82	0.85
	$E_{z,6} = -1.052$	$E_{z,7} = -1.168$	$E_{z,8} = -1.275$		
	section 1	section 2	section 3	section 4	section 5
$\Omega = 10$	$-\frac{\partial P_1}{\partial Z} = 193.66$	$\frac{-\partial P_2}{\partial Z} = 194.81$	$-\frac{\partial P_3}{\partial Z} = 196.32$	$\frac{-\partial P_4}{\partial Z} = 198.17$	$-\frac{\partial P_5}{\partial Z} = 200.33$
	$E_{z,1}^* = -0.153$	$E_{z,2}^* = -0.214$	$E_{z,3}^* = -0.272$	$E_{z,4}^* = -0.329$	$E_{z,5}^* = -0.384$
	section 6	section 7	section 8	$|Q^*|$	$|E_z^*|$
	$-\frac{\partial P_6}{\partial Z} = 202.78$	$-\frac{\partial P_7}{\partial Z} = 205.49$	$-\frac{\partial P_8}{\partial Z} = 208.43$	38.5	0.35
	$E_{z,6}^* = -0.437$	$E_{z,7}^* = -0.487$	$E_{z,8}^* = -0.534$		

Figure 4.2: The velocity profile $|V^*|$, pressure drop P and potential distribution $U_m - \Psi_m$ in a non-uniform circular microchannel for $K = 10$ with $\Omega = 0$ and 10, for pressure-driven flow. R is a normalized radius where $R = 1$ and 0 present the wall and center line, respectively.

Pressure and electric field distribution of pressure driven flow

For pressure driven flow through a nonuniform microchannel, a nonlinear pressure distribution and nonuniform strengths of electric field, $E_{z,m}$ are caused. We always set $P = 0$ and $U_m - \Psi_m = 0$ as reference value at the beginning of the microchannel. The results for the magnitude of velocity $|V^*|$, pressure drop P and axial potential $U_m - \Psi_m$ along the channel for $\Omega = 0$ and 10 are shown in Figure 4.2. We see that the velocity profiles remain parabolic along the microchannel. When $\Omega = 10$, the magnitude of velocity is smaller, since viscosity of liquid makes flow lag behind the

101

variation of pressure. It is noted that the pressure gradient in Figure 4.2 is indeed nonlinear along the channel, as seen in Table 4.1 from the tabulated results. We see that as surface potential increases, pressure gradient increases along the flow direction. This is due to the fact that a larger pressure gradient is required to compensate for the decrease in flow rate due to stronger electroviscous effect. When $\Omega = 10$, pressure distribution is almost the same as that of $\Omega = 0$. Their slight difference can be found in Table 4.1. The potential distribution along the axis of microchannel is also nonlinear. As zeta potential increases, the strength of electric field also increases. The reason is due to a stronger electric field to make up a net zero current. The strength of electric field is smaller when $\Omega = 10$. These difference are shown in Table 4.1 and Figure 4.2. In Figure 4.2, $K = 10$ implies a diluted solution for a fixed microchannel size. We also plotted the corresponding results in Figure 4.3 for a more concentrated solution $K = 1000$ with $\Omega = 0$. When $K = 1000$ (a thinner EDL), the pressure gradient varies slightly (see Table 4.2) as compared to that for $K = 10$, since electroviscous effect is smaller for a more concentrated solution. However, the strength of electric field is several orders smaller than that of $K = 10$ as a smaller electric field is sufficient to maintain a net zero current. Comparing Figure 4.2 with Figure 4.3, because flow of $K = 1000$ are nearly affected by the electroviscous effect, velocity profiles keep better parabolic curves than those of along $K = 10$ in each section.

Pressure and electric field distribution of electric field driven flow

For electric-field-driven flow through a non-uniform microchannel, a non-uniform pressure distribution will result from the different surface potentials and electric fields in each section so as to maintain flow rate and current continuities. In actual experiments, electroosmosis system is often opened to atmosphere so that the total pressure difference between the two ends of a microchannel is zero.

102

Pressure driven flow
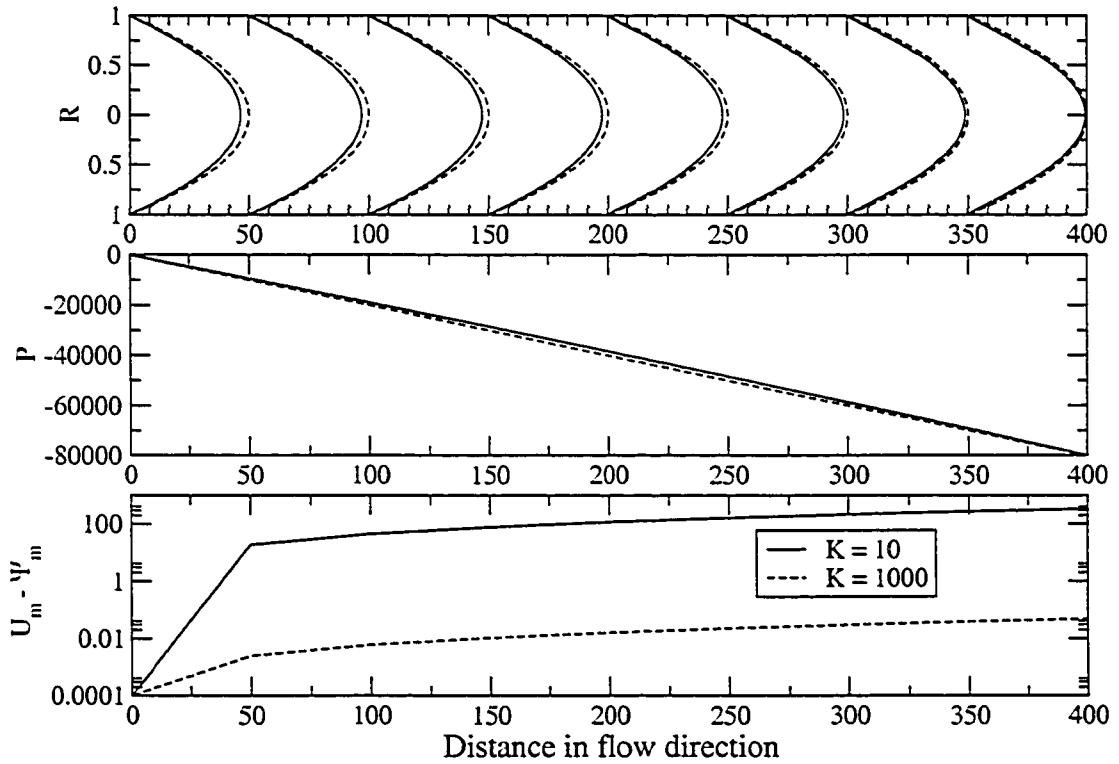
Figure 4.3: The velocity profile $|V^*|$, pressure drop P and potential distribution $U_m - \Psi_m$ in a non-uniform circular microchannel for $K = 10$ and 1000 with $\Omega = 0$, for pressure-driven flow. R is a normalized radius where $R = 1$ and 0 present the wall and center line, respectively.

The results for the magnitude of velocity $|V^*|$, pressure drop P and axial potential $U_m - \Psi_m$ along the channel for $\Omega = 0$ and 10 are shown in Figure 4.4 with $K = 1000$; its tabulated results are given in Table 4.3. In Figure 4.4, we find that the velocity profile has a parabolic feature at the two ends of the microchannel when $\Omega = 0$. In the middle of the microchannel, velocity profiles are more similar to typical electroosmosis flow. The pressure distribution corresponds well to the velocity profiles, since the pressure gradient in the middle of the channel is much smaller than those at the two ends. Pressure distribution well accords with the velocity profiles, since the induced pressure gradients in the middle of the microchannel become much smaller than those at the

Table 4.2: Pressure gradient $-\frac{\partial P_m}{\partial Z}$, electric field strength $E_{z,m}$, magnitude of the flow rate $|Q^*|$ and the strength of total streaming potential E_z in a non-uniform circular microchannel for $K = 10$ and 1000 with $\Omega = 0$, for pressure-driven flow.

$K = 10$	section 1	section 2	section 3	section 4	section 5
	$-\frac{\partial P_1}{\partial Z} = 187.82$ $E_{z,1} = -0.376$	$-\frac{\partial P_2}{\partial Z} = 190.06$ $E_{z,2} = -0.522$	$-\frac{\partial P_3}{\partial Z} = 192.98$ $E_{z,3} = -0.664$	$-\frac{\partial P_4}{\partial Z} = 196.55$ $E_{z,4} = -0.8$	$-\frac{\partial P_5}{\partial Z} = 200.7$ $E_{z,5} = -0.93$
	section 6	section 7	section 8	$|Q^*|$	E_z
	$-\frac{\partial P_6}{\partial Z} = 205.37$ $E_{z,6} = -1.052$	$-\frac{\partial P_7}{\partial Z} = 210.5$ $E_{z,7} = -1.168$	$-\frac{\partial P_8}{\partial Z} = 216.02$ $E_{z,8} = -1.275$	72.82	-0.85
$K = 10^3$	section 1	section 2	section 3	section 4	section 5
	$-\frac{\partial P_1}{\partial Z} = 199.998$ $E_{z,1} = -5e-5$	$-\frac{\partial P_2}{\partial Z} = 199.998$ $E_{z,2} = -7e-5$	$-\frac{\partial P_3}{\partial Z} = 199.999$ $E_{z,3} = -9e-5$	$-\frac{\partial P_4}{\partial Z} = 199.998$ $E_{z,4} = -1.1e-4$	$-\frac{\partial P_5}{\partial Z} = 200$ $E_{z,5} = -1.3e-4$
	section 6	section 7	section 8	$|Q^*|$	E_z
	$\frac{\partial P_6}{\partial Z} = 200$ $E_{z,6} = -1.5e-4$	$\frac{\partial P_7}{\partial Z} = 200.002$ $E_{z,7} = -1.7e-4$	$\frac{\partial P_8}{\partial Z} = 200.003$ $E_{z,8} = -1.9e-4$	78.54	$-1.2e-4$

two ends of the microchannel. This phenomenon has been experimentally observed by Herr et al. [84] and numerically predicted by Ren and Li [81]. When $\Omega = 10$, a slightly larger pressure drop is found where the flow velocity is smaller than that for $\Omega = 0$. Toward the end of the channel with a larger zeta potential, the characteristic oscillation becomes more noticeable from the velocity profile. Similar velocity profile of oscillating flow without EDL effect can be found in [72, 122].

A direct comparison of the results for $K = 10$ and 1000 are shown in Figure 4.5 and its tabulated results are given in Table 4.4. In Table 4.4, we see that the validity of the assumption of uniform electric field [81, 82, 83, 84] depends on the values of K. When $K = 1000$, the strength of electric field changes only slightly; when $K = 10$, a larger decrease in E_z is more apparent for electroosmosis flow. When $K = 10$ which corresponds to the case of a diluted solution, the velocity profile in the thicker diffusion layer of EDL is parabolic (see Figure 4.5). Because of a thicker EDL, two inflection points are found in the velocity profile at the end of the channel with a larger zeta potential. The electroosmosis flow for $K = 10$ is slower due to smaller ionic concentration. As the flow rate for $K = 10$ is smaller, less pressure drop is induced. From Figure 4.5, we can find that the electroosmtic flow of a concentrated solution is more sensitive to heterogeneity of surface potential.

104

Electric field driven flow
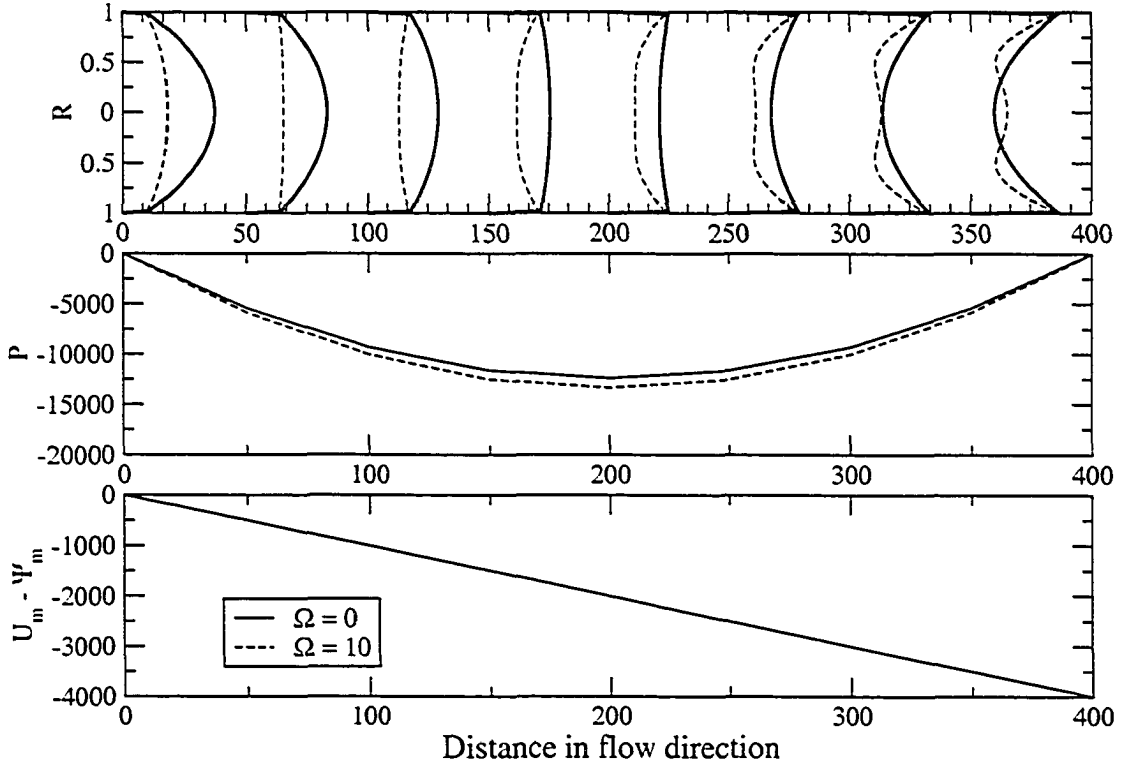
Figure 4.4: The velocity profile $|V^*|$, pressure drop P and potential distribution $U_m - \Psi_m$ in a non-uniform circular microchannel for $K = 1000$ with $\Omega = 0$ and 10, for electric-field-driven flow. R is a normalized radius where $R = 1$ and 0 present the wall and center line, respectively.

4.3.2 Electrokinetic slip flow in a microchannel with nonuniform surface potential and hydrophobicity

Here, different slip coefficients and surface potentials along microchannel are considered. We assume that slip coefficients are only determined by hydrophobicities of each section; Surface potentials, the concentration of the solution, frequencies do not influence slip coefficients. So, we only study the coupled effect of slip coefficient and surface potential distribution. We have selected the following values for our calculations: the amplitude of normalized total pressure gradient, $P^*(\Omega) = 2 \times 10^2$, the

105

Table 4.3: Pressure gradient $-\frac{\partial P_m}{\partial Z}$, electric field strength $E_{z,m}$ and magnitude of the flow rate $|Q^*|$ in a non-uniform circular microchannel for $K = 1000$ with $\Omega = 0$ and 10, for electric-field-driven flow.

	section 1	section 2	section 3	section 4	section 5
$\Omega = 0$	$-\frac{\partial P_1}{\partial Z} = 108.64$ $E_{z,1} = 10.014$	$\frac{-\partial P_2}{\partial Z} = 77.53$ $E_{z,2} = 10.011$	$-\frac{\partial P_3}{\partial Z} = 46.45$ $E_{z,3} = 10.008$	$-\frac{\partial P_4}{\partial Z} = 15.4$ $E_{z,4} = 10.004$	$-\frac{\partial P_5}{\partial Z} = -15.61$ $E_{z,5} = 10$
	section 6	section 7	section 8	$|Q^*|$	
	$-\frac{\partial P_6}{\partial Z} = -46.58$ $E_{z,6} = 9.994$	$-\frac{\partial P_7}{\partial Z} = -77.49$ $E_{z,7} = 9.988$	$-\frac{\partial P_8}{\partial Z} = -108.34$ $E_{z,8} = 9.981$	73.23	
$\Omega = 10$	section 1	section 2	section 3	section 4	section 5
	$-\frac{\partial P_1}{\partial Z} = 117.07$ $E_{z,1}^* = 10.014$	$-\frac{\partial P_2}{\partial Z} = 83.54$ $E_{z,2}^* = 10.011$	$-\frac{\partial P_3}{\partial Z} = 50.05$ $E_{z,3}^* = 10.008$	$-\frac{\partial P_4}{\partial Z} = 16.59$ $E_{z,4}^* = 10.004$	$-\frac{\partial P_5}{\partial Z} = -16.83$ $E_{z,5}^* = 10$
	section 6	section 7	section 8	$|Q^*|$	
	$-\frac{\partial P_6}{\partial Z} = -50.19$ $E_{z,6}^* = 9.994$	$-\frac{\partial P_7}{\partial Z} = -83.5$ $E_{z,7}^* = 9.988$	$-\frac{\partial P_8}{\partial Z} = -116.74$ $E_{z,8}^* = 9.8$	34.28	

amplitude of the strength of total electric field, $E_z^*(\Omega) = 10$, the normalized conductivity, $\Sigma = 3.85$. For pressure driven flow, $K = 1$ is used. For electroosmotic flow, $K = 10$ is used. A nonuniform microchannel consists of 8 sections with the same normalized length $L_m = 50$. In each section, normalized surface potentials $\Psi_{s,m}$ are respectively: 0.96, 1.37, 1.76, 2.15, 2.54, 2.93, 3.32, 3.71. Normalized slip coefficients B_m are respectively: -0.01, -0.012, -0.014, -0.016, -0.018, -0.02, -0.022, -0.024. Two sequences of the changes of slip coefficients and surface potentials are considered

1. slip coefficients increase as the surface potentials increase (solid line) and

2. slip coefficients decrease as the surface potentials increase (dashed line)

We believe other pairs of slip coefficient and surface potential distributions will cause some interesting results. We may do this in the future.

In Figure 4.6, nonlinear pressure and potential distributions are found for pressure driven flow. There are only slight differences of velocity profiles, pressure distributions and potential distributions for the two cases. In the middle of the microchannel, we can find velocity profiles are almost the same. Both cases have the same amplitude of total flow rate, $|Q^*| = 72.27$ and the same the strength of total streaming

106

Electric field driven flow
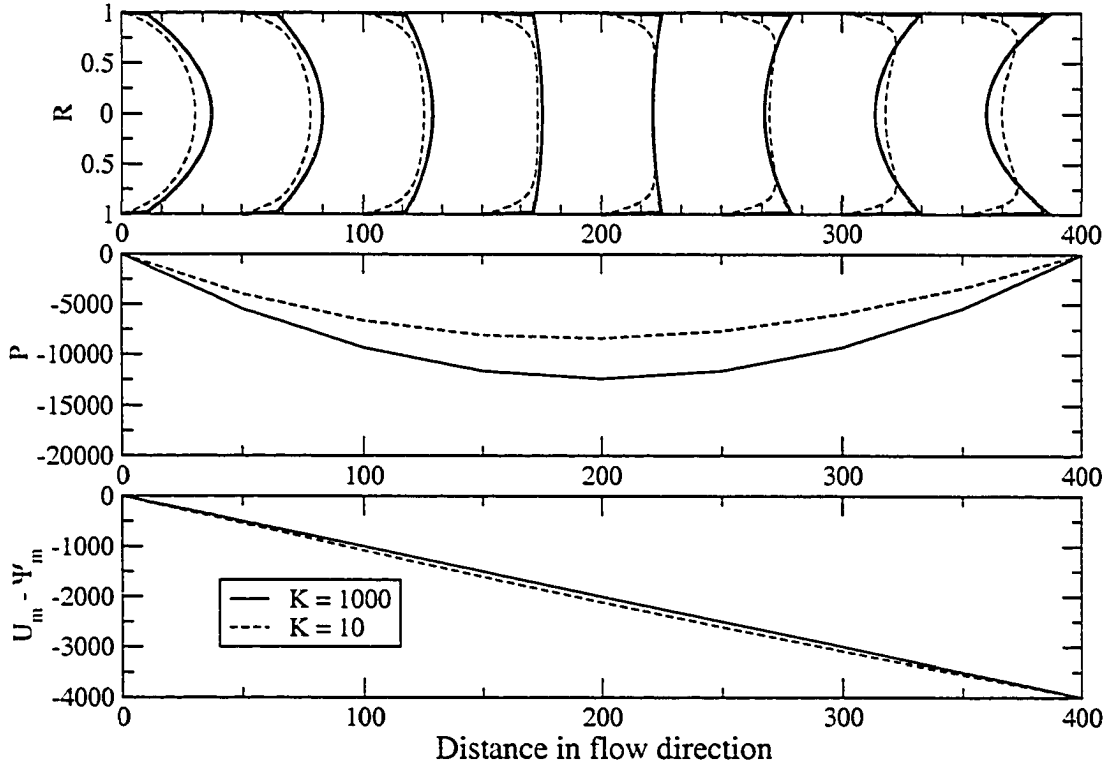
Figure 4.5: The velocity profile $|V^*|$, pressure drop P and potential distribution $U_m - \Psi_m$ in a non-uniform circular microchannel for $K = 10$ and 1000 with $\Omega = 0$, for electric-field-driven flow. R is a normalized radius where $R = 1$ and 0 present the wall and center line, respectively.

potential, $E_z = 71.99$. This means that the outputs of such microchannel cannot reflect the heterogeneity inside it. Because the nonuniform pressure and electric field always try to minimize the difference between any two sections, the slight difference of velocity profiles between two cases is easy to understand. If a section has a larger slip coefficient, its maximum velocity of flow has to be smaller in order to keep flow rate continuity.

We plot the velocity profiles, pressure and potential distributions for electric field driven flow in Figure 4.7. We also find the nonlinear pressure and potential distributions. Both cases have the same amplitude of total flow rate, $|Q^*| = 69.38$. Comparing

107

Table 4.4: Pressure gradient $-\frac{\partial P_m}{\partial Z}$, electric field strength $E_{z,m}$, and magnitude of the flow rate $|Q^*|$ in a non-uniform circular microchannel for $K = 1000$ and 10 with $\Omega = 0$, for electric-field-driven flow.

	section 1	section 2	section 3	section 4	section 5
$K = 1000$	$-\frac{\partial P_1}{\partial Z} = 108.64$ $E_{z,1} = 10.014$	$-\frac{\partial P_2}{\partial Z} = 77.53$ $E_{z,2} = 10.011$	$-\frac{\partial P_3}{\partial Z} = 46.45$ $E_{z,3} = 10.008$	$-\frac{\partial P_4}{\partial Z} = 15.4$ $E_{z,4} = 10.004$	$-\frac{\partial P_5}{\partial Z} = -15.61$ $E_{z,5} = 10$
	section 6	section 7	section 8	$|Q^*|$	
	$-\frac{\partial P_6}{\partial Z} = -46.58$ $E_{z,6} = 9.994$	$-\frac{\partial P_7}{\partial Z} = -77.49$ $E_{z,7} = 9.988$	$-\frac{\partial P_8}{\partial Z} = -108.34$ $E_{z,8} = 9.981$	73.23	
$K = 10$	section 1	section 2	section 3	section 4	section 5
	$\frac{\partial P_1}{\partial Z} = 79.01$ $E_{z,1} = 10.9$	$\frac{\partial P_2}{\partial Z} = 53.37$ $E_{z,2} = 10.69$	$\frac{\partial P_3}{\partial Z} = 29.1$ $E_{z,3} = 10.45$	$\frac{\partial P_4}{\partial Z} = 6.36$ $E_{z,4} = 10.19$	$\frac{\partial P_5}{\partial Z} = -14.74$ $E_{z,5} = 9.91$
	section 6	section 7	section 8	$|Q^*|$	
	$-\frac{\partial P_6}{\partial Z} = -34.09$ $E_{z,6} = 9.61$	$-\frac{\partial P_7}{\partial Z} = -51.64$ $E_{z,7} = 9.3$	$-\frac{\partial P_8}{\partial Z} = -67.37$ $E_{z,8} = 8.97$	58.04	

with Figure 4.6, to maintain the flow rate continuity, the pressure differences between the two cases become more apparent than that of pressure driven flow. This means slip coefficients play a more important role in electroosmotic flow.

4.4 Oscillating streaming potential and electroosmosis of multilayer membranes and a nondestructive method to image an unknown multilayer membrane

4.4.1 Introduction

Due to the requirement of mechanical strength, multilayer membranes with graded chemical, physical and mechanical properties are widely used in filtration, desalination and separation processes [123]. However, characterizing the electrochemical properties of multilayer membranes, such as zeta potential, is typically based on any given electrokinetic model through streaming potential [124, 125, 126, 127, 128] or electroosmosis [129, 130, 131, 132, 133] measurements. It is noted that traditional electrokinetic model [32, 110, 119] does not consider the detailed multilayer structure and hence the measured zeta potential can only be called the apparent zeta potential. Obviously, a single apparent zeta potential could not fully describe the electrokinetic

108

Pressure driven flow
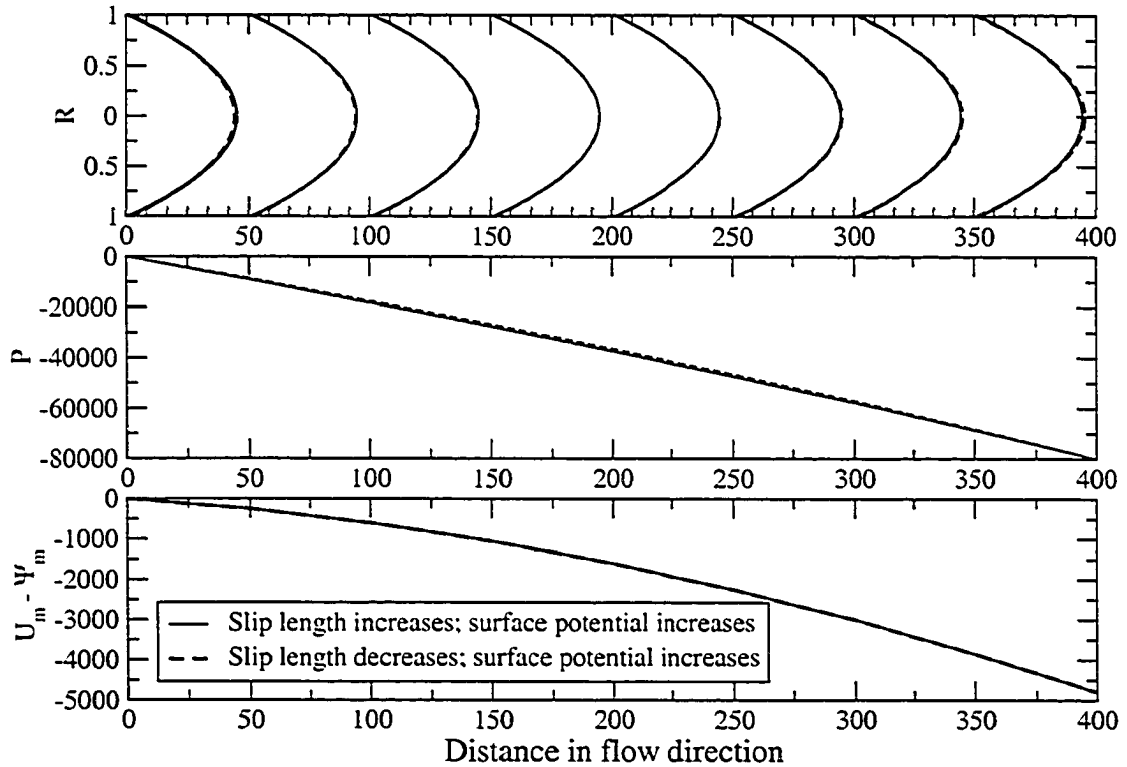


Figure 4.6: The velocity profile $|V^-|$, pressure and potential distributions in a nonuniform microchannel for $K = 1$ at $\Omega = 0$, for pressure driven flow.

properties of multilayer membranes. On the other hand, electrokinetic transport phenomena in multilayer membranes are complex due to its heterogeneous porosities and variation of pore sizes and zeta potentials for each layer. It is, therefore, important to study the nature of electrokinetic flow inside each layer. It would also be of interest to characterize the role of each layer on electrokinetic flow. Thus, there is a need to develop a detailed model to determine its electrokinetic property and flow behavior inside a multilayer membrane. Furthermore, a fundamental understanding of electrokinetic flow in multilayer membranes also provides guidelines for the design and characterization of multilayer membranes.

The first step in this topic has been performed by Szymczyk *et. al.* [134, 135]. For

109

Electric field driven flow
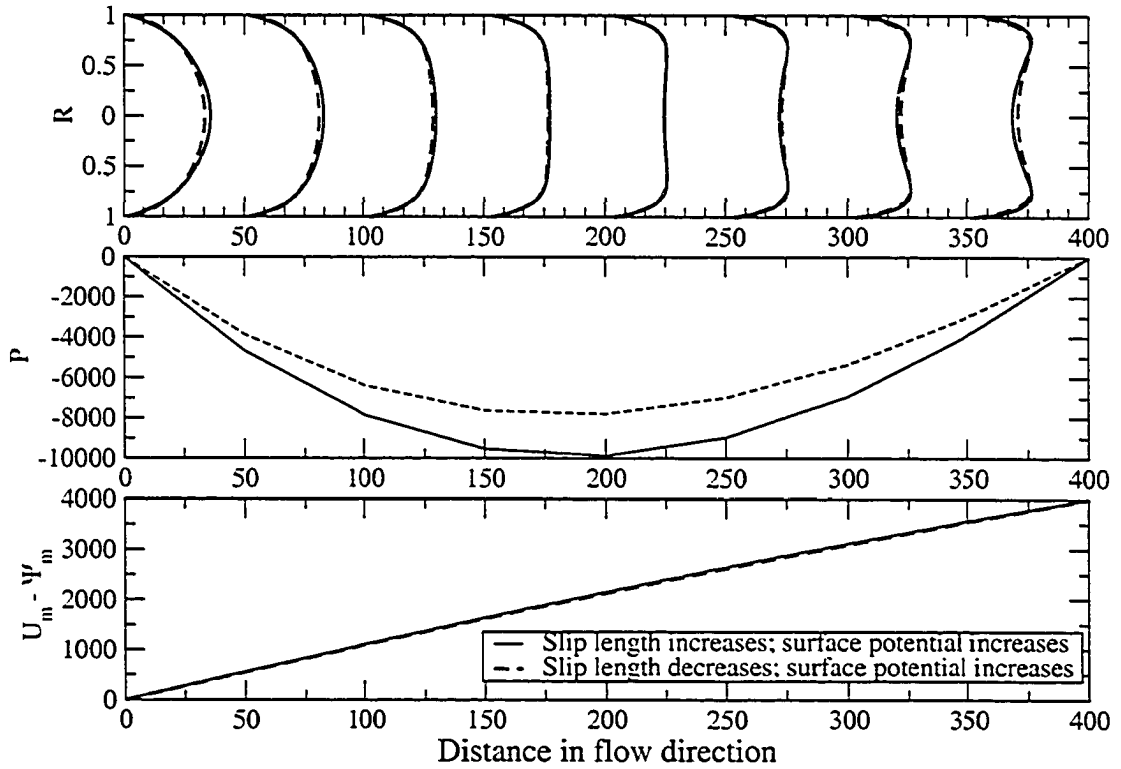
Figure 4.7: The velocity profile $|V^*|$, pressure and potential distributions in the nonuniform microchannel for $K = 10$ at $\Omega = 0$, for electric field driven flow.

membranes with two or three layers, they theoretically established a relationship between the global streaming potential of multilayer membranes and that of individual layers. Good agreement was obtained between the experimental data and those from theoretical considerations. In the case of streaming potential, we extend their work here and provide a more general solution for the velocity, pressure, electric field distribution, current and flow rate in each layer of a multilayer membrane. In addition, electroosmosis is also a popular method to determine zeta potential of membrane [129, 130, 131, 132, 133]. Due to the requirement of flow rate and current continuity, pressure gradients are induced inside each layer during electroosmosis and it is necessary to understand the pressure distribution inside a multilayer membrane. Thus,

110

we also extend our model to describe electroosmosis (electric-field-driven flow). Since an alternating electric or time-dependent pressure field can be used to characterize such membranes [136], we have expressed our oscillating solutions for more general time-dependent problems through superposition of time-harmonic solutions weighted by the appropriate Fourier coefficients. A formula for zeta potential measurements of multilayer membranes by streaming potential or electroosmosis measurements is also proposed. We find that the oscillating responses of multilayer membranes could allow determination of all features of each layer. Changing the frequency of oscillations as input, one would have enough information to solve for all properties for each layer. A non-destructive frequency determination method for zeta potentials could also be developed for unknown multilayer membranes.
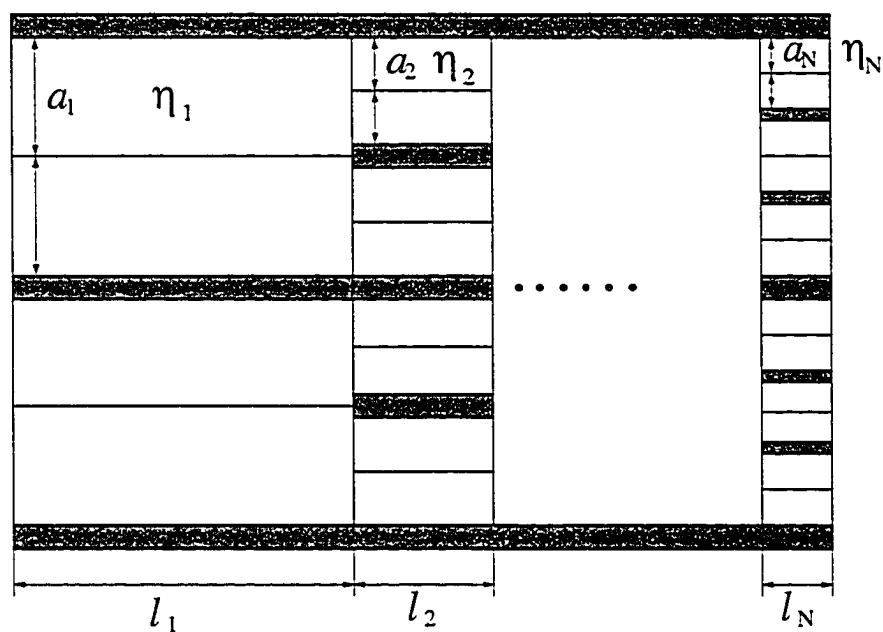
Figure 4.8: The schematic of multilayer membrane

111

4.4.2 Pressure and potential distribution in a multilayer membrane

For a multilayer membrane with N layers (Figure4.8), we assume that each pore in each layer has the same property. For an individual pore in mth layer (subscript m imply quantities relate to mth layer), we consider the boundary value problem for oscillating electrolyte flow though it driven by oscillating pressure gradient and electric field; local cylindrical coordinate systems (r, θ, z) are used where the z-axis is taken to coincide with the pore central axis. Because of the heterogeneity of multilayer membranes, each layer has its own parameters: the normalized pressure gradient, P_m^*, the normalized strength of electric field, $E_{z,m}^*$, zeta potential, ζ_m, radius of pore, a_m, porosity, η_m, the amount of pores, N_m, thickness of mth layer of membrane, l_m, the normalized thickness of mth layer of membrane, L_m, and the normalized total thickness L. For brevity, we ignore the difference between surface potential and zeta potential.

Basically, we can consider a multilayer membrane as many nonuniform circular microchannels. Each layer of the multilayer membrane corresponds to each section of the nonuniform microchannels. We should note that the number of microchannels and the radius of each layer are different. But, flow rate and current continuity should be always satisfied. For each layer, $E_{z,m}^*$ and P_m^* are field quantities and uniform in every pores. $I_{P,m}^*$, $I_{E,m}^*$, $Q_{P,m}^*$ and $Q_{E,m}^*$ are additive. For the whole membrane, the total current and flow rate of one layer are the same as those of other layers due to continuity of current and flow rate. The total pressure drop and potential drop of multilayer membrane are the summation of each layer. So, we have the following relationship.

$$\frac{N_1}{N_m} = \frac{\eta_1}{\eta_m} \frac{a_m^2}{a_1^2} , \qquad (4.4.1)$$

$$Q_{total} = Re[Q_{total}^* e^{j\Omega \tau}] = Re[N_m(Q_{P,m}^*(\Omega)P_m^*(\Omega) + Q_{E,m}^*(\Omega)E_{z,m}^*(\Omega))e^{j\Omega \tau}] , \quad (4.4.2)$$

112

$$I_{total} = Re[I^*_{total}e^{j\Omega\tau}] = Re[N_m(I^*_{P,m}(\Omega)P^*_m(\Omega) + I^*_{E,m}(\Omega)E^*_{z,m}(\Omega))e^{j\Omega\tau}] \, , \quad (4.4.3)$$

$$\Delta P = Re[P^*Le^{j\Omega\tau}] = Re[\sum_{m=1}^{N} P^*_m L_m e^{j\Omega\tau}] \, , \quad (4.4.4)$$

$$\Delta U = Re[E^*_z Le^{j\Omega\tau}] = Re[\sum_{m=1}^{N} E^*_{z,m} L_m e^{j\Omega\tau}] \, . \quad (4.4.5)$$

Based on those Eqs. 4.4.1 – 4.4.5, we can determine the relationship of the normalized pressure gradient and strength of electric field between all layers. We will express all quantities as functions of the corresponding quantities of the first layer.

Streaming potential (pressure driven flow)

In this case, known input is total pressure gradient P^*. At equilibrium, Eq. 2.2.29 becomes

$$E^*_{z,m} = -\frac{I^*_{P,m}}{I^*_{E,m}}P^*_m \quad (m = 1......N) \, . \quad (4.4.6)$$

Continuity of current is satisfied automatically. From Eq.4.4.2, we have

$$N_m(Q^*_{P,m}(\Omega)P^*_m(\Omega) + Q^*_{E,m}E^*_{z,m}) = N_1(Q^*_{P,1}(\Omega)P^*_1(\Omega) + Q^*_{E,1}E^*_{z,1}) \, . \quad (4.4.7)$$

Substituting Eq. 4.4.6 in Eq. 4.4.7, we can find the relationship between the pressure gradient in the mth layer and that of the first layer,

$$P^*_m = \frac{N_1}{N_m}\frac{Q^*_{P,1} - \frac{(I^*_{P,1})^2}{I^*_{E,1}}}{Q^*_{P,m} - \frac{(I^*_{P,m})^2}{I^*_{E,m}}}P^*_1 \quad (4.4.8)$$

From Eq. 4.4.4, we have

$$P^*L = P^*_1 \sum_{m=1}^{N} L_m \frac{N_1}{N_m}\frac{Q^*_{P,1} - \frac{(I_{P,1})^2}{I_{E,1}}}{Q^*_{P,m} - \frac{(I_{P,m})^2}{I_{E,m}}} \quad (4.4.9)$$

According to known pressure gradient, we can solve the pressure gradient of every layer. The total streaming potential (potential drop) should be the summation of

113

potential drop in each layer,

$$E_z^* = P^* \sum_{m=1}^{N} \left[-L_m \frac{I_{P,m}^*}{I_{E,m}^*} \frac{N_1}{N_m} \frac{Q_{P,1}^* - \frac{(I_{P,1})^2}{I_{E,1}}}{Q_{P,m}^* - \frac{(I_{P,m})^2}{I_{E,m}}} \quad \frac{1}{\sum_{m=1}^{N} L_m \frac{N_1}{N_m} \frac{Q_{P,1}^* - \frac{(I_{P,1})^2}{I_{E,1}}}{Q_{P,m}^* - \frac{(I_{P,m})^2}{I_{E,m}}}} \right] . \quad (4.4.10)$$

Electroosmosis (electric field driven flow)

In this case, known inputs are total strength of electric field and pressure gradient (Normally, we open the both sides of electroosmotic system in atmosphere to eliminate effect of hydrostatic so that $P^* = 0$). Continuities of current and flow rate can be expressed as

$$N_m(Q_{P,m}^*(\Omega)P_m^*(\Omega) + Q_{E,m}^* E_{z,m}^*) = N_1(Q_{P,1}^*(\Omega)P_1^*(\Omega) + Q_{E,1}^* E_{z,1}^*) , \quad (4.4.11)$$

$$N_m(I_{P,m}^*(\Omega)P_m^*(\Omega) + I_{E,m}^* E_{z,m}^*) = N_1(I_{P,1}^*(\Omega)P_1^*(\Omega) + I_{E,1}^* E_{z,1}^*) . \quad (4.4.12)$$

Note that $Q_{E,m}^* = I_{P,m}$. P_m^* and E_m^* can be solved from Eqs. 4.4.11 and 4.4.12

$$P_m^* = \frac{N_1}{N_m} \frac{I_{P,m}^* I_{P,1}^* - I_{E,m}^* Q_{P,1}^*}{(I_{P,m}^*)^2 - I_{E,m}^* Q_{P,m}^*} P_1^* + \frac{N_1}{N_m} \frac{I_{P,m}^* I_{E,1}^* - I_{E,m}^* I_{P,1}^*}{(I_{P,m}^*)^2 - I_{E,m}^* Q_{P,m}^*} E_{z,1}^* , \quad (4.4.13)$$

$$E_{z,m}^* = \frac{N_1}{N_m} \frac{I_{P,m}^* Q_{P,1}^* - Q_{P,m}^* I_{P,1}^*}{(I_{P,m}^*)^2 - I_{E,m}^* Q_{P,m}^*} P_1^* + \frac{N_1}{N_m} \frac{I_{P,m}^* I_{P,1}^* - Q_{P,m}^* I_{E,1}^*}{(I_{P,m}^*)^2 - I_{E,m}^* Q_{P,m}^*} E_{z,1}^* , \quad (4.4.14)$$

Following Eqs. 4.4.4 and 4.4.5, we can obtain a set of equations

$$P^* L = P_1^* \sum_{m=1}^{N} L_m \frac{N_1}{N_m} \frac{I_{P,m}^* I_{P,1}^* - I_{E,m}^* Q_{P,1}^*}{(I_{P,m}^*)^2 - I_{E,m}^* Q_{P,m}^*} + E_{z,1}^* \sum_{m=1}^{N} L_m \frac{N_1}{N_m} \frac{I_{P,m}^* I_{E,1}^* - I_{E,m}^* I_{P,1}^*}{(I_{P,m}^*)^2 - I_{E,m}^* Q_{P,m}^*} ,$$

$$(4.4.15)$$

$$E_z^* L = P_1^* \sum_{m=1}^{N} L_m \frac{N_1}{N_m} \frac{I_{P,m}^* Q_{P,1}^* - Q_{P,m}^* I_{P,1}^*}{(I_{P,m}^*)^2 - I_{E,m}^* Q_{P,m}^*} + E_{z,1}^* \sum_{m=1}^{N} L_m \frac{N_1}{N_m} \frac{I_{P,m}^* I_{P,1}^* - Q_{P,m}^* I_{E,1}^*}{(I_{P,m}^*)^2 - I_{E,m}^* Q_{P,m}^*} .$$

$$(4.4.16)$$

For brevity, let's write Eqs. 4.4.16 and 4.4.16 as

$$P^* L = A_{11}' P_1^* + A_{12}' E_{z,1}^* , \quad (4.4.17)$$

$$E_z^* L = A_{21}' P_1^* + A_{22}' E_{z,1}^* , \quad (4.4.18)$$

114

where

$$A'_{11} = \sum_{m=1}^{N} L_m \frac{N_1}{N_m} \frac{I^*_{P,m}I^*_{P,1} - I^*_{E,m}Q^*_{P,1}}{(I^*_{P,m})^2 - I^*_{E,m}Q^*_{P,m}} \, ,$$

$$A'_{12} = \sum_{m=1}^{N} L_m \frac{N_1}{N_m} \frac{I^*_{P,m}I^*_{E,1} - I^*_{E,m}I^*_{P,1}}{(I^*_{P,m})^2 - I^*_{E,m}Q^*_{P,m}} \, ,$$

$$A'_{21} = \sum_{m=1}^{N} L_m \frac{N_1}{N_m} \frac{I^*_{P,m}Q^*_{P,1} - Q^*_{P,m}I^*_{P,1}}{(I^*_{P,m})^2 - I^*_{E,m}Q^*_{P,m}} \, ,$$

$$A'_{22} = \sum_{m=1}^{N} L_m \frac{N_1}{N_m} \frac{I^*_{P,m}I^*_{P,1} - Q^*_{P,m}I^*_{E,1}}{(I^*_{P,m})^2 - I^*_{E,m}Q^*_{P,m}} \, . \tag{4.4.19}$$

Solving the above two equations, we can obtain

$$P^*_1 = \frac{A'_{22}L}{A'_{11}A'_{22} - A'_{21}A'_{12}}P^* - \frac{A'_{12}L}{A'_{11}A'_{22} - A'_{21}A'_{12}}E^*_z \, , \tag{4.4.20}$$

$$E^*_{z,1} = -\frac{A'_{21}L}{A'_{11}A'_{22} - A'_{21}A'_{12}}P^* + \frac{A'_{11}L}{A'_{11}A'_{22} - A'_{21}A'_{12}}E^*_z \, , \tag{4.4.21}$$

Then, $E^*_{z,m}$ and P^*_m could be

$$P^*_m = \frac{N_1}{N_m} \frac{I^*_{P,m}I^*_{P,1} - I^*_{E,m}Q^*_{P,1}}{(I^*_{P,m})^2 - I^*_{E,m}Q^*_{P,m}} \left(\frac{A'_{22}L}{A'_{11}A'_{22} - A'_{21}A'_{12}}P^* - \frac{A'_{12}L}{A'_{11}A'_{22} - A'_{21}A'_{12}}E^*_z \right)$$

$$+ \frac{N_1}{N_m} \frac{I^*_{P,m}I^*_{E,1} - I^*_{E,m}I^*_{P,1}}{(I^*_{P,m})^2 - I^*_{E,m}Q^*_{P,m}} \left(-\frac{A'_{21}L}{A'_{11}A'_{22} - A'_{21}A'_{12}}P^* + \frac{A'_{11}L}{A'_{11}A'_{22} - A'_{21}A'_{12}}E^*_z \right) , \tag{4.4.22}$$

$$E^*_{z,m} = \frac{N_1}{N_m} \frac{I^*_{P,m}Q^*_{P,1} - Q^*_{P,m}I^*_{P,1}}{(I^*_{P,m})^2 - I^*_{E,m}Q^*_{P,m}} \left(\frac{A'_{22}L}{A'_{11}A'_{22} - A'_{21}A'_{12}}P^* - \frac{A'_{12}L}{A'_{11}A'_{22} - A'_{21}A'_{12}}E^*_z \right)$$

$$+ \frac{N_1}{N_m} \frac{I^*_{P,m}I^*_{P,1} - Q^*_{P,m}I^*_{E,1}}{(I^*_{P,m})^2 - I^*_{E,m}Q^*_{P,m}} \left(-\frac{A'_{21}L}{A'_{11}A'_{22} - A'_{21}A'_{12}}P^* + \frac{A'_{11}L}{A'_{11}A'_{22} - A'_{21}A'_{12}}E^*_z \right) , \tag{4.4.23}$$

If both sides of electroosmotic system open to atmosphere, which implies $P^* = 0$, we can know from Eq. 4.4.22 that $P^*_m \neq 0$. Because of the heterogeneity of multilayer membranes, pressure gradients are induced to make the continuities of current and flow rate. We also can derive expressions of total current I^*_{total} and total flow rate Q^*_{total}, which are measurable by experiments.

$$I^*_{total} = N_m(I^*_{P,m}P^*_m + I^*_{E,m}E^*_{z,m}) \, , \tag{4.4.24}$$

$$Q^*_{total} = N_m(Q^*_{P,m}P^*_m + I^*_{P,m}E^*_{z,m}) \, . \tag{4.4.25}$$

115

Note that N_m is measurable or calculable by $N_m = \frac{n_m S}{\pi a_m^2}$, where S is the area of the multilayer membrane. Let's focus on a common electroosmosis experimental system with $P^* = 0$.

$$I_{total}^* = N_1 \frac{(A_{11}' I_{E,1}^* - A_{12}' I_{P,1}^*)L}{A_{11}' A_{22}' - A_{21}' A_{12}'} E_z^* \,, \qquad (4.4.26)$$

$$Q_{total}^* = N_1 \frac{(A_{11}' I_{P,1}^* - A_{12}' Q_{P,1}^*)L}{A_{11}' A_{22}' - A_{21}' A_{12}'} E_z^* \,, \qquad (4.4.27)$$

$$\frac{Q_{total}^*}{I_{total}^*} = \frac{A_{11}' I_{P,1}^* - A_{12}' Q_{P,1}^*}{A_{11}' I_{E,1}^* - A_{12}' I_{P,1}^*} \,. \qquad (4.4.28)$$

Eq. 4.4.28 is a function of frequency Ω, which includes all information of each layer, such as zeta potential, thickness, porosity and pore size.

4.4.3 A nondestructive method to characterize an unknown multilayer membrane by oscillating electric fields

For better relating the following discussion to the real experiments, we give out dimensional quantities of velocity, flow rate and current of mth section:

$$v_{P,m}^*(r,\omega) = \frac{1}{j\omega\rho_d}\left[1 - \frac{J_0\left(r\sqrt{\frac{-j\omega}{\nu}}\right)}{J_0\left(a_m\sqrt{\frac{-j\omega}{\nu}}\right)}\right] \,, \qquad (4.4.29)$$

$$v_{E,m}^*(r,\omega) = \frac{\epsilon\kappa^2\zeta_m}{(\kappa^2\nu - j\omega)\rho_d}\left[\frac{J_0(j\kappa r)}{J_0(j\kappa a_m)} - \frac{J_0\left(r\sqrt{\frac{-j\omega}{\nu}}\right)}{J_0\left(a_m\sqrt{\frac{-j\omega}{\nu}}\right)}\right] \,, \qquad (4.4.30)$$

$$i_{P,m}^*(\omega) = \frac{2\pi\epsilon\kappa^2\zeta_m}{\rho_d}\left\{\frac{a_m}{\omega\kappa}\frac{J_1(j\kappa a_m)}{J_0(j\kappa a_m)}\right.$$
$$\left. - \frac{\nu a_m}{\omega^2 + j\omega\kappa^2\nu}\left[j\kappa\frac{J_1(j\kappa a_m)}{J_0(j\kappa a_m)} - \sqrt{\frac{-j\omega}{\nu}}\frac{J_1\left(a_m\sqrt{\frac{-j\omega}{\nu}}\right)}{J_0\left(a_m\sqrt{\frac{-j\omega}{\nu}}\right)}\right]\right\} \qquad (4.4.31)$$

116

$$i_{E,m}^*(\omega) = \frac{-2\pi\epsilon^2\kappa^4\zeta_m^2}{(\kappa^2\nu - j\omega)\rho_d}\left\{\frac{a_m^2}{2}\left[1 + \frac{J_1^2(j\kappa a_m)}{J_0^2(j\kappa a_m)}\right] - \frac{\nu a_m}{j\omega - \kappa^2\nu}\right.$$

$$\left. \times \left[j\kappa\frac{J_1(j\kappa a_m)}{J_0(j\kappa a_m)} - \sqrt{\frac{-j\omega}{\nu}}\frac{J_1\left(a_m\sqrt{\frac{-j\omega}{\nu}}\right)}{J_0\left(a_m\sqrt{\frac{-j\omega}{\nu}}\right)}\right]\right\} + \pi a_m^2\sigma_m \ , \quad (4.4.32)$$

$$q_{P,m}^*(\omega) = \frac{2\pi}{j\omega\rho_d}\left[\frac{a_m^2}{2} - \frac{a_m}{\sqrt{\frac{-j\omega}{\nu}}}\frac{J_1\left(a_m\sqrt{\frac{-j\omega}{\nu}}\right)}{J_0\left(a_m\sqrt{\frac{-j\omega}{\nu}}\right)}\right] \ , \quad (4.4.33)$$

$$q_{E,m}^*(\omega) = I_{P,m}^*(\omega) \ . \quad (4.4.34)$$

where J_0, J_1, ρ_d, ν and σ are the zeroth- and first-order Bessel functions of the first kind, liquid density, kinematic viscosity and conductivity of electrolyte. We can find $q_{E,m}^* = i_{P,m}^*$, which satisfies Onsager's theorem [53].

When $\omega \to 0$, Eqs.(4.4.29)-(4.4.34) reduces to those of steady state.

$$v_{P,m}^*(r,0) = \frac{1}{4\nu\rho_d}(a_m^2 - r^2) \ ,$$

$$v_{E,m}^*(r,0) = -\frac{\epsilon\zeta_m}{\nu\rho_d}\left(1 - \frac{J_0(j\kappa r)}{J_0(j\kappa a_m)}\right) \ ,$$

$$i_{P,m}^*(0) = -\frac{\epsilon\zeta_m\pi a^2}{\nu\rho_d}\left[1 - \frac{2}{j\kappa a_m}\frac{J_1(j\kappa a_m)}{J_0(j\kappa a_m)}\right] \ ,$$

$$i_{E,m}^*(0) = -\frac{\epsilon^2\zeta_m^2\pi a_m^2\kappa^2}{\nu\rho_d}\left[1 - \frac{2}{j\kappa a_m}\frac{J_1(j\kappa a_m)}{J_0(j\kappa a_m)} + \frac{J_1^2(j\kappa a_m)}{J_0^2(j\kappa a_m)}\right] + \pi a_m^2\sigma_m \ ,$$

$$q_{P,m}^*(0) = \pi a_m^2\frac{a_m^2}{8\nu\rho_d} \ ,$$

$$q_{E,m}^*(0) = -\frac{\epsilon\zeta_m\pi a_m^2}{\nu\rho_d}\left[1 + 2\frac{jJ_1(j\kappa a_m)}{\kappa a_m J_0(j\kappa a_m)}\right] = I_{P,m}^*(0) \ . \quad (4.4.35)$$

In the next parametric study, we mainly use dimensional quantities. All derivation in section 4.4.2 can be easily used instead of corresponding dimensional quantities.

Here, we use a typical three layer membrane as an example, which has those parameters Table 4.5 For parametric study, those parameters are determined: $\epsilon = 7.0832 \times 10^{-10}$ C/V m, $\rho = 1 \times 10^3$ kg/m^3, $\mu = 0.9 \times 10^{-3}$ kg/ms, $\nu = 0.9 \times 10^{-6}$ m^{2}s^{-1}, $e = 1.6021 \times 10^{-19}$ C, $k = 1.3805 \times 10^{-23}$ J/molK and $T = 298$ K. We choose 0.1 M KCl as testing solution. Its conductivity $\sigma = 1.28217$ S/m [118].

117

Table 4.5: Physical and chemical properties of multilayer membrane

	Support layer (layer 1)	Intermediate layer (layer 2)	Skin layer (layer 3)
Thickness (mm)	1	0.5	0.1
Mean pore size (μm)	10	1	0.1
Porosity	30%	25%	20%

4.4.4 Pressure and electric field distribution under streaming potential

Assuming total pressure gradient $p^* = 10^8$ Pa/m, if $\zeta_1 = -100$ mV, $\zeta_2 = -50$ mV and $\zeta_3 = -75$ mV, we calculate the complex streaming potentials for $\omega = 50, 5000, 500000$ Hz in Table 4.6, where we define $-\partial p/\partial z = Re[p^* e^{j\omega t}]$ and $E'_z = Re[E'^*_z e^{j\omega t}]$. From

Table 4.6: Frequency-dependent the electric field strength of streaming potentials for $\zeta_1 = -100$ mV, $\zeta_2 = -50$ mV and $\zeta_3 = -75$ mV multilayer membrane

	E'^*_z (V/m)	$|E'^*_z|$(V/m)	phase angle of E'^*_z (degree)
$\omega = 50$ Hz	$-4.35432 + 3.24187 \times 10^{-6} j$	4.35432	180
$\omega = 5000$ Hz	$-4.35432 + 0.00032421 j$	4.35432	179.996
$\omega = 500000$ Hz	$-4.35482 + 0.033604 j$	4.35495	179.558

Table 4.6. We see that when the input frequency changes from 50 to 500000 Hz, the total streaming potential changes slightly. This implies that a traditional (steady state) model can be used to determine the streaming potential by means of only the amplitudes of the properties even when a high frequency oscillation pressure is used. We note that if the difference in amplitude and phase angle can be detected, one can solve the set of equations for all the unknown parameters. Since zeta potential is the most important chemical property of membrane, we study here how zeta potential of each layer affects the streaming potential, pressure and electric field distributions in Table 4.7.

It is noted that when zeta potential of each layer are interchanged, the pressure

118

Table 4.7: Pressure gradient (Pa/m) and electric field strength (V/m) in multilayer membrane ($p* = 10^8$ Pa/m, $\omega = 0$ Hz)

	Layer 1	Layer 2	Layer 3	E'_z (V/m)
$\zeta_1 = -100$ mV, $\zeta_2 = -50$ mV, $\zeta_3 = -75$ mV	$p_1 = 102318$, $E'_{z,1} = -0.6276 \times 10^{-2}$	$p_2 = 1.2278 \times 10^7$, $E'_{z,2} = -0.3757$	$p_3 = 1.5376 \times 10^9$, $E'_{z,3} = -67.7$	−4.35432
$\zeta_1 = -100$ mV, $\zeta_2 = -75$ mV, $\zeta_3 = -50$ mV	$p_1 = 102417$, $E'_{z,1} = -0.628 \times 10^{-2}$	$p_2 = 1.229 \times 10^7$, $E'_{z,2} = -0.5633$	$p_3 = 1.53752 \times 10^9$, $E'_{z,3} = -45.77$	−3.04051
$\zeta_1 = -50$ mV, $\zeta_2 = -100$ mV, $\zeta_3 = -75$ mV	$p_1 = 102317$, $E'_{z,1} = -0.3139 \times 10^{-2}$	$p_2 = 1.2279 \times 10^7$, $E'_{z,2} = -0.7489$	$p_3 = 1.5376 \times 10^9$, $E'_{z,3} = -67.73$	−4.46897
$\zeta_1 = -50$ mV, $\zeta_2 = -75$ mV, $\zeta_3 = -100$ mV	$p_1 = 102183$, $E'_{z,1} = -0.3135 \times 10^{-2}$	$p_2 = 1.226 \times 10^7$, $E'_{z,2} = -0.562$	$p_3 = 1.5377 \times 10^9$, $E'_{z,3} = -88.63$	−5.717
$\zeta_1 = -75$ mV, $\zeta_2 = -50$ mV, $\zeta_3 = -100$ mV	$p_1 = 102183$, $E'_{z,1} = -0.47 \times 10^{-2}$	$p_2 = 1.226 \times 10^7$, $E'_{z,2} = -0.375$	$p_3 = 1.5377 \times 10^9$, $E'_{z,3} = -88.63$	−5.6596
$\zeta_1 = -75$ mV, $\zeta_2 = -100$ mV, $\zeta_3 = -50$ mV	$p_1 = 102417$, $E'_{z,1} = -0.4713 \times 10^{-2}$	$p_2 = 1.229 \times 10^7$, $E'_{z,2} = -0.7544$	$p_3 = 1.5375 \times 10^9$, $E'_{z,3} = -45.769$	−3.0978

gradient and electric field would be different. These results are also plotted in Figure 4.9 for the pressure distribution and Figure 4.10 for electric field distribution. In this case, when zeta potential of each layer interchanges, the pressure changes slightly, but not the electric field distribution. From this specific example, we obtain a larger streaming potential when $\zeta_3 = -100$ mV, suggesting that the skin layer (layer 3) significantly controls the electrokinetic property of this multilayer membrane.

4.4.5 Pressure and electric field under electroosmosis

Assuming $p^* = 0$ (this is true for most electroosmosis experiments) and $E''_z = 10^5$ V/m, if $\zeta_1 = -100$ mV, $\zeta_2 = -50$ mV and $\zeta_3 = -75$ mV, we calculate the complex q_{total}/i_{total} from Eq. 4.4.28 for $\omega = 50, 5000, 500000$ Hz Table 4.8. Because electroosmosis is often used to measure zeta potential, polarization of electrodes and/or concentration polarization on the membrane surface can become the major influencing factor of experimental error [136, 137]. Experience has shown that the effective way to prevent electrodes from polarizing is to use an alternating electric field as input. A traditional (steady state) formula is often employed to calculate the zeta

119

Pressure driven flow
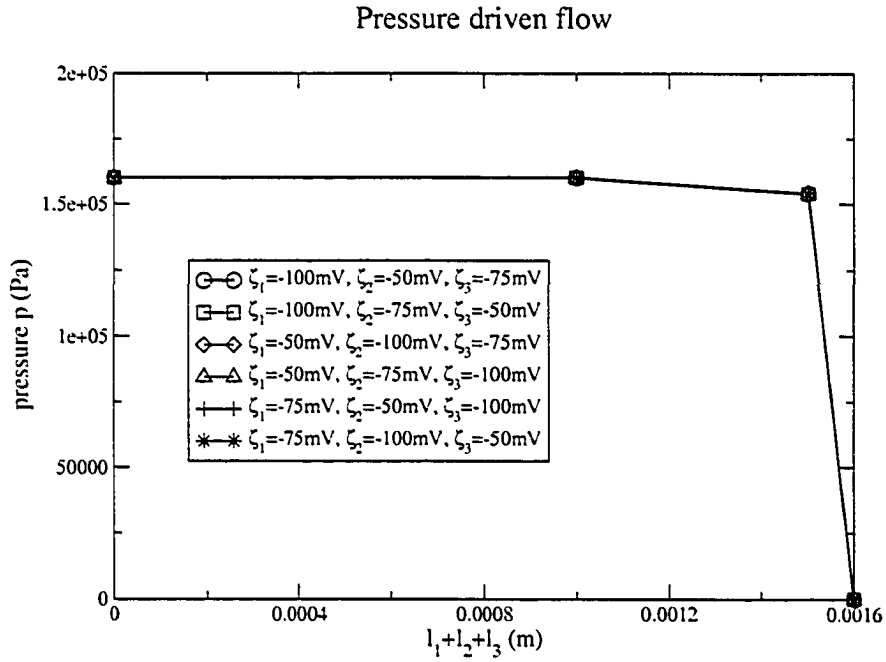
Figure 4.9: Pressure distribution in a three-layer multilayer membrane for pressure-driven flow at $\omega = 0$ Hz, where each layer has a different ζ potential.

potential, as in [136, 137]. From Table 4.8, we find that frequency is not a strong function of the amplitudes for the properties in consideration. Thus, a steady state formula can in principle be used.

Normally, electroosmotic experiments are opened to the atmosphere for a hydrostatic equilibrium. However, because of the heterogeneity of multilayer membrane, a pressure gradient is induced to maintain the current and flow rate continuities. In Table 4.9, we study the pressure and electric field distribution of multilayer membrane

Table 4.8: Frequency-dependent q_{total}/i_{total} for a three-layer multilayer membrane where $\zeta_1 = -100$ mV, $\zeta_2 = -50$ mV and $\zeta_3 = -75$ mV.

	q_{total}/i_{total} (m^3/sA)	$\lvert q_{total}/i_{total}\rvert$ (m^3/sA)	phase angle of $\frac{q_{total}}{i_{total}}$ (degree)
$\omega = 50$ Hz	$4.35432 \times 10^{-8} - 3.24187 \times 10^{-14}j$	4.35432×10^{-8}	-0.0000426578
$\omega = 5000$ Hz	$4.35432 \times 10^{-8} - 3.24207 \times 10^{-12}j$	4.35432×10^{-8}	-0.004266
$\omega = 500000$ Hz	$4.35495 \times 10^{-8} - 3.36 \times 10^{-10}j$	4.35495×10^{-8}	-0.44212

120

Pressure driven flow
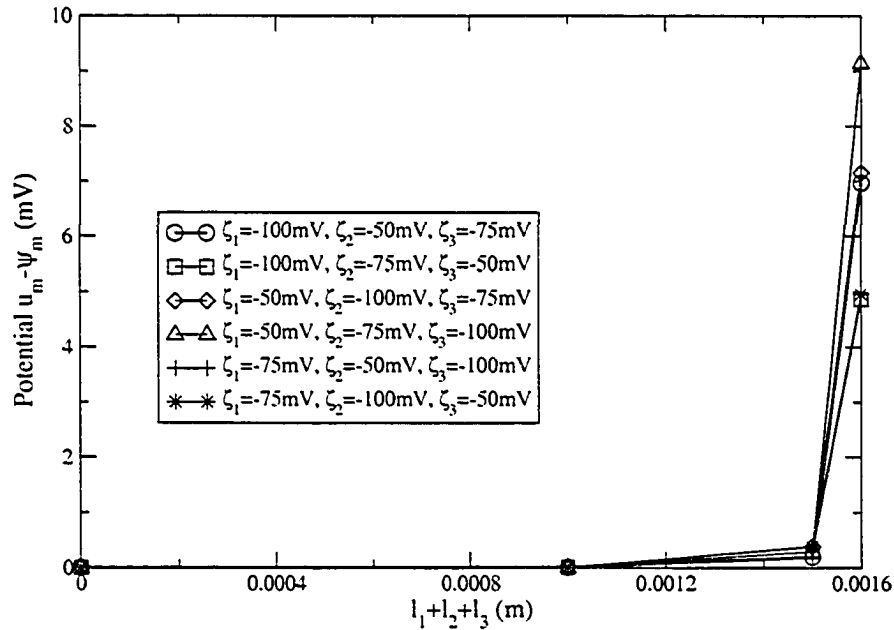
Figure 4.10: Electric field distribution in a three-layer multilayer membrane for pressure-driven flow at $\omega = 0$ Hz, where each layer has a different ζ potential.

and find that such pressure gradient can be as high as 10^8 Pa/m.

From Table 4.9, when zeta potentials of each layer interchanges, the pressure gradient and electric field would change. These results are also plotted in Figure 4.11 for pressure distribution and Figure 4.12 for electric field distribution. When zeta potential of each layer interchanges, the electric field changes slightly, but not the pressure distribution. From the results in this specific example, a larger ratio of flow rate to current is obtained when $\zeta_3 = -100$ mV, suggesting that the property of the skin layer dominates the electrokinetic feature of multilayer membrane and the support layer has less influence on the total electrokinetic flow. From Tables 4.6–4.9, we find that the values of $E_z'^*$ are the same as those of q_{total}/i_{total}, implying that the total quantities of a multilayer membrane also satisfy the well-known Onsager's principle of reciprocity [53].

121

Table 4.9: Pressure gradient (Pa/m) and electric field strength (V/m) in a three-layer multilayer membrane with $p^* = 0$, $E_z'^* = 10^5$ V/m and $\omega = 0$ Hz.

	Layer 1	Layer 2	Layer 3	$\frac{q_{total}}{I_{total}}$ (m^3/sA)
$\zeta_1 = -100$ mV, $\zeta_2 = -50$ mV, $\zeta_3 = -75$ mV	$p_1 = -150644$, $E_{z,1}' = 91637$	$p_2 = 1.31481 \times 10^7$, $E_{z,2}' = 109891$	$p_3 = -6.4234 \times 10^7$, $E_{z,3}' = 134174$	4.35432×10^{-8}
$\zeta_1 = -100$ mV, $\zeta_2 = -75$ mV, $\zeta_3 = -50$ mV	$p_1 = -261661$, $E_{z,1}' = 91576$	$p_2 = -1.5657 \times 10^7$, $E_{z,2}' = 109665$	$p_3 = 8.09 \times 10^7$, $E_{z,3}' = 135916$	3.04051×10^{-8}
$\zeta_1 = -50$ mV, $\zeta_2 = -100$ mV, $\zeta_3 = -75$ mV	$p_1 = 118669$, $E_{z,1}' = 91755.6$	$p_2 = -1.657 \times 10^7$, $E_{z,2}' = 109630$	$p_3 = 8.167 \times 10^7$, $E_{z,3}' = 134295$	4.46897×10^{-8}
$\zeta_1 = -50$ mV, $\zeta_2 = -75$ mV, $\zeta_3 = -100$ mV	$p_1 = 224597$, $E_{z,1}' = 91837.5$	$p_2 = 1.15368 \times 10^7$, $E_{z,2}' = 109940$	$p_3 = -5.993 \times 10^7$, $E_{z,3}' = 131925$	5.71702×10^{-8}
$\zeta_1 = -75$ mV, $\zeta_2 = -50$ mV, $\zeta_3 = -100$ mV	$p_1 = 89673.9$, $E_{z,1}' = 91788$	$p_2 = 2.64432 \times 10^7$, $E_{z,2}' = 110049$	$p_3 = -1.33813 \times 10^8$, $E_{z,3}' = 131876$	5.65962×10^{-8}
$\zeta_1 = -75$ mV, $\zeta_2 = -100$ mV, $\zeta_3 = -50$ mV	$p_1 = -127262$, $E_{z,1}' = 91644.5$	$p_2 = -3.05 \times 10^7$, $E_{z,2}' = 109513$	$p_3 = 1.53665 \times 10^8$, $E_{z,3}' = 135989$	3.09775×10^{-8}

Traditional method to measure zeta potential collects only a set of limited data: streaming potential, streaming current and flow rate can be measured by pressure-driven flow (pressure is an input); electroosmotic current and flow rate can be measured by electric-field-driven flow (electric field is an input and pressure drop is zero). Because the pressure gradient and strength of electric field are respectively proportional to the measured quantities in pressure-driven-flow and electric-field-driven flow, one cannot change pressure gradient and strength of electric field directly to obtain more independent equations. Since Eq. 4.4.28 is a complex function of frequency and can be reduced to the form of Eq. 2.2.23, each measurement provides two equations from the amplitude and phase angle of Eq. 2.2.23. Two equations are not enough to determine all details of a multilayer membrane. If one can measure the minor difference (amplitude or phase angle) of any given quantities in terms of frequencies, all information of a multilayer membrane can be determined. This is made possible by providing more equations to determine all parameters in multilayer membranes. This method might be a potential application to determine the properties of an unknown multilayer membrane, including thickness, pore size and zeta potentials of each layer.

122

Electric field driven flow
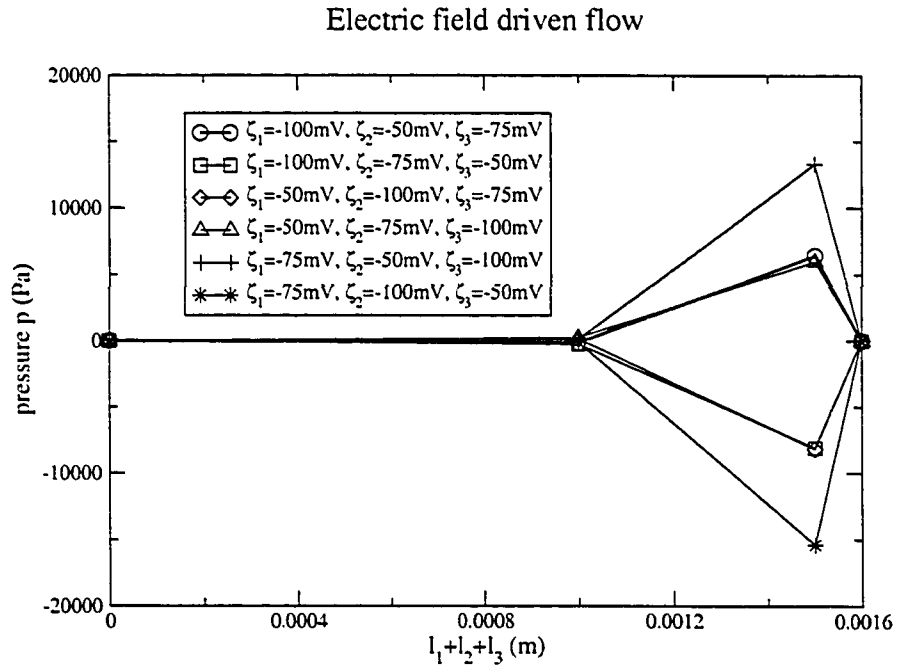
Figure 4.11: Pressure distribution in a three-layer multilayer membrane for electric field driven flow at $\omega = 0$, where each layer has a different ζ potential.

4.5 Conclusions

In this chapter, a model of oscillating electrokinetic flow through a microchannel with nonuniform surface potential and hydrophobicity is created. Our model reflects more details of electrokinetic flow in a nonuniform microchannel. Pressure driven flow (streaming potential) and electric field driven flow (electroosmosis) are studied. According to our solutions, nonlinear pressure distribution and electric field distribution in each section can be obtained. To keep current and flow rate continuity, nonuniform induced electric field (for pressure driven flow) and nonuniform induced pressure distribution (for electric field driven flow) can be predicted by this model. Extending this model to a multilayer membrane, we can predict pressure and potential distribution in every layer of a multilayer membrane. We find that structure's nonuniformity

123

Electric field driven flow
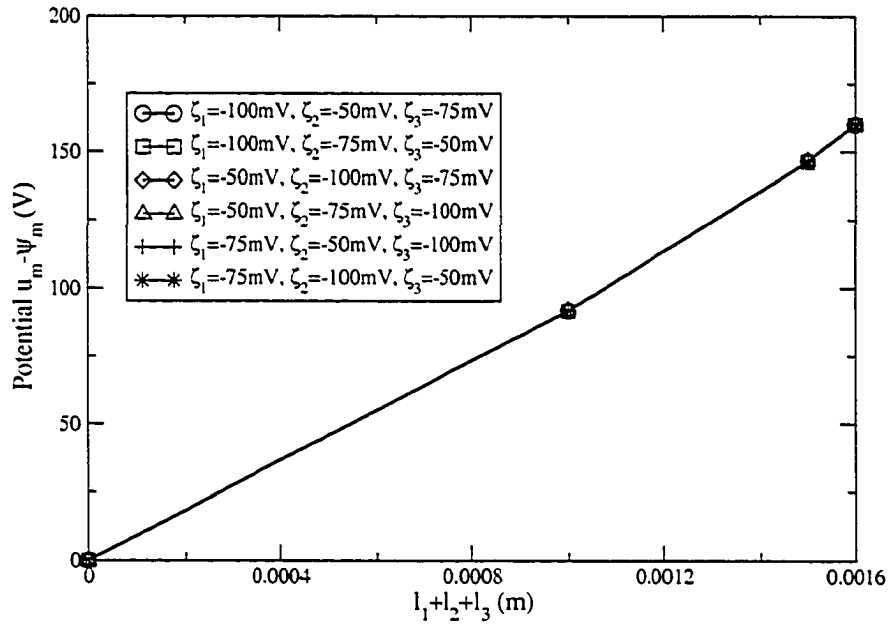
Figure 4.12: Electric field distribution in a three-layer multilayer membrane for electric field driven flow at $\omega = 0$, where each layer has a different ζ potential.

can be reflected by the feedback signals of an oscillating input. So, we propose a nondestructive method to image an unknown multilayer membrane by oscillating electric fields. Obviously, this method can also be used to image a nonuniform microchannel. This model also provides a guide to pattern microchannel surface.

124

Chapter 5

Electrokinetic Microchannel Battery by Means of Streaming Current and Streaming Potential

5.1 Introduction

The conversion of energy from one form to another, or the production of useful work, has long been an important element of engineering and scientific research. The larger goals of research into energy-based systems have been to further develop the technology, better understand any fundamental processes and improve efficiencies. Chemical energy, for example, can be readily converted into mechanical work by classical devices such as internal combustion and steam engines. Similarly, the potential energy of dammed water, and its associated hydrostatic pressure, can be exploited by turbines to be another source of mechanical work. If necessary, electric generators could be employed to convert any produced mechanical work into electrical work. Batteries and fuel cells are devices that avoid the creation of mechanical work and directly convert chemical energy into electrical work. As a green energy source, mechanical energy sources, such as water, wind and tide are always good choices for energy conversion. However, moving parts are needed during these energy conversion processes, which does not match the miniature size requirement of MEMS device. This chapter presents a novel approach and device that is part of this same broad family

125

of energy-based systems, but uses the interactions between electrokinetics and microfluidics to directly convert the hydrostatic pressure of a liquid into electrical work without moving parts. Since the energy source for this device is stored within the potential energy of water and converts it directly to electrical work as the water flows through small diameter channels, it is referred to as an electrokinetic microchannel battery. Initial theoretical discussion of energy conversion in ultrafine capillaries has been done by Morrison and Osterle [138, 139]. This chapter develops the theory for the operation of these devices with external load. Some initial experimental results have been obtained.

Because of the presence of charge distribution in EDL, the microflow can transport net charges from one end of a microchannel to another end. Liquid flow through a microchannel by means of an external pressure gradient can result in a convection current, known as the streaming current, and a streaming potential between two ends of microchannels due to the accumulation of ions or charges. In equilibrium, the conduction current induced by the streaming potential will balance the streaming current so that the total current of the microfluidic system becomes zero. The streaming current is typically on the order of nano amphere per kPa of pressure drop in a single microchannel. Though this magnitude is small, we propose here a method to enlarge such a current. We hypothesize that if more than one microchannel are assembled in parallel, the streaming current are indeed additive and can be significant. With current fabrication technology, it is possible to assemble an array of microchannels with a large surface area to volume ratio. The larger this ratio, the more are the number of movable ions and hence a larger streaming current can result. On the other hand, streaming potential varies at a wide range. Using capacitors to store electric energy, streaming potential can be applied to charge capacitors. Based on a well-designed capacitor circuit and microchannel array, we might obtain a electrokinetic battery to consistently provide electric energy. Alternatively, the requirement of a

126

complex micro/nano-fabrication can be eliminated by using natural porous materials or readily available porous membranes. In this chapter, we propose the concept of an electrokinetic battery which consists of an array of microchannels or a membrane with nanopores. An electrical circuit model of the battery is proposed for more general time-dependent flow in a single microchannel; the results are employed to construct the governing equations for a multichannel model. Good agreement was found between the predicted results and those from experiments for pressure-driven flow in micropore glass filter.

5.2 Electrokinetic flow and electric circuit analysis of a single microchannel

5.2.1 Controlling Equations and Boundary Conditions

We begin by considering a model for pressure-driven and time-dependent electrokinetic flow through a single circular microchannel. For an individual microchannel without an external circuit, (see Figure 5.1), we consider the boundary value problem for oscillating liquid flow in an infinitely extended circular microchannel; R_0 and R_s are the bulk electrolyte and surface resistances, respectively, in a single microchannel. A cylindrical coordinate system (r, θ, z) is used where the z-axis is taken to coincide with the microchannel central axis. All field quantities are taken to depend on the radial coordinate r and time t. The boundary value problem with the relevant field equations and boundary conditions are described below.

To involve the effect of the resistance of microchannel, we re-define current, which is different from 2.3.3 in chapter 2. Then, the electric current density along the microchannel may be integrated over the channel cross-section to give the electric current

$$i = 2\pi \int_0^a \rho v r \, dr + \frac{E_z' l}{\bar{R}} \, , \tag{5.2.1}$$

127

R_S

R_0

i_c

Representative circuit

$+$ $-$

i_c
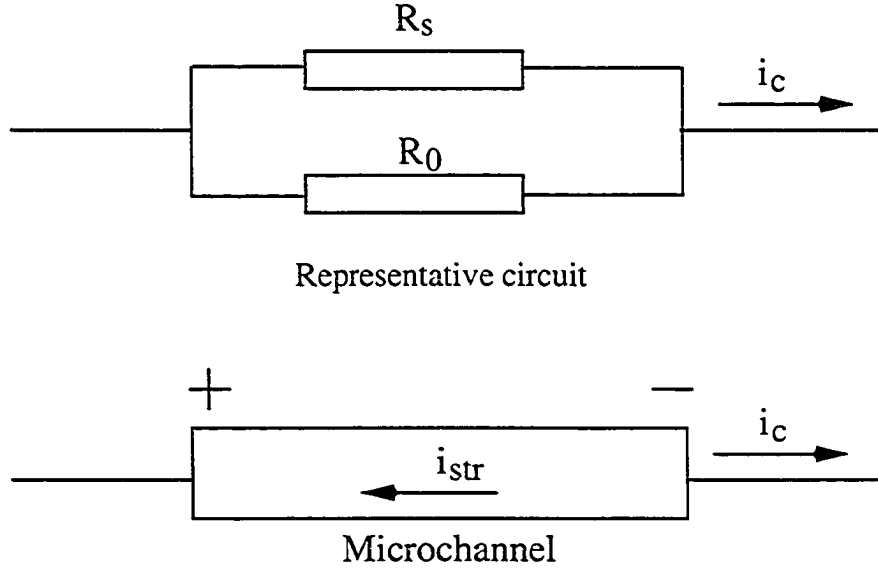
i_{str}

Microchannel

Figure 5.1: Schematic of a single microchannel circuit. i_c and i_{str} are the conduction and streaming currents, respectively; R_0 and R_s are the bulk electrolyte and surface resistances, respectively, in a single microchannel.

where

$$\overline{R} = \frac{R_0 R_s}{R_0 + R_s} \ .$$

$\overline{R}$, R_0, R_s and l are the total resistance, bulk electrolyte resistance, surface resistance and the microchannel length, respectively. The first term on the right side of Eq.(5.2.1) is due to bulk convection and the second term to conduction current. Because of the assumption of an infinitely extended microchannel, the contribution to the current due to concentration gradients vanishes. For a $(z_0 : z_0)$ electrolyte, we have $\rho_1 - \rho_2 = 2ez_0n_\infty \cosh(z_0 e\psi/kT)$. The Debye-Hückel approximation implies that $\cosh(z_0 e\psi/kT) \approx 1$ and $\rho_1 - \rho_2 = 2z_0 en_\infty$. With this simplification, the conductivity of bulk electrolyte, σ, can be written as

$$\sigma = \frac{2z_0^2 e^2 n_\infty D}{kT} \ . \tag{5.2.2}$$

The resistances R_0 and R_s are defined as

$$R_0 = \frac{l}{\sigma \pi a^2} \ , \quad R_s = \frac{l}{\lambda_s P_w} \tag{5.2.3}$$

128

Real and imaginary parts of function (a) and (b)
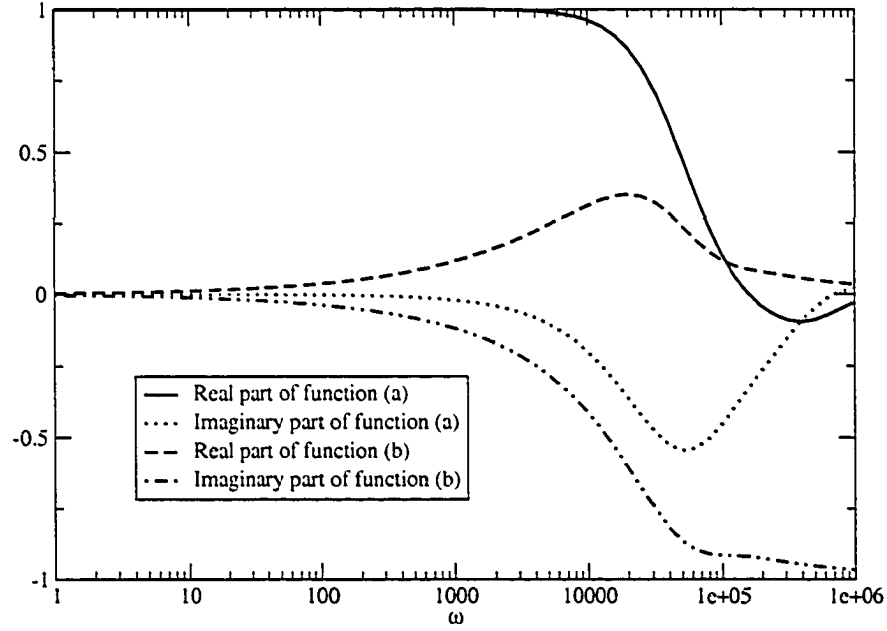
Figure 5.2: Real and imaginary parts of functions (a) $J_0\left(0.5a\sqrt{\frac{-j\omega}{\nu}}\right)/J_0\left(a\sqrt{\frac{-j\omega}{\nu}}\right)$

and (b) $J_1\left(a\sqrt{\frac{-j\omega}{\nu}}\right)/J_0\left(a\sqrt{\frac{-j\omega}{\nu}}\right)$

where λ_s is the surface conductivity and $P_w = 2\pi a$ is the wetted perimeter.

5.2.2 Analytical solution

According to Eqs. 2.3.6, the corresponding dimensional velocity, flow rate and current are listed below

$$v_P^*(r,\omega) = \frac{1}{j\omega\rho_d}\left[1 - \frac{J_0\left(r\sqrt{\frac{-j\omega}{\nu}}\right)}{J_0\left(a\sqrt{\frac{-j\omega}{\nu}}\right)}\right], \qquad (5.2.4)$$

$$v_E^*(r,\omega) = \frac{\epsilon\kappa^2\psi_s}{(\kappa^2\nu - j\omega)\rho_d}\left[\frac{J_0(j\kappa r)}{J_0(j\kappa a)} - \frac{J_0\left(r\sqrt{\frac{-j\omega}{\nu}}\right)}{J_0\left(a\sqrt{\frac{-j\omega}{\nu}}\right)}\right], \qquad (5.2.5)$$

129

$$i_P^*(\omega) = \frac{2\pi\epsilon\kappa^2\psi_s}{\rho_d}\left\{\frac{a}{\omega\kappa}\frac{J_1(j\kappa a)}{J_0(j\kappa a)} - \frac{\nu a}{\omega^2 + j\omega\kappa^2\nu}\times\right.$$

$$\left.\left[j\kappa\frac{J_1(j\kappa a)}{J_0(j\kappa a)} - \sqrt{\frac{-j\omega}{\nu}}\frac{J_1\left(a\sqrt{\frac{-j\omega}{\nu}}\right)}{J_0\left(a\sqrt{\frac{-j\omega}{\nu}}\right)}\right]\right\}, \qquad (5.2.6)$$

$$i_E^*(\omega) = \frac{-2\pi\epsilon^2\kappa^4\psi_s^2}{(\kappa^2\nu - j\omega)\rho_d}\left\{\frac{a^2}{2}\left[1 + \frac{J_1^2(j\kappa a)}{J_0^2(j\kappa a)}\right] - \frac{\nu a}{j\omega - \kappa^2\nu}\right.$$

$$\left.\times\left[j\kappa\frac{J_1(j\kappa a)}{J_0(j\kappa a)} - \sqrt{\frac{-j\omega}{\nu}}\frac{J_1\left(a\sqrt{\frac{-j\omega}{\nu}}\right)}{J_0\left(a\sqrt{\frac{-j\omega}{\nu}}\right)}\right]\right\} + \frac{l}{R}, \qquad (5.2.7)$$

$$q_P^*(\omega) = \frac{2\pi}{j\omega\rho_d}\left[\frac{a^2}{2} - \frac{a}{\sqrt{\frac{-j\omega}{\nu}}}\frac{J_1\left(a\sqrt{\frac{-j\omega}{\nu}}\right)}{J_0\left(a\sqrt{\frac{-j\omega}{\nu}}\right)}\right], \qquad (5.2.8)$$

$$q_E^*(\omega) = \frac{2\pi\epsilon\kappa^2\psi_s}{(\kappa^2\nu - j\omega)\rho_d}\left[\frac{a}{j\kappa}\frac{J_1(j\kappa a)}{J_0(j\kappa a)} - \frac{a}{\sqrt{\frac{-j\omega}{\nu}}}\frac{J_1\left(a\sqrt{\frac{-j\omega}{\nu}}\right)}{J_0\left(a\sqrt{\frac{-j\omega}{\nu}}\right)}\right]. \qquad (5.2.9)$$

where J_0, J_1, ρ_d and ν are the zeroth- and first-order Bessel functions of the first kind, liquid density and kinematic viscosity, respectively. In terms of the Bessel functions, we plot the real and imaginary parts of functions (a) $J_0\left(0.5a\sqrt{\frac{-j\omega}{\nu}}\right)/J_0\left(a\sqrt{\frac{-j\omega}{\nu}}\right)$ and (b) $J_1\left(a\sqrt{\frac{-j\omega}{\nu}}\right)/J_0\left(a\sqrt{\frac{-j\omega}{\nu}}\right)$ in Figure 5.2. We define the first term of $i_E^*(\omega)$ as $i_{E,1}^*(\omega)$ and can be expressed as

$$i_{E,1}^*(\omega) = \frac{-2\pi\epsilon^2\kappa^4\psi_s^2}{(\kappa^2\nu - j\omega)\rho_d}\left\{\frac{a^2}{2}\left[1 + \frac{J_1^2(j\kappa a)}{J_0^2(j\kappa a)}\right]\right.$$

$$\left. - \frac{\nu a}{j\omega - \kappa^2\nu}\left[j\kappa\frac{J_1(j\kappa a)}{J_0(j\kappa a)} - \sqrt{\frac{-j\omega}{\nu}}\frac{J_1\left(a\sqrt{\frac{-j\omega}{\nu}}\right)}{J_0\left(a\sqrt{\frac{-j\omega}{\nu}}\right)}\right]\right\} \qquad (5.2.10)$$

The streaming current i_{str} is defined as the first term of Eq.(5.2.1) or $i_{str} = Re[(i_P^*p^* + i_{E,1}^*E_z'^*)e^{j\omega t}] = Re[i_{str}^*e^{j\omega t}]$, where $E_z' = Re[E_z'^*e^{j\omega t}]$.

130

When $\omega \to 0$, Eqs.(5.2.5)-(5.2.9) reduce to those of steady state.

$$v_P^*(r,0) = \frac{1}{4\nu\rho_d}(a^2 - r^2) \,,$$

$$v_E^*(r,0) = -\frac{\epsilon\psi_s}{\nu\rho_d}\left(1 - \frac{J_0(j\kappa r)}{J_0(j\kappa a)}\right) \,,$$

$$i_P^*(0) = -\frac{\epsilon\psi_s\pi a^2}{\nu\rho_d}\left[1 - \frac{2}{j\kappa a}\frac{J_1(j\kappa a)}{J_0(j\kappa a)}\right] \,,$$

$$i_E^*(0) = -\frac{\epsilon^2\psi_s^2\pi a^2\kappa^2}{\nu\rho_d}\left[1 - \frac{2}{j\kappa a}\frac{J_1(j\kappa a)}{J_0(j\kappa a)} + \frac{J_1^2(j\kappa a)}{J_0^2(j\kappa a)}\right] + \frac{l}{\overline{R}} \,,$$

$$q_p^*(0) = \pi a^2\frac{a^2}{8\nu\rho_d} \,,$$

$$q_E^*(0) = -\frac{\epsilon\psi_s\pi a^2}{\nu\rho_d}\left[1 + 2\frac{jJ_1(j\kappa a)}{\kappa a J_0(j\kappa a)}\right] \,,$$

$$i_{E,1}^*(0) = -\frac{\epsilon^2\psi_s^2\pi a^2\kappa^2}{\nu\rho_d}\left[1 - \frac{2}{j\kappa a}\frac{J_1(j\kappa a)}{J_0(j\kappa a)} + \frac{J_1^2(j\kappa a)}{J_0^2(j\kappa a)}\right] \,. \tag{5.2.11}$$

5.3 Circuit analysis of multi-microchannel array by means of streaming current

Since the streaming current of a single microchannel is small and of the order of nano amphere, we combine n microchannels to obtain a larger current (Figure 5.3) for an external load R_L. For this circuit, there are nR_0 and nR_s; the streaming currents are additive and hence result in ni_{str}^*.

$$ni_{str}^* = E_z'^* l\frac{\frac{1}{n}\overline{R} + R_L}{\frac{1}{n}\overline{R}R_L} \tag{5.3.1}$$

We can solve for $E_z'^*$ as

$$E_z'^* = \frac{-i_P^* p^*}{i_{E,1}^* + l\frac{\frac{1}{n}\overline{R}+R_L}{\overline{R}R_L}} \tag{5.3.2}$$

and the current passing the external load R_L is

$$i_L^* = -\frac{i_P^* p^*}{\frac{R_L i_{E,1}^*}{l} + \frac{R_L}{R} + \frac{1}{n}} \,. \tag{5.3.3}$$

131
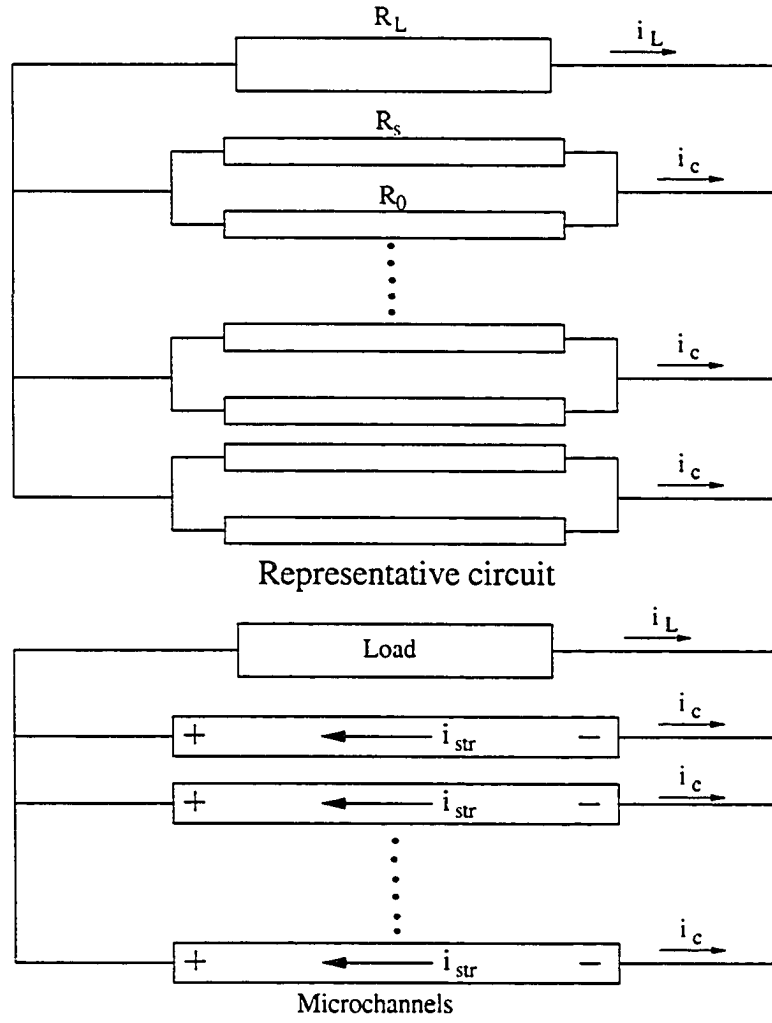
Figure 5.3: Schematic of a microchannel array circuit, where $ni_{str} = ni_c + i_L$.

At steady state, Eq.(5.3.3) becomes

$$i_L = -\frac{-\frac{\partial p}{\partial z}i_p^*(0)}{\frac{R_L i_{E,1}^*(0)}{l} + \frac{R_L}{R} + \frac{1}{n}}.$$

(5.3.4)

Normally, bulk conductivities of solution σ and surface conductivities σ_s are small. For example, the conductivity of DIUF water is of the order of 10^{-4} S/m [66]; the conductivity of 0.1 M KCl is of the order of 1 S/m [118]; surface conductivity is of the order of 10^{-8} or 10^{-9} S [66, 140]. In addition to small cross section, this will normally make the resistance of microchannels four or five order larger than the resistance of an

132

external circuit R_L. Since R_L is relatively small, the streaming potential can become negligibly small. Thus, we may ignore a part of the streaming current induced by streaming potential, $i_{E,1}E_z'^*$. We can obtain the current i_L which passes through R_L as

$$i_L = Re[i_P^* p^* e^{j\omega t}] \frac{\overline{R}}{R_L + \frac{1}{n}\overline{R}} \tag{5.3.5}$$

When $\overline{R}/n \gg R_L$, $i_L = nRe[i_P^* p^* e^{j\omega t}]$. When $n \rightarrow \infty$, $i_L = Re[i_P^* p^* e^{j\omega t}]\overline{R}/R_L$. It is anticipated that the magnitude of i_L can be significant as $n \rightarrow \infty$, depending on the ratio of $\overline{R}/R_L$ and the design of microchannel array.

Streaming currents
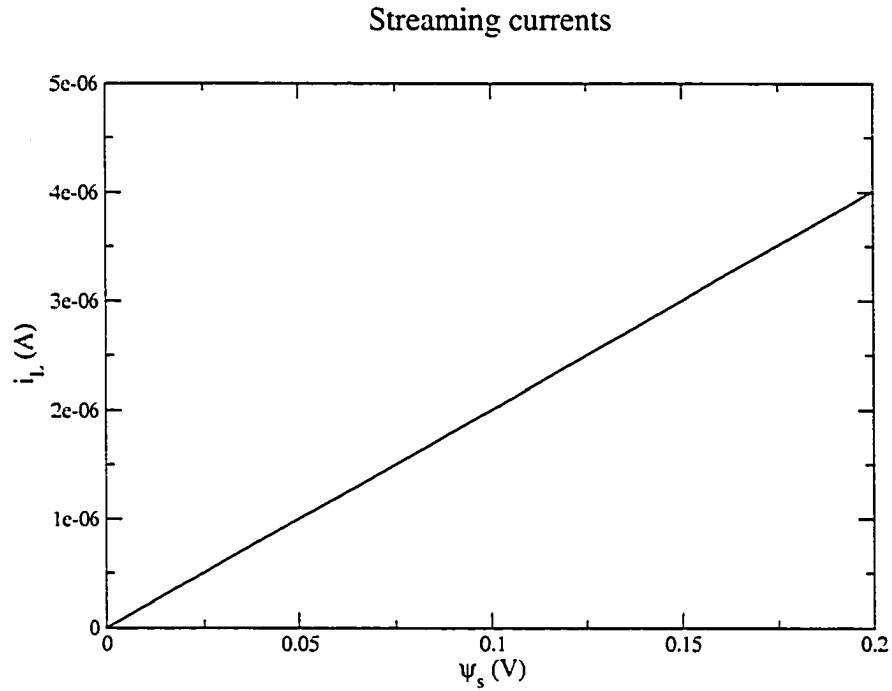
Figure 5.4: Effect of surface potential ψ_s on external current i_L for $\kappa = 1 \times 10^6$ m^{-1} and $l = 10^{-2}$ m.

Based on Eq.(5.3.4), we study here how the external current i_L changes with respect to the surface potential ψ_s, the reciprocal of Debye length (or EDL thickness) of EDL κ and the length of microchannel l. The following parameters were assumed for our parametric study: $e = 1.6021 \times 10^{-19}$ C, $n = 1 \times 10^5$, $\sigma_s = 10^{-8}$ S, $\sigma = 1 \times 10^{-4}$

133

Streaming potential
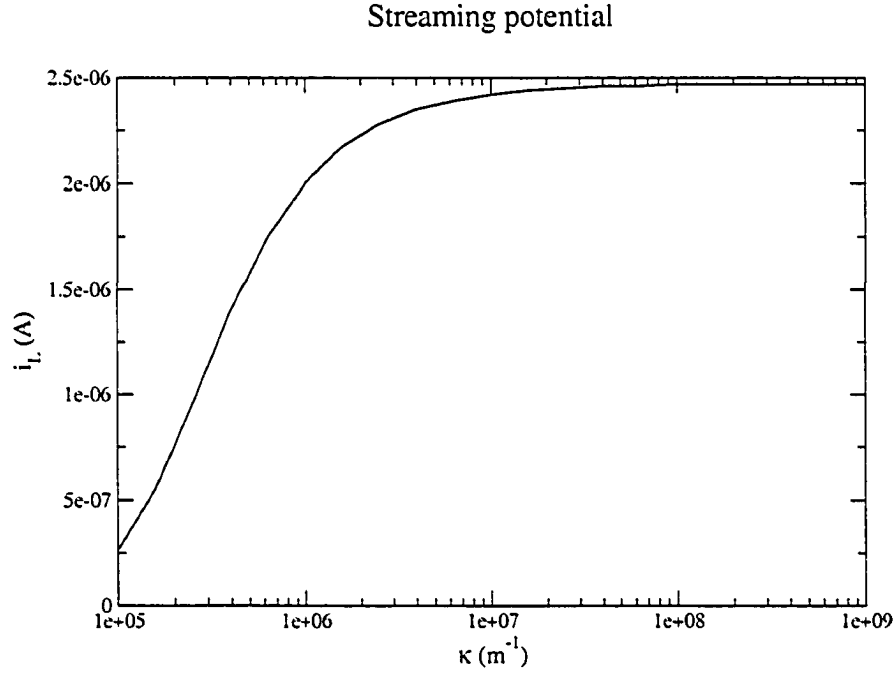
Figure 5.5: Effect of the reciprocal EDL thickness κ on external current i_L for $\psi_s = 100$ mV and $l = 10^{-2}$ m.

S/m, $a = 10$ μm, $\epsilon = 80 \times 8.854 \times 10^{-12}$ $CV^{-1}m^{-1}$, $R_L = 10\Omega$, $\nu = 0.9 \times 10^{-6}$ m^2s^{-1} and $\rho = 10^3$ kgm^{-3}. Since $\partial p/\partial z = \Delta p/\Delta z = \Delta p/l$, we fix Δp to be 10^4 Pa. When $\kappa = 1 \times 10^6$ m^{-1} and $l = 10^{-2}$ m, we plot the effect of ψ_s on i_L in Figure 5.4. When surface potential increases, the external current increases linearly. Since higher surface potential causes higher charge density in EDL, more movable charges or ions will induce a larger streaming current. For $\psi_s = 100$ mV and $l = 10^{-2}$ m, we plot the external current i_L with the reciprocal EDL thickness κ in Figure 5.5 for κ between 10^5 m^{-1} to 10^9 m^{-1}. The corresponding EDL thickness varies from 10 μm to 1 nm. Phenomenologically, dilute solution causes a thicker EDL; concentrated solution has a thinner EDL. In Figure 5.5, we see that the external current i_L increases as κ increases due to the increase in solution concentration. However, as κ approaches 1×10^8 m^{-1}, the external current reaches a plateau. For $\psi_s = 100$ mV and $\kappa = 1 \times 10^6$ m^{-1}, we show in Figure 5.6 the effect of microchannel length l on the external current

134

Streaming currents
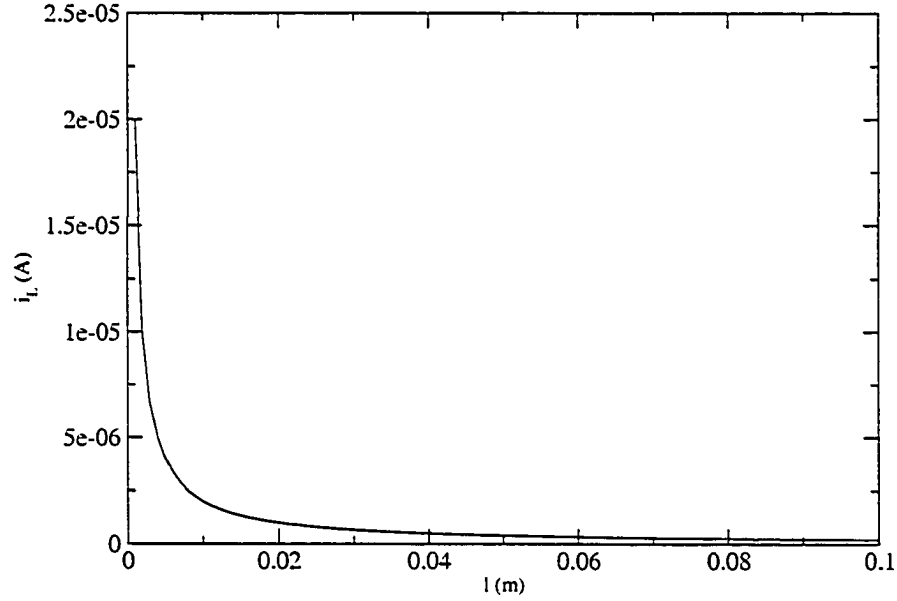
Figure 5.6: Effect of microchannel length l on external current i_L for $\psi_s = 100$ mV and $\kappa = 1 \times 10^6$ m^{-1}.

i_L. Since the pressure gradient $\partial p / \partial z$ is proportional to the external current i_L and decreases with increasing l, one would expect i_L to decrease linearly with l. The non-linear behaviour given in Figure 5.6 can be explained as follows. Since the supplied pressure drop Δp is held constant, the pressure gradient $\partial p / \partial z$ decreases as length L increases and hence i_L decreases. On the other hand, $i_L = Re[i_p^* p^* e^{j\omega t}]\overline{R}/R_L$ for $n \rightarrow \infty$. Since a longer microchannel causes larger $\overline{R}$, i_L increases with l. The effects of pressure gradient and resistance on I_L counteract each other. Since the rate of decrease in i_L caused by pressure drop is faster than the increasing rate caused by $\overline{R}$, i_L decreases non-linearly with l.

135
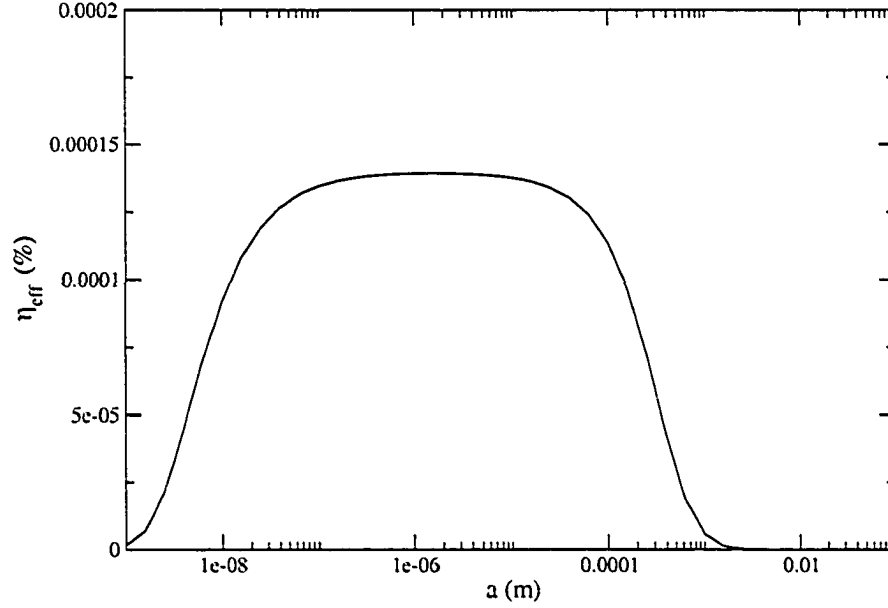
Figure 5.7: Effect of microchannel radius a on the efficiency of electrokinetic battery for $l = 10^{-3}$ m, $R_L = 10 \ \Omega$ and $\kappa = 1 \times 10^9$ m^{-1}.

5.4 Efficiency analysis for the electrokinetic battery by means of streaming current

Using traditional definition of flow work [141], we define the efficiency η_{eff} as the ratio of the rate of electrical work produced to the rate of flow work consumed. For steady state, employing the fifth and sixth equation of Eq.(5.2.11), Eqs.(5.3.2) and (5.3.4) for the definition of flow work yields

$$
\begin{aligned}
\eta_{eff} &= \frac{\text{the rate of electrical work produced}}{\text{the rate of flow work consumed}} \\
&= \frac{i_L^2 R_L}{-\Delta p n q} = \frac{i_L^2 R_L}{-\frac{\partial p}{\partial z} l n q} \\
&= \frac{i_P^{*2} R_L}{n l \left[\frac{R_L i_{E,1}^*}{l} + \frac{R_L}{R} + \frac{1}{n} \right]^2 \left[q_P^* - q_E^* i_P^* \frac{n \bar{R} R_L}{n \bar{R} R_L i_{E,1}^* + l R + n l R_L} \right]}
\end{aligned}
\tag{5.4.1}
$$

The specific constants have been given earlier and were employed for the calculation of efficiency. For $n = 10^6$, $l = 10^{-3}$ m, $R_L = 10 \ \Omega$ and $\kappa = 1 \times 10^9$ m^{-1}, we plot the effect of microchannel radius a on the efficiency of electrokinetic battery in Figure

136
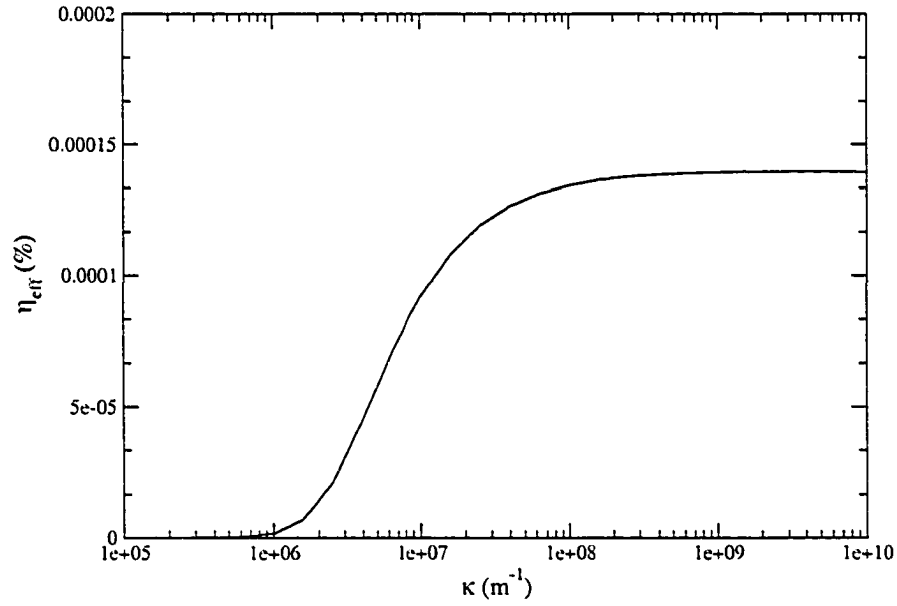
Figure 5.8: Effect of the reciprocal EDL thickness on the efficiency of electrokinetic battery for $l = 10^{-3}$ m, $R_L = 10$ Ω and $a = 1$ μm.

5.7. There exists a maximum efficiency between $a = 1$ μm and $a = 100$ μm. When $a \rightarrow 0$, the efficiency approaches zero as the solid/liquid interface approaches zero and hence the number of movable ions. In this case, there is no induced current and the efficiency becomes zero. When $a \rightarrow \infty$, the surface area of EDL increases and, because the surface area is of the order a and that of the flow rate is of the second order of a, the flow increases at a faster rate. Thus, more pressure is needed to drive the flow and hence the efficiency approaches zero. In Figure 5.8, we find that the efficiency for dilute solutions (small κ) is smaller and that of the concentrated solutions (large κ) is higher. However, when κ is larger than 1×10^8 m^{-1}, the efficiency approaches a plateau. This is due to the fact that, when the solution concentration increases for large κ, EDL thickness decreases and the amount of movable ions in EDL becomes saturated. In Figure 5.9, we plot the effect of microchannel length l on the electrokinetic battery efficiency. From Eq. (5.2.6), i_p^* is independent of the microchannel length l and contribute largely to the total streaming current. However,

137
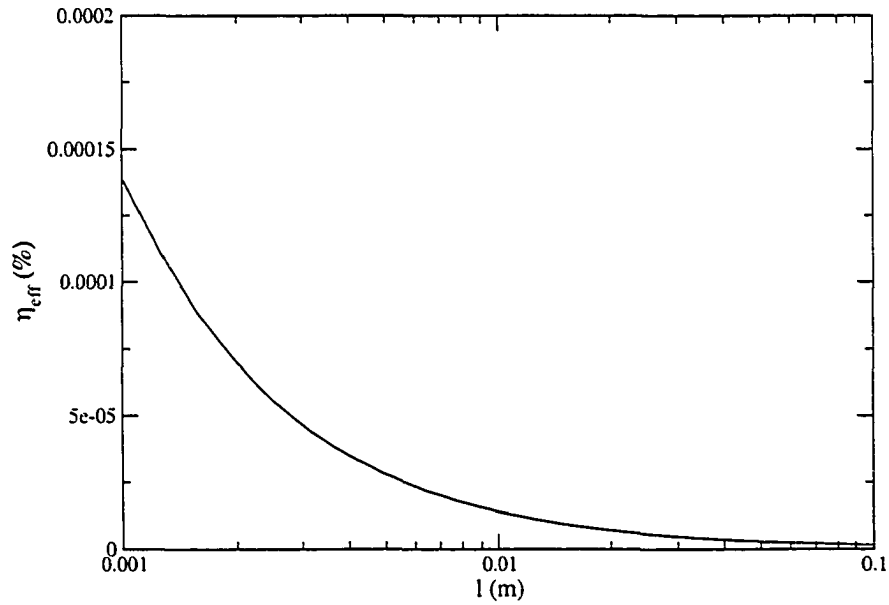
Figure 5.9: Effect of microchannel length on the efficiency of electrokinetic battery for $\kappa = 1 \times 10^9$ m^{-1}, $R_L = 10\ \Omega$ and a=1 μm.

a longer microchannel requires larger pressure drop to drive the flow and hence cannot provide a higher efficiency. In Figure 5.10, we plot the effect of the external load R_L on the efficiency. When $R_L \to 0$, a large external current i_L can be obtained and the electrical work is zero. When $R_L \to \infty$, we obtain a zero external current i_L and zero electrical work. In addition, there exists a maximum efficiency when $R_L = 10^4\ \Omega$.

5.5 Natural electrokinetic battery by means of streaming current

5.5.1 Model prediction and experimental results

In reality, porous materials, such as glass filter, membrane, rock, and soil, could be considered as a natural electrokinetic battery. The use of natural materials avoids complex micro/nanofabrication procedures to produce microchannel arrays with a large surface area to volume ratio. In addition, natural porous material can have a

138
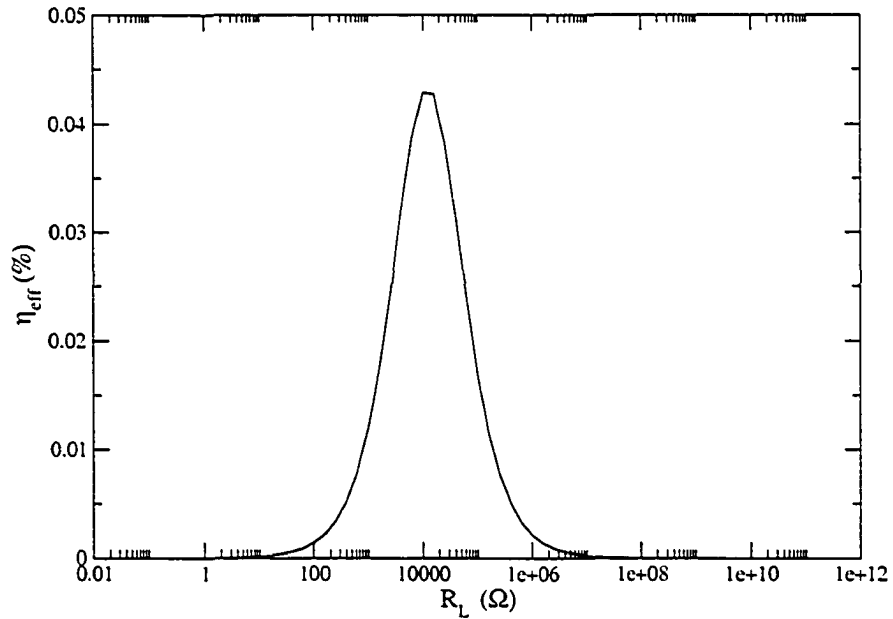
Figure 5.10: Effect of external load R_L on the efficiency of electrokinetic battery for $\kappa = 1 \times 10^9$ m^{-1}, $l = 10^{-3}$m and $a = 1$ μm.

high porosity ratio up to 60%. To explore this, we designed an experimental system shown in Figure 5.11 to illustrate our electrokinetic battery idea by means of streaming current, using a commercial porous glass filter. In our experimental system (Figure 5.11), the porous glass filter is 20 mm in diameter with a pore size from 10 μm to 16 μm (Schott DURAN, Mainz, Germany). Two Teflon O-rings of 2 mm thickness were used to hold the filter disc in position. Two meshed Ag/AgCl electrodes were used to measure the streaming current. A Keithley 2000 digital multimeter (Keithley Instruments, Germering, Germany) was used to record the current. There is a 30 cm height difference between the inlet and outlet to make water pass through the filter disc under an hydrostatic pressure. Deionized water (MILLIPORE, Billerica, Massachusetts, USA) and tap water were used as the testing liquid. In this experiment, we focus on steady flow passing through the filter disc. In this case, the digital multimeter measures the streaming current, i_{str}. Since the internal resistor

139
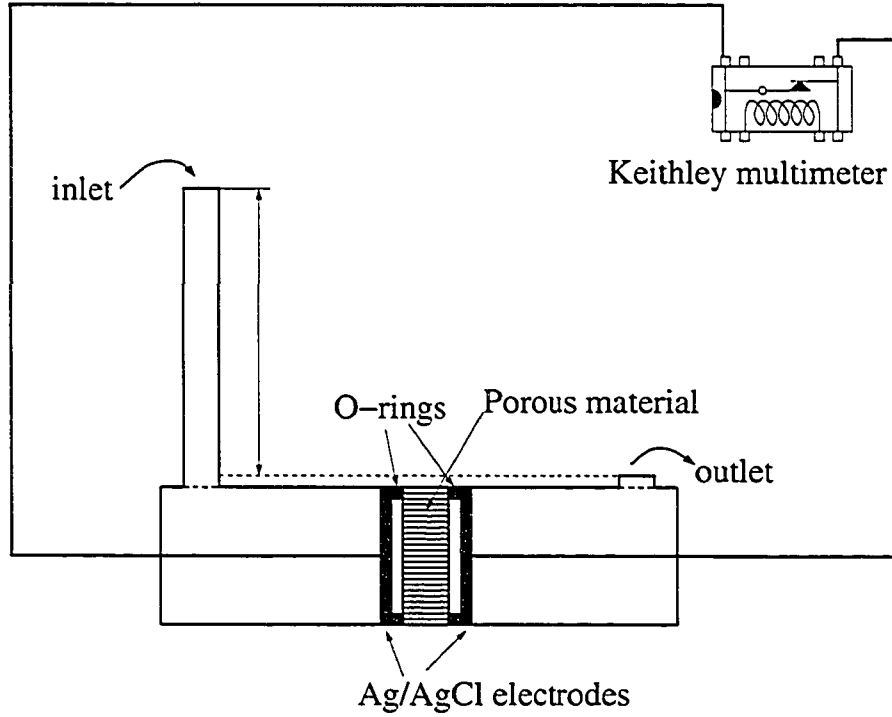
Figure 5.11: Schematic of an experimental system for electrokinetic battery

for 10 mA range is negligible compared to the resistance of glass filter, the streaming potential becomes relatively small. Thus, we ignore the current induced by the streaming potential, $i_{E,1}^* E_z'$, so that $i_{str} = i_P(-\partial p/\partial z)$. The number of pores in the glass filter n can be calculated from

$$n = \eta \frac{A}{\pi a^2} , \tag{5.5.1}$$

where η is the porosity of glass filter and A is the effective area of the filter. Considering the thickness of O-rings, we calculated the effective area to be $\pi(10 - 2)^2$ mm^2. For the purpose of calculations, we selected an average microchannel radius of $a = 6.5$ μm. Since η was not available from product description, we assumed a typical porosity of $\eta = 30\%$ and obtained $n = 0.3\pi(8 \times 10^3)/(\pi 6.5^2) \approx 4.5 \times 10^5$. Since the bulk conductivity of the pure water λ_0 is 0.5 μS/m and the surface conductivity λ_s is the order of 10^{-9} S or 10^{-8} S [66, 140, 142], we employ $i_L = n i_P(-\partial p/\partial z)$ to predict

140

Table 5.1: Predicted external current i_L for a set of possible ψ_s and κ^{-1} values.

	$\psi_s = 50$ mV	$\psi_s = 100$ mV	$\psi_s = 150$ mV	$\psi_s = 200$ mV
$\kappa^{-1}=1$ μm	1651 nA	3301 nA	4952 nA	6603 nA
$\kappa^{-1}=3$ μm	765 nA	1530 nA	2295 nA	3060 nA
$\kappa^{-1}=10$ μm	114 nA	227 nA	341 nA	454 nA

the measured current.

To estimate the measured current, we employed the following constants that correspond to our experimental conditions: $n \approx 4.5 \times 10^5$, $\sigma_s = 10^{-8}$ S, $\sigma = 5 \times 10^{-5}$ S/m, $l = 3$ mm, $\epsilon = 80 \times 8.854 \times 10^{-12}$ CV^{-1}m^{-1}, $\nu = 0.9 \times 10^{-6}$ m^{2}s^{-1}, $\rho = 10^3$ kgm^{-3}, and $e = 1.6021 \times 10^{-19}$, $-\partial p/\partial z = 9.8 \times 10^5$ Pa m^{-1}. For simplicity, we assume all hydrostatic pressure drop on microchannels. It should be noted that the value of ψ_s depends on both the concentration or pH of solution and channel wall material. The larger ψ_s, the more noticeable the electrokinetic effect. Thus, one would observe a larger streaming current for larger ψ_s. The Debye length (or EDL thickness) κ^{-1} for distilled water [66, 142] ranges from several micrometers to 1 mm. However, neither ψ_s nor κ^{-1} is known. Using Eq.(5.3.4), we show in Table 5.1 the estimated external currents for a number of surface potentials ψ_s and EDL thickness κ^{-1}. Our model predicts that the external current I_L can vary between 10^2 to 10^3 nA. In actual measurement, we obtained an average maximum current of 760 nA for deionized water. The measured current gradually decreases due to polarization of electrodes at the solution/electrode interface. When tap water was used as the testing liquid, the measured current reached 1500 nA due to a higher ionic concentration. The results illustrated in Table 5.1 are in good agreement with these experiment values. Our electrokinetic battery model is shown to predict correctly the order of magnitude for the external current i_L. The exact i_L can be determined when ψ_s and κ^{-1} are known.

141
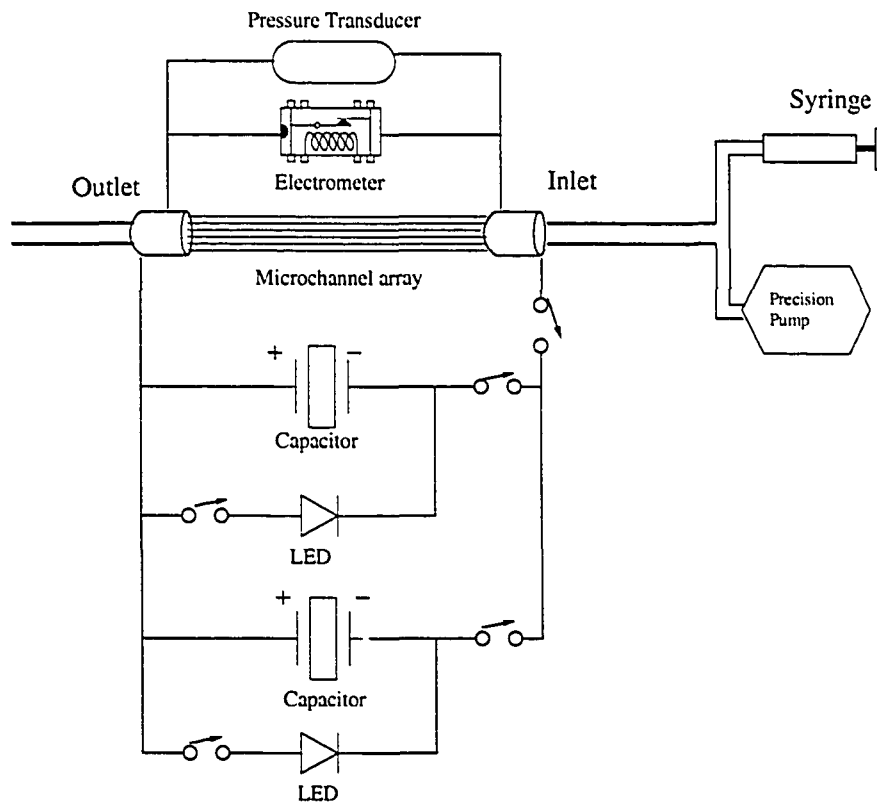
Figure 5.12: Schematic of an electrokinetic battery by means of streaming potential

5.6 Electrokinetic battery by means of streaming potential

The mechanism of electrokinetic battery by means of streaming current is to make most of streaming current pass through a load R_L with low resistance. Somehow, the obtained current i_L is still not too large unless we connect more microchannels together. But, the small size requirement of MEMS devices limits the number of microchannels. In the above experiment of the section 5.5.1, the potential between the two ends of microchannels is relatively low. Such streaming current and potential are too low to become practical.

However, collected electricity is applicable to provide power to external load. The streaming potential could be high up to several ten volts depending on the pair of

142
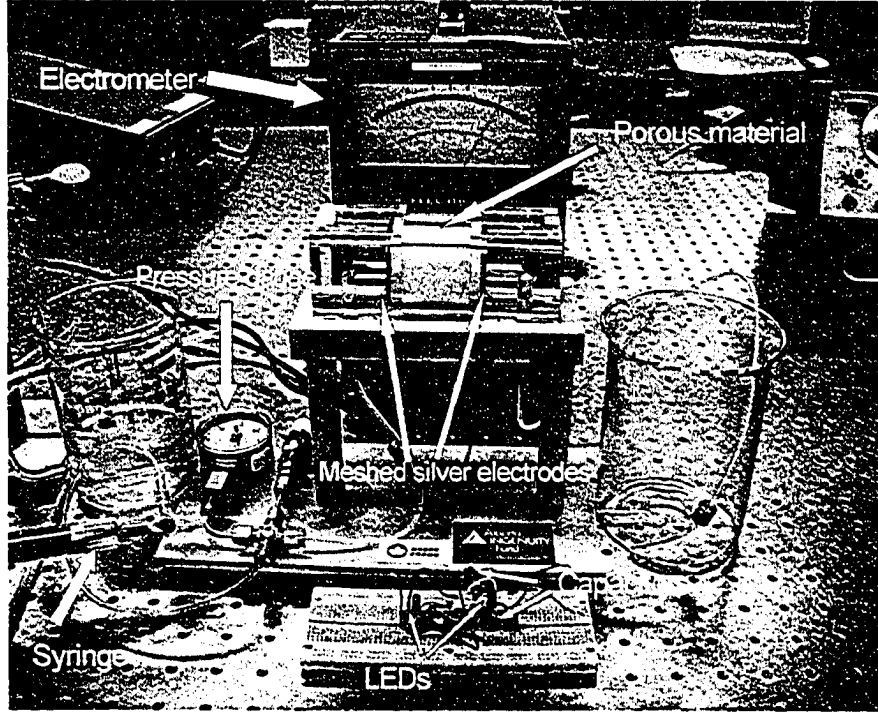
Figure 5.13: Picture of an electrokinetic battery by means of streaming potential

liquid-solid and pressure gradient. If we connect a capacitor with the microchannel array, ideally (without considering the leakage of capacitor), potential of the charged capacitor can be up to the steaming potential.

Let's summarize the expressions of streaming current i_{str}, streaming potential Δu, flow rate q for a single microchannel with radius a:

$$\Delta u = \frac{\epsilon\zeta\left[1 - \frac{2}{j\kappa a}\frac{J_1(j\kappa a)}{J_0(j\kappa a)}\right]}{\epsilon^2\zeta^2\kappa^2\left[1 - \frac{2}{j\kappa a}\frac{J_1(j\kappa a)}{J_0(j\kappa a)} + \frac{J_1^2(j\kappa a)}{J_0^2(j\kappa a)}\right] - \sigma\mu}\Delta p ,\tag{5.6.1}$$

$$i_{str} = -\frac{\epsilon\zeta\pi a^2}{\mu}\left[1 - \frac{2}{j\kappa a}\frac{J_1(j\kappa a)}{J_0(j\kappa a)}\right]\frac{\Delta p}{l} + \frac{\epsilon^2\zeta^2\pi a^2\kappa^2}{\mu}$$

$$\times\left[1 - \frac{2}{j\kappa a}\frac{J_1(j\kappa a)}{J_0(j\kappa a)} + \frac{J_1^2(j\kappa a)}{J_0^2(j\kappa a)}\right]\frac{\Delta u}{l} ,\tag{5.6.2}$$

$$q = \pi\frac{a^4}{8\mu}\frac{\Delta p}{l} + \frac{\epsilon\psi_s\pi a^2}{\nu\rho_d}\left[1 + 2\frac{jJ_1(j\kappa a)}{\kappa a J_0(j\kappa a)}\right]\frac{\Delta u}{l} ,\tag{5.6.3}$$

where Δp is the pressure drop between the two ends of the microchannel and l is

143
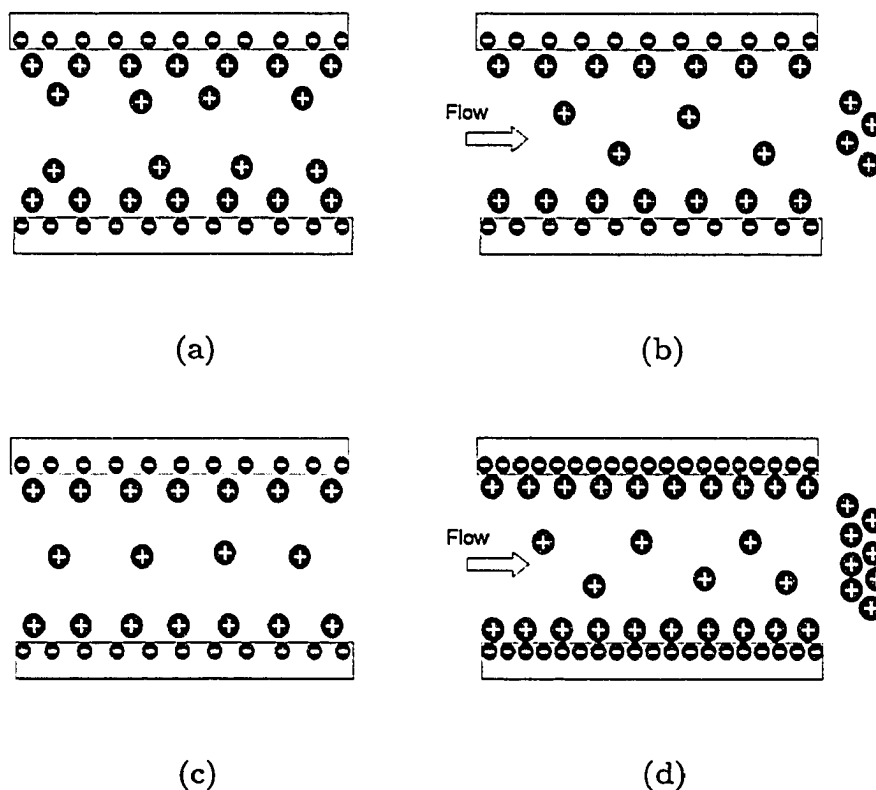
Figure 5.14: A schematic of the mobile-ion-drain method. (a) Surface has adopted a charge when in contact with water and EDL forms; (b) A stable streaming potential exists due to the water flow and accumulation of mobile ions; (c) The mobile ions in (b) have been drained and the surface will disassociate and become negatively charged; (d) The surface has become more negatively charged when flow resumes, resulting in a larger streaming potential.

the microchannel length. As an illustration of this concept, a prototype has been built using a natural ceramic rod with nearly 9 million build-in microchannels as an electrokinetic battery by means of streaming potential in Figures 5.12, 5.13. A simple syringe or precision pump is used to drive water into a ceramic rod and the two ends are connected by an electrometer (Keithley 610B, Keithley Instruments, Germany). The ceramic rod (Small Parts Inc.) is 2 inch in length with an outer diameter of 1 inch, a porosity of 50% and a pore radius of 3 μm. The two electrodes consisting of a silver meshed network were placed at the two ends of the ceramic rod and in

144

connection with the electrometer. All other connections are plastic or Teflon in order to minimize the influence of conductivity on the potential. The electrical energy is collected by means of two 100 μF capacitors which are alternatively charged and discharged for two LEDs. Deionized ultrafiltered (DIUF) water (Fisher Scientific) having a conductivity of 2.0 $\times 10^{-4}$ S/m was used as the testing liquid. Water was selected here because of its simplicity. Pushing the syringe by hand (Figures 5.12, 5.13), a streaming potential of over 20 V and a streaming current of over 30 μA can be easily obtained. After about 8 seconds, the two LEDs light-up alternatively in every 10–12 seconds, depending on the input pressure.

In order to examine the above phenomenon further, we have employed an automatic syringe pump which provides a constant flow rate of 400 ml/hr DIUF water through the porous ceramic rod. Initially, the observed streaming potential was stable at 1.5 V with a streaming current of 4 μA. We found that, by repeat pumping and draining the water, the streaming potential can be increased to 6.3 V with a streaming current of 7.5 μA at the same flow rate. This phenomenon is particularly intriguing as one can increase the streaming potential and current without increasing pressure. These procedures are described below as a mobile-ion-drain method. As shown schematically in Figure 5.14a, water is initially stationary with respect to the channel walls and ions distribute themselves due to a charged surface. Water is then forced into the channel (Figure 5.14b), causing a stable potential difference (streaming potential) across the two ends due to accumulation of the mobile ions at the outlet. When pumping is stopped (water is stationary), some of the mobile (counter) ions previously at the outlet had escaped by following the stream of water. Figure 5.14c illustrates this schematically by losing four counter ions. Here, the system is no longer neutral and in deficit of four counter ions. The only way to recover equilibrium is to obtain them from the surface by dissociation. Thus, the system will reach another equilibrium by further dissociation, resulting in a more negatively charged

145

surface. This is further supported by experimental evidence that a small potential difference exists, which is opposite to the streaming potential, even when there is no flow; that is, the system has become negatively charged. When pumping resumes (Figure 5.14d), there will be more mobile ions due to the increase in surface charge density and hence a higher streaming potential will result. If stop pumping again, the small potential difference, opposite to the streaming potential, becomes larger. This further supports the surface becomes more negative. After repeat pumping and drainage to eleventh times, we obtained a nearly saturated 6.3 V streaming potential and 7.5 μA streaming current. This potential was then used to charge up two 100 μF capacitors alternatively. Figure 5.15 shows the charging process for such a capacitor by forcing DIUF water through our electrokinetic battery. This process can be described below as the voltage of the capacitor u_c is expressed by $u_c = \Delta u(1 - e^{-t/RC})$, where t, C and R are the time, capacitance and the total resistance of the circuit. From this relationship, we determined R to be 8.8×10^5 Ω. The two capacitors were being charged and discharged alternatively and were capable of powering two LEDs in every sixteen seconds.

Using traditional definition of flow work [141], we define the efficiency η_{eff} of our system as the ratio of the rate of electrical work produced to the rate of flow work consumed.

$$\eta_{eff} = \frac{\text{the rate of electrical work produced}}{\text{the rate of flow work consumed}}$$
$$= \frac{\Delta u i_{str}}{\Delta p n q}. \qquad (5.6.4)$$

With $\Delta u = 6.3$ V, $i_{str} = 7500$ nA, $\Delta p = 1.04 \times 10^5$ Pa and $q = 400$ ml/hr, we obtained an efficiency η_{eff} of 0.313%. If we subsitute Eqs.(5.5.1, 5.6.1, 5.6.2 and 5.6.3) into (5.6.4), this efficiency depends only on the properties of the solid/liquid pair and is independent of the pressure drop Δp and the channel length l. Even though a 2 inch long porous ceramic rod is selected here, the length of the porous material has no

146

impact on its efficiency and can, in principle, be reduced to the order of millimeters. A thin filter disk can also be other alternative for our water battery. The efficiency is e:
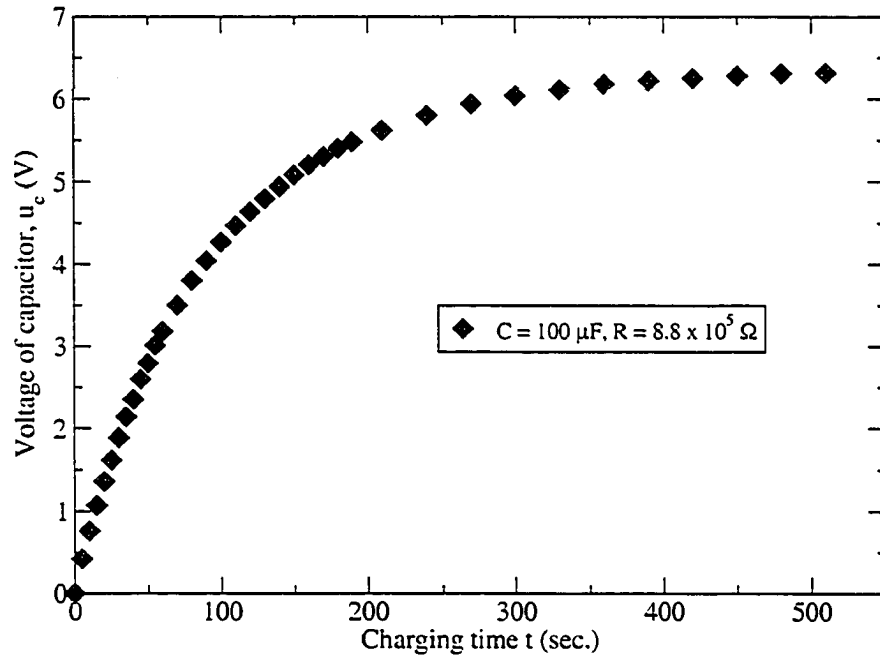
Figure 5.15: The charging process for a 100 μf capacitor

5.7 Conclusions

Pressure-driven-flow in a microchannel induces a streaming current and streaming potential due to the presence of an electrical double layer between the electrolyte solution and solid surface. We propose here two methods, by means of streaming current and streaming potential, to develop an electrokinetic battery consisting of an array of microchannels that converts the mechanical energy of a liquid into electrical work. Our preliminary experiments to illustrate the electrokinetic battery idea by means of streaming current.

147

We have proposed another design of electrokinetic battery by means of streaming potential, which makes this idea practical to light up LEDs. A mobile-ion-drain method has also been demonstrated to increase the streaming potential without increasing pressure drop. The electrokinetic battery demonstrated here is environmentally friendly, with no emission and moving parts. The fact that most biological systems are highly charged might have important implication on our system as alternative for the choice of liquids and solids and as improvement on efficiency to generate electricity by means of a pressurized biological solution.

Chapter 6

Dynamic Interfacial Effect of Electroosmotic Slip Flow with a Moving Capillary Front

6.1 Introduction

Lab-on-a-chip utilizing electroosmotic flow (EOF) has become an established technology for the detection and analysis of minute chemical and biological samples [18, 143]. The processes typically involve injection (or loading), mixing, separation and detection of sample solution through microchannels. Normally, electroosmotic mobility (EOM) is used to provide a qualitative measure for the efficiency of a given Lab-on-a-chip device by means of the current monitoring [144, 145] and fluorescent dye methods [146, 147]. It is noted that determination of EOM from the above methods rely on the assumption of continuous flow which may not truly describe the time-dependent electroosmotic injection process. During loading processes, liquids travel between two electrodes from, e.g., a reservoir to one end of the channel; this motion is indeed dynamic and time-dependent. A three-phase (solid-liquid-vapor) contact line is always presented between the two electrodes until the moving capillary front has reached one end of the electrode. Depending on the three-phase contact angle, a large Laplace pressure can develop across the moving capillary front (as shown in Figure 6.1) which has not been considered in the current monitoring and fluorescent dye methods. The

149

extend of such effects depends strongly on the contact angle θ at solid-liquid interface. In the case where $\theta < 90°$, capillary penetration occurs which induces fluid motion by capillary action; on the contrary, when $\theta > 90°$, capillary depression will result as additional resistance against the flow direction. Thus, the presence of a moving capillary front can have important implication on EOF. Obviously, wettability (or surface hydrophobicity) in terms of the contact angles can play an important role. Whether the existence of a capillary pressure across the liquid-vapor interface is to induce or suppress EOF depends solely on the phenomenological contact angles. It is the purpose of this work to model EOF by consideration of the capillary pressure, in addition to EDL.

As a matter of fact, surface hydrophobicity has an additional role in terms of the hydrodynamic behavior. Many authors have reported experimental observation of liquid slip at the solid-liquid interface which increases flow velocity and hence reduction in the hydrodynamic drag. Watanabe et al. [98] observed water slippage in a 16 mm diameter acrylic-resin-coated pipe and obtained a 14% drag reduction. Tretheway and Meinhart measured the velocity profile of water flowing through a 30 × 300 μm^2 octadecyltrichlorosilane (OTS) coated microchannel and observed slippage of fluid [99]. Zhu and Granick [100] measured the hydrodynamic force of water against a methyl-terminated self-assembled monolayer (SAM) on mica and found that when the flow rate exceeds a critical level, partial slip occurs. Their results could only be explained by consideration of liquid slip. By now, the widely accepted slip boundary condition is that from Navier [87, 88], which relates the velocity at solid surface to be proportional to shear stress. Clearly, these results suggested the occurrence of liquid slip for water flow over hydrophobic surfaces. The effect is expected to be more prominent in microfluidics. However, none of above studies have considered electrokinetic effect (as in EOF) and liquid slip simultaneously until recently by us [120, 148].

150

Indeed, there are three competing effects in electroosmotic flow in the presence of a solid-liquid moving capillary front: (1) electrokinetics; (2) Laplace pressure; and (3) solid-liquid adhesion. As in EOF, the presence of an electrical double layer (EDL) causes liquid movement when an external electric field is applied; while the existence of a liquid-vapor moving front may induce or suppress flow velocity, it depends on the phenomenological contact angle. The solid-liquid interaction (adhesion) can manifest itself as liquid slip at the solid-liquid interface in reducing hydrodynamic drag. In fact, extensive numerical simulations [60, 63, 149, 150] of EOF have been performed in the literature that are based exclusively on traditional computational fluid dynamics method without consideration of these surface effects. Various theoretical models and predictions are also available, but limited only to EDL effect. Recent studies of ours have considered the combined effects of EDL and surface hydrophobicity on steady-state electroosmotic flow. Nevertheless, a model of EOF accounting for the effects of EDL, capillary pressure and solid-liquid adhesion is not available and is the focus of this study. Our work was largely inspired by recent active research [151, 152, 153, 154, 155, 156] in using hydrophobic polymeric materials as alternative substrates for Lab-on-a-chip fabrication.

6.2 Theoretical framework

6.2.1 Fundamental equation of capillary rise flow

The penetration of liquid into capillary or porous body due to surface tension was first investigated by Lucas [157] and Washburn [158] who found that the capillary rise height is proportional to the square root of the penetration time, resulting in a well-known Lucas-Washburn equation. Subsequent research include consideration of inertia [159, 160, 161], inlet length [162], energy dissipation [163] and surfactant [164, 165] effect on capillary penetration. Ichikawa [166] studied interface motion of capillary flow in horizontal microchannels. Erickson *et al.* [167] simulated capillary-driven flow

151
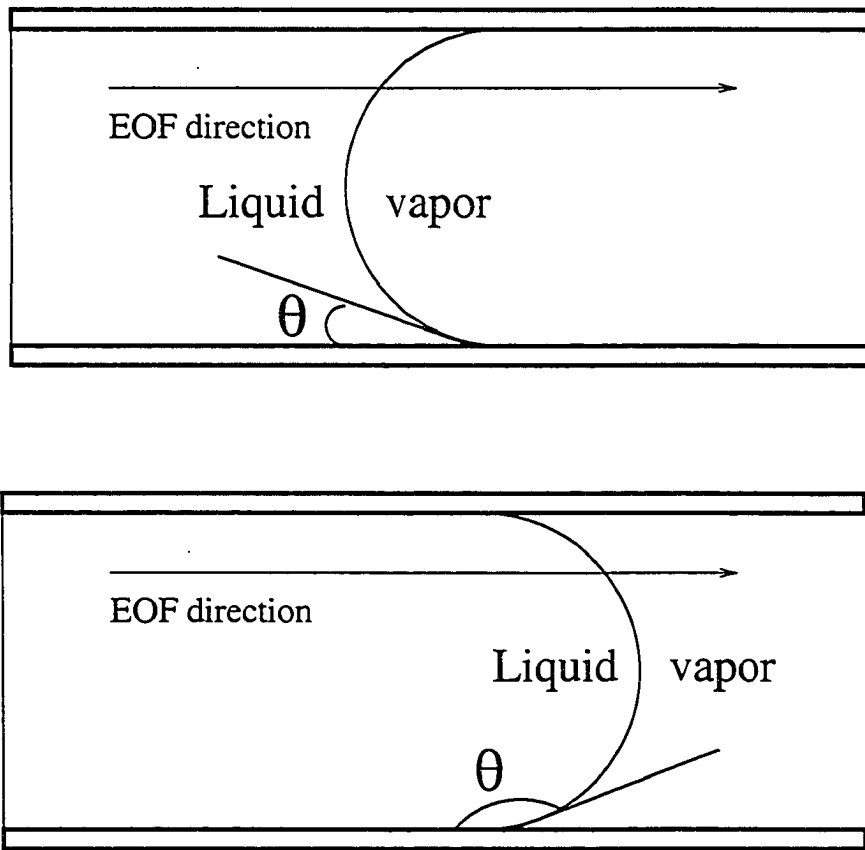
Figure 6.1: Schematic illustration of capillary penetration ($\theta < 90°$) and capillary depression ($\theta > 90°$).

in nonuniform cross-section capillaries. Levine *et al.* [168] and Shikhmurzaev [169] studied the flow behavior in the vicinity of moving contact line. Recent applications of the phenomena employed electrocapillary pressure to control fluid in multichannel array [170]; Zhao *et al.* [171] patterned surface free energy inside microchannels to drive flow along hydrophilic pathways. This dynamic behavior of capillary flow with a moving front is strongly influenced by the surface tensions of the solid and liquid, as manifested by the contact angle at the three-phase contact line given by the Young equation.

We consider here a viscous incompressible liquid rising along a cylindrical capillary with a constant contact angle θ at the solid-liquid-vapor three-phase interface where

152
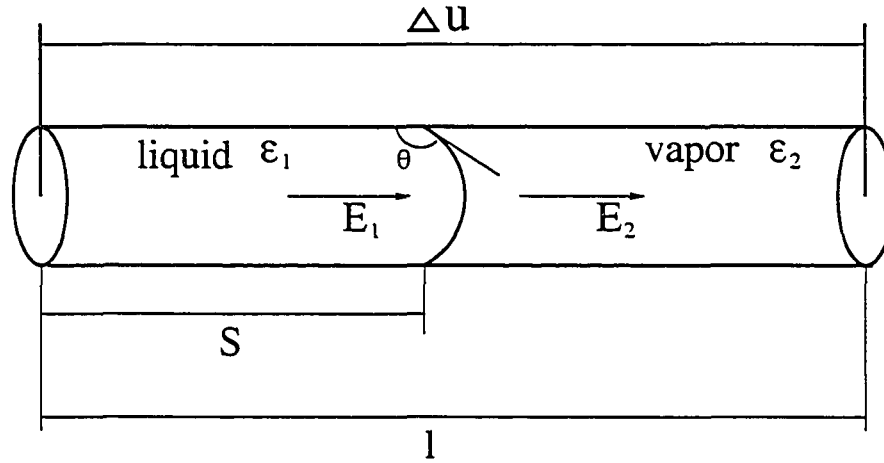
Figure 6.2: Schematic of electroosmotic flow in a circular microchannel with a moving capillary front when $\theta > 90°$.

the unbalanced pressure difference or Laplace pressure is the driving force for the capillary rising flow. Obviously, when the Laplace pressure is balanced by gravitational force, there will be no capillary penetration. During the rising process, the following Newton dynamics equation equation can be used to describe the flow behavior:

$$\rho_d \pi a^2 \left[\frac{\partial}{\partial t} \left(h(t) \frac{\partial h(t)}{\partial t} \right) \right] = 2\pi a \gamma_{lv} \cos\theta - \pi a^2 \rho g h(t) - 8\pi\mu h(t) \frac{\partial h(t)}{\partial t} , \quad (6.2.1)$$

where ρ_d, a, t, $h(t)$, γ_{lv}, g and μ are the liquid density, capillary radius, time, height of capillary rise, liquid-vapor surface tension, acceleration of gravity and liquid viscosity, respectively. The left hand side of Eq.(6.2.1) is basically an inertia term; the first term on the right of Eq.(6.2.1) is due to the Laplace pressure, the second term to hydrostatic pressure and the third to viscous drag. Here, a Poiseuille flow profile is assumed throughout the capillary [165].

6.2.2 Continuous electroosmotic slip flow

We consider here electric field as the only external force to drive liquid movement. As for EOF, the effects of EDL and surface hydrophobicity in terms of liquid slippage have been modeled in our previous study. Based on the linearized Poisson-Boltzmann

153

equation, Yang and Kwok [172] provided the analytical solutions for electrokinetic slip flow without the moving capillary front in circular hydrophobic microchannels. The velocity profile solutions are summarized here:

$$v_E(r) = -\frac{\epsilon_1 \psi_s E_1}{\mu} \left[1 - \frac{J_0(j\kappa r)}{J_0(j\kappa a)} + j\beta\kappa \frac{J_0(j\kappa a)}{j\kappa a} \right] , \qquad (6.2.2)$$

$$q = -\frac{\epsilon_1 \psi_s \pi a^2 E_1}{\mu} \left[1 + j\beta\kappa \frac{J_1(j\kappa a)}{J_0(j\kappa a)} - \frac{2}{j\kappa a} \frac{J_1(j\kappa a)}{J_0(j\kappa a)} \right] , \qquad (6.2.3)$$

where v_E, ϵ_1, ψ_s, E_1, r, J_0, J_1, κ, β and q are the axial velocity, permittivity of solution, surface potential of capillary wall, strength of electric field in solution, radial coordinate of the cylindrical coordinate system, zeroth-order Bessel functions of the first kind, first-order Bessel functions of the first kind, reciprocal of the electrical double layer thickness, slip coefficient and flow rate, respectively; and j is a complex number as $j = \sqrt{-1}$. For a $(z_0 : z_0)$ electrolyte, κ can be written as

$$\kappa = \sqrt{\frac{2n_\infty e^2 z_0^2}{\epsilon_1 kT}} , \qquad (6.2.4)$$

where e is the elementary charge; n_∞ is the ionic concentration in an equilibrium electrochemical solution at the neutral state where $\psi = 0$; k is the Boltzmann constant; and T is the absolute temperature. A slip coefficient β is used to determine the boundary condition which satisfies

$$v_E(a) = \beta \frac{\partial v_E(a)}{\partial r} . \qquad (6.2.5)$$

It is noted that $-\beta$ is typically defined as the slip length. The charge density ρ in a circular microchannel can be expressed as

$$\rho = -\epsilon_1 \kappa^2 \psi_s \frac{J_0(j\kappa r)}{J_0(j\kappa a)} . \qquad (6.2.6)$$

6.2.3 Molecular-kinetic theory of slip

At the solid-liquid-vapor three-phase interface, Young's equation relates the contact angle with the surface tensions of solid and liquid as

$$\gamma_{lv} \cos\theta_Y = \gamma_{sv} - \gamma_{sl} , \qquad (6.2.7)$$

154

where θ_Y is the Young contact angle, i.e., a contact angle that can be inserted into Young's equation; γ_{lv}, γ_{sl} and γ_{sv} are the liquid-vapor, solid-liquid and solid-vapor surface tensions, respectively. The solid surface tensions γ_{sl} and γ_{sv} affect directly the phenomenological angle θ when γ_{lv} is fixed. Here, we assume the phenomenological angles θ used in our calculations are identical to the Young angles θ_Y. These angles represent surface hydrophobicity and affect liquid slippage at the solid-liquid interface. Since surface tensions originated from intermolecular forces and can be related to the thermodynamic work of cohesion and adhesion, the slip length can, in principle, be related to molecular kinetic phenomena between the solid-liquid interface. The first contribution to connect slip coefficient with contact angle was by Tolstoi [173]; Blake [95] later reviewed Tolstoi's theory and discussed the results regarding liquid adsorption at the solid surface. By means of molecular and thermodynamic theories, Tolstoi derived

$$\beta = -\delta \left[e^{\alpha A \sigma_{lv}[1 - \cos\theta]/kT} - 1 \right] , \tag{6.2.8}$$

where δ, A and α are the average distance between the centers of adjacent liquid molecules, the effective surface and the fraction of A composed of solid surface. Here, we consider liquid molecule as a sphere and $A = \pi\delta^2$. It is noted that the predictions from this theory are in good agreement [95] with those obtained by Churaev *et al.* [174].

6.2.4 Electroosmotic slip flow with a moving capillary front

The results from the previous sections are used here to derive the equations for electroosmotic slip flow with a moving capillary front. We assume that the EOF with a moving front is quasi-steady and laminar throughout the channel [175], so that it satisfies Eq.(6.2.2). From Eq.(6.2.2), we can obtain the shear force τ as

$$\tau = \mu\frac{\partial v_E}{\partial r} = -\epsilon_1\psi_s E_1 j\kappa\frac{J_1(j\kappa r)}{J_0(j\kappa a)} . \tag{6.2.9}$$

155

Noting that

$$q = \pi a^2 \frac{ds}{dt} ,$$ (6.2.10)

the total viscous drag force F_v can be expressed as

$$F_v = 2\pi a s(t) \tau|_{r=a} = 2\pi a \mu s(t) \frac{ds}{dt} \frac{j\kappa \frac{J_1(j\kappa a)}{J_0(j\kappa a)}}{1 + j\beta\kappa \frac{J_1(j\kappa a)}{J_0(j\kappa a)} - \frac{2}{j\kappa a} \frac{J_1(j\kappa a)}{J_0(j\kappa a)}} .$$ (6.2.11)

where s is the displacement or traveled distance by the liquid. The capillary force F_c due to Laplace pressure can be expressed as

$$F_c = 2\pi a \gamma_{lv} \cos\theta .$$ (6.2.12)

Finally, the body force F_E due to external electric field and charge distribution can be written as

$$F_E = 2\pi s(t) E_1 \int_0^a \rho r dr = -2\pi s(t) E_1 \epsilon_1 \kappa^2 \psi_s \frac{a}{j\kappa} \frac{J_1(j\kappa a)}{J_0(j\kappa a)} .$$ (6.2.13)

For a given EOF that has traveled a distance s, the Newton dynamics equation is

$$\rho_d \pi a^2 \left[s\frac{d^2 s}{dt^2} + \left(\frac{ds}{dt}\right)^2 \right] = F_c + F_E + F_v$$

$$= 2\pi a \gamma_{lv} \cos\theta - 2\pi s(t) E_1 \epsilon_1 \kappa^2 \psi_s \frac{a}{j\kappa} \frac{J_1(j\kappa a)}{J_0(j\kappa a)}$$

$$+ 2\pi a \mu s(t) \frac{ds}{dt} \frac{j\kappa \frac{J_1(j\kappa a)}{J_0(j\kappa a)}}{1 + j\beta\kappa \frac{J_1(j\kappa a)}{J_0(j\kappa a)} - \frac{2}{j\kappa a} \frac{J_1(j\kappa a)}{J_0(j\kappa a)}}$$ (6.2.14)

For EOF of electrolytes, κa is normally larger than 1000 and $-jJ_1(j\kappa a)/J_0(j\kappa a) \approx 1$. Thus, Eq.(6.2.14) could be simplified to

$$\rho_d \pi a^2 \left[s\frac{d^2 s}{dt^2} + \left(\frac{ds}{dt}\right)^2 \right] = 2\pi a \left[\gamma_{lv}cos(\theta) - s(t) E_1 \epsilon_1 \kappa\psi_s - \frac{\mu\kappa}{1 - \beta\kappa} s(t) \frac{ds}{dt} \right]$$ (6.2.15)

If a total external potential Δu is applied across the two ends of a microchannel (as shown in Figure 6.2), the strength of electric field in solution E_1 and in vapor E_2 across the liquid-vapor interface will satisfy the following relationships:

$$\epsilon_1 E_1 = \epsilon_2 E_2$$

$$E_1 = \frac{\Delta u \epsilon_2}{\epsilon_1 l + (\epsilon_2 - \epsilon_1)s} .$$ (6.2.16)

156
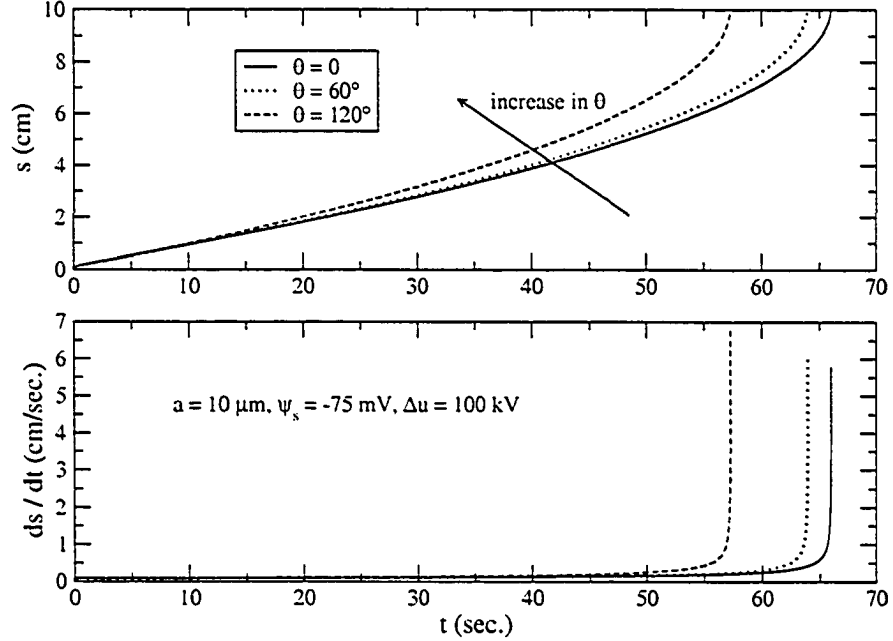
Figure 6.3: Dynamic behavior of electroosmotic flow (EOF) for a 0.01 M 1:1 electrolyte solution in a 10 μm circular microchannel with different surface hydrophobicities when the applied electric potential Δu is 100 kV.

When $s = l$, $E_1 = \Delta u/l$ and the flow is continuous. The initial conditions for Eq.(6.2.14) or (6.2.15) are $s(0) = 0$ and $ds(0)/dt = 0$ at $t = 0$. However, Eqs.(6.2.14) or (6.2.15) has a singularity at $t = 0$; thus, we have selected $s(0) = s_0$ and $ds(0)/dt = 0$ as the new initial conditions, where s_0 is a very small initial travel distance by the liquid front.

6.3 Parametric study and discussion

We study here the effects of surface hydrophobicity and Laplace pressure on EOF. Using a 1:1 electrolyte solution, we have selected the following values for our calculations: $T = 298$ K, $\epsilon_1 = 78.5 \times 8.854 \times 10^{-12}$ CV^{-1}m^{-1}, $\epsilon_2 = 8.854 \times 10^{-12}$ CV^{-1}m^{-1} $\gamma_{lv} = 72.8$ mJ/m^2, $a = 10$ μm, $\delta = 0.282$ nm, $\rho_d = 10^3$ kg/m^3, $\mu = 0.9 \times 10^{-3}$ kg

157

$m^{-1}s^{-1}$, $l = 10$ cm, $s_0 = 0.1$ cm and $\psi_s = -75$ mV. It is noted that Debye-Hückel approximation still provides a good agreement with experiments when zeta potential is up to 100 mV [33]. Here we set the surface potential ψ_s to be a constant in all subsequent calculations. In fact, the value of ψ_s depends on the channel wall material, concentration and pH of solution. In terms of α in Eq.(6.2.8), no description has been given for its determination. We have employed the assumption made by Tolstoi [173] that $\alpha A = \pi \delta^2 / 6$.

Figure 6.3 displays the dynamics of electroosmotic flow for different surface hydrophobicities in terms of the traveled distance s and velocity ds/dt with $\alpha = 1/6$. The variations of surface hydrophobicity and slip coefficient are reflected by selecting a range of contact angles from 0 to 120° with an applied potential Δu of 100 kV. The results suggest that EOF with surfaces having $\theta = 0°$ is slowest; while that for a higher angle $\theta = 120°$ is fastest. Nevertheless, the traveled distance and instantaneous velocity for all cases are nearly identical until the moving front has traveled to $s \sim 5$ cm, i.e., half of the entire channel. For $s > 5$ cm, the instantaneous velocity of the moving front increases drastically near the end of the microchannel for $\theta = 120°$. It is noted that such a small difference in the traveled distance and velocity between $\theta = 0°$ and 120° during the early part of an actual EOF experiment might not be easily detected. It is also clear from Figure 6.3 that the effect of surface hydrophobicity on flow velocity becomes increasingly important only when the liquid front approaches the end of the channel which, however, could not be easily observed experimentally as the liquid front has already traveled near the end of the electrode. The end velocities at $s = 10$ cm are 5.8 cm/s, 6.0 cm/s and 6.9 cm/s for $\theta = 0°$, 60° and 120°, respectively, and they represent the steady-state continuum velocities without a moving capillary front. From these results, we found that the more hydrophobic the surfaces, the faster the flow velocity; and the presence of a moving capillary front has very little effect on the EOF.

158

Closer scrutiny, however, suggests a different story. To elucidate this, we reduced the applied potential Δu from 100 kV to 10 kV and replotted the result in Figure 6.4. From the results, an opposite trend is apparent: the EOF takes longer to travel ($s = 10$ cm) as the contact angle increases, contrary to the results shown in Figure 6.3. Intuitively, increase in surface hydrophobicity should reduce the solid-liquid interaction (adhesion) and hence faster EOF (i.e., liquid slips). This expectation is not met in Figure 6.4. In fact, increase in the contact angle causes a larger Laplace pressure that suppresses EOF and hinders flow performance. A given amount of body force by electric field is required to overcome this resistance. As the external potential is reduced from 100 kV to 10 kV in this geometry, the body force by electric field is on the order of the Laplace pressure. Thus, the electric field is working against the capillary pressure. The increase in slip velocity as a result of a higher contact angle could not compensate for the increase in this capillary pressure: the more hydrophobic the surfaces, the longer it takes to travel a given distance, e.g., 10 cm. The maximum allowable contact angle θ in this system is found to be 107°. For $\theta > 107°$, the Laplace pressure is too strong to be overcome by the electric field Δu of 10 kV; and the liquid simply does not move. The resulting velocities at 10 cm for $\theta = 0°$, 30° and 107° are, respectively, 0.58 cm/s, 0.6 cm/s and 0.66 cm/s. These represent the continuum flow velocities that increase with the contact angle (i.e. surface hydrophobicity), contrary to the actual traveled time shown in Figure 6.4. Thus, the continuum methods without consideration of a moving capillary front contain no information on the capillary pressure and is inadequate to describe the loading process of EOF when a liquid-vapor interface is presented.

6.4 Conclusions

The presence of a liquid-vapor interface affects the hydrodynamic behavior of electroosmotic flow (EOF) with a moving capillary front. We have provided a model

159

Electroosmosis flow with a capillary moving front
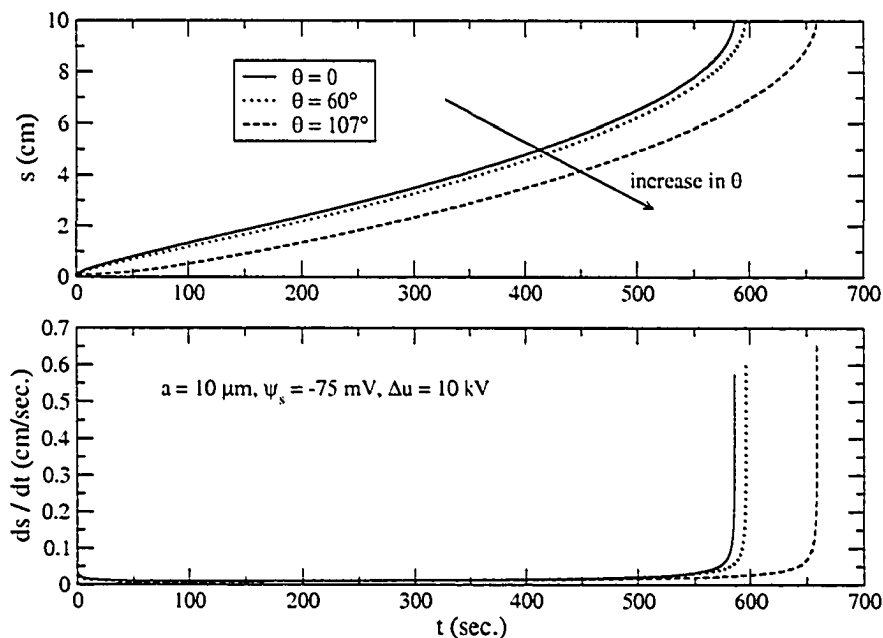
Figure 6.4: Dynamic behavior of electroosmotic flow (EOF) for a 0.01 M 1:1 electrolyte solution in a 10 μm circular microchannel with different surface hydrophobicities when the applied electric potential Δu is 10 kV. For $\theta > 107°$, the electric field cannot overcome the Laplace pressure, resulting in zero flow velocity.

for EOF by consideration of a liquid-vapor interface with a Laplace pressure and the solid-liquid interaction as slip. While liquid slip on hydrophobic surfaces increases flow velocity, the presence of a capillary pressure across the liquid-vapor interface can suppress EOF and decrease flow performance significantly. The continuum description of EOF is shown to be inadequate during the loading process when a liquid-vapor capillary front is presented. There is no clear trend for the effect of surface hydrophobicity on EOF and the outcome depends strongly on whether the applied electric field could overcome the resistance given by the Laplace pressure.

160

Chapter 7

Further Discussion beyond Possion-Boltzmann Model

7.1 Introduction

Poisson-Boltzmann equation is the most popular model of EDL and has been success-fully applied for many problems. However, it still suffer from several defects. These imperfections include [32]

1. The finite sizes of the ions are neglected.

2. Non-Coulombic interaction between counter- and co-ions and surface is disre-garded.

3. Incomplete dissociation of the electrolyte is ignored.

4. The solvent is consider to be primitive.

5. The surface charge is assumed to be homogeneous and smeared-out.

6. Image forces between ions and the surface are neglected.

Ion size is an obvious feature, which should be considered, especially for a very narrow microchannel. When the surface potential is higher than 100mV, Poisson-Boltzmann equation predicts local concentrations far exceeding the space physically available [32]. Ion-ion correlations are still very important and should appear in Poisson-Boltzmann

161

equation. If the surface charge is not homogeneous, image forces in the solid also play an important role.

To overcome Poisson-Boltzmann equation's shortcomings, some improvements have been done in recent thirty years [39, 40, 41, 42, 43, 44, 45]. Basically, all new models come from the statistical mechanics. Monte Carlo (MC) method has been used to simulate EDL near a charged wall [176, 177, 178, 179]. Molecular dynamics (MD) method has also been used to calculate the charge distributions and some thermodynamic parameters of EDL in a charged micropore [180, 181]. Integral equation theory has been used to model ionic profiles in EDL. The hypernetted chain (HNC) and mean spherical approximation (MSA) equations are accurate to describe the primitive electrolyte near a planar layer [182, 183]. A review about electric double layer from the statistical mechanics point of view has been published [46]. Two systematical study of EDL by integral equation theory should be mentioned here: Cassou's hypernetted chain-mean spherical (HNC/MS) integral equation [40, 41, 42] and Outhwaite's modified Poisson-Boltzmann equation [44, 45, 184, 185]. The former reflects the ionic size effect, ionic concentration effect and ionic interaction. Other than the above effects, the latter model includes the image force of solid surface.

Obviously, more molecular parameters are involved in those model and more expensive computation are required. The question remains: How much improvement do those models make? In this chapter, we use Outhwaite's modified Poisson-Boltzmann equation (MPB) to compare with three currently popular models: linearized Poisson-Boltzmann equation with Debye-Hückel approximation (LPB), Poisson-Boltzmann equation (PB), modified Gouy-Chapman model (MGC). Using five different exclusion-volume terms, Outhwaite proposed five models named MPB1, MPB2, MPB3, MPB4 and MPB5, respectively [44, 45, 184, 185]. Theoretically, MPB5 includes the most information of the electrolyte and needs more computational time. But, several simulation results of MPB4 were better than those of MPB5 [185]. Cui *et al.* chose MPB4

162

theory to study interface phenomena between two immiscible electrolyte solutions [186, 187, 188]. Here, we also choose MPB4 to simulate ionic and potential profiles of EDL.

7.2   Theory of models

Let us consider EDL of a $(z_0 : z_0)$ electrolyte in a parallel-plate microchannel (Figure 2.16), and Assume y' is the direction normal to the planar plate and the origin at the microchannel wall 1.2. Poisson-Boltzmann equation (PB) and its boundary conditions are

$$\frac{\partial^2 \frac{z_0 e \psi(y)}{kT}}{\partial y^2} = \kappa^2 \sinh\left(\frac{z_0 e \psi(y)}{kT}\right) ,$$

$$\psi(h) = \psi_s \text{ and } \psi(\infty) = 0 \text{ or } \frac{\partial \psi(\infty)}{\partial y} = 0 . \tag{7.2.1}$$

The linearized Poisson-Boltzmann equation (LPB) is

$$\frac{\partial^2 \psi(y)}{\partial y^2} = \kappa^2 \psi . \tag{7.2.2}$$

Burgreen and Nakache [55] obtained the completely analytical solution of Poisson-Boltzmann equation, Eqs. 7.2.1:

$$\kappa y = \alpha \left[F(\alpha, \frac{\pi}{2}) - F(\alpha, \theta) \right] , \tag{7.2.3}$$

where $F(\alpha, \theta)$ is the elliptic integral of the first kind and

$$\theta = \sin^{-1} \left[\frac{\cosh(\frac{e z_0 \psi(0)}{2kT})}{\cosh(\frac{e z_0 \psi(y)}{2kT})} \right] ,$$

$$\alpha = \left[\cosh(\frac{e z_0 \psi(0)}{2kT}) \right]^{-1} . \tag{7.2.4}$$

$\psi(0)$ is the potential at the center (y=0), which is defined by the expression:

$$\kappa h = \alpha \left[F(\alpha, \frac{\pi}{2}) - F(\alpha, \theta_0) \right] . \tag{7.2.5}$$

163

where θ_0 is defined by the following expression:

$$\theta = \sin^{-1} \left[\frac{\cosh(\frac{ez_0\psi(0)}{2kT})}{\cosh(\frac{ez_0\psi_s}{2kT})} \right] . \tag{7.2.6}$$

If h is much larger than κ^{-1}, Eq. 7.2.3 to Eq. 7.2.6 can be simplified as [34, 189]

$$\psi(y') = \frac{4kT}{ez_0} \tanh^{-1} \left[\tanh(\frac{ez_0\psi_s}{4kT}) exp(-\kappa y') \right] . \tag{7.2.7}$$

The modified Gouy-Chapman theory was proposed by Henderson and Blum [190] and Torrie and Valleau [191], which assumes ions form a plane at the closest approach to the solid surface. So that, the ionic size effect is included in such model. Then, the whole EDL are divided into two regions and potential can be expressed as:

$$\psi(y') = \frac{d\psi}{dy'}y' + \psi_s \quad , \quad 0 \le y' \le a_0/2 ,$$

$$\frac{\partial^2 \frac{z_0e\psi(y')}{kT}}{\partial y'^2} = \kappa^2 \sinh \left(\frac{z_0e\psi(y')}{kT} \right) \quad , \quad y' \ge a_0/2 , \tag{7.2.8}$$

where $\psi_s = \psi(y' = 0)$. The modified Gouy-Chapman theory (MGC) looks simple and reflects the ionic size effect. However, a more sophisticated model is needed to overcome more defects of Poisson-Boltzmann equation.

Here, we simply list used equations of Outhwaite's modified Poisson-Boltzmann theory [44, 45, 184, 185] in simulation. Like MGC model, the MPB theory devide the EDL into two regions. The MPB equation becomes:

$$\psi(y') = \frac{d\psi}{dy'}y' + \psi_s \quad , \quad 0 \le y' \le a_0/2 ,$$

$$\frac{\partial^2 \psi(y')}{\partial y'^2} = -\frac{1}{\epsilon} \sum_i z_i e n_\infty g_{0i}(y') \quad , \quad y' \le a_0/2 . \tag{7.2.9}$$

where $g_{0i}(y')$ is the singlet distribution function for an ion i at a normal distance y'

164

from the wall into the electrolyte. Other relative expressions are:

$$g_{0i}(y') = \xi_i exp\left\{-\frac{z_i e}{2kT}\left[\frac{z_i e}{4\pi\epsilon a_0}(F - F_0) + F\psi(y' + a_0) + F\psi(y' - a_0)\right.\right.$$
$$\left.\left. -\frac{F-1}{a_0}\int_{y'-a_0}^{y'+a_0}\psi X dX\right]\right\} ,$$

$$\xi_i(y') = 1 + \frac{8\pi a_0^3 n_\infty}{3} + \pi\sum_i n_\infty \int_{max(a_0/2, y'-a_0)}^{y'+a_0} [(X - y')^2 - a_0^2]g_{0i}(X)\, dX ,$$

$$\kappa'^2(y') = \frac{1}{\epsilon kT}\sum_i z_i^2 e^2 n_\infty g_{0i}(y') ,$$

$$F = (1 + f\delta_2)/[(1 + \kappa')(1 - f\delta_1)] \qquad y' \geqslant 3a_0/2 ,$$

$$f = (\epsilon - \epsilon_w)/(\epsilon + \epsilon_w) ,$$

$$F = (4 + f\delta_3)/[4 + \kappa'(a_0 + 2y') + f\delta_4] \qquad a_0/2 \leqslant y' \leqslant 3a_0/2 ,$$

$$\delta_2 = exp[2\kappa'(a_0 - y')]\sinh(\kappa'a_0)/(2\kappa'a_0) ,$$

$$\delta_1 = \delta_2[\kappa'a_0\cosh(\kappa'a_0) - \sinh(\kappa'a_0)]/[(1 + \kappa'a_0)\sinh(\kappa'a_0)] ,$$

$$\delta_3 = \{a_0 - 2y' + \sqrt{a_0^2 + 2a_0 y'} + 1/\kappa' - exp[\kappa'(\sqrt{a_0^2 + 2a_0 y'} - a_0 - 2y')]\}/y' ,$$

$$\delta_4 = \{\delta_3 - (a_0/y')(1 + exp[\kappa'(\sqrt{a_0^2 + 2a_0 y'} - a_0 - 2y')])\}$$

$$F_0 = \lim_{y'\to\infty} F = (1 + \kappa a_0)^{-1} , \quad \kappa = \lim_{y'\to\infty}\kappa' , \tag{7.2.10}$$

where $\xi_i(y')$ is the exclusive volume term, f is the imaging factor, ϵ_w is the dielectric constant of the wall, $\kappa'(y')$ is the local Debye-Hückel parameter and κ is the bulk Debye-Hückel length. Outhwaite provided a good numerical method to solve this modified Poisson-Boltzmann theory [44, 45, 184, 185, 192]. Note that, for the ion point limit of MPB ($a_0 \to 0$), MPB equation cannot reduce to traditional PB equation, since it still includes two correction: the local variation of the Debye-Hückel parameter κ' and the classical screened self-image term f [45].

In Figure 7.1, we plot the dimensionless mean electrostatic potentials $z_0 e\psi(y')/kT$ of MPB, MGC, PB, LPB, for 0.1976M and (1:1) electrolyte at $z_0 e\psi(y')/kT = 5.0$ and $f = 0$. Our result of MPB4 is the same as that in the Figure 2 of [44]. In this case, we find that these models make apparent difference only in a thin region of EDL.

165

Potential distribution of EDL
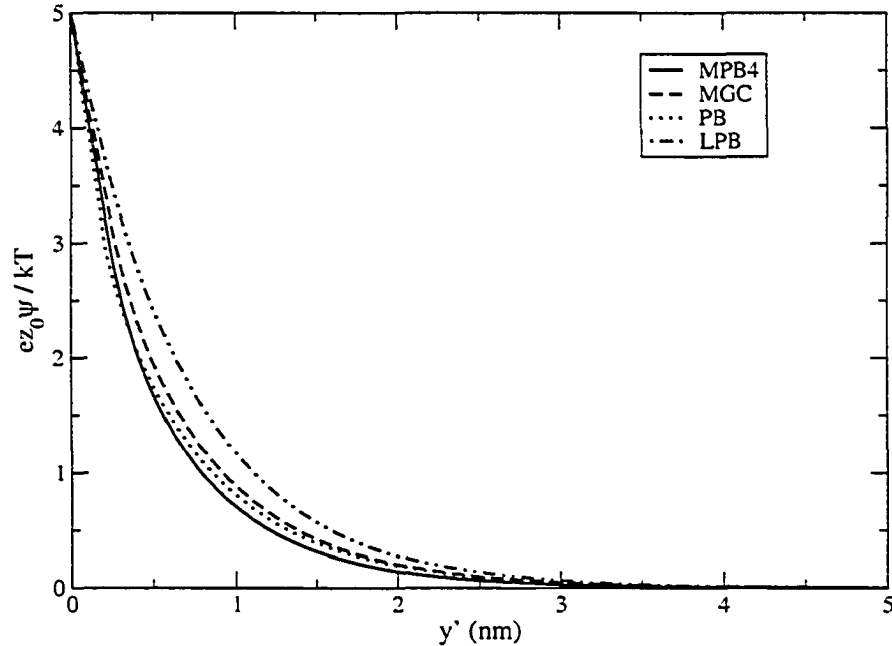
Figure 7.1: Dimensionless mean electrostatic potentials $z_0 e\psi(y')/kT$ of MPB, MGC, PB, LPB, for 0.1976M and (1:1) electrolyte at $z_0 e\psi(y')/kT = 5.0$, $a_0 = 0.425nm$ and $f = 0$.

Out of the distance 4 nm from the solid wall, all these models have no distinguished difference. If $\epsilon_w \rightarrow \infty$, $f \rightarrow -1$; and if $\epsilon_w \rightarrow 1$, $f \rightarrow 0.975$. The above two cases correspond to the highest and lowest limitation of image factors. The former corresponds to a metallic surface; the latter coresponds to a isulating surface. Most of glass has the dielectric constant at the order of 10. Here, we choose 5 as glass's dielectric constant, so that $f = 0.88$. In Figure 7.2, we only can find slight difference among these results with different image factors. So, in this case, image force has a weak effect. In Figure 7.3, we plot the dimensionless mean electrostatic potentials $z_0 e\psi(y')/kT$ predicted by MPB4 for different ionic sizes. K^+ is of radius 0.138 nm; Na^+ is of 0.102 nm; Li^+ is of 0.076 nm. We find that ionic sizes significantly affect potential profile.

166

Potential distribution of EDL
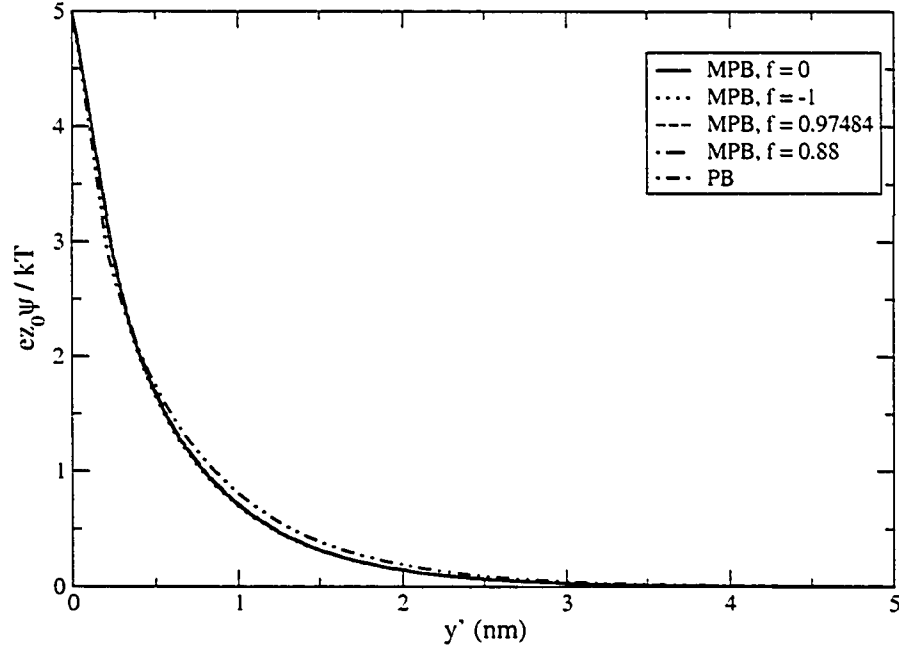
Figure 7.2: Dimensionless mean electrostatic potentials $z_0 e\psi(y')/kT$ of PB and MPB, for 0.1976M and (1:1) electrolyte at $z_0 e\psi(y')/kT = 5.0$, $a_0 = 0.425nm$ and different image factors.

7.3 MPB theory for electrokinetic flow in microchannels

For the parallel-plate microchannel (Figure 2.16), all dimensional controlling equations are:

$$\frac{\partial^2 \psi(y)}{\partial y^2} = \kappa^2 \psi$$

$$\psi(\pm h) = \psi_s \quad , \quad \frac{\partial \psi}{\partial y}(0) = 0 , \qquad (7.3.1)$$

$$-\frac{1}{\mu}\frac{\partial p}{\partial z} + \frac{\partial^2 v}{\partial^2 y} + \frac{1}{\mu}\rho E_z' = \frac{1}{\nu}\frac{\partial v}{\partial t} ,$$

$$v(h,t) = \beta\frac{\partial v}{\partial y}(h,t) \quad , \quad \frac{\partial v}{\partial y}(0,t) = 0 , \qquad (7.3.2)$$

167

Potential distribution of EDL
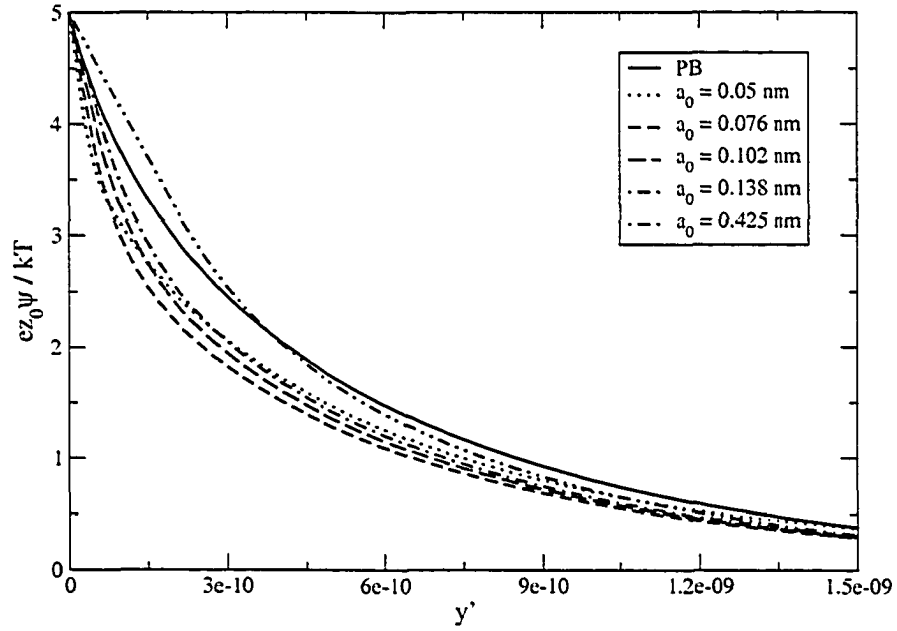
Figure 7.3: Dimensionless mean electrostatic potentials $z_0 e\psi(y')/kT$ of PB and MPB, for 0.1976M and (1:1) electrolyte at $z_0 e\psi(y')/kT = 5.0$, $f = 0$ and different ionic sizes.

The definition of volumetric flow rate, q, per unit width of the parallel plate is

$$q = 2 \int_0^h v \, dy \, , \tag{7.3.3}$$

whereas the electric current is

$$i(t) = 2 \int_0^h \rho v dy + \frac{2z_0^2 e^2 n_\infty D}{kT}(2h)E_z' \, , \tag{7.3.4}$$

168

where we can define $\frac{2z_0^2 e^2 n_\infty D}{KT} = \sigma$, conductivity of electrolyte [38]. Using LPB model, we obtain the dimensional velocity, current and flow rate.

$$v_P(y) = \frac{1}{2\mu}(h^2 - y^2 - 2\beta h) \,,$$

$$v_E(y) = \frac{\epsilon\psi_s}{\mu}\left(\frac{\cosh(\kappa y)}{\cosh(\kappa h)} - 1 + \beta\kappa\frac{\sinh\kappa h}{\cosh\kappa h}\right) \,,$$

$$i_P = -\frac{2\epsilon\psi_s h}{\mu}\left[1 - \frac{\sinh(\kappa h)}{\kappa h\cosh(\kappa h)} - \beta\kappa\frac{\sinh(\kappa h)}{\cosh(\kappa h)}\right] \,,$$

$$i_E = -\frac{2\kappa^2\epsilon^2\psi_s^2}{\mu\cosh(\kappa h)}\left[\frac{1}{\cosh(\kappa h)}\left(\frac{h}{2} + \frac{\sinh(\kappa h)\cosh(\kappa h)}{2\kappa}\right) - \frac{\sinh(\kappa h)}{\kappa}\right.$$
$$\left. + \beta\frac{\sinh^2(\kappa h)}{\cosh\kappa h}\right] + 2h\sigma \,,$$

$$q_P = \frac{1}{\mu}(\frac{2}{3}h^3 - 2\beta h^2) \,,$$

$$q_E = \frac{2h\epsilon\psi_s}{\mu}\left(\frac{1}{\kappa h}\frac{\sinh(\kappa h)}{\cosh(\kappa h)} - 1 + \beta\kappa\frac{\sinh(\kappa h)}{\cosh(\kappa h)}\right) \,. \tag{7.3.5}$$

If we use MGC, MPB, we cannot obtain exact analytical solutions of electrokinetic flow. However, solving Poisson equation and Navier-Stokes equation and using definitions of current and flow rate, we can obtain semi-analytical solutions:

$$v_P(y) = \frac{1}{2\mu}(h^2 - y^2 - 2\beta h) \,,$$

$$v_E(y) = \frac{\epsilon}{\mu}\left(\psi(y) - \psi_s + \beta\frac{d\psi(y)}{dy}\big|_{y=h}\right)$$

$$i_P = \frac{\epsilon}{\mu}\left(-2\psi_s h + 2\int_0^h \psi(y)dy + 2\beta h\frac{d\psi(y)}{dy}\big|_{y=h}\right)$$

$$i_E = \frac{2\epsilon^2}{\mu}\left[-\int_0^h\left(\frac{d\psi}{dy}\right)^2 dy + \beta\left(\frac{d\psi(y)}{dy}\big|_{y=h}\right)^2\right] + 2h\sigma \,,$$

$$q_P = \frac{1}{\mu}(\frac{2}{3}h^3 - 2\beta h^2) \,,$$

$$q_E = \frac{2\epsilon}{\mu}\left[\int_0^h \psi(y)\, dy + h\left(\beta\frac{d\psi(y)}{dy}\big|_{y=h} - \psi_s\right)\right] \tag{7.3.6}$$

Assuming 0.1M KCl electrlyte, we use the following parameters: surface potential $\psi_s = -100$ mV, conductivity $\sigma = 1.28217$ S/m [38], $h = 10$ μm, $\mu = 0.9 \times 10^{-3}$ kgm^{-1}s^{-1}, $\epsilon = 78.5 \times 8.854 \times 10^{-12}$ CV^{-1}m^{-1}, $\rho = 10^3$ kgm^{-3}, $e = 1.6021 \times 10^{-19}$ C,

169

$-\partial p/\partial z = 1 \times 10^6$ Pa m^{-1} (for pressure driven flow), $E'_z = 10^5$ Vm^{-1} (for electric field driven flow). Using LPB, PB, and MPB models, we list the strengths of streaming potentials, the flow rates of pressure driven flows and the flow rates of electric field driven flows in Table 7.1 for $\beta = 0$ and in Table 7.2 for $\beta = -0.1\mu$m. If $\beta = 0$ (without slip), from Table 7.1, we find LPB, PB, and MPB give out very close results of strengths of streaming potentials, flow rates of pressure driven flows and flow rates of electric field driven flows. To find deviation caused by different models for electrokinetic slip flows, we choose a slip length $\beta = -0.1$ μm in Table 7.2. We find models have significant effects on the strength of streaming potentials and the flow rates of electric field driven flows, but not on the flow rates of pressure driven flows. These parametric study is based on an assumption that we can change slip length and surface potential independently. However, it is a big challenge to make a hydrophobic surface with high surface potential. Because the differences among LPB, PB and MPB become smaller for lower surface potential, the differences of the strength of streaming potential and the flow rate of electric field driven flow induced by models should decrease. For electric field driven flow, considering the effect of external electric field on ionic distribution, we cannot conclude which model is better. Experiemental results are needed.

Table 7.1: Comparison of the the strengths of streaming potentials, the flow rates of pressure driven flows and the flow rates of electric field driven flows for LPB, PB and MPB at $\beta = 0$

	E'_z (V/m) for pressure driven flow	q (m^3/s) for pressure driven flow	q (m^3/s) for electric field driven flow
LPB	-0.0602122	7.40741×10^{-7}	1.54438×10^{-8}
PB	-0.0602441	7.40741×10^{-7}	1.54441×10^{-8}
MPB	-0.0602328	7.40741×10^{-7}	1.54445×10^{-8}

170

Table 7.2: Comparison of the the strengths of streaming potentials, the flow rates of pressure driven flows and the flow rates of electric field driven flows for LPB, PB and MPB at $\beta = -0.1 \ \mu$m.

	E'_z (V/m) for pressure driven flow	q (m^3/s) for pressure driven flow	q (m^3/s) for electric field driven flow
LPB	-6.62121	7.61889×10^{-7}	1.62143×10^{-6}
PB	-12.9245	7.59283×10^{-7}	2.84699×10^{-6}
MPB	-12.684	7.59402×10^{-7}	2.08075×10^{-6}

7.4 Conclusions

Beyond the Poisson-Boltzmann equation, we use modified Poisson-Boltzmann model to study potential and charge density distribution of EDL. The difference of potential profiles between these models is only found in the 1-2 nm range from the solid surface. Furthermore, we compare electrokinetic slip flow described by the modified Poisson-Boltzmann model with those predicted by the Poisson-Boltzmann equation and the linearized Poisson-Boltzmann equation. By considering a hydrophobic surface with low surface potential, the Poisson-Boltzmann equation is adequate for microchannel flow. This research is also a good stating point for nanofluidics, since ionic size effect, image force effect and local Debye-Hückel parameter effect are included in MPB theory. For extremely strong external electric field, we need experimental results to verify the validities of those models.

171

Chapter 8

A Promising Slip Coating: Self-Assembled Monolayers (SAMs) and Experiments

8.1 Introduction

A recent advance in the fabrication of nanoscale coatings is the use of the so-called Self-Assembled Monolayers (SAMs) [193, 194, 195, 196]. These films are two-dimensional organic assemblies that form by the spontaneous adsorption of functionalized, long-chain molecules onto metal or metal oxide supports. They provide models to systematically study a wide range of interface/surface phenomena. The organic and biological properties of these films are largely controlled by the end groups of the molecules and can be manipulated by tailoring the end functional groups. SAMs are of technical interest for the fabrication of sensors, protective layers, lubrication, and as patternable materials [156]. They provide a pathway for a better understanding of many technological systems where interfacial events play a dominant role.

The history of SAMs can be traced to the earlier papers of Zisman *et al.* [197], where glass surfaces were exposed to dilute solutions of long-chained alcohols in hexadecane. Oriented monolayer films were then formed on the substrate that were not wetted by the solvent. Zisman et al. further studied various surfactant-like molecules including long-chained amines, carboxylic acids and amides on metal and metal oxide

172

surfaces [198, 199]. The systems considered by Zisman et al. exhibit only modest stabilities and were limited only to low-energy hydrophobic surfaces. Nuzzo *et al.* [200] later extended Zisman's approach by relying on a stronger and specific interactions between sulphur and gold for molecular self-assembly. The specific interaction between gold and sulfur allows adsorption of thiols not only onto gold, but also other surfaces such as silver, copper, mercury, GaAs and InP. The mechanism of such self-assembly originated from a large interfacial driving energy when those of the metal substrates are reduced. This specific adsorption is stronger than the physisorbed molecular film by the Langmuir-Blodgett technique which relies on packing of molecules and subsequently transfer to surfaces. Among the metals for self-assembly, self-assembled monolayers (SAMs) derived from the adsorption of organothiols onto gold have been extensively investigated for studying their potential uses as corrosion inhibitors, resist layers, components of chemical sensors, and models for organic and biological surfaces.

As a nanoscale coating for MEMS devices, SAMs exhibit many advantages, such as ease of preparation, low density of defects to be useful in many applications, amenable to vary interfacical properties (physical, chemical, electrochemical and biochemical) [156], and small thickness on the order of nanometers. Comparing with the thickness of traditional polymer coating on the order of μm, SAMs is certainly the best choice to control interface/surface properties of microchannels.

8.2 Effect of polycrystallinity on wettability of SAMs

SAMs is a single atomic layer of long-chain molecules. Intuitively, the surface properties of SAMs coatings should be determined by the exposed end functional groups. However, formation of SAMs can be influenced by surface nanostructre and the adsorption process of molecular self-assemby. In this section, we will study effects of polycrystallinity of substrates on hydrophobicity of SAMs by means of contact angle ,

Ellipsometry, Fourier Transform Infrared Spectroscopy (FTIR) and the Atomic Force Microscopy (AFM) measurment.

8.2.1 Experimental section

Materials

Silicon wafers of test grade were obtained from Wafer World (West Palm Beach, FL) in circular discs of about 10 cm diameter and were cut into rectangular shapes of about 2.5 cm × 5 cm. Gold shot (99.999%) and titianium shot (99.995%) were obtained from Kurt J. Lesker (Clairton, PA). Ethanol (100%) was obtained from the Chemistry Dept. at the University of Alberta. Octadecanethiol [$CH_3(CH_2)_{17}SH$] was obtained from Aldrich and used as received. Six liquids were chosen for contact angle measurements. Selection was based on the following criteria: (1) they should include a wide range of intermolecular forces; (2) they should be non-toxic; and (3) the liquid surface tension should be higher than the anticipated solid surface tension [201].

Preparation of SAMs

Supported gold films were prepared by sequentially evaporating titanium ($\sim$ 10 nm) and gold ($\sim$ 100 nm) onto small rectangular silicon wafers in a diffusion-pumped vacuum chamber at $\sim 10^{-6}$ torr. The chamber was backfilled with air and the substrates were used within 48 h of preparation. The evaporated surfaces were rinsed with ethanol before SAMs formation. SAMs were prepared by immersing into 1 mM of $CH_3(CH_2)_{17}SH$ in ethanol overnight. The resulting surfaces were rinsed with ethanol and blown dry by nitrogen before use. Evaporated gold substrates were also flame annealed for $\sim$ 30 s using a bunsen burner under ambient laboratory condition. After $\sim$ 1 minute, the annealed substrate was then immersed into 1 mM of $CH_3(CH_2)_{17}SH$ in ethanol overnight [109].

174

Characterization of SAMs

SAMs were first characterized by a Sopra GES5 Variable Angle Spectroscopic Ellipsometer. The ellipsometry measurements were performed using a rotating polarizer in the tracking analyzer mode. A broad band of light (300 to 850 nm) from a 75 W Xe-arc lamp is linearly polarized and directed onto the film surface at an incident angle of 75° from the surface normal. Each bare gold substrate were measured by the ellipsometer as references immediately after evaporation. After immersion into 1 mM of octadecanethiol/ethanol solution overnight, a new set of data for each substrate were measured again using an ambient-film-substrate model for regression with known refractive index (n and k) for octadecanethiol absorbed onto gold. The refractive index for octadecanethiol absorbed onto gold as a function of wavelength was independently obtained from a Sopra GXR Grazing X-ray Reflectometer, rather than assuming an index of refraction (e.g. $n = 1.46$) at a given wavelength (e.g. $\lambda = 6328$ Å) as typically performed in the literature. Such spectroscopic measurements are expected to provide more accurate results in ellipsometer thickness since the optical constants for a range of wavelengths were used simultaneously.

Reflectance Infrared spectra of SAM of octadecanethiol onto Au were obtained using a ThermoNicolet Nexus 670 spectrometer equipped with a VeeMax glazing angle accessory. A p-polarized light was incident at 70° from the surface normal and the reflected light was detected by means of a MCT-A detector cooled with liquid nitrogen. The spectra resolution was 2 cm^{-1}. Spectra were referenced to the corresponding bare (anneal and non-annealed) Au substrates and 1024 scans were obtained for good signal-to-noise ratios. An infrared gain of 2 was selected for all reflectance infrared (IR) measurements to ensure that the input IR signals are constant. Samples were rinsed with ethanol and blown dry by N_2 prior to characterization.

The atomic force Microscopy (AFM) measurements were performed using a Digital

Instruments Nanoscope IIIa atomic force microscope (Digital Instruments, Santa Barbara, CA). Standard silicon nitride cantilevered probes were used with a force/spring constant in the range between 0.06 – 0.58 N/m. The AFM images of annealed and non-annealed Au surfaces were captured by using contact mode under ambient laboratory conditions. The surfaces were cut into 1 cm × 1 cm samples to fit onto a 1.5 cm × 1.5 cm sample stage.

Contact angle measurements

Contact angle is an accurate and sensitive method to determine wettability (surface tensions) of solid surfaces. By means of low-rate dynamic contact angle measurements using an automated drop shape analysis, Kwok et al. [85, 202, 203, 204] systematically studied contact angles of a series of liquids with continuously varying surface tension on various polymer-coated silicon wafer surfaces.

Characterizations by Ellipsometry, FT-IR and AFM

The ellipsometer thickness for octadecanethiol $CH_3(CH_2)_{17}SH$ absorbed onto annealed gold was consistently 21Å; whereas that formed on the non-annealed Au varied between 20–21Å. While this difference is not statistically significant, we noticed that the experimental $\tan \Psi$ and $\cos \Delta$ for the non-annealed-Au samples did not always match those of the theoretical curves. Nevertheless, our thicknesses are consistent with those reported in the literature [215].

The reflectance spectra for SAMs derived from octadecanethiol on Au and annealed-Au are shown in Figure 8.1. In the both spectra of Figure 8.1, the asymmetric methylene peaks appeared at ~ 2918 cm^{-1}. This indicates a primarily trans-zigzag extended hydrocarbon chain with few gauche conformers. Both spectra demonstrate that SAMs of octadecanethiol absorbed onto Au and annealed Au are highly crystalline. However, the intensities of the methylene peaks are larger on Au and smaller on the annealed Au. The difference in the peak intensity could reflect different canted

176
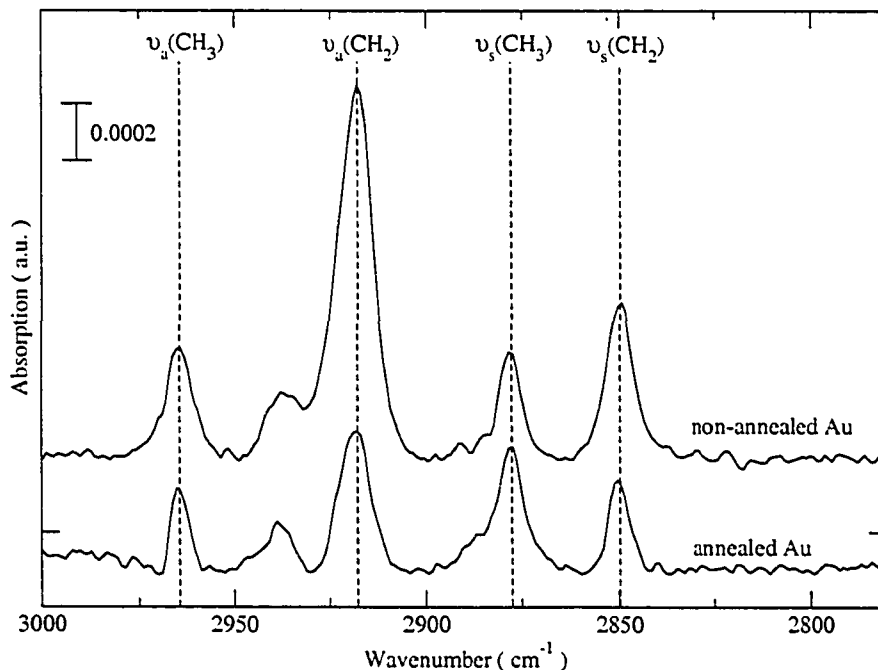
Figure 8.1: Grazing incidence polarized infrared spectra for SAMs of octadecanethiol $CH_3(CH_2)_{17}SH$ absorbed onto evaporated (non-annealed) and annealed gold. The approximate positions of the methylene modes are 2918 (asym) and 2850 (sym) cm^{-1}, and those for the methyl modes are 2964 (asym), 2935 (sym, Fermi resonance), and 2879 (sym) cm^{-1}. The spectra have been offset vertically for clarity.

orientations for the polymethylene chains on these surfaces or different amount of the polymethylene chains that the IR detected. Since the tilt of chain on the Au substrate for alkanethiolate SAMs is known to be $\sim 30°$ and this structural orientation is unlikely to be changed by annealing, we speculate that the difference in the intensity of the asymmetric and symmetric methylene peaks appear at ~ 2918 cm^{-1} and 2850 cm^{-1} indicates different amount of polymethylene chains that were detected by the IR. The spectrum for the adsorbed layer of octadecanethiol on non-annealed-Au exhibits a higher dichroic ratio (~ 2) for the methylene adsorption modes $[\nu_a(CH_2)/\nu_s(CH_2)]$; and that on the annealed-Au exhibits a much lower dichroic ratio (~ 1.3). We also note that the intensities of the methyl modes at 2964 (asym), 2935 (sym, Fermi resonance), and 2879 (sym) cm^{-1} for the two substrates in Figure 8.1 are similar. These features in the spectra provide evidence that SAM of octadecanethiol on the

177
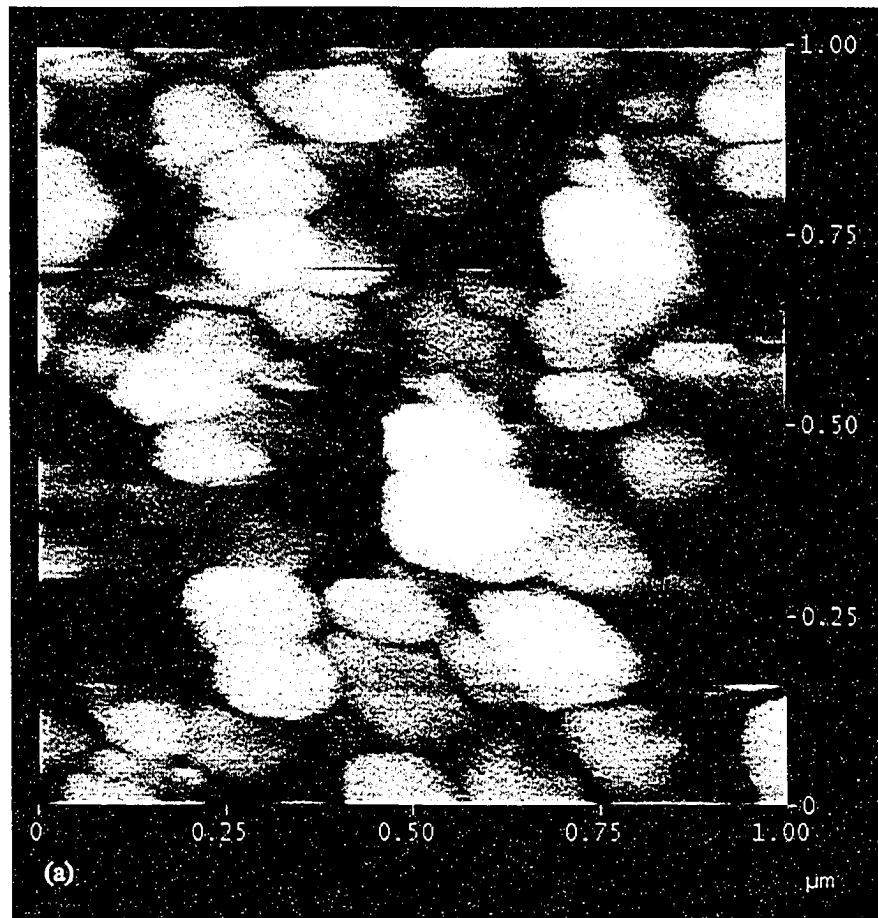
Figure 8.2: AFM images of annealed Au for a scan size of 1 μm.

non-annealed Au has a structure that is not the same as that on the annealed Au. Independent AFM images shown in Figures 8.2 and 8.2 suggest that the annealed Au has larger terraces [as much as 200 nm]; while that of the non-annealed Au has much smaller gold steps [109].

178
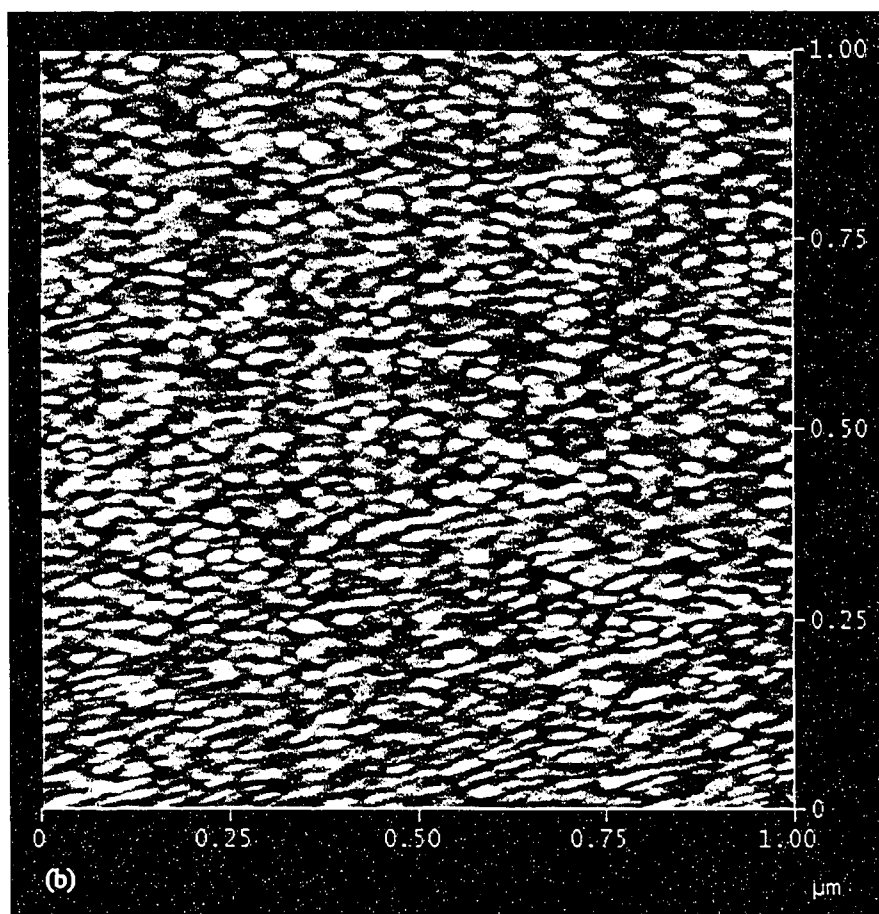
Figure 8.3: AFM images of non-annealed Au for a scan size of 1 μm.

8.3 Experimental investigation of liquid slippage on SAMs

In this section, we will investigate the slippage of flow on SAMs coatings. Octade-canethiol SAMs on annealed and non-annealed gold substrates are used as hydrophobic coating. 16-Mercaptohexadecanoic acid [$HS(CH_2)_{15}CO_2H$] SAM is used as a hydrophilic coating.

In our experiments, we assume that if a liquid can wet a lyophobic coating, the liquid does not slip in microchannels with such coating. Vinogradova [86] pointed out that the advancing contact angle $\theta_a \geq 70°$ is the threshold advancing contact angle of

179
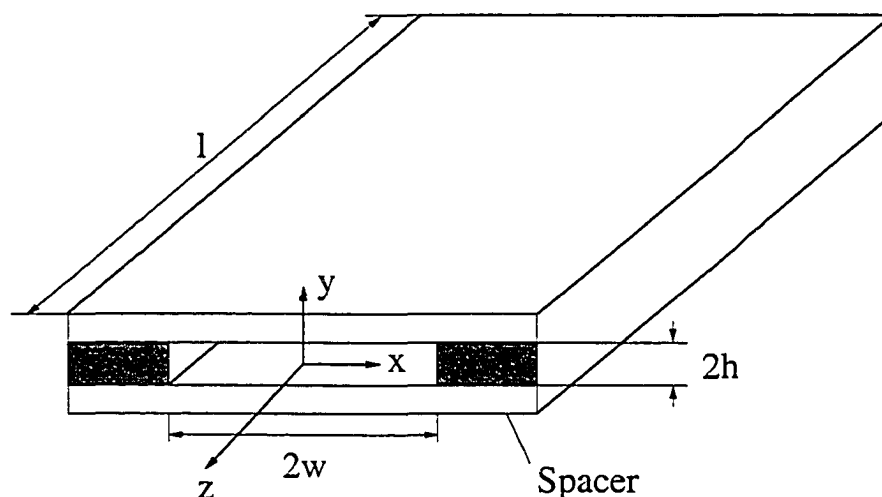
Figure 8.4: Illustration of the microchannel formed between two microscope slides

slippage. Churaev $et\ al.$ [174] observed flow increase in capillaries with $\theta_a \geq 70°$, but not in capillaries with $\theta_a < 70°$. Baudry [227] did not observe slippage of glycerol on a surface with $\theta_a = 62°$. Here, we use ethanol as the wetting liquid. The liquid-vapor surface tension of ethanol, γ_{lv}, is 21.97 mJ/m^2; while that of the octadecanethiol SAM is known to be 20 mJ/m^2 [109]. Ethanol should have a small contact angle on SAMs of octadecanethiol $CH_3(CH_2)_{17}SH$ absorbed onto thermally annealed Au or non-annealed Au.

As discussed in previous chapters, electroviscous phenomena and slippage have counter effects on the flows. Since electrokinetic phenomena are not the main objective of this experiments, we hope to independently study slippage of flow on octadecanethiol SAMs. Here, we use 0.001 M KCl solution as testing liquid. To eliminate electroviscous effects, we short the two electrodes between the inlet and outlet of the microchannel.

The microchannel actually has a rectangular cross section (see Figure 8.4). Since $w \gg h$, the rectangular microchannel can be considered a parallel-plate microchannel. Without electroviscous effects, the flow rate of flow in the parallel-plate microchannel

180
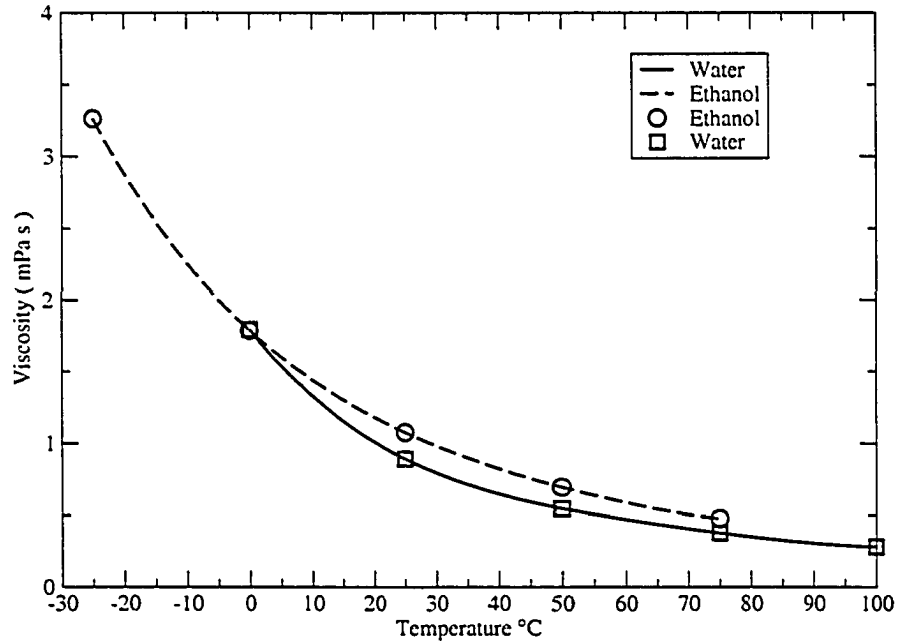
Figure 8.5: The viscosity of water and ethanol as a function of temperature

is

$$q = \frac{1}{\mu}\left(-\frac{dp}{dz}\right)\left(\frac{2}{3}h^3 - 2\beta h^2\right) .$$

(8.3.1)

Because liquids' viscosities change with temperature, we should record the temperature at real time to find corresponding viscosity at the temperature. In Table 8.1, we list the viscosities of ethanol and water at different temperatures [228]. In Figure 8.5, two functions of viscosities of water and ethanol, with respect to temperature, are obtained by fitting experimental data of Table 8.1 [229].

In experiments, the measured pressure drop is the total pressure drop, which includes pressure decay at inlet and outlet [66, 140]. In the entrance region, the flow was not a fully developed laminar flow. The entrance region length l_{in} is given by [66, 140]

$$l_{in} = 0.02(2h)Re \quad , \quad Re = \frac{\rho_d v_m D_h}{\mu} ,$$

(8.3.2)

181

Table 8.1: Viscosities of liquids

Temperature	Viscosity of water (mPa s)	Viscosity of ethanol (mPa s)
-25°		3.262
0°	1.793	1.786
25°	0.890	1.074
50°	0.547	0.694
75°	0.378	0.476
100°	0.282	

where $D_h = 4hw/(h+w)$ is hydraulic diameter of the rectangular microchannel Figure 8.4, ρ_d is density of liquid and v_m is the mean velocity. In this region, the pressure drop is calculated by

$$\Delta p_{in} = \frac{k_{in}\rho_d l_{in}}{2D_h} v_m^2 \, , \qquad (8.3.3)$$

where k_{in} is the friction coefficient given by [66, 140]

$$\Delta k_{in} = \frac{96}{Re} + \frac{1}{Re}\left[\frac{0.774}{l_{in}/4hRe} - \frac{0.00089}{(l_{in}/4hRe)^2}\right] \, , \qquad (8.3.4)$$

At the exit of the flow, the cross section is greatly increased. As the flow leaves the parallel slit microchannel, it becomes turbulent. The pressure decay at the outlet is estimated by [66, 140]

$$\Delta p_{out} = \frac{\rho_d}{2} v_m^2 \, , \qquad (8.3.5)$$

Thus, the flow rate and the pressure gradient in Eq. 8.3.1 are

$$q = \frac{q_{measured}}{2w} \, ,$$
$$\frac{dp}{dz} = \frac{\Delta p_{measured} - \Delta p_{in} - \Delta p_{out}}{l - l_{in}} \, . \qquad (8.3.6)$$

8.3.1 Experimental set-up

We constructed an experimental system shown in Figure 8.6. The precision pump delivers liquids to the test section from the testing liquid reservoir. The test section

182
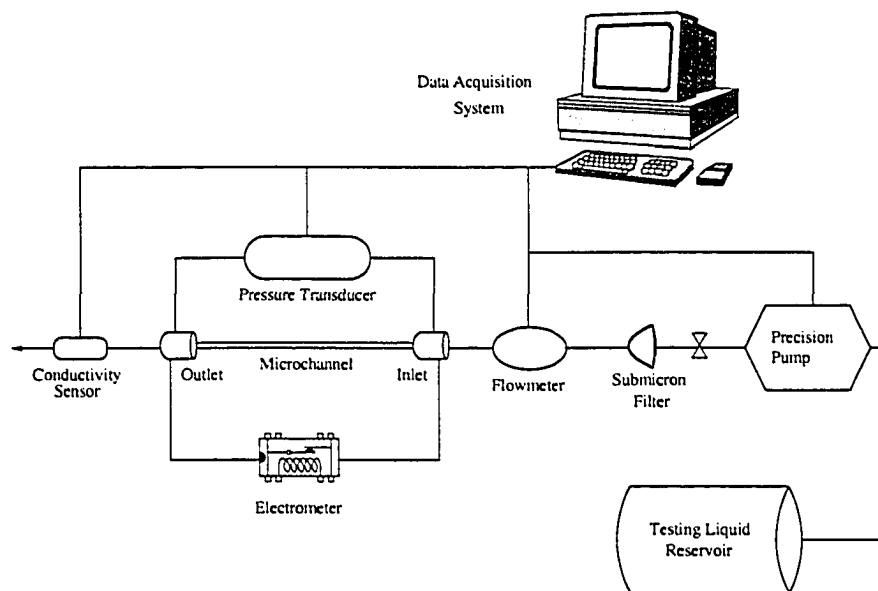
Figure 8.6: Schematic of the experimental system

includes a submicron filter, a flow-meter, an electro-meter, a pressure transducer, a microchannel, a data acquisition system and a conductivity sensor. The corresponding suppliers and operating ranges are illustrated in Table 8.2. Inlet and outlet of the microchannel will make up of two sumps to hold probes of electrometer and pressure transducer. All connection parts, valves, and tubings are plastic or Teflon to minimize the influence for conductivity. A stopwatch is used to measure the time it takes for accumulation. The weight of the collected liquid can be measured by an electronic balance. Thus, the flow rate can be calculated by the weight, time and liquid density. This redundant procedure provides an additional check on the reading from the flow meter and the precision pump. The tolerance of the flow rate provided by the precision pump is controlled within 1%.

183

Table 8.2: Equipments used for microchannel experimental setup.

Equipment	Supplier	Model #	Operating Range
Data acquisition system	Dycor	CIO-DAS08jr "Wizard" Software	8 channel
Flow-meter	Thermal Instruments	600-9/316SS/ Tube Connection	2.5 - 500 cc/h
Precision pump	ISCO	LC-5000	0.06 - 400 cc/h
Pressure transducer	Omega	PX26-030DV CX136-4	+/-30 psi
Conductivity sensor	WJF instrumentation	HI 710 HI 7639	0.0 - 199.9 mS/cm
Multimeter	Hewlett-Packard	HP 3478A	1mV - 10V
Filter	Fisher Scientific	Anotop25 Polycap75	5mL 5-25L

8.3.2 Experimental section

Materials

Microscope slides with size $25 \times 75 \times 1$ mm were obtained from Fisher Scientific. Deionized ultrafiltered (DIUF) water was obtained from Fisher Scientific. Strips of a thin plastic shim were obtained from Small Parts Inc.. Octadecanethiol [$CH_3(CH_2)_{17}SH$], 16-Mercaptohexadecanoic acid [$HS(CH_2)_{15}CO_2H$] and KCl were obtained from Aldrich. Ethanol (100%) was obtained from the Chemistry Dept. at the University of Alberta. Platinum electrodes were obtained from A-M Systems Inc.. Epoxy was obtained from Devcon.

Fabrication of microchannel

Microscope slides are firstly cutted into the size of $25 \times 45 \times 1$ mm. Supported gold films were prepared by sequentially evaporating titanium (~ 10 nm) and gold (~ 100 nm) onto the cut rectangular microscope slides in a diffusion-pumped vacuum chamber at $\sim 10^{-6}$ torr. The chamber was backfilled with air and the substrates were used within 48 h of preparation. The evaporated surfaces were rinsed with ethanol before SAMs

184

formation. Octadecanethiol or 16-Mercaptohexadecanoic acid SAMs were prepared by immersing into 1 mM of $CH_3(CH_2)_{17}SH$ or 1mM of $HS(CH_2)_{15}CO_2H$ in ethanol overnight. The resulting surfaces were rinsed with ethanol and blown dry by nitrogen before use. Some evaporated gold substrates were also flame annealed for $\sim$ 30 s using a bunsen burner under ambient laboratory condition. After $\sim$ 1 minute, the annealed substrate was then immersed into 1 mM of $CH_3(CH_2)_{17}SH$ in ethanol overnight.

After coating SAMs on microscope slides, to form a microchannel, two strips of a thin plastic shim were used as the spacer and put between a pair of silicon plates in the length direction along the sides of the plates, so that a flow passage of $2w$ width was formed. Then, a specially designed clapper, which can provide a constant torque, was used to fix the relative position of the plates and the thin spacers. Finally, epoxy resin was applied to bond the two microscope slides together and to seal all the openings except the inlet and outlet of the microchannel. The cross section of such microchannel is illustrated in Figure 8.4.

The width and length of the microchannel can be accurately measured by using a precision gauge. To determine the height of the microchannels was the biggest challenge. Since we try to detect the slip length, which is at the range from several nm to 1 or 2 μm, optical microscopes cannot guarantee enough resolution. Then the channel height was calibrated by an indirect method that involves the flow of a wetting liquid (ethanol) through the microchannel. For eliminating electroviscous effects, we always short current between the two electrodes. The liquid flow in such a case is basically a Poiseuille laminar flow. Therefore, the channel height can be determined from the measured pressure drop and flow rate by using the Poiseuille flow equation [66]. The channel heights determined in this way were used in this study.

185

Experimental data for -COOH microchannel
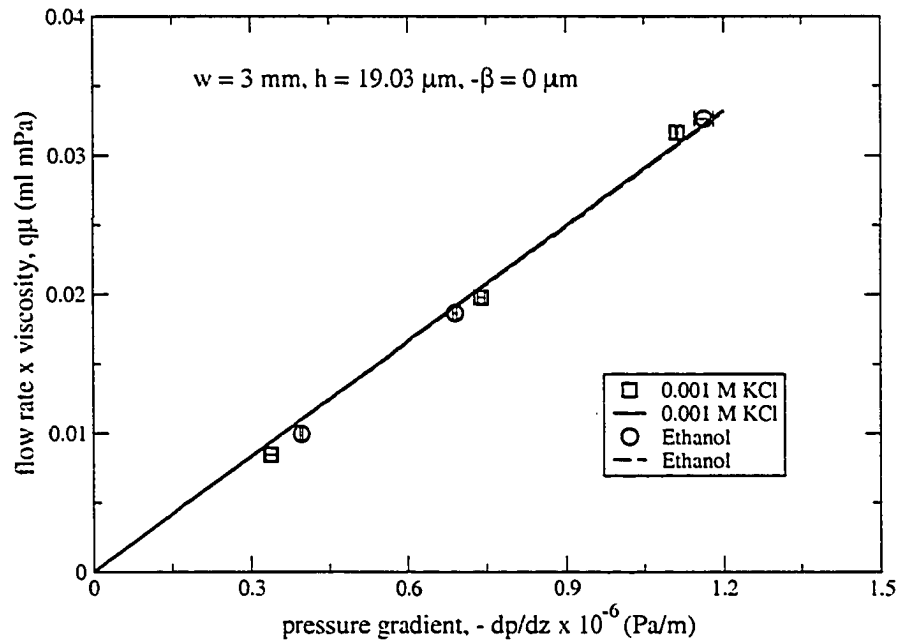
Figure 8.7: Experimental data of 0.001 M KCl and ethanol in -COOH microchannel

Experimental process, results and discussion

In each measurement, the pump was set to maintain a constant flow rate. The flow was considered to have reached a steady state when the readings of the pressure drop was stable. At steady state, the temperature, flow rate and pressure drop were recorded. For a given channel and testing liquid, the measurements for all the parameters were repeated at least twice for the same flow rate in the same day. For a given channel, all data were produced in the same day. The next day, all measurements were repeated and the results were found to be reproducible.

In Figure 8.7, we give out measured experimental data of 0.001 M KCl and ethanol in -COOH microchannel. The solid and dashed lines are fitted function of the product of flow rate and viscosity with respect to pressure gradient for 0.001 M KCl and ethanol, respectively. The solid line is almost identical to the dashed one. This

186

Experimental data for -CH₃ microchannel with non-annealed gold
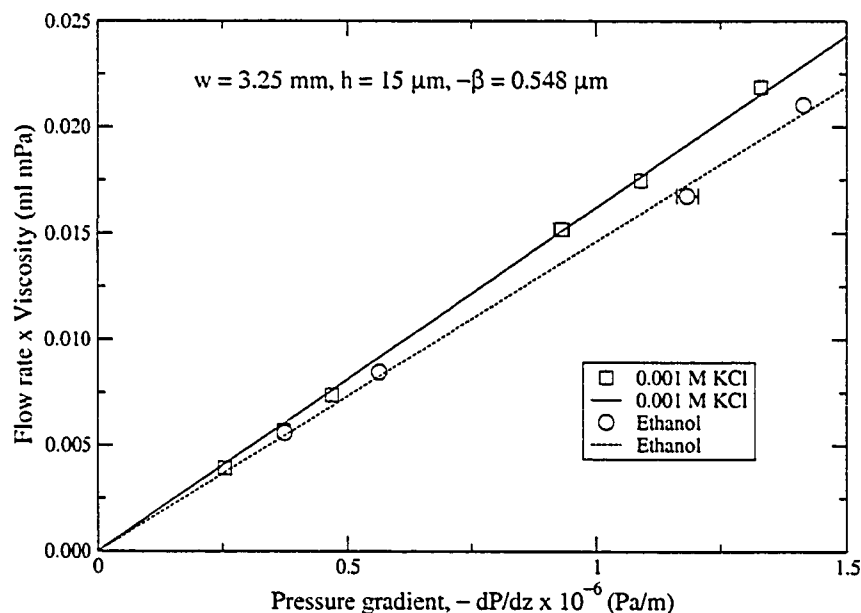
Figure 8.8: Experimental data of 0.001 M KCl and ethanol in -CH₃ microchannel with non-annealed gold

means no slip happen on hydrophilic surface exposing -COOH function groups. In Figure 8.8, we give out the measured experimental data of 0.001 M KCl and ethanol in microchannel with Octadecanethiol [$CH_3(CH_2)_{17}SH$] coated on non-annealed gold. From experimental data, the calculated slip length is 0.548 μm, which is the same order of other experimental results [99, 101, 100]. In Figure 8.9, we provide the measured experimental data of 0.001 M KCl and ethanol in microchannel with Octadecanethiol [$CH_3(CH_2)_{17}SH$] coated on annealed gold. From experimental data, the calculated slip length is 0.355 μm, which is smaller than that of the microchannel with Octadecanethiol [$CH_3(CH_2)_{17}SH$] coated on non-annealed gold. This accords with the contact angle measurements of our previous study [109].

187

Experimental data for -CH₃ microchannel with annealed gold
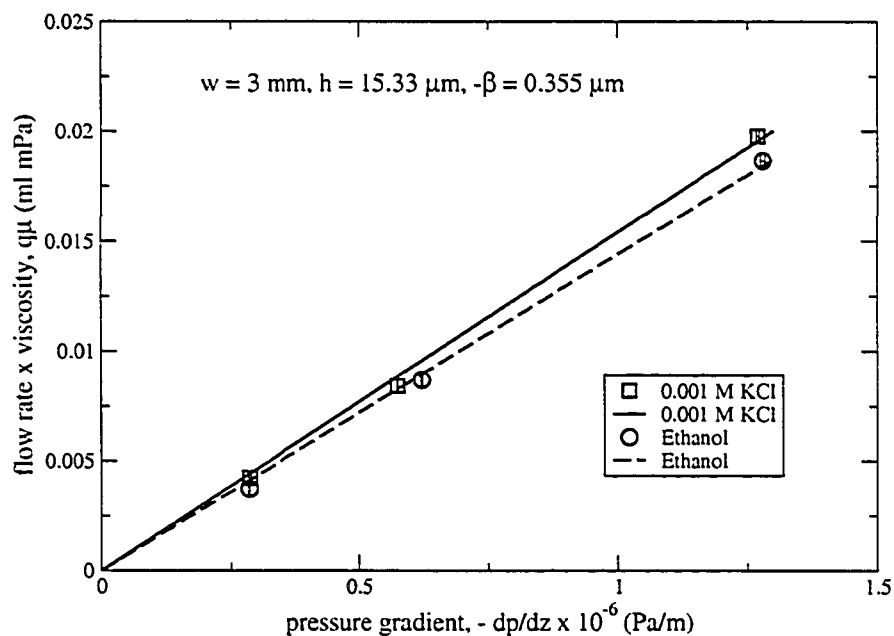
Figure 8.9: Experimental data of 0.001 M KCl and ethanol in -CH$_3$ microchannel with annealed gold

8.4 Conclusions

In this chapter, we experimentally observed slippage of flow on hydrophobic surfaces. The formation of SAMs affects contact angle phenomena of water, and hence the flow behavior of water flow. The slip length of Octadecanethiol SAMs on annealed gold is larger than that of Octadecanethiol SAMs on non-annealed gold, so are the contact angle of water.

188

Chapter 9

Summary and Future Work

9.1 Summary

In this thesis, fundamental research of microfluidics has been performed. On theoretical side,

1. analytical solutions of arbitrary time-dependent electrokinetic slip flow in microchannels with circular, parallel-plate and rectangular cross sections are obtained;

2. oscillating streaming potential and electroviscous effects are studied;

3. a method to determine zeta potential and slip length simultaneously has been proposed, which provides a more accurate model for zeta potential measurements on hydrophobic surfaces at microscale;

4. with the continuity of flow rate and current, nonlinear pressure and electric field distributions in nonuniform microchannels are found;

5. for pressure or electric driven flow through a multilayer membrane, pressure and electric field distributions in each layer are obtained;

6. a nondestructive method to characterize and detect multilayer membranes is proposed;

189

7. a model of electroosmotic flow with moving front is proposed, which includes effects of EDL, wettability and capillary force;

8. effects of four EDL models on ionic distribution in EDL and microflow in the parallel-plate microchannel are studied;

9. circuit and efficiency analysis of electrokinetic battery has been performed.

On experimental side,

1. by means of streaming current and streaming potential, two novel designs of electrokinetic battery consisting of an array of microchannels are proposed [108];

2. preliminary experimental results confirm the feasibility of electrokinetic battery;

3. based on long-term experimental observation, a mobile ion drain method to increase surface charge density is used to improve efficiency of electrokinetic battery;

4. a promising slip coating SAMs is proposed;

5. slippage of flow on hydrophobic SAMs is observed by our experimental system and corresponding slip lengths are determined.

9.2 Future work

Microfluidics is a promising and developing area. Related physical and chemical phenomena are waiting for being revealed and explained. It is anticipated that further study on both theory and experiments would be helpful. On the theoretical side,

1. based on a deeper understanding of interactions between liquid molecules and solid surfaces, we can find the quantitative relation between slip length and contact angle (or wettability);

2. by considering effects of inlet and outlet of microchannels on ionic distribution, we can obtain a more precise prediction of electrokinetic flow in the entire microchannel;

3. we should extend the model of electroosmotic flow with moving front into more complex geometries, such as rectangular microchannel, T-shape microchannel;

4. with a better understanding of EDL mechanism, we will find ways to improve efficiency of the electrokinetic battery;

5. we also should extend our current research area microfluidics to nanofluidics and biofluidics.

On the experimental side,

1. to support theoretical study, we will systematically build the relationship between slip length and contact angle for various coatings, such as SAMs, polymers and plasma modified surfaces;

2. to improve efficiency of the electrokinetic battery, we will test electrokinetic battery made of different materials;

3. to study effects of surfaces on efficiency of the electrokinetic battery, we will change solid surfaces of the electrokinetic battery by means of various surface modification methods.

Bibliography

[1] Mems 1999-emerging applications and markets. Technical report, System, 1999.

[2] N. T. Nguyen, X. Y. Huang, and T. K. Chuan. Mems-micropumps: A review. *J. Fluid Eng. - T ASME*, 124:384–392, 2002.

[3] S. Shoji and M. Esashi. Microflow devices and systems. *J. Micromech. Microeng.*, 4:157–171, 1994.

[4] P. Gravesen, J. Branebjerg, and O. S. Jensen. microfluidics- a review. *J. Micromech. Microeng.*, 3:168–182, 1993.

[5] F. K. Jiang, Y. C. Tai, C. M. Ho, and W. J. Li. A micromachined polysilicon hot-wire snemometer. In *Tech. Dig. Proc. Solid-State Sens. Actuator Workshop*, pages 264–267, Cleveland Height, OH, 1994.

[6] J. Liu, Y. C. Tai, K. Hong, and C. M. Ho. Mems for presure distribution studies of gaseous flows in microchannel. In *An Investigation of Micro Structures, sensors, Actuators, Machines and Systems.*, pages 110–115, New York, 1996.

[7] J. Fraden. *AIP Handbook of Mordern Sensors*. New York, 1993.

[8] F. K. Jiang, Y. C. Tai, B. Gupta, R. Goodman, S. Tung, J. Huang, and C. M. Ho. A surface-micromachined shear-stress imager. In *An Investigation of Micro Structures, sensors, Actuators, Machines and Systems.*, pages 110–115, New York, 1996.

[9] F. M. White. *Fluid Mechanics*. McGraw-Hill, 1986.

[10] S. F. Bart, L. S. Tavrow, M. Mehregany, and J. H. Lang. Microfabricated electrohydrodynamic pumps. *Sen. Actuators A*, 21-23:193–197, 1990.

192

[11] D. J. Harrison, A. Manz, and P. G. Glavina. Electroosmotic pumping within a chemical sensor system integrated on silicon. In *Proc. of Inter. Conf. on Solid-State Sensor and Actuator Transducers'91*, pages 792–795, 1991.

[12] H. Matsumoto and J. E. Colgate. Preliminary investigation of micropumping based on electrical control of interfacial tension. In *IEEE 3rd Int. workshop on MEMS (MEMS'90)*, pages 105–110, 1990.

[13] J. Lee and C. J. Kim. Liquid micromotor driven by continuous electrowetting. In *IEEE 11th Int. workshop on MEMS (MEMS'98)*, pages 538–543, 1998.

[14] P. J. Blackshear. Implantable drug-delivery systems. *Sci. Am.*, 241:52–59, 1979.

[15] R. D. Penn, J. A. Paice, W. Gottschalk, and A. D. Ivankovich. Cancer pain relief using chronic morphine infusion - early experience with programmable implanted drug pump. *J. Neurosurg.*, 61:302–306, 1984.

[16] C. E. Hunt, C. A. Desmond, D. R. Ciarlo, and W. J. Benett. Direct bonding of micromachined silicon wafers for laser diode heat exchanger applications. *J. Micromech. Microeng.*, 1(3):152–156, 1991.

[17] C. Harris, M. Despa, and K. Kelly. Design and fabrication of a cross flow micro heat exchanger. *J. Microelectromech. Syst.*, 9(4):502–508, 2000.

[18] D. J. Harrison, K. Fluri, K. Seiler, Z. H. Fan, C. S. Effenhauser, and A. Manz. Micromachining a miniaturized capillary electrophoresis-based chemical-analysis system on a chip. *Science*, 261:895–897, 1993.

[19] P. C. H. Li and D. J. Harrison. Transport, manipulation, and reaction of biological cells on-chip using electrokinetic effects. *Anal. Chem.*, 69:1564–1568, 1997.

[20] K. Seiler, Z. H. Fan, K. Fluri, and D. J. Harrison. Electroosmotic pumping and valveless control of fluid flow within a manifold of capillaries on a glass chip. *Anal. Chem.*, 66:3485–3491, 1994.

[21] G. Ocbvirk, M. Munroe, T. Tang, R. Oleschuk, K. Westra, and D. J. Harrison. Electrokinetic control of fluid flow in native poly(dimethylsiloxane) capillary electrophoresis devices. *Electrophoresis*, 21:107–115, 2000.

[22] A. Hibara, M. Tokeshi, K. Uchiyama, H. Hisamoto, and T. Kitamori. Integrated multilayer flow system on a microchip. *Anal. Sci.*, 17:89–93, 2001.

[23] B. H. Weigl, R. L. Bardell, and C. R. Cabrera. Lab-on-a-chip for drug development. *Adv. Drug Delivery Rev.*, 55:349–377, 2003.

[24] G. T. A. Kovacs. *Micromachined transducers sourcebook*. McGraw-Hill, 1998.

[25] J. C. McDonald, D. C. Duffy, J. R. Anderson, D. T. Chiu, H. Wu, O. J. Schueller, and G. M. Whitesides. Fabrication of microfluidic systems in poly(dimethylsiloxane). *Electrophoresis*, 21(1):27–40, 2000.

[26] D. J. Beebe, J. S. Moore, Q. Yu, R. H. Liu, M. L. Kraft, B. H. Jo, and C. Devadoss. Microfluidic tectonics: a comprehensive construction platform for microfluidic systems. *Proc. Natl. Acad. Sci. USA*, 79(25):13488–13493, 2000.

[27] H. Becker and L. E. Locascio. Polymer microfluidic devices. *Talanta*, 56:267–287, 2002.

[28] C. M. Ho and Y. C. Tai. Micro-electro-mechanical-systems (mems) and fluid flow. *Annu. Rev. Fluid Mech.*, 30:579–612, 1998.

[29] J. Israelachvili. *Intermolecular and surface forces*. New York Academic., 2nd ed edition, 1991.

[30] F. F. Reuss. *Memoires de la Societé Imperiale de naturalistes de Moscou*, 2:327, 1809.

[31] G. Quinke. *Pogg. Ann. Physik*, 107:1, 1859.

[32] J. Lyklema. *Fundamentals of Interface and Colloid Science*, volume II. Academic Press, 1995.

[33] R. J. Hunter. *Introduction to Modern Colloid Science*. Oxford Science Publication, 1993.

[34] R. J. Hunter. *Foundations of colloid science*. Oxford University Press, New York, 2nd ed. edition, 2001.

[35] H. L. F. Helmholtz. *Wied. Ann.*, 7:337, 1879.

[36] G. Gouy. *J. Phys. Radium*, 9:457, 1910.

[37] D. L. Chapman. *Phil. Mag.*, 25:475, 1913.

[38] J. H. Masliyah. *Electrokinetic Transport Phenomena*. Alberta Oil Sands Technology and Research Authority, 1994.

[39] H. Greberg and R. Kjellander. Charge inversion in electric double layers and effects of different sizes for counterions and coions. *J. Chem. Phys.*, 108:2940–2953, 1998.

[40] E. González-Tovar, M. Lozada-Cassou, and W. Olivares. Electrokinetic flow in ultrafine slits - ionic size effects. *J. Chem. Phys.*, 94:2219–2231, 1991.

[41] W. Olivares, B. Sulbarán, and M. Lozada-Cassou. Electrokinetic transport-coefficients for confined electrolytes - ionic concentration effect. *J. Phys. Chem.*, 97:4780–4785, 1993.

[42] W. Olivares, B. Sulbarán, and M. Lozada-Cassou. Static and transport-properties of symmetrical and asymmetric in micropores at fixed surface-potential. *J. Chem. Phys.*, 103:8179–8188, 1995.

[43] P. Zaini, H. Modarress, and G. A. Mansoori. The concentrations of electrolytes in charged cylindrical pores: the hydrostatic hypernetted chain/mean sphearical approximation. *J. Chem. Phys.*, 104:3382–3840, 1996.

[44] C. W. Outhwaite, L. B. Bhuiyan, and S. Levine. Theory of electric double layer using a modified poisson-boltzmann equation. *J. Chem. Soc. Faraday Trans II*, 76:1388–1408, 1980.

[45] L. B. Bhuiyan, C. W. Outhwaite, and S. Levine. Numerical solution of a modified poisson-boltzmann equation for 1:2 and 2:1 electrolytes in the diffuse layer. *Molec. Phys.*, 42(6):1271–1290, 1981.

[46] S. L. Carnie and G. M. Torrie. The statistical mechanics of electric double layer. *Adv. Chem. Phys.*, 56:142, 1984.

[47] D. J. Shaw. *Introduction to Colloid and Surface Chemistry*. Butterworths, London, 3rd ed. edition, 1980.

[48] Y. J. Song and T. S. Zhao. Modelling and test of a thermally-driven phase-change nonmechanical micropump. *J. Micromech. Microeng.*, 11:713–719, 2001.

[49] J. N. Pfrahler. *Advances in Thermal Modeling of Electronic Components and Systems*, volume II, Chap.3. ASME Press, New York, 1990.

[50] M. von Smoluchowski. Versuch einer mathematischen theorie der koagulation-skinetik kolloider lösungen. *Z. Phys. Chem.*, 93:129–168, 1918.

[51] M. Smoluchowski. *Krak. Anz.*, page 182, 1903.

[52] P. Debye and E. Hückel. *Physik. Z.*, 24:185, 305, 1923.

[53] C. L. Rice and R. Whitehead. Electrokinetic flow in a narrow cylindrical capillary. *J. Phys. Chem.*, 69:4017–4024, 1965.

[54] S. Levine, J. R. Marriott, and K. Robinson. Theory of electrokinetic flow in a narow parallel-plate channel. *Journal of the Chemical Society-Faraday Trans. II*, 71:1–11, 1975.

[55] D. Burgreen and F. R. Nakache. Electrokinetic flow in ultrafine capillary slits. *J. Phys. Chem.*, 68:1084–1091, 1964.

[56] S. Levine, J. R. Marriott, G. Neale, and N. Epstein. Theory of electrokinetic flow in fine cylindrical capillaries at high zeta-potential. *J. Colloid Interface Sci.*, 52:136–149, 1975.

196

[57] C. Yang, D. Q. Li, and J. H. Masliyah. Modeling forced liquid convection in rectangular microchannels with electrokinetic effects. *Int. J. Heat Mass Transfer*, 41:4229–4249, 1998.

[58] G. M. Mala, D. Li, and J. D. Dale. Heat transfer and fluid flow in microchannels. *Int. J. Heat Mass Transfer*, 40:3079–3088, 1997.

[59] W. R. Bowen and F. Jenner. Electroviscous effect in charged capillaries. *J. Colloid Interface Sci.*, 173:388–395, 1995.

[60] L. Hu, J. D. Harrison, and J. H. Masliyah. Numerical model of electrokinetic flow for capillary electrophoresis. *J. Colloid Interface Sci.*, 215:300–312, 1999.

[61] S. J. liu and J. H. Masliyah. On non-newtonian fluid flow in ducts and porous media. *Chem. Eng. Sci.*, 53(6):1175–1201, 1998.

[62] L. Ren and D. Li. Theoretical studies of microfluidic dispensing processes. *J. Colloid Interface Sci.*, 254(2):384–395, 2002.

[63] F. Bianchi, R. Ferrigno, and H. H. Girault. Finite element simulation of an electroosmotic-driven flow division at a t-junction of microscale dimension. *Anal. Chem.*, 72(9):1987–1993, 2000.

[64] M. M. Rahman and F. Gui. Experimental measurements of fluid flow and heat transfer in microchannel cooling passages in a chip substrate. *Adv. Electron. Packaging*, 4(2):685, 1993.

[65] D. Sinton, L. Ren, and D. Li. Visualization and numerical modelling of microfluidic on-chip injection processes. *J. Colloid Interface Sci.*, 260:431–439, 2003.

[66] L. Ren, D. Li, and W. Qu. Electro-viscous effects on liquid flow in microchannels. *J. Colloid Interface Sci.*, 233:12, 2001.

[67] P. M. Reppert, F. D. Morgan, D. P. Lesmes, and L. Jouniaux. Frequency-dependent streaming potential. *J. Colloid Interface Sci.*, 234:194–203, 2001.

[68] O. Söderman and B. Jönsson. Electro-osmosis: Velocity profiles in different geometries with both temporal and spatial resolution. *J. Chem. Phys.*, 105:10300, 1996.

[69] J. G. Santiago. Electroosmotic flows in microchannels with finite inertial and pressure forces. *Anal. Chem.*, 73:2353, 2001.

[70] J. K. Huan and H.C. Tseng. Transient electrokinetic flow in fine capillaries. *J. Colloid Interface Sci.*, 242:450, 2001.

[71] C. Yang. In F. Tay, editor, *Microfluidics and BioMEMS*. Kluwer Academic, Dordrecht, 2002.

[72] N. Rott. *Theory of Laminar Flow*. Princeton Univ. Press, Princeton, NJ, 1964.

[73] S. Uchida. The pulsating viscous flow superimposed on the steady laminar motion of incompressible fluid in a circular pipe. *ZAMP*, 7:403–421, 1950.

[74] D. G. Drake. On the flow in a channel due to a periodic pressure gradient. *Qt. J. Mech. Appl. Math*, 18:1–10, 1965.

[75] V. O'Brien. Pulsatile fully developed flow in rectangular channels. *Journal of The Franklin Institute*, 300:225–230, 1975.

[76] C. Fan and B. T. Chao. Unsteady, laminar, incompressible flow through rectangular ducts. *ZAMP*, 16:351–360, 1965.

[77] W. Norde and E. E. Rouwendal. Streaming potential measurements as a tool to study protein adsorption-kinetics. *J. Colloid Interface Sci*, 139:169–176, 1990.

[78] A. Ajdari. Electroosmosis on inhomogeneously charged surfaces. *Phys. Rev. Lett.*, 75:755, 1995.

[79] A. Ajdari. Generation of transverse fluid currents and forces by an electric field: Electro-osmosis on charge-modulated and undulated surfaces. *Phys. Rev. E*, 53:4996, 1996.

198

[80] A. D. Stroock, M. Weck, D. T. Chiu, W. T. S. Huck, P. J. A. Kenis, R. F. Ismagilov, and G. M. Whitesides. Pattening electro-osmotic flow with patterned surface charge. *Phys. Rev. Lett.*, 84:3314–3317, 2000.

[81] L. Q. Ren and D. Q. Li. Electroosmotic flow in heterogeneous microchannels. *J. Colloid Interface Sci.*, 243:255–261, 2001.

[82] J. L. Anderson and W. K. Idol. Electroosmosis through pores with nonuniformly charged walls. *Chem. Eng. Commun*, 38:93–106, 1985.

[83] C. A. Keely, T. A. A. M. Van de Goor, and D. McManigill. Modeling flow profiles and dispersion in capillary electrophoresis with nonuniform ζ potential. *Anal. Chem.*, 66:4236–4242, 1994.

[84] A. E. Herr, J. I. Molho, J. G. Santiago, M. G. Mungal, and T. W. Kenny. Electroosmotic capillary flow with nonuniform zeta potential. *Anal. Chem.*, 72:1053–1057, 2000.

[85] D. Y. Kwok and A. W. Neumann. Contact angle measurement and contact angle interpretation. *Adv. Colloid Interface Sci.*, 81:167–249, 1999.

[86] O. I. Vinogradova. Slippage of water over hydrophobic surface. *Int. J. Miner. Process.*, 56:31–60, 1999.

[87] C. L. M. H. Navier. *Mem. Acad. R. Sci. Inst. France*, 1:414, 1823.

[88] S. Goldstein. *Modern Developments in Fluid Dynamics*, volume 2. Dover, 1965.

[89] P. G. de Gennes. Écoulements viscosimétriques de polymères enchevêtrés. *C.R. Acad. Sci. B*, 288:219–220, 1979.

[90] W. L. Li, J. W. Lin, S. C. Lee, and M. D. Chen. Effects of roughness on rarefied gas flow in long microtubes. *J. Micromech. Microeng.*, 12(2):149–156, 2002.

[91] J. C. Harley, Y. F. Huang, H. H. Bau, and J. N. Zemel. Gas-flow in micro-channels. *J. fluid Mech.*, 284:257–274, 1995.

199

[92] A. Beskok and G. E. Karniadakis. A model for flows in channels, pipes and ducts at micro and nano scales. *Microscale Therm. Eng.*, 3:43–77, 1999.

[93] F. Brochard and P. G. de Gennes. Shear-dependent slippage at a polymer r solid interface. *Langmuir*, 8:3033–3037, 1992.

[94] R. Pit, H. Hervet, and L. Léger. Direct experimental evidence of slip in hexadecane: solid interfaces. *Phys. Rev. Lett.*, 85(5):980, July 2000.

[95] T. D. Blake. Slip between a liquid and a solid-tolstoi, d. m. (1952) theory reconsideration. *Colloids Surf.*, 47:135, 1990.

[96] H. Helmoholtz and G. Von Piotrowski. Über reibung tropfbarer flüssigkeiten. *Sitzungsberichte der Kaiserlich Akademie der Wissenschaften*, 40:607–685, 1860.

[97] E. Schnell. Slippage of water over nonwettable surfaces. *J. Appl. Phys.*, 27:1149–1152, 1956.

[98] K. Watanabe, Y. Udagawa, and H. Udagawa. Drage reduction of newtonnian fluid in a circular pipe with highly water-repellant wall. *J. Fluid Mech.*, 381:225–238, 1999.

[99] D. C. Tretheway and C. D. Meinhart. Apparent fluid slip at hydrophobic microchannel walls. *Phys. Fluid*, 14:L9–L12, March 2002.

[100] Y. X. Zhu and S. Granick. Rate-dependent slip of newtonian liquid at smooth surfaces. *Phys. Rev. Lett.*, 87(9):096105-1, August 2001.

[101] N. V. Churaev, J. Ralston, , I. P. Sergeeva, and V. D. Sobolev. Electrokinetic properties of methylated quartz capillaries. *Adv. Colloid Interface*, 96:265–278, 2002.

[102] J. T. Cheng and N. Giordano. Fluid flow through nanometer-scale channels. *Phys. Rev. E*, 65:031206, 2002.

[103] C. Cottin-Bizonne, S. Jurine, J. Baudry, J. Crassous, F. Restagno, and É. Charlaix. Nanorheology: An investigation of the boundary condition at hydrophobic and hydrophilic interfaces. *Eur. Phys. J. E*, 9:47–53, 2002.

[104] P. A. Thompson and S. M. Troian. A general boundary condition for liquid flow at solid surfaces. *Nature*, 389:360–362, September 1997.

[105] J. L. Barrat and L. Bocquet. Large slip effect at a nonwetting fluid-solid interface. *Phys. Rev. Lett.*, 82:4671, 1999.

[106] J. L. Barrat and L. Bocquet. Influence of wetting properties on hydrodynamic boundary conditions at a fluid/solid interface. *Faraday Discuss*, 112:119, 1999.

[107] B. Li and D. Y. Kwok. Discrete boltzmann equation for microfluidics. *Phys. Rev. Lett.*, 19:12450, 2003.

[108] J. Yang, F. Z. Lu, L. W. Kostiuk, and D. Y. Kwok. Electrokinetic microchannel battery by means of electrokinetic and microfluidic phenomena. *J. Micromech. Microeng.*, 13:963–970, 2003.

[109] J. Yang, J. M. Han, K. Isaacson, and D. Y. Kwok. Effects of surface defects, polycrystallinity, and nanostructure of self-assembled monolayers for octadecanethiol adsorbed onto au on wetting and its surface energetic interpretation. *Langmuir*, 19:9231–9238, 2003.

[110] A. Bhattacharyya, J. H. Masliyah, and J. Yang. Oscillating laminar electrokinetic flow in infinitely extended circular microchannels. *J. Colloids Interface Sci.*, 261:12–20, 2003.

[111] J. Yang, A. Bhattacharyya, J. H. Masliyah, and D. Y. Kwok. Oscillating laminar electrokinetic flow in infinitely extended rectangular microchannels. *J. Colloids Interface Sci.*, 261:21–31, 2003.

[112] A. Shadowitz. *The Electromagnetic Field*. Dover, 1975.

[113] G. M. Mala, D. Li, C. Werner, H. J. Jacobasch, and Y. B. Ning. Flow characteristics of water through a microchannel between two parallel plates with electrokinetic effects. *Int. J. Heat Liquid Flow*, 18:489–496, 1997.

[114] J. V. Beck. *Heat Conduction Using Green's Functions*. Hemisphere, 1992.

[115] P. Mazur and J. T. G. Overbeek. *Rec. Trav. Chim.*, 70:83, 1951.

[116] M. Abramowitz and I.A. Stegun. *Handbook Of Mathematical Functions*. Dover, New York, 1972.

[117] R. G. Packard. *J. Chem. Phys.*, 21:303–307, 1953.

[118] J. S. Newman. *Electrochemical Systems*. Prentice Hall, Englewood Cliffs, 2nd, ed edition, 1991.

[119] J. Yang and D. Y. Kwok. Time-dependent laminar electrokinetic slip flow in infinitely extended rectangular microchannels. *J. Chem. Phys.*, 118:354–363, 2003.

[120] J. Yang and D. Y. Kwok. A new method to determine zeta potential and slip coefficient simultaneously. *J. Phys. Chem. B*, 106:12851–12855, 2002.

[121] J. Yang and D. Y. Kwok. Effect of liquid slip in electrokinetic parallel-plate microchannel flow. *J. Colloids Interface Sci.*, 260:225–233, 2003.

[122] L. M. Fu, J. Y. Lin, and R. J. Yang. Analysis of electroosmotic flow with step change in zeta potential. *J. Colloid Interface Sci.*, 258:266–275, 2003.

[123] A. Szymczyk, P. Fievet, J. C. Reggiani, and J. Pagetti. Characterisation of surface properties of ceramic membranes by streaming and membrane potential. *J. Membr. Sci.*, 146:277–284, 1998.

[124] J. Kim K., A. G. Fane, M. Nystrom, A. Pihlajamaki, W. R. Bowen, and H. Mukhtar. Evaluation of electroosmosis and streaming potential for measurement of electric charges of polymeric membranes. *J. Membr. Sci.*, 116:149–159, 1996.

[125] M. Pontié, X. Chasseray, D. Lemordant, and J. M. Lainé. The streaming potential method for the characterization of ultrafiltration organic membranes and the control of cleaning treatments. *J. Membr. Sci.*, 129:125–133, 1997.

[126] D. Möckel, E. Staude, M. Dal-Cin, K. Darcovich, and M. Guiver. Tangential flow streaming potential measurements: Hydrodynamic cell characterization and zeta potentials of carboxylated polysulfone membranes. *J. Membr. Sci.*, 145:221, 1998.

[127] J. A. Iba nez, J. Forte, A. Hernandez, and F. Tejerina. Streaming potential and phenomenological coefficients in nuclepore membranes. *J. Membr. Sci.*, 36:45, 1988.

[128] P. Fievet, A. Szymczyk, C. Labbez, B. Aoubiza, y C. Simon, z A. Foissy, and J. Pagett. Determining the zeta potential of porous membranes using electrolyte conductivity inside pores. *J. Colloid Interface Sci.*, 235:383–390, 2001.

[129] W. Koh and J. L. Anderson. Electroosmosis and electrolyte conductance in charged microcapillaries. *AIChE J.*, 21:1176, 1975.

[130] C. K. Lee and J. Hong. Characterization of electric charges in microporous membranes. *J. Membr. Sci.*, 39:79, 1988.

[131] W. R. Bowen and H. Mukhtar. Properties of microfiltration membranes - the surface electrochemistry of mixed-oxide ceramic membranes. *Colloids Surf. A*, 81:93, 1993.

[132] A. Vernhet, M. N. Bellon-Fontaine, and A. Doren. Comparison of 3 electrokinetic methods to determine the zeta-potential of solid surfaces. *J. Chim. Phys.*, 91:1728, 1994.

[133] M. Mullet, P. Fievet, J. C. Reggiani, and Pagetti. Surface electrochemical properties of mixed oxide ceramic membranes: zeta-potential and surface charge density. *J. Membr. Sci.*, 123:255, 1997.

203

[134] A. Szymczyk, P. Fievet, J. C. Reggiani, and J. Pagetti. Determination of the filtering layer electrokinetic properties of multi-layer ceramic membrane. *Desalination*, 116:81–88, 1998.

[135] A. Szymczyk, C. Labbez, P. Fievet, B. Aoubiza, and C. Simon. Streaming potential through multilayer membranes. *AICHE J*, 47:2349–2358, 2001.

[136] J. Wang, Z. Liu, Q. H. He, F. X. Ding, and N. J. Yuan. Determination of zeta-potential by measuring electroosmosis flux in an alternating electric field and its application in the study of membrane fouling. *Separ. Sci. Technol.*, 35:1195–1206, 2000.

[137] Z. Liu, , H. Yang, Z. Huang, J. Wang, F. X. Ding, and N. J. Yuan. Multichannel flow electrophoresis in an alternating electric field. *Separ. Sci. Technol.*, 31:2257–2271, 1996.

[138] J. F. Osterle. Electrokinetic energy conversion. *J. Appl. Mech.*, 31:161–164, 1964.

[139] F. A. Morrison and J. F. Osterle. Electrokinetic energy conversion in ultrafine capillaries. *J. Chem. Phys.*, 43:2111–2115, 1965.

[140] C. Werner, H. Körber, R. Zimmermann, S. Dukhin, and H.-J. Jacobasch. Extended electrokinetic characterization of flat solid surface. *J. Colloid Interface Sci.*, 208:329–346, 1998.

[141] R. E. Sonntag, C. Borgnakke, and G. J. Van Wylen. *Fundamentals of Thermodynamics, Fifth Edition*. John Wiley and Sons, Inc., 1998.

[142] D. Erickson, D. Q. Li, and C. Werner. An improved method of determining the ζ-potential and surface conductance. *J. Colloid Interface Sci.*, 232:186–197, 2000.

[143] D. R. Reyes, D. Iossifidis, P. A. Auroux, and A. Manz. Micro total analysis systems. 1. introduction, theory and technology. *Anal. Chem.*, 74:2623–2636, 2002.

[144] X. H. Huang, M.J. Gordon, and R. N. Zare. Current-monitoring method for measuring the electroosmotic flow rate in capillary zone electrophoresis. *Anal. Chem.*, 60:1837–1838, 1988.

[145] S. L. R. Barker, M. J. Tarlov, H. Canavan, J. J. Hickman, and L. E. Locascio. Plastic microfluidic devices modified with polyelectrolyte multilayers. *Anal. Chem.*, 72:4899–4903, 2000.

[146] P. H. Paul, M. G. Garguilo, and D. J. Rakestraw. Imaging of pressure- and electrokinetically driven flows through open capillaries. *Anal. Chem.*, 70:2459–2467, 1998.

[147] D. C. Duffy, J. C. Mcdonald, O. J. A. Schueller, and G. M. Whitesides. Rapid prototyping of microfludic systems in poly(dimethylsiloxane). *Anal. Chem.*, 70:4974–4984, 1998.

[148] J. Yang and D. Y. Kwok. Analytical treatment of flow in infinitely extended circular microchannels and the effect of slippage to increase flow efficiency. *J. Micromechan. Microeng.*, 13:115–123, 2003.

[149] N. A. Patankar and H. H. Hu. Numerical simulation of electroosmotic flow. *Anal. Chem.*, 70:1870–1881, 1998.

[150] V. Mengeaud, J. Josserand, and H. H. Girault. Mixing processes in a zigzag microchannel: Finite element simulation and optical study. *Anal. Chem.*, 74:4279–4286, 2002.

[151] H. Schulz, D. Lyebyedyev, H. C. Scheer, K. Pfeiffer, G. Bleidiessel, G. Grützner, and J. Ahopelto. Master replication into thermosetting polymers for nanoimprinting. *J. Vac. Sci. Technol. B*, 18:3582–3585, 2000.

[152] T. Borzenko, M. Tormen, G. Schmidt, L. W. Molenkamp, and H. Janssen. Polymer bonding process for nanolithography. *Appl. Phys. Lett.*, 79:2246–2248, 2001.

205

[153] R. W. Jaszewski, H. Schift, J. Gobrecht, and P. Smith. Hot embossing in polymers as a direct way to pattern resist. *Microelectron. Eng.*, 41/42:575–578, 1998.

[154] B. A. Grzybowski, R. Haag, N. Bowden, and G. M. Whitesides. Generation of micrometer-sized patterns for microanalytical applications using a laser direct-write method and microcontact printing. *Anal. Chem.*, 70:4645–4652, 1998.

[155] E. Delamarche, A. Bernard, H. Schmid, B. Michel, and H. Biebuyck. Patterned delivery of immunoglobulins to surfaces using microfluidic networks. *Science*, 276:779–781, 1997.

[156] Y. Xia and G. M. Whitesides. Soft lithography. *Angew. Chem. Int. Ed.*, 37:550, 1998.

[157] R. Lucas. *Kolloid Z.*, 23:15, 1918.

[158] E. W. Washburn. The dynamics of capillary flow. *Phys. Rev.*, 17:273, 1921.

[159] E. K. Rideal. *Philos. Mag. VI*, 44:1152, 1922.

[160] A. A. Duarte, D. E. Strier, and D. H. Zanette. The rise of a liquid in a capillary tube revisited: A hydrodynamical approach. *Am. J. Phys.*, 64:413, 1996.

[161] D. Quéré. Inertial capillarity. *Euro. Phys. Lett.*, 39:533, 1997.

[162] J. Szekely, A. W. Neumann, and Y. K. Chuang. The rate of capillary penetration and the applicability of the washburn equation. *J. Colloid Interface Sci.*, 35:273, 1971.

[163] G. L. Batten. Liquid imbibition in capillaries and packed-beds. *J. Colloid Interface Sci.*, 102:513, 1984.

[164] A. Hamraoui, K. Thuresson, T. Nylander, K. Eskilson, and V. Yaminsky. Dynamic wetting and dewetting by aqueous solutions containing amphiphilic compounds. *Prog. Colloid Polymer Sci.*, 116:113–119, 2000.

[165] B. V. Zhmud, F. Tiberg, and K. Hallstensson. Dynamics of capillary rise. *J. Colloid Interface Sci.*, 228:263, 2000.

[166] N. Ichikawa and Y. Satoda. Interface dynamics of capillary flow in a tube under negligible gravity condition. *J. Colloid Interface Sci.*, 162:350, 1994.

[167] D. Erickson, D. Q. Li, and C. B. Park. Numerical simulations of capillary-driven flows in nonuniform cross-section capillaries. *J. Colloid Interface Sci.*, 250:422–430, 2002.

[168] S. Levine, J. Lowndes, E. J. Watson, and G. Neale. A theory of capillary rise of a liquid in a vertical cylindrical tube and in a parallel-plate channel: Washburn equation modified to account for the meniscus with slippage at the contact line. *J. Colloid Interface Sci.*, 73:136, 1980.

[169] Y. D. Shikhmurzaev. Dynamic contact angles and flow in vincinity of moving contact line. *AICHE J.*, 42:601, 1996.

[170] M. W. J. Prins, W. J. J. Welters, and J. W. Weekamp. Fluid control in multi-channel structures by electrocapillary pressure. *Science*, 291:277, 2001.

[171] B. Zhao, J. S. Moore, and D. J. Beebe. Surface-directed liquid flow inside microchannels. *Science*, 291:1023, 2001.

[172] J. Yang and D. Y. Kwok. Microfluid flow in circular microchannel with electrokinetic effect and navier's slip condition. *Langmuir*, 19:1047–1053, 2003.

[173] D. M. Tolstoi. *Dokl. Akad. Nauk. SSSR.*, 85:1089, 1952.

[174] N. V. Churaev, V. D. Sobolev, and A. N. Somov. Slippage of liquids over lyophobic solid-surfaces. *J. Colloid Interface Sci.*, 97:574, 1984.

[175] J. Lowndes. The numerical simulation of the steady movement of a fluid meniscus in a capillary tube. *J. Fluid Mech.*, 101:631, 1980.

[176] B. Jamnik and V. Vlachy. Monte-carlo and possion-boltzmann study of electrolyte exclusion from charged cylindrical micropores. *J. Am. Chem. Soc.*, 115:660–666, 1993.

207

[177] L. Guldbrand, B. Jönsson, H. Wennerström, and P. Linse. Electrical double layer forces a monte-carlo study. *J. Chem. phys.*, 80:2221, 1984.

[178] D. Bratko, B. Jönsson, and H. Wennerström. Electrical double-layer interfactions with image charges. *Chem. Phys. Lett.*, 128:449, 1986.

[179] J. P. Valleau, R. Ivkov, and G. M. Torrie. Colloid stability - the forces between charged surfaces in an electrolyte. *J. Chem. Phys.*, 95:520, 1991.

[180] W. Y. Lo, K. Y. Chan, and K. L. Mok. Molecular-dynamics simulation of ions in charged capillaries. *J. Phys. Condens. Matter*, 6:A145, 1994.

[181] W. Y. Lo, K. Y. Chan, M. Lee, and K. L. Mok. Molecular simulation of electrolytes in nanopores. *J. Electroanal. Chem.*, 450:265, 1998.

[182] M. Plischke and D. Henderson. The primitive model of the electric double-layer-nonsymmetric electrolytes. *J. Chem. Phys.*, 90:5738, 1989.

[183] D. Henderson and M. Plischke. Pair and singlet correlation-functions of inhomogeneous fluids calculated using the ornstein-zernike equation. *J. Phys. Chem.*, 92:7177, 1988.

[184] C. W. Outhwaite and L. B. Bhuiyan. A further treatment of the exclusion-volume term in the modified poisson-boltzmann theory of electric double layer. *J. Chem. Soc. Faraday Trans II*, 78:775–785, 1982.

[185] C. W. Outhwaite and L. B. Bhuiyan. An improved modified poisson-boltzmann theory of electric double layer. *J. Chem. Soc. Faraday Trans II*, 79:707–718, 1983.

[186] Q.Z. Cui, Y.X. Zhou, G. Y. Zhu, and E. K. Wang. The application of the mpb4 theory to the interface between two immiscible electrolyte solutions .4. the differential capacitance of the water/nitrobenzene interface in the presence of 2:2 electrolyte. *Chinese Chem. Lett.*, 7:647–650, 1996.

[187] Q.Z. Cui, Y.X. Zhou, G. Y. Zhu, and E. K. Wang. The application of the mpb4 theory to the interface between 2 immiscible electrolyte-solutions . 2. the

208

differential capacitance of the water 1,2-dichloroethane interface. *J Electroanal. Chem.*, 383:7–12, 1995.

[188] Q.Z. Cui, Y.X. Zhou, G. Y. Zhu, and E. K. Wang. The application of the mpb4 theory to the interface between 2 immiscible electrolyte-solutions . 1. the differential capacitance of the water nitrobenzene interface. *J Electroanal. Chem.*, 372:15–19, 1994.

[189] P. Dutta and A. Beskok. Analytical solution of combined electroosmotic/pressure driven flows in two-dimensional straight channels: finite debye layer effects. *Anal. Chem.*, 73:1979–1986, 2001.

[190] D. Henderson and L. Blum. Some exact results and application of mean spherical approximation to charged hard spheres near a charged hard wall. *J. Chem. Phys.*, 69:5441, 1978.

[191] G. M. Torrie and J. P. Valleau. Monte-carlo study of an electrical double-layer. *Chem. Phys. Lett.*, 65:343, 1979.

[192] C. W. Outhwaite. Numerical solution of a poisson-boltzmann theory for a primitive model electrolyte with size and charge asymmetric. *J. Chem. Soc. Faraday Trans II*, 83:949–959, 1987.

[193] C. D. Bain and G. M. Whitesides. Modeling organic-surfaces with self-assembled monolayers. *Angew. Chem. Int. Ed.*, 28(4):506, 1989.

[194] G. M. Whitesides and P. E. Laibinis. Wet chemical approaches to the characterization of organic-surfaces-self-assembled monolayers, wetting, and the physical organic-chemistry of the solid liquid interface. *Langmuir*, 6:87, 1990.

[195] A. Ulman. *Introduction to Thin Organic Films: From Langmuir-Blodgett to Self-Assembly.* Academic Press, Boston, 1991.

[196] L. H. Dubois and R. G. Nuzzo. Synthesis, structure, and properties of model organic-surfaces. *Ann. Rev. Mater. Sci.*, 43:437, 1992.

[197] W. C. Bigelow, D. L. Pickett, and W. A. Zisman. Oleophobic monolayers. i. films adsorbed from solution in nonpolar liquids. *J. Colloid Interface*, page 513, 1946.

[198] R. L. Shuler and W. A. Zisman. Wave-damping and film-pressure studies of polydimethylsiloxane monolayers on organic liquid substrates. *J. Phys. Chem.*, pages 1397–1405, 1975.

[199] M. K. Bernett and W. A. Zisman. Surface chemical properties of highly fluorinated polymers. *Adv. Chem. Ser.*, 8:199–211, 1975.

[200] R. G. Nuzzo, F. A. Fusco, and D. L. Allara. Spontaneously organized molecular assemblies. 3. preparation and properties of solution adsorbed monolayers of organic disulfides on gold surfaces. *J. Am. Chem. Soc.*, 109:2358–2368, 1987.

[201] D. Y. Kwok, H. Ng, and A. W. Neumann. Experimental study on contact angle patterns: Liquid surface tensions less than solid surface tensions. *J. Colloid Interface Sci.*, 225(2):323, 2000.

[202] D. Y. Kwok, T. Gietzelt, K. Grundke, H. J. Jacobasch, and A. W. Neumann. Contact angle measurements and contact angle interpretation .1. contact angle measurements by axisymmetric drop shape analysis and a goniometer sessile drop technique. *Langmuir*, 13:2880, 1997.

[203] D. Y. Kwok, R. Lin, M. Mui, and A. W. Neumann. Low-rate dynamic and static contact angles and the determination of solid surface tensions. *Colloids Surfaces A: Physicochem. Eng. Aspects*, 116:63, 1996.

[204] D. Y. Kwok, C. N. C. Lam, A. Li, A. Leung, R. Wu, E. Mok, and A. W. Neumann. Measuring and interpreting contact angles: a complex issue. *Colloids Surfaces A: Physicochem. Eng. Aspects*, 142:219, 1998.

[205] D. Y. Kwok, C. N. C. Lam, and A. W. Neumann. Wetting behavior and solid surface tensions for a 70 : 30 copolymer of polystyrene and poly(methyl methacrylate). *Colloid J.*, 62(3):324, 2000.

[206] D. Y. Kwok, R. Wu, A. Li, and A. W. Neumann. Contact angle measurements and interpretation: wetting behavior and solid surface tensions for poly(alkyl methacrylate) polymers. *J. Adhesion Sci. Tech.*, 14(5):719, 2000.

[207] D. Y. Kwok, A. Leung, A. Li, C. N. C. Lam, R. Wu, and A. W. Neumann. Low-rate dynamic contact angles on poly(n-butyl methacrylate) and the determination of solid surface tensions. *Colloid Polym. Sci.*, 276:459, 1998.

[208] D. Y. Kwok, A. Leung, C. N. C. Lam, A. Li, R. Wu, and A. W. Neumann. Low-rate dynamic contact angles on poly(methyl methacrylate) and the determination of solid surface tensions. *J. Colloid Interface Sci.*, 206:44, 1998.

[209] D. Y. Kwok, C. N. C. Lam, A. Li, K. Zhu, R. Wu, and A. W. Neumann. Low-rate dynamic contact angles on polystyrene and the determination of solid surface tensions. *Polym. Eng. Sci.*, 38:1675, 1998.

[210] D. Y. Kwok, A. Li, and A. W. Neumann. Low-rate dynamic contact angles on poly(methyl methacrylate/ethyl methacrylate, 30/70) and the determination of solid surface tensions. *J. Polym. Sci. B: Polym. Phys.*, 16:2039, 1999.

[211] Y. Rotenberg, L. Boruvka, and A. W. Neumann. Determination of surface-tension and contact-angle from the shapes of axisymmetric fluid interfaces. *J. Colloid Interface Sci.*, 93:169, 1983.

[212] P. Cheng, D. Q. Li, L. Boruvka, Y. Rotenberg, and A. W. Neumann. Automation of axisymmetric drop shape-analysis for measurement of interfacial-tensions and contact angles. *Colloids Surfaces*, 43:151, 1990.

[213] S. Lahooti, O. I. del Río, P. Cheng, and A. W. Neumann. Axisymmetric drop shape analysis. In J. K. Spelt and A. W. Neumann, editors, *Applied Surface Thermodynamics*, pages 441–507. Marcel Dekker Inc., New York, 1996.

[214] D. Y. Kwok, C. J. Budziak, and A. W. Neumann. Measurements of statitic and low-rate dynamic contact angles by means of an automated capillary rise technique. *J. Colloid Interface Sci.*, 173:143, 1995.

[215] P. E. Laibinis, G. M. Whitesides, D. L. Allara, Y. T. Tao, A. N. Parikh, and R. G. Nuzzo. Comparison of the structures and wetting properties of self-assembled monolayers of n-alkanethiols on the coinage metal surfaces, copper, silver, and gold. *J. Am. Chem. Soc.*, 113:7152, 1991.

[216] P. E. Laibinis, R. G. Nuzzo, and G. M. Whitesides. Structure of monolayers formed by coadsorption of two n-alkanethiols of different chain lengths on gold and its relation to wetting. *J. Phys. Chem.*, 96:5097, 1992.

[217] A. W. Neumann. Contact angles and their temperature dependence: thermodynamic status, measurement, interpretation and application. *Adv. Colloid Interface Sci.*, 4:105, 1974.

[218] W. Guo and G. K. Jennings. Use of underpotentially deposited metals on gold to affect the surface-catalyzed formation of polymethylene films. *Langmuir*, 18:3123, 2002.

[219] W. Haiss, D. Lackey, J. K. Sass, and K. H. Bescoke. Atomic resolution scanning tunneling microscopy images of au(111) surfaces in air and polar organic-solvents. *J. Chem. Phys.*, 95:2193, 1991.

[220] E. Delamarche, B. Michel, H. Kang, and Ch. Gerber. Thermal stability of self-assembled monolayers. *Langmuir*, 10:4103, 1994.

[221] Y. S. Shon and T. R. Lee. Chelating self-assembled monolayers on gold generated from spiroalkanedithiols. *Langmuir*, 15:1136, 1999.

[222] D. J. Vanderah, C. W. Meuse, V. Silin, and A. L. Plant. Synthesis and characterization of self-assembled monolayers of alkylated 1-thiahexa(ethylene oxide) compounds on gold. *Langmuir*, 14:6916, 1998.

[223] R. D. Weinstein, D. Yan, and G. K. Jennings. Self-assembled monolayer films from liquid and supercritical carbon dioxide. *Ind. Eng. Chem. Res.*, 40:2046, 2001.

[224] J. Drelich and J. D. Miller. Examination of neumann's equation-of-state for interfacial tensions. *J. Colloid Interface Sci.*, 167:217, 1994.

[225] A. Amirfazli, D. Y. Kwok, J. Gaydos, and A. W. Neumann. Line tension measurements through drop size dependence of contact angle. *J. Colloid Interface Sci.*, 205:1, 1998.

[226] J. Drelich, J. L. Wilbur, J. D. Miller, and G. M. Whitesides. Contact angles for liquid drops at a model heterogeneous surface consisting of alternating and parallel hydrophobic/hydrophilic strips. *Langmuir*, 12:1913, 1996.

[227] J. Baudry, E. Charlaix, A. Tonck, and D. Mazuyer. Experimental evidence for a large slip effect at a nonwetting fluid-solid interface. *Langmuir*, 17:5232, 2001.

[228] D. R. Lide, editor. *CRC handbook of chemistry and physics.* Cleveland : Chemical Rubber Pub. Co., 82nd edition, 2001/2002.

[229] E. Hatschek. *The viscosity of liquids.* London, G. Bell and sons, ltd., 1928.